ORNL/SPR-2025/4089
M2LW-25OR0403043

Light Water Reactor Sustainability Program

Reliability Analysis of the Concrete Biological Shield in Aging Nuclear Infrastructure Under Accidental Loads

Mohammed Alnaggar[1]
Samantha Sabatino[1]
Yann Le Pape[1]
Carlo Parisi[2]
Zhenglai Shen[1]
Abdo Elmeliegy[2]
[1]Oak Ridge National Laboratory
[2]Idaho National Laboratory

August 2025

U.S. Department of Energy
Office of Nuclear Energy

ORNL/SPR-2025/4089
M2LW-25OR0403043

Reliability Analysis of the Concrete Biological Shield in Aging Nuclear Infrastructure Under Accidental Loads

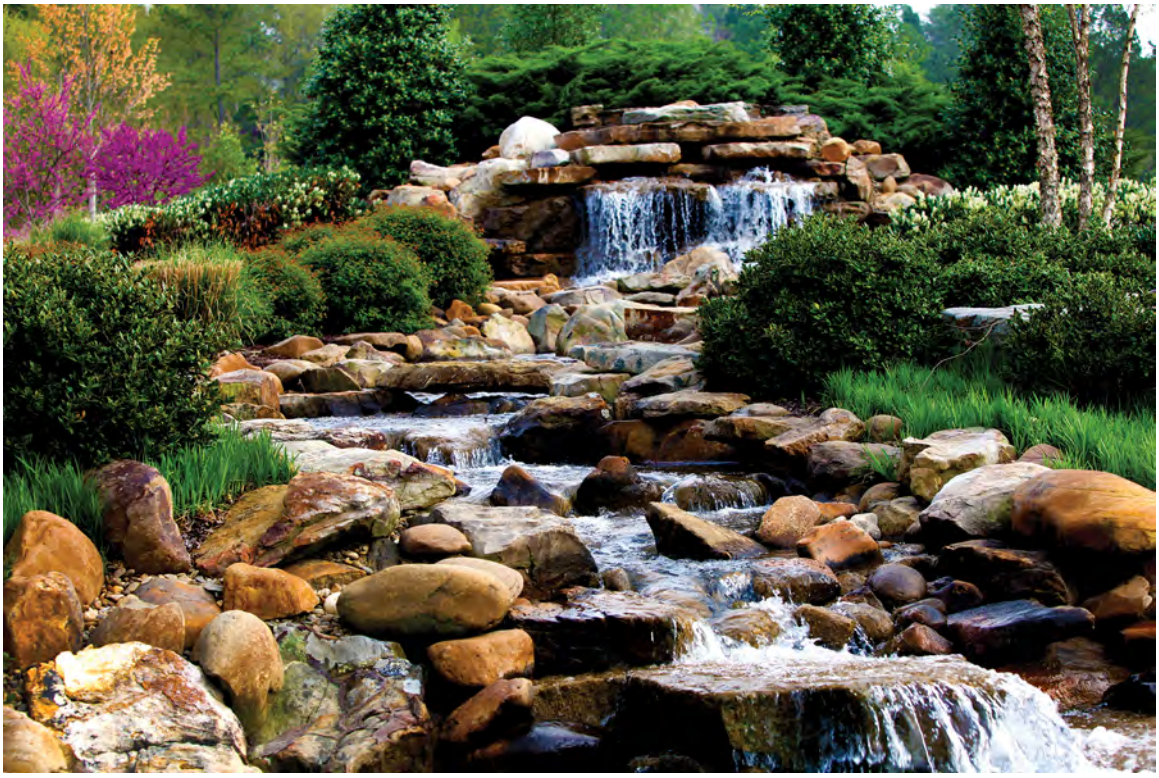

Mohammed Alnaggar
Samantha Sabatino
Yann Le Pape
Carlo Parisi
Zhenglai Shen
Abdo Elmeliegy

August 2025

OAK RIDGE National Laboratory

ORNL IS MANAGED BY UT–BATTELLE LLC FOR THE US DEPARTMENT OF ENERGY

ORNL/SPR-2025/4089
M2LW-25OR0403043

Nuclear Energy and Fuel Cycle Division

RELIABILITY ANALYSIS OF THE CONCRETE BIOLOGICAL SHIELD IN AGING NUCLEAR INFRASTRUCTURE UNDER ACCIDENTAL LOADS

Mohammed Alnaggar
Samantha Sabatino
Yann Le Pape
Carlo Parisi
Zhenglai Shen
Abdo Elmeliegy

August 2025

Prepared by
OAK RIDGE NATIONAL LABORATORY
Oak Ridge, TN 37831
managed by
UT-BATTELLE LLC
for the
US DEPARTMENT OF ENERGY
under contract DE-AC05-00OR22725

CONTENTS

LIST OF FIGURES

LIST OF TABLES

LIST OF ABBREVIATIONS

ACI	American Concrete Institute
APS	Arizona Public Service
ASCE	American Society of Civil Engineers
ASME	American Society of Mechanical Engineers
ASR	alkali–silica reaction
BC	boundary condition
BPVC	Boiler and Pressure Vessel Code
BWR	boiling water reactor
CBS	concrete biological shield
CCB	concrete containment building
CDF	cumulative distribution function
CMPD	core mid-plane distance
COV	coefficient of variation
DBA	design basis accident
DBE	design basis earthquake
DEGB	double-ended guillotine break
DOE	US Department of Energy
EFPY	equivalent full-power year
FEA	finite element analysis
FEM	finite element method
IAEA	International Atomic Energy Agency
ID	inner diameter
JCAMP	Japan Concrete Aging Management Program
JCSS	Joint Committee on Structural Safety
LDPM	lattice discrete particle model
LHS	Latin hypercube sampling
LOCA	loss-of-coolant accident
LWR	light-water reactor
MCNP	Monte Carlo N-Particle
MCS	Monte Carlo simulation
NRC	US Nuclear Regulatory Commission
NSSS	nuclear steam supply system
OBE	operating basis earthquake
OD	outer diameter
ODE	ordinary differential equation
ONS	Oconee Nuclear Station
PDF	probability density function
PSA	probabilistic safety assessment
PWR	pressurized water reactor
RIVE	radiation-induced volumetric expansion
RPV	reactor pressure vessel
RSBM	rigid-body spring model
RVSS	reactor vessel structural support
SAM	semi-analytical model
SRP	Standard Review Plan
SSE	safe shutdown earthquake
TMI	Three Mile Island
VERA	Virtual Environment for Reactor Applications

EXECUTIVE SUMMARY

The structural integrity of the concrete biological shield (CBS) and reactor pressure vessel (RPV) supports in nuclear power plants is critical for maintaining safety during operational conditions and design basis accident scenarios. These systems are exposed to diverse and challenging environments, including vertical and horizontal static and dynamic loads, thermal stresses, and long-term neutron irradiation degradation that progressively alters mechanical properties and structural performance. This document provides a systematic evaluation of the structural capacity of CBS and RPV supports. The work documented herein utilized advanced modeling approaches and probabilistic reliability assessments to quantify these supports' performance under extreme loading and material degradation conditions.

This study utilized the lattice discrete particle model (LDPM) to analyze failure mechanisms at a mesoscale level and thus provide detailed insights into fracture behavior for both plain and reinforced concrete. The analysis considered varying reinforcement ratios and different depths of irradiation-induced damage. To evaluate structural reliability, probabilistic methods such as Monte Carlo simulations (MCSs) combined with Latin hypercube sampling (LHS) are employed. The reliability assessment focuses on multiple ultimate limit states; scenarios that involve both single-event and combined-event loading conditions were simulated, including the loss-of-coolant accident (LOCA) and safe shutdown earthquake (SSE). These scenarios were analyzed under horizontal loading alone and under combined horizontal and vertical loading to investigate how load transfer mechanisms are influenced by different conditions.

The analysis highlights that reinforcement levels strongly influence load resistance, with higher steel reinforcement ratios yielding improved structural reliability. However, as depth of irradiation damage increases, the concrete's mechanical properties deteriorate, which substantially affects the interplay between vertical compression and horizontal load capacity. At shallow degradation depths, vertical loads enhance horizontal capacity due to increased friction under the shoe. However, at greater depths, vertical loads promote more extensive crack propagation, compression-induced shear, and partial crushing under the shoe, leading to reduced horizontal load capacity. Reliability indices demonstrate compliance with nuclear regulatory standards for moderate accident scenarios under minimal degradation but reveal critical vulnerabilities under severe loading conditions and deeper irradiation damage penetration. Despite increases in concrete strength, ultimate failure is consistently governed by steel yielding, as reduced lever arms and reduced confinement under irradiation exacerbate localized stresses.

These findings highlight the importance of re-evaluating the long-term integrity of the CBS and RPV support designs in aging nuclear infrastructure. They also suggest potential opportunities for conducting more advanced studies, particularly those that investigate dynamically coupled extreme loading scenarios (e.g., not statically additive), such as simultaneous seismic and LOCA events, while accounting for irradiation induced degradation, to further validate and refine the conclusions of this study. Such rigorous simulations and integrated analyses are essential for confirming the reliability trends observed and to develop enhanced design strategies that ensure structural safety under complex, multi-hazard conditions.

FOREWORD

It is anticipated that this report will not only serve as a resource for researchers, engineers, and policy-makers in the nuclear energy sector but will also inspire innovations in the modeling, design, and maintenance of aging infrastructure. Addressing the challenges of an aging nuclear fleet is a critical step toward safeguarding nuclear energy as a sustainable and secure power source for future generations.

ACKNOWLEDGMENTS

This research was sponsored by the US Department of Energy (DOE) Office of Nuclear Energy Light Water Reactor Sustainability Program Cross-Pathway Activities between the Materials Research Pathway and the Risk-Informed Systems Analysis Pathway under contract DE-AC05-00OR22725 with UT-Battelle LLC / Oak Ridge National Laboratory (ORNL). The authors would like to kindly thank and acknowledge the help of Xiang (Frank) Chen from ORNL and Svetlana Lawrence from Idaho National Laboratory (INL) in completing this report.

ABSTRACT

The long-term safety and reliability of aging nuclear infrastructure depend critically on the structural performance of the concrete biological shield under extreme accidental loads. This study integrates thermal hydraulic simulations using RELAP5, mesoscale structural analysis through lattice discrete particle model, and probabilistic reliability assessments to evaluate the concrete biological shield's behavior under combined load scenarios such as loss-of-coolant accident and seismic events. The findings provide insights into degradation mechanisms, failure probabilities, and strategies to enhance the resilience of nuclear facilities.

1. INTRODUCTION

The structural integrity of the concrete biological shield (CBS) and reactor pressure vessel (RPV) supports is critical to ensuring the safety and reliability of nuclear power plants, particularly as these facilities' operational lifespans are extended. The CBS plays an essential role in containing radiation and shielding personnel and the environment, whereas the RPV supports provide stability and alignment for the reactor core assembly. Failure of either system during extreme accident scenarios, such as a loss-of-coolant accident (LOCA) or safe shutdown earthquake (SSE), could result in catastrophic consequences, including radiation release, core damage, or structural collapse. Because many reactors now operate beyond their originally intended design life, understanding the long-term effects of degradation mechanisms on these components is a pressing necessity for the nuclear industry [1]. Updated regulatory guidance, such as IAEA SSR-2/1 on safety requirements for nuclear power plants [2], highlights the importance of maintaining the structural integrity of critical systems under prolonged operation.

A significant challenge for the longevity of CBS and RPV supports is the deterioration caused by neutron irradiation. Radiation exposure over the timescale of decades leads to radiation-induced volumetric expansion (RIVE) and associated material degradation, including microcracking, reduced compressive strength, and weakening of the bond between concrete and reinforcement steel [1]. These effects result in diminished load-bearing capabilities and exacerbate failure modes under extreme loading conditions, such as concrete crushing, reinforcement yielding, and crack propagation. This deterioration directly correlates with findings in the American Society of Mechanical Engineers (ASME) Boiler and Pressure Vessel Code (BPVC) Section III [3] and International Atomic Energy Agency (IAEA) TECDOC-1025 [4], which emphasize the need for ongoing monitoring and evaluation of structural materials under irradiation. Furthermore, the interaction between vertical and horizontal loads introduces additional complexities. While vertical loads may initially contribute to horizontal resistance in slightly degraded systems, under more severe levels of damage, these vertical forces can amplify failure mechanisms. This interplay highlights the need for a comprehensive understanding of load transfer behavior in systems subjected to progressive degradation.

In addition to material degradation, aging infrastructure also faces the growing likelihood of experiencing coupled accident scenarios, in which multiple extreme loads, such as seismic forces, thermal shocks, and irradiation damage, act simultaneously [1]. These compounded loading conditions place additional stress on critical structural systems already weakened by long-term degradation. Traditional design codes and deterministic evaluations, such as those outlined in American Society of Civil Engineers (ASCE) 43-05 for seismic design criteria for nuclear facilities [5], often provide conservative guidance but may not fully account for the probabilistic nature of material degradation, variability in operational conditions, or the combined effects of extreme loads. The IAEA Safety Standards Series NS-G-1.6 [6], focusing on severe accident management, also calls for a deeper probabilistic understanding of extreme load combinations

over the life cycle of nuclear facilities. This highlights the need for advanced probabilistic approaches to evaluate the reliability of these systems under realistic aging and loading conditions.

The study documented herein addresses these challenges by investigating the mesoscale structural behavior and reliability of the CBS and RPV supports under irradiation-induced degradation and extreme loading scenarios. Using the lattice discrete particle model (LDPM), advanced simulations are conducted to capture complex failure mechanisms at the mesoscale level, including fracture localization, bond loss between rebar and concrete, and progressive material damage. The analysis builds upon international best practices for structural modeling—such as the guidance found in Eurocode 2 for the design of concrete structures [7]—and incorporates varying reinforcement ratios to study performance under different configurations and degradation depths. A probabilistic reliability assessment was performed using Monte Carlo simulation (MCS) with Latin hypercube sampling (LHS) to complement those mechanical simulations. This approach provides statistical insights into failure probabilities across multiple ultimate limit states under both single and compounded accident scenarios, such as LOCA and SSE. Particular attention was given to how the interplay between vertical and horizontal loads changes with increasing levels of degradation.

The goal of this investigation is to provide critical insights into the long-term performance of aging CBS and RPV supports, ultimately informing life extension programs, advanced maintenance protocols, and updated design standards. International organizations, including the US Nuclear Regulatory Commission (NRC) (“Regulatory Guide 1.35," addressing in-service surveillance) [8], provide a framework for evaluating the quality assurance of concrete structures in reactors, which aligns with the findings and recommendations presented in this study. The results of this study can be leveraged to enhance safety margins, identify areas for future research, and lay the groundwork for improved predictive tools and design strategies to mitigate risks associated with aging nuclear infrastructure [1]. Finally, this study also highlights the need for further research into coupled extreme loading scenarios to fully capture the interactions that drive structural failure.

This document is structured as follows.

- **Section 2: Motivation and Theoretical Background**
  This section examines the challenges associated with aging nuclear infrastructure, including irradiation-induced material degradation, reductions in mechanical performance, and the complex interaction of vertical and horizontal loads under extreme scenarios. The importance of understanding these factors to ensure long-term safety and reliability is emphasized.
- **Section 3: RELAP5 Thermal Hydraulic Analysis**
  This section focuses on the use of RELAP5 for simulating thermal hydraulic scenarios, such as LOCAs. The effects of these scenarios on the thermal and mechanical loads of structural components, including the CBS and RPV supports, are analyzed as inputs for subsequent structural simulations.
- **Section 4: Structural Simulation of the CBS under Accidental Loads**
  This section describes the methodology and results of structural simulations for the CBS under accidental loads. It evaluates how accidental combinations, such as LOCA and seismic events, influence the structural integrity and progression of damage in the CBS.
- **Section 5: LDPM Simulations**
  LDPM was employed to conduct mesoscale simulations capturing the fundamental mechanical behavior of concrete under irradiation and degradation. This section highlights how cracking, bond weakening, and concrete–rebar interaction evolve in the presence of extreme loads.

- **Section 6: Probabilistic Reliability Assessment**
  This section outlines the probabilistic methods used to evaluate structural reliability. MCS with LHS was employed to quantify the failure probabilities of CBS and RPV supports under different degradation levels, loading conditions, and material uncertainties.
- **Section 7: Conclusions**
  Key findings and broader implications are summarized, and their significance for the safety, design, and maintenance of aging nuclear facilities is elucidated. This section also identifies open challenges and areas for future research, including the study of coupled extreme events and the development of multidisciplinary modeling approaches.

2. CBS AND RPV SUPPORT SYSTEM OVERVIEW

2.1 CBS GENERAL DESIGN PRINCIPLES

The CBS in pressurized water reactors (PWRs) is a reinforced concrete system that must both attenuate neutron and gamma radiation and transmit actions from the RPV and associated nuclear steam supply system (NSSS) components to the foundation [9, 10]. Structural design and detailing for strength, serviceability, and durability shall conform to the nuclear applications of the American Concrete Institute (ACI) concrete code, including load combinations applicable to internal nuclear structures [11]. Regulations also require that internal structures not create conditions that could cause a LOCAs and that they retain the capability to limit consequences in case of postulated events [9, 10].

The general design principles for the CBS are governed by safety, durability, and compliance with applicable nuclear regulatory standards. A CBS must provide both structural stability and radiation attenuation to ensure the protection of plant personnel, the public, and critical reactor components. Its geometric configuration, material composition, and construction methodology are engineered to withstand the full spectrum of operational and accidental loadings throughout the plant's design life.

2.1.1 Shielding Adequacy

Shielding adequacy is governed by material composition and section thickness. PWRs' biological shields predominantly employ structural concrete with natural aggregates rather than heavy-aggregate concretes more common in selected non-US designs [12]. The hydrogen content associated with bound and free water in the cementitious matrix contributes significantly to neutron moderation; moderation and absorption within the CBS act in combination with wall thickness to reduce fast-neutron dose outside the reactor cavity [13, 14]. A typical PWR CBS thickness is on the order of 1.5–2.2 m, with overall wall heights tailored to containment geometry and equipment clearances [14, 15]. These dimensions reflect the dual requirement of radiation attenuation and mechanical load transfer.

Concrete mix designs for nuclear shields may incorporate heavy aggregates to enhance shielding performance, but the balance between workability, constructability, and mechanical strength remains a critical design consideration.

2.1.2 Load Transfer and Structural Behavior

Load transfer is controlled by the support concept and the steel–concrete interface. The RPV imposes a large sustained vertical reaction and attracts lateral actions from operational, seismic, and accident sources. These actions are transmitted through shoe blocks, ring girders, skirts or columns, or cantilevered members into the CBS and then to the foundation [15–17]. Embedded steelwork such as welded plates, anchor groups, and brackets establishes lateral restraint, and shimming practices are used to set clearances that accommodate thermal expansion while minimizing unintended restraint forces during heatup [15, 16].

The interface must be verified against concrete edge pryout, bearing or crushing, and combined shear–tension limit states. Analytical and experimental studies provide models and data for multiple-row anchorages and supplementary reinforcement [18–20].

The design process further involves careful evaluation of reinforced concrete behavior under sustained and dynamic loads, considering time-dependent phenomena such as creep, shrinkage, and irradiation-induced degradation. Key objectives include maintaining sufficient shielding against neutron and gamma radiation, minimizing deformation that could compromise containment penetrations, and integrating with other safety-related structures.

2.1.3 Thermal and Radiological Environment

The thermal and radiological environment adjacent to the cavity governs the long-term performance of the near-surface concrete. In-service temperatures for nuclear concrete are maintained within the applicable ACI envelope to limit thermally driven degradation [11]. At core mid-elevation, the inner face of the CBS experiences sustained fast-neutron flux and gamma dose whose magnitudes and gradients depend on plant configuration and shielding details. Studies of light-water reactors (LWRs) show that radiation levels at the surface of the CBS can be high enough to change the concrete's mechanical properties in a thin outer layer, along with associated gamma dose and some gamma heating [14, 21–23].

Irradiation effects in concrete are primarily governed by the response of rock-forming minerals and the cementitious matrix. RIVE of susceptible aggregates introduces internal eigenstrains in the irradiated skin, which is constrained by the cooler, less-irradiated backwall. The constraint produces biaxial compressive stress states in hoop and vertical directions and promotes opening of radially oriented cracks at the cavity face [24, 25]. Structural and mesoscale modeling specific to biological shields indicates that crack localization remains confined to a depth that is small compared with the total wall thickness, so the remaining cross section continues to carry gravity and lateral actions [25, 26]. Plant-informed assessments and laboratory-to-field scaling show that the affected depth increases gradually with operating time and local field intensity, which is in agreement with microstructural observations and three-dimensional discrete or rigid-body spring representations [27–29].

Shielding configuration exerts a first-order influence on the radiation field that reaches the CBS. When comparing configurations with and without a water-filled neutron shield tank located between the vessel and the biological shield, both moderation and absorption upstream of the concrete reduce the rate of irradiation-induced property change and crack evolution [14, 30]. In plants without such a tank, the near-surface concrete at the elevation of the core midplane experiences higher fluence, and support embedment regions located close to the cavity require increased attention in surveillance and analysis [14, 23].

2.1.4 Regulatory Framework

Regulatory guidance from the NRC, as outlined in the Standard Review Plan (Standard Review Plan (SRP)), establishes the acceptance criteria for CBS performance under normal, upset, and emergency conditions [9]. The SRP provides guidance to staff in performing safety reviews of construction permit or operating license applications (including requests for amendments) under 10 CFR Part 50 and early site permit, design certification, combined operating license, standard design approval, or manufacturing license applications under 10 CFR Part 52 [31].

Section 3.8.3 of the SRP addresses "Concrete and Steel Internal Structures of Steel or Concrete Containments." To perform safety-related functions, these structures must be capable of resisting loads and load combinations to which they may be subjected and must be designed such that they do not become the initiator of a LOCA. If such an accident were to occur, then the structures must be able to mitigate its consequences by protecting the containment and other engineered safety features from effects such as jet forces and whipping pipes [9].

PWR dry containment internal structures include concrete supports for the reactor, the primary shield, and the reactor cavity. Depending on the PWR design, the support and shield functions can be combined (e.g., the CBS directly supports the reactor) or separated (e.g., the reactor is supported by embedded steel columns).

Concrete Supports for Reactor

> *The PWR vessel must be designed to be supported and restrained to resist normal operating loads [e.g., static loads and thermal loads], seismic loads, and loads induced by postulated pipe rupture, including LOCAs. The support and restraint system must be designed to restrain the movement of the vessel to within allowable limits under the applicable load combinations. However, the support system must be designed to minimize resistance to the thermal movements expected during operation. With these functional requirements in mind, the review evaluates the general arrangement and principal features of the reactor vessel supports, with an emphasis on the methods of transferring loads from the vessel to the support and ultimately to the structure and its foundations* [9].

Primary Shield Wall and Reactor Cavity

> *The primary shield wall forms the reactor cavity and usually supports and restrains the reactor vessel. It is often a thick wall that surrounds the reactor vessel and may be anchored through the liner plate to the containment base slab. The review evaluates the general arrangement and principal features of the wall and cavity, including the reinforcement and anchorage system* [9].

2.1.5 Summary

The CBS shall be proportioned and reinforced to provide biological shielding, deliver defined and redundant paths for vertical and lateral actions from the RPV and connected systems into the foundation, and retain structural function despite the presence and slow growth of an irradiation-affected zone at the inner surface [9, 11, 22]. These principles, supported by validated computational models and experimental evidence, establish the basis for the modeling, simulation, and probabilistic evaluations presented in this report.

2.2 REACTOR SUPPORT DESIGN

Several designs of RPV support systems exist in PWRs operating in the United States. These systems are critical because they govern how operational, seismic, and postulated accident loads are transmitted from the vessel to the CBS and ultimately into the foundation. The evaluation and design of these systems require careful consideration of material behavior under combined effects, construction tolerances, inspection protocols, and the incorporation of redundancy in load paths. Engineering judgment, supported by validated computational models and experimental evidence, is essential to confirm compliance with applicable nuclear safety codes and standards.

Appendix D of NUREG/CR-7280 provides detailed descriptions of the reactor support systems used in several US plants [22]. These support arrangements can be categorized as vertical column support systems, neutron shield tanks, support skirts, shoe-type supports, and ring girder supports. The relative susceptibility of these configurations to in-service irradiation-induced and LOCA-induced degradation of the CBS varies depending on geometry, contact footprint, embedment depth, and shielding configuration. Each of these factors influences how stresses are distributed into the CBS and determines the location and intensity of irradiation fields that drive material degradation.

The core midplane elevation is the most critical reference plane for assessing irradiation effects because it corresponds to the maximum fast-neutron flux and fluence in the biological shield during normal operation. At an 80-year projection, the CBS inner surface at this elevation is expected to be subjected to fast-neutron flux of approximately 0.1–0.2 $\times$ 10^{11} n·cm^{-2}·s^{-1} ($E>$ 0.1 MeV), a fast-neutron fluence of 2.0–6.0 $\times$ 10^{19} n·cm^{-2} ($E>$ 0.1 MeV), a gamma dose rate near 10 kGy·h^{-1}, a cumulative gamma

dose of roughly 100 MGy, and gamma heating close to 0.02 $W \cdot g^{-1}$ [14, 21, 22]. These radiation levels are sufficient to trigger RIVE in susceptible aggregates. The resulting eigenstrains and volumetric expansion drive tensile microcracking, reduce stiffness and strength, and degrade the steel–concrete bond in reinforced or anchored regions [22, 32].

The depth of irradiation-induced damage is denoted δ and is a key parameter for updating structural capacity models of each support type. Analyses indicate that at the plane of core mid-elevation, the cracking and damage depth in the CBS develops over time to approximately $\delta \approx 11$ cm at 80 year with proportionally lower values at earlier times. This progression reflects restrained RIVE and associated near-surface microcracking in the irradiated zone [22].

The following subsections describe the major support configurations, explain how geometry and load transfer characteristics influence irradiation exposure profiles, and present analytical update relationships that explicitly incorporate δ as the depth of irradiation-induced degradation. This framework establishes the technical basis for assessing long-term performance and maintaining regulatory compliance across all categories of RPV support systems.

2.2.1 Vertical Columns

In this design, the reactor loads are transferred to the base mat located beneath the reactor cavity through steel columns, the number of which varies from one design to another.

Arkansas Nuclear One (ANO) Unit 2

At ANO Unit 2, a Combustion Engineering two-loop PWR, only three vertical columns are present (see Figure 1).

Prairie Island Units 1 and 2

Prairie Island Units 1 and 2 are Westinghouse two-loop PWRs. Each unit is supported by six steel columns welded to or braced by a surrounding metal band at the top, all of which are embedded in the CBS wall (Figure 2).

The function of the columns is limited to transferring vertical loads. These columns are embedded in the CBS, but their structural design treats them as independent from the surrounding concrete, thereby neglecting potential interactions. Such interactions may primarily affect the concrete surrounding the columns. For example, Risner et al. [29] found that irradiation-induced energy deposition in embedded steel columns causes an increase in the heating rate by a multiplying factor of approximately 8.

That study has not been extended to analyze heat transfer and its consequences on the material properties; furthermore, thermal gradient–induced degradation in the surrounding concrete has not been analyzed.

Horizontal loads are carried by a horizontal bracket system embedded in the concrete at an elevation immediately below the RPV nozzle. Each nozzle is supported by a ventilated hollow box pad to limit the temperature in the column, the bracket, and the supporting concrete. The design temperature at the bottom of the plate is 150°F. This temperature also corresponds to the American Concrete Institute 349 code design value for in-service concrete temperature.

2.2.2 Neutron Shield Tank

Some designs include a shield tank that is attached to the CBS wall.

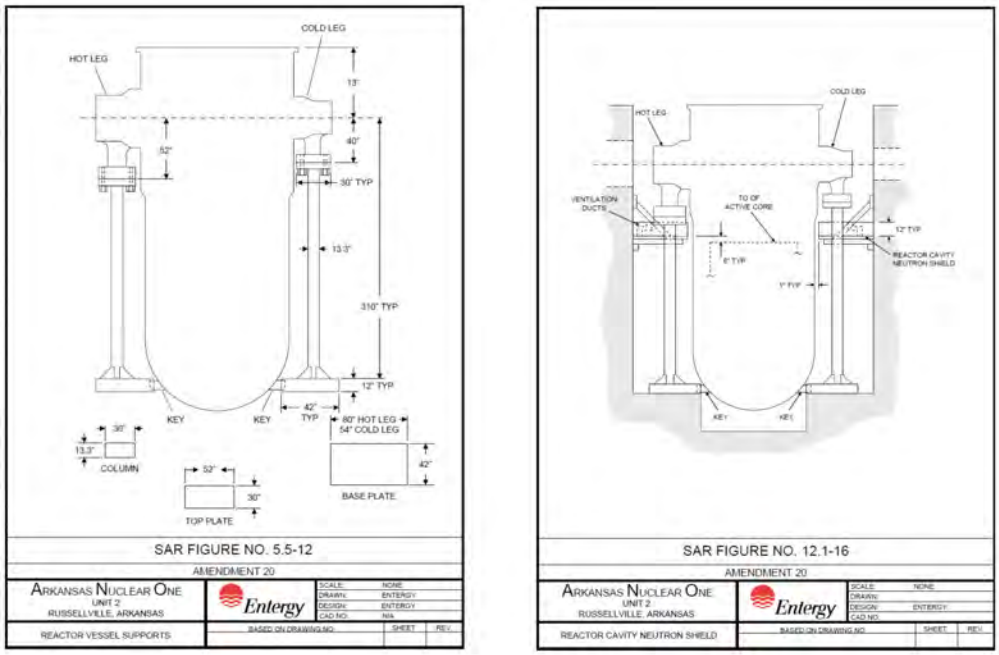

Figure 1. ANO reactor vessel support design (left) and reactor cavity neutron shield (right). Entergy Operations, Inc., 2016, ANO Unit 2, Safety Analysis Report Amendment 26, Docket No. 50-368, Russellville, AR, ADAMS Accession No. ML18092A457.

Beaver Valley

At the Beaver Valley plant,

> *... the reactor vessel structural support (RVSS) is a cylindrical, skirt-supported, double-walled structure designed to transfer loading to the reinforced concrete mat of the containment structure and to the surrounding primary shield wall; it is fabricated of SA-516, Gr-70 plate.* ***This component support is designed to restrain vertical, lateral, and rotational movement of the reactor vessel while permitting thermal expansion/contraction of the reactor vessel during plant operation.*** *The reactor vessel is set on leveling devices between each of the six RPV loop nozzle pads and the top of the support structure. This support is also designed to provide neutron shielding and thermal protection to the surrounding structure by means of a water-filled annular section, as well as to house and cool the ex-core neutron detectors* [33].

See Figure 3 for a drawing of the neutron shield tank.

> *The reactor vessel support/leveling device, fabricated with material in compliance with the ASTM A-668-72 Type K material specification, is shown on Figure 4. The triple wedge shape device is positioned (without mechanical attachment) between each of the six reactor vessel nozzle pads and a lubricated plate which is fastened to the top surface of the reactor vessel structural support. The functional requirement of the RPV support/leveling device is to provide vertical adjustment at each RPV nozzle restraint pad during installation of the reactor vessel. Each support/leveling device has a screw assembly to produce relative horizontal translation of the wedge shaped plates, which results in a limited vertical adjustment of the reactor vessel during installation. During all plant conditions, this support system is designed to transfer only vertically downward (compression) loads from the reactor vessel nozzle pads to the reactor vessel structural support. Upward loads are reacted by gib keys* [33].

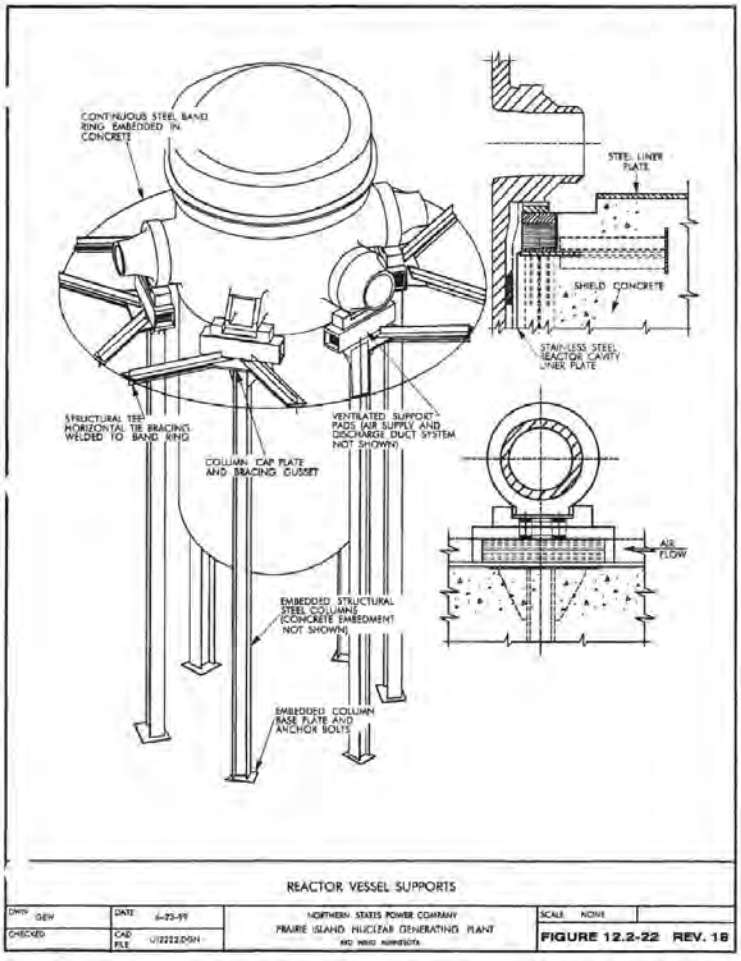

Figure 2. Prairie Island reactor vessel support design. Xcel Energy, 2018, Prairie Island Nuclear Generating Plant Units 1 and 2, Updated Safety Analysis Report Revision 35, Dockets 50-282 and 50-306, Welch, MN. ADAMS Accession No. ML18155A440 – Chapter 5; ML18155A456 – Chapter 12.

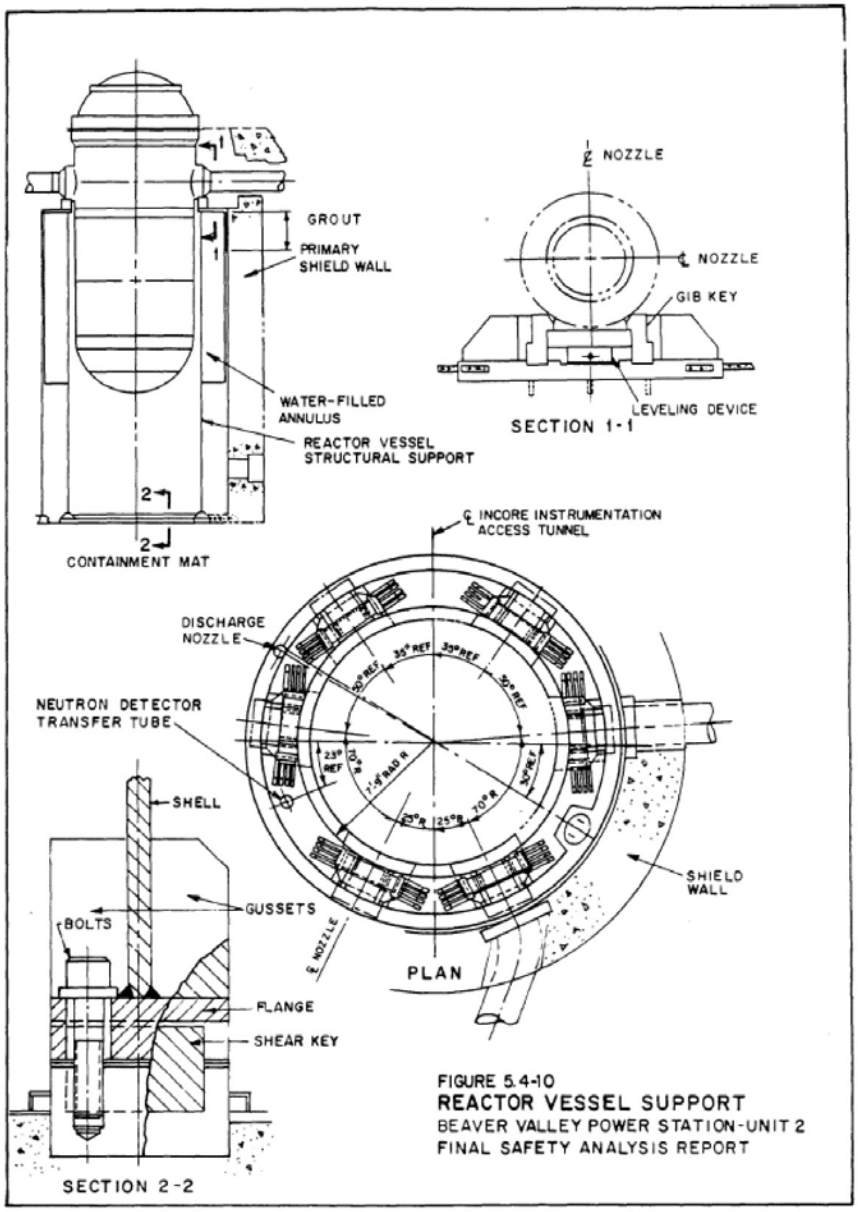

Figure 3. Beaver Valley Unit 2 reactor vessel support design – neutron shield tank [33].

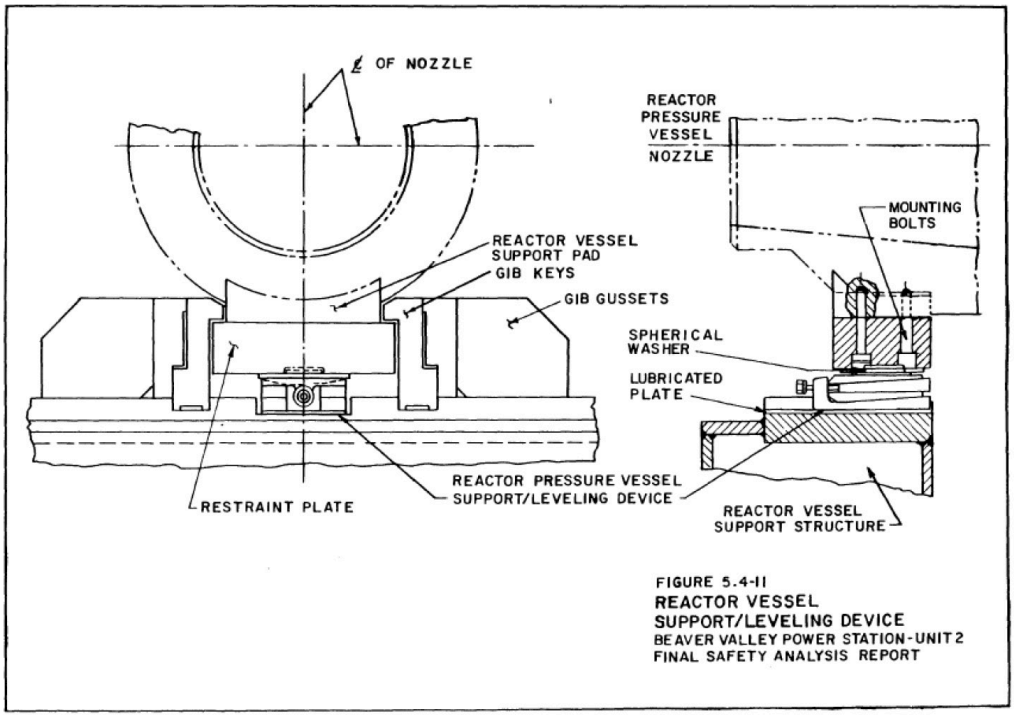

Figure 4. Beaver Valley Unit 2 reactor vessel support shoe design [33].

North Anna Units 1 and 2

North Anna Units 1 and 2 are Westinghouse three-loop PWRs.

Supported by shoes under all six nozzles, each RPV rests directly on a neutron shield tank that is grouted into the shield wall [22]. The neutron shield tank is designed to resist a differential pressure of 130 psi (~0.9 MPa). The presence of the neutron shield tank causes an important attenuation of the fast-neutron flux, which affects the CBS wall. The support elements are directly located above the shield tank, thus transferring the load to the RVSS.

2.2.3 Support Skirt

Other RPVs are directly supported by a steel skirt located under the vessel resting directly on the base mat. Similar designs are found in boiling water reactors (BWRs).

Three Mile Island

Three Mile Island (TMI) is a two-loop Babcock and Wilcox PWR.

> *The reactor vessel is bolted to reinforced concrete foundation designed to support and position the vessel and withstand the forces imposed on it by a combination of loads, including the weight of vessel and internals, thermal expansion of the piping, design basis earthquake, and dynamic load following reactor trip. The foundation, in addition, restrains the vessel during the combined forces imposed by circumferential rupture of a 36 inch reactor outlet line and a simultaneous maximum hypothetical earthquake. The vessel foundation is also designed to provide accessibility for the installation and later inspection of in-core instrumentation, piping and nozzles, to contain duct work and vent space for cooling air, to remove heat losses from the vessel insulation, and, to provide a drainage line for leak detection* [34].

Arkansas Nuclear One, Unit 1

Arkansas Nuclear One, Unit 1 is a two-loop Babcock and Wilcox PWR.

> *The reactor vessel supports include a support skirt and support flange. The reactor vessel support skirt is a cylindrical structure that supports the reactor vessel. The support skirt rests on a sole plate. The sole plate is fixed to a supporting, reinforced concrete pedestal through a steel flange bolted to the pedestal. The evaluation boundary of the reactor vessel support skirt begins at the weld of the skirt to the reactor vessel transition forging and terminates at the bottom of the skirt flange. The evaluation boundary also includes the exposed surface of the anchor bolts and shear pins. The reactor vessel support skirt was designed, fabricated, tested, and inspected in accordance with ASME Section III (Reference 2.4-5). The support skirt consists of two carbon steel semi-circular rings welded together to form a cylinder. This cylinder is welded to the bottom of the reactor vessel transition forging. The cylinder has holes for ventilation of the reactor vessel cavity. The anchor bolts are prestressed to accommodate the loads of a design basis seismic event* [35].

Although Entergy and Exelon [34, 35] have not provided any drawings of the support system, these drawings can be found in "Oconee Nuclear Station Units 1, 2, and 3 Application for Subsequent License Renewal Appendix E – Applicant's Environmental Report" [36]. Figure 5 and Figure 6 present the general support assembly and a detail of the support connection with the concrete pedestal, respectively. "The support flange is bolted to the concrete with 48 bolts spaced equally around the outside of the flange, and 48 bolts spaced equally around the inside part of the flange" [36]. It clarifies key geometric features, load paths, and any relevant dimensional relationships, ensuring that the technical discussion is directly supported by visual evidence.

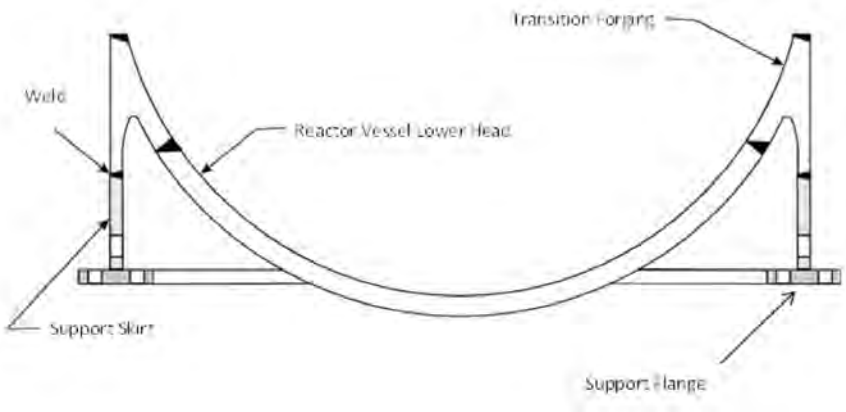

Figure 5. Reactor pressure vessel support assembly at Oconee Nuclear Station.

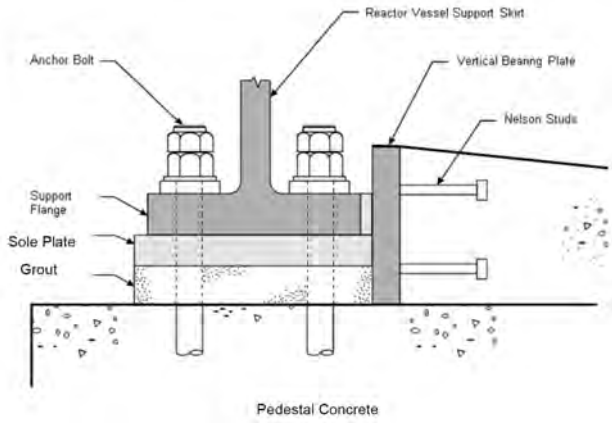

Figure 6. Reactor pressure vessel support embedment detail at Oconee Nuclear Station.

2.2.4 Shoe Supports

In the absence of a neutron shield tank, the nozzle supports are placed directly on the CBS wall. These support regions must be evaluated with respect to material behavior under combined effects, construction tolerances, inspection protocols, and the incorporation of redundancy in load paths. Engineering judgment, supported by validated computational models and experimental evidence, is essential to confirm compliance with applicable nuclear safety codes and standards.

Examples of such shoe-type support configurations are found in multiple US and international designs. Their engineering significance lies in how localized load transfer interacts with irradiation exposure, which drives degradation in concrete properties over long-term operation.

Geometry and Global Relevance

Shoe-type supports employ discrete structural steel shoes located beneath the RPV nozzles. An upper shoe element rigidly attached to the nozzle forging transfers vertical, radial, and tangential reactions to a lower shoe or box that bears on and is anchored to the CBS top surface or into recessed seating pockets via high-strength anchor bolts. Because the contact footprint is small relative to the vessel diameter, the concrete experiences localized bearing and anchor-edge stresses near the shoe bases. This arrangement is common in US three-loop Westinghouse and Combustion Engineering plants and has been implemented in some international designs, such as early French units and Soviet-era adaptations. Farley Units 1 and 2 exemplify a US shoe-type configuration [37–39].

Irradiation Exposure and Degradation Process

Shoe anchorage zones commonly align with the nozzle beltline and therefore lie within the region of peak irradiation fields at the core midplane. Under the 80-year radiation fields summarized in prior sections, susceptible aggregates undergo RIVE, producing tensile microcracking that initiates from the CBS inner face and propagates inward. The developing crack network reduces the effective elastic modulus E_c and compressive strength f_c in the cover and bearing layer. In addition, it diminishes the steel–concrete bond due to loss of confinement and mechanical interlock [22, 32].

Analytical Relationships

For wedge/pry-out–governed plain concrete modes adjacent to edges, the residual shear capacity can be expressed as

$$\frac{V(\delta)}{V_0} \approx 1 - \frac{\delta}{c_{\text{edge}}}, \tag{1}$$

where c_{edge} is the effective edge distance, $V(\delta)$ is the reduced shear capacity at irradiation-damage depth δ, and V_0 is the original unirradiated shear capacity.

For bond-governed anchored steel, the effective bond length decreases as irradiation damage progresses inward. This can be represented as

$$l_{\text{eff}} = \max(0,\, l_0 - \delta)\,, \qquad \tau_b(\delta) \approx \tau_{b0}\,\frac{l_{\text{eff}}}{l_0}, \tag{2}$$

where l_{eff} is the effective bonded length after accounting for the irradiated depth δ, l_0 is the original bonded length, $\tau_b(\delta)$ is the reduced average bond stress over the remaining effective length, and τ_{b0} is the reference (unirradiated) mean bond stress. Hook-dependent contributions are rendered ineffective once δ reaches the reinforcement cover depth [22].

Shoe-type nozzle supports impose concentrated stresses on the CBS and align with regions of maximum irradiation exposure. The combined mechanical and radiological conditions lead to localized degradation

mechanisms that must be incorporated explicitly into structural capacity assessments, where δ represents the principal parameter that governs the reduction in effective anchorage and bond performance. Several examples of shoe-type designs are provided below.

Calvert Cliffs Units 1 and 2

Calvert Cliffs Units 1 and 2 are Combustion Engineering–designed two-loop PWRs. The support design is described as follows:

> *The reactor vessel is supported vertically and horizontally by three pads welded to the underside of the reactor vessel nozzles. Each assembly consists of the following – [Figure 7]:*
>
> *a. A support foot (SA-508 CL2) welded to a reactor coolant nozzle;*
>
> *b. A socket [American Society for Testing and Materials (ASTM A283-67)] bolted to the support foot with Allenoy cap screws; and*
>
> *c. A sliding bearing (ASTM B22, Alloy E) whose spherical crown fits into the socket and whose flat sliding surface rests on a base plate (AISI-4140).*
>
> *The arrangement of the vessel supports allows radial growth of the reactor vessel due to thermal expansion while maintaining it centered and restrained from movement caused by seismic disturbances.*
>
> *The functions of the supports are:*
>
> *1. Restrain the vessel to maintain the integrity of emergency core cooling systems and to prevent the rupture of additional primary pipes should LOCA occur due to single pipe rupture;*
>
> *2. Permit slow radial thermal expansion of the vessel under normal operation; and*
>
> *3. Restrain the vessel against seismic and LOCA jet forces [40].*

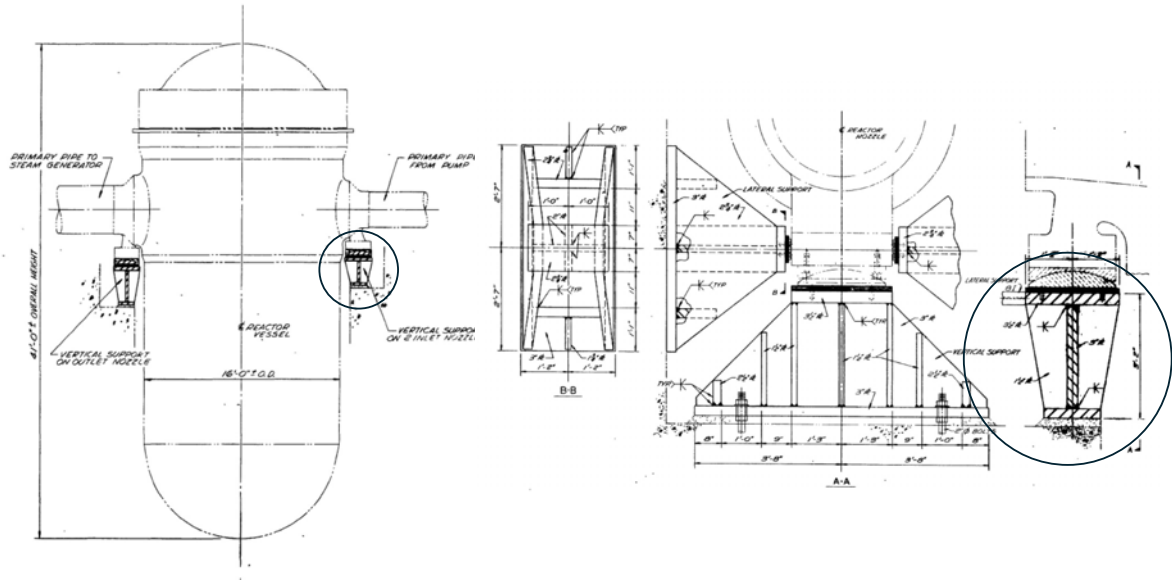

Figure 7. Calvert Cliffs Units 1 and 2 reactor core position relative to supports (left) and reactor vessel support detail (right) [40].

Farley Units 1 and 2

In these Westinghouse three-loop PWRs, the reactor vessel supports rest directly on the CBS wall.

> *Supports for the reactor vessel are individual, air-cooled, rectangular-box structures beneath the vessel nozzles bolted to the primary shield wall concrete (as shown in Figure 8). Each box structure consists of a horizontal top plate that receives loads from the reactor vessel shoe, a horizontal bottom plate supported by and transferring loads to the primary shield wall concrete, and connecting vertical plates. The supports are air-cooled to maintain the supporting concrete temperature at or below 190°F at a flow rate of 2,000 ft^3/min with an air temperature of 120°F to meet the acceptance criteria for the localized concrete temperature of 200°F. However, recognizing the potential degradation of the RPV supports subjected to sustained temperatures higher than 150°F, Farley Nuclear Plant has committed (NEL letter #00-279 to USNRC) to an augmented program to inspect the structural components including portions of the RVSS in the containment buildings as part of the maintenance rule structural monitoring program. This program will ensure that significant cracking of RVS that could affect the structural support of the reactor vessel or cause out of plumbness conditions will be detected and corrected* (NRC commitment CTS #10533).

H. B. Robinson

In the H. B. Robinson Nuclear Generating Station, also a Westinghouse three-loop PWR, follows the design described below:

> *The reactor vessel support structure consists of a circular box section ring girder, fabricated of carbon steel plates. The bottom flange of the girder is in continuous contact (except for openings for neutron detectors) with a non-yielding concrete foundation. The reactor vessel has three supports located at alternate nozzles. Each support bears on a support shoe, which*

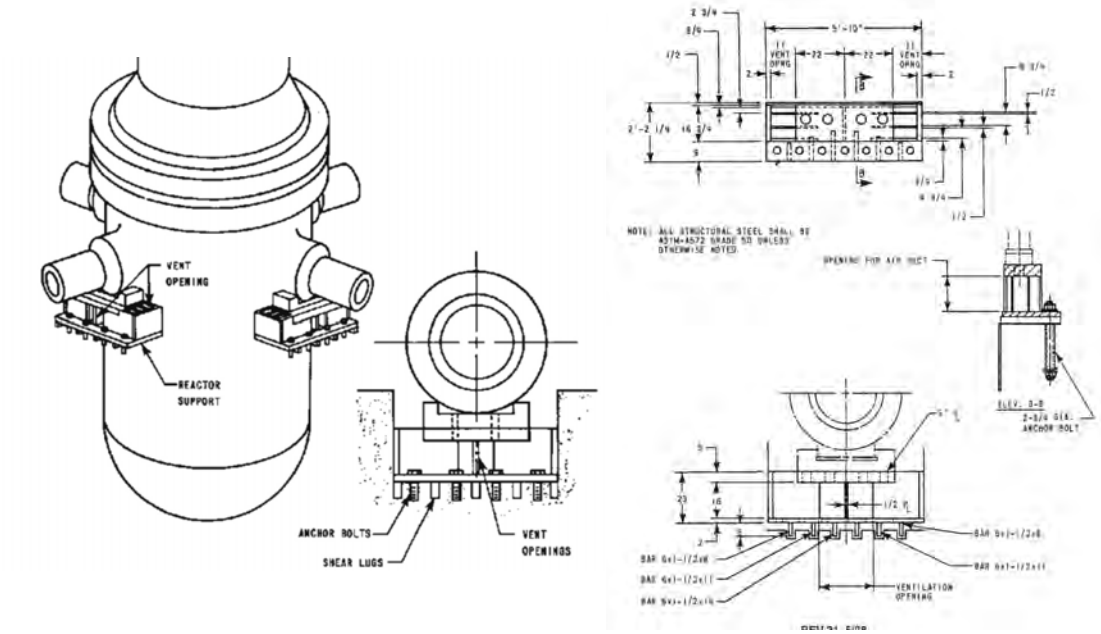

Figure 8. Farley Units 1 and 2 reactor vessel support design (left) and reactor vessel support box (right) [37].

> *is fastened to the support structure. The support shoe is a structural member that transmits the support loads to the supporting structure. Each support shoe is designed to restrain vertical, lateral, and rotational movement of the reactor vessel, but allows for thermal growth by permitting radial sliding on bearing plates* [41].

Shearon Harris Unit 1

Shearon Harris units are also Westinghouse three-loop PWRs.

> *The reactor pressure vessel (RPV) is supported and restrained to resist normal operating loads, seismic loads, and loads induced by the postulated pipe ruptures, including a LOCA. The RPV is supported at six points, the three inlet and three outlet nozzles, so that adjacent supports are 50 or 70 degrees apart. Steel pads, which are an integral part of the nozzles, rest on a steel bearing block atop a steel support pedestal.*

The drawing of the supports for this reactor shows the same reactor vessel support design as that of Farley Units 1 and 2 [22] (see Figure 8).

> *The steel support pedestal is welded to a stiffened base plate at its bottom. The base plate is attached to the reinforced concrete by anchor bolts. The base plate has shear bars on its underside to resist part of the lateral loads, including piping loads.*
>
> *Supports for the reactor vessel are individual air cooled rectangular box structures beneath the vessel nozzles bolted to the primary shield wall concrete. Each box structure consists of a horizontal top plate that receives loads from the reactor vessel shoe, a horizontal bottom plate which transfers the loads to the primary shield wall concrete, and connecting vertical plates. The supports are air cooled to maintain the supporting concrete temperature within acceptable levels.*

The technical drawings are not available, but the nozzle support description appears to be comparable to that of Farley's.

> *The transfer of horizontal seismic and postulated accident loads from the RPV and the connecting piping system into the concrete primary shield wall is performed through embedded steel structures. These structures consist of billet plates welded to vertical circular plates, anchored into the concrete wall by using anchor bolts and embedded structural steel assemblies. The gap between the vertical RPV supports and the horizontal RPV supports is shimmed in the cold condition with a predetermined allowance for thermal expansion.*

2.2.5 Cantilever Beam System

Although decommissioned and dismantled, the Westinghouse-designed Trojan vessel support system provides an important design study, possibly comparable to that of the Davis–Besse Nuclear Power Station. It is composed of upper and lower beam structures joined by pinned columns (Figure 9). The lower beam is located closest to the core midplane, where the fast-neutron fluence is nearly at its maximum.

The vertical short column is embedded in the concrete at a distance ranging from approximately 10 to 25 cm from the reactor cavity. This concrete region is highly susceptible to irradiation-induced degradation, as it is directly exposed to elevated fast-neutron fluxes and cumulative doses. The evaluation of such regions requires careful consideration of material behavior under combined effects, construction tolerances, inspection protocols, and redundancy in load paths. Engineering judgment, supported by validated computational models and experimental evidence, remains essential to confirm compliance with applicable nuclear safety codes and standards.

According to Biwer et al. [22], cantilever systems can also be located directly under the nozzle (Figure 10), thereby avoiding the need for pinned short columns. In either configuration, portions of the support system remain in regions subjected to high fast-neutron fluxes, making them prone to irradiation-driven degradation processes.

Geometry and Global Relevance

Cantilever beam supports embed horizontal steel members into the CBS wall, projecting inward to engage the RPV shell or brackets. The embedment length develops flexure and shear through bond, bearing, and shear-friction along the steel–concrete interface. This geometry is relatively uncommon globally but appears in the Trojan plant (US) and in some experimental reactors where lateral space constraints preclude skirts or full rings [42].

Irradiation Exposure and Degradation Process

With embedments located at or near the reactor core mid-plane, RIVE-induced cracking propagates along steel interfaces and through the concrete cover. This degradation reduces confinement, weakens bond, and increases slip between steel and concrete. The reduction in effective bonded length l_{eff} directly controls the decrease in transferable moment and shear capacity.

Analytical Relationships

For bond-governed cantilever embedments, the transferable flexural capacity can be updated to account for irradiation-induced damage as

$$M_u(\delta) = \tau_b(\delta)\,\pi d_b\, l_{\text{eff}}\, z, \qquad l_{\text{eff}} = \max(0,\, l_0 - \delta)\,, \qquad \frac{\tau_b(\delta)}{\tau_{b0}} = \frac{l_{\text{eff}}}{l_0}, \tag{3}$$

where $M_u(\delta)$ is the reduced flexural capacity transferable by the embedment at irradiation damage depth δ, $\tau_b(\delta)$ is the reduced average bond stress over the remaining effective length, d_b is the characteristic bar or beam diameter, l_{eff} is the effective bonded length after accounting for the irradiated depth, l_0 is the original bonded length, z is the internal lever arm for the cantilever action, and τ_{b0} is the reference (unirradiated) mean bond stress [22].

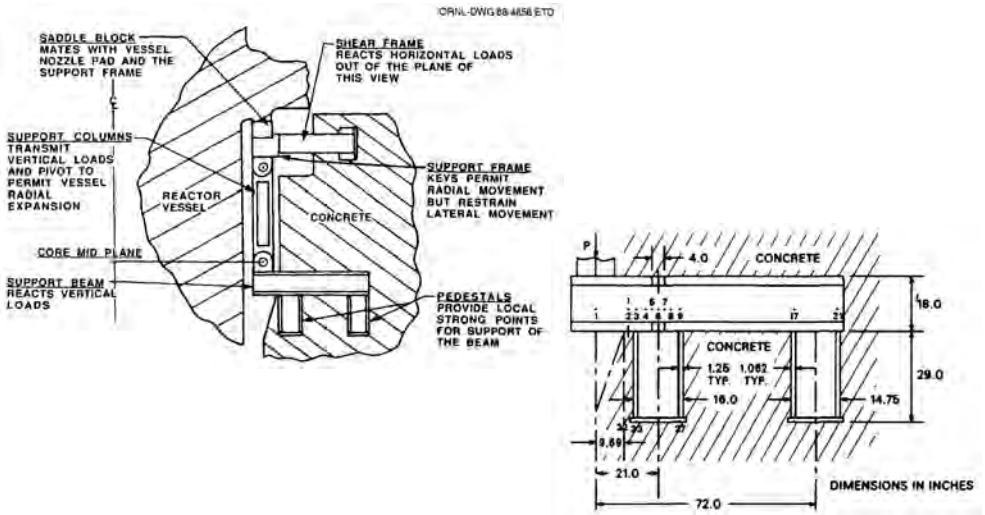

Figure 9. Radial section through Trojan reactor vessel supports showing principal structural and kinematic elements and details of the support beam [42].

2.2.6 Ring Girder

Geometry and Global Relevance

Ring girder supports employ a continuous circular steel girder positioned beneath the RPV shell, often near the nozzle beltline elevation. The girder's lower flange bears on a reinforced concrete pedestal or the CBS upper surface, distributing vertical load circumferentially and lowering peak local bearing pressures compared to discrete shoes. US examples include H.B. Robinson, while French EDF 900/1300 MWe units and Russian VVER-1000s employ similar welded rings [38, 39]. German KONVOI plants combine ring elements with pads to balance load distribution and allow radial thermal movement.

Irradiation Exposure and Degradation Process

When the girder bearing plane is near the core midplane, the pedestal contact zone lies in the highest fluence/dose region. RIVE within the surface layer reduces flatness and redistributes contact pressures, potentially creating localized stress concentrations. Where reinforcement intersects the bearing plane, microcracking reduces shear friction and dowel effectiveness.

Analytical Relationships

The compressive strength in the irradiated layer can be updated as

$$f_c(\delta) = \chi_c(\delta) f_{c0}, \qquad P_{\text{bear}}(\delta) = f_c(\delta) A_{\text{bear}}, \tag{4}$$

where $f_c(\delta)$ is the reduced compressive strength of irradiated concrete in the bearing layer at depth δ, $\chi_c(\delta)$ is a reduction factor derived from irradiated material data, f_{c0} is the unirradiated compressive strength, $P_{\text{bear}}(\delta)$ is the reduced bearing capacity at the interface, and A_{bear} is the effective contact area [22].

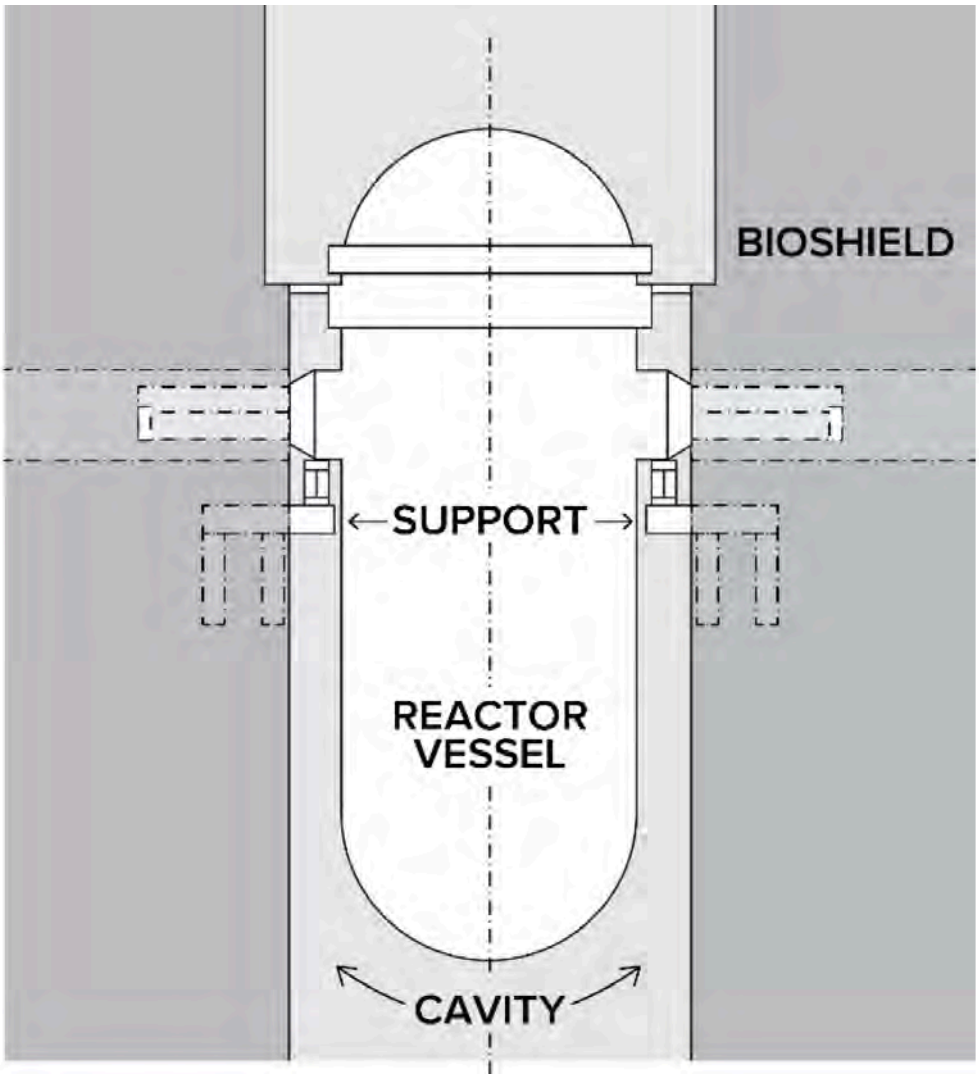

Figure 10. Schematic illustration of cantilever support located directly under the nozzle [22].

2.2.7 Summary

Table 1 provides a summary of the RPV support system data collected by Biwer et al. [22]. The table is organized according to support categories: column, skirt, shield tank, cantilever brackets, and shoe. The estimated distance between the fuel's mid-core elevation and the support is also provided. This distance is reported as the core mid-plane distance (CMPD). It is expected that the concrete in the vicinity of the support will be more susceptible to irradiation-induced damage as the CMPD decreases. The different types of support are categorized according to the significance of possible irradiation-induced damage of the concrete in the vicinity of the support.

Low Significance

Information collected on *base skirt supports* was limited. Most Babcock and Wilcox PWRs in commercial operation incorporate a support skirt design similar to that used for BWRs. It appears that all in-service and accidental loads are directly transferred to the concrete foundation through the base skirt assembly.

This area, which is located directly under the RPV, receives irradiation doses lower than the estimated damage threshold.

> *72 equivalent full-power year (EFPY) fluence at the Oconee Nuclear Station (ONS) RPV support embedment is estimated at* 1.63×10^{18} *n*.cm^{-2} *(*$E > 0.1$ MeV*) and gamma dose at* 1.75×10^{9} *rad. As such, the embedment concrete and grout are not susceptible to irradiation [damage] [36].*

When a neutron shield tank is present, it is expected that the fast-neutron flux will be dramatically reduced, thus preventing any significant irradiation-induced damage to the CBS [30].

Moderate Significance

Column support–based systems rely exclusively on steel columns to transfer vertical loads to the foundation. The potential irradiation-induced degradation of the concrete surrounding the columns does not appear to affect their function. Lateral loads are transferred to the CBS wall through embedded horizontal brackets (e.g., Prairie Island) or anchors [e.g., Palo Verde – Arizona Public Service (APS))]. Although this region is subjected to lower fast-neutron fluence, the anchor bond properties and the resistance of surrounding concrete may be affected by irradiation-induced damage.

High Significance

Support systems directly located under the nozzles include shoes resting on the CBS wall or a cantilever system embedded in the concrete. Some systems also include a ring girder located below the nozzle pads. The role of the ring girder in the distribution of vertical and horizontal loads from the RPV to the CBS has yet to be studied. Nevertheless, shoe-type and cantilever beam supports are essential for transferring both vertical and horizontal loads from the RPV to the CBS. The possible effects of irradiation on these systems require further study.

Table 1 presents detailed data supporting the design considerations discussed in the text. These values are essential for validating analytical models, performing verification calculations, and ensuring compliance with acceptance criteria.

Table 1. Summary of RPV support configuration – simplified and reorganized by support types from Biwer et al. [22]

Design	Plant	Support types / numbers	CMPD
		Column supports	
WH (2-l.)	Point Beach (1,2)	6 (4 RPV nozzle / 2 RPV brackets), ring girder	12 ft
WH (2-l.)	Prairie Island	6 (4 RPV nozzle / 2 RPV brackets), ring girder, embedded column	n.a.
CE (2-l.)	ANO-2	3 RPV nozzle (2 inlet / 1 outlet)	6 ft
CE (2-l.)	Palo Verde 1–3	4 RPV nozzle (upper column attached to CBS for lateral support)	8.5–15 ft (lat. support – base)
WH (3-l.)	V.C. Summer 1	6 RPV nozzle, embedded steel beam and column assembly	0 ft
		Base skirt supports	
BW (2-l.)	ANO-1	base skirt	n.a.
BW (2-l.)	Oconee (1,2)	base skirt	15 ft
BW (2-l.)	TMI 1	base skirt	13 ft
		Neutron shield tank (NST)	
WH (3-l.)	Beaver Valley (1,2)	6 RPV nozzle, shoe on NST / concrete skirt	6–31 ft (grout–c. skirt)
WH (3-l.)	North Anna (1,2)	6 RPV nozzle, shoe on NST / concrete skirt	31 ft (c. skirt)
WH (3-l.)	Surry (1,2)	RPV nozzle, shoe on NST / concrete skirt	31 ft (c. skirt)
		Cantilever brackets	
BW (2-l.)	Davis Besse	4 RPV inlet nozzle	2.3 ft
WH (3-l.)	Turkey Point (3,4)	Shoe supports sitting on embedded cantilevered steel beam and column assembly	0 ft
		Shoe resting on CBS	
WH (2-l.)	Ginna	6 (4 RPV nozzle / 2 RPV brackets)	3 ft
CE (2-l.)	Calvert Cliff (1,2)	3 RPV nozzle (2 inlet / 1 outlet), direct support on concrete	2.8 ft
CE (2-l.)	Palisades	3 RPV nozzle (2 inlet / 1 outlet), unclear config.	7.5 ft
CE (2-l.)	Millstone 2	3 RPV nozzle (2 inlet / 1 outlet)	n.a.
CE (3-l.)	St. Lucie (1,2)	3 RPV nozzle (2 inlet / 1 outlet). Pads on embedded horizontal beams	7.5 ft
CE (2-l.)	Waterford 3	4 RPV inlet nozzle. shoe support on embedded ring girder	3 ft
WH (3-l.)	J. Farley (1,2)	6 RPV nozzle, direct concrete support	7.5 ft
WH (3-l.)	H.B. Robinson 2	3 RPV alt. nozzle, direct concrete support	n.a.
WH (3-l.)	Shearon Harris	6 RPV nozzle, direct support on concrete	7.5 ft

BW - Babcock and Wilcox; CE - Combustion Engineering; WH - Westinghouse; 2/3-l - two/three-loop; CMPD - core mid-plane distance

2.3 DESIGN LOADS AND ACCIDENTAL LOAD CASES

The CBS and RPV support structures are designed for a comprehensive set of load cases that reflect both normal operating conditions and potential accident scenarios. Nuclear power plant structures are subject to a wide range of design and accidental loads over their operating life. These include dead loads from self-weight, live loads from maintenance activities, thermal loads due to operational heat-up and cool-down cycles, and environmental actions such as wind forces, shrinkage, and temperature gradients.

Accidental load cases, as defined by regulatory criteria, account for extreme but credible events that challenge structural integrity and safety margins. Among these, the LOCA and earthquake-induced ground motion are key design-basis events. Each induces fundamentally different stress states: LOCAs drive high internal pressure and thermal gradients, whereas seismic excitation imparts inertia forces through horizontal and vertical accelerations. In advanced evaluations, it is increasingly important to also consider the potential for these loads to act in combination, either sequentially or simultaneously, particularly in risk-informed safety assessments.

Seismic design is based on site-specific response spectra, with structural detailing aimed at achieving ductile behavior and preventing catastrophic failure modes. The design framework considers both the operating basis earthquake (OBE) and the safe shutdown earthquake (SSE) and aims to ensure that structural elements maintain both their load-carrying capacity and shielding performance under seismic demands. Load combinations are evaluated using strength and serviceability limit states to confirm that critical components retain both structural integrity and biological shielding functions during and after design-basis events.

The PWR vessel must be supported and restrained to withstand normal operating loads, seismic loads, and design basis accident loads, including those induced by postulated pipe ruptures such as those occurring in a LOCA. The support and restraint system must be designed to limit vessel movement to within allowable limits under the applicable load combinations. These requirements are imposed to ensure that the support system provides sufficient restraint under extreme events while minimizing unintended restraint against thermal movements during normal operation.

For the primary shield wall, LOCA-related loads include differential pressure across the reactor cavity created by a pipe break near the reactor nozzles. This loading acts either on the entire cavity or on portions of it and must be included explicitly in structural checks. The combined presence of pressure transients, jet impingement, pipe whip, and cavity pressure differentials places significant demands on both the shield wall and embedded support elements.

Special consideration is also required for irradiation effects, which can alter concrete modulus, tensile capacity, and fracture toughness over time. These long-term changes influence the safety margins of the CBS and must be incorporated into structural assessments for both normal and accidental load combinations.

The evaluation of these load cases requires consideration of material behavior under combined effects, construction tolerances, inspection protocols, and redundancy in load paths. Engineering judgment, supported by validated computational models and experimental evidence, is essential to confirm compliance with applicable nuclear safety codes and standards.

The following subsections examine the magnitude and nature of LOCA-induced loads; seismic design loading, including both operating basis earthquakes (OBEs) and SSEs; and scenarios in which combined loading governs structural demands. The narrative draws on recently published analyses [22, 43].

2.3.1 In-Service Loads

In general, in-service normal loads include dead loads *D* such as those caused by the weight of the RPV resting on its support structure; live loads *L* such as those from an overhead or traveling crane, dead weight of equipment, piping, cable trays, and so on, *L'*; and water loads *F* from the refueling cavity. Irradiation-induced expansion is an additional loading scenario that was introduced recently in a structural performance analysis associated with license extension applications.

2.3.2 Accidental Loads

Accidental loads include hypothetical low-frequency earthquake loads generated by an OBE *E*[1] or an SSE *E'*.[2]

In addition to environmental loads, abnormal loads are generated by a postulated high-energy pipe break accident within the containment and/or compartment thereof. A LOCA falls under that category. During a LOCA event, the discharged pressurized water from a pipe break at a reactor vessel nozzle will result in three types of LOCA dynamic and transient loads acting simultaneously on the reactor vessel support and the primary shielding wall:

1. Temperature (T) and pressure (P) increase in the reactor cavity and the containment building
2. Jet thrust force at the break (M)
3. Forces from the differential pressure as the decompression wave travels through reactor internals (i.e., reactor internal LOCA blowdown loads) that do not affect the CBS

"The loading transients depend on the postulated break conditions, the postulated break locations, and on the operating conditions and geometry of the system." [44].

These three loads must be combined with the load from the seismic event as part of the load combination in the licensing basis design.

Because of the coolant pressure, a LOCA is expected to produce higher transient and dynamic loading in a PWRs than in BWRs: "the overall safety significance is considered to be much less because of the lower operating pressures in primary systems in PWRs" (compared to that in BWRs) [44].

Pressurization and Heating of the Reactor Cavity

Pipe breaks at an RPV nozzle cause the release of steam into the annulus between the RPV and the CBS.

Depending on the temperature of the steam and its cooling speed while being transported in the cavity, transient thermal loading and pressurization of the CBS wall may occur.

In the report entitled "Assessment of the Effect of the In-Service Irradiation-Induced Degradation on the Structural Performance of Biological Shields during a Loss of Coolant Accident", it is approximated that the released steam would uniformly fill the annulus, thus producing time-dependent temperature and pressure that are uniformly applied to the inner surface of the CBS [45]. NUREG-0609 suggests that the asymmetry of the break may create differential pressure and temperature in the annulus between the closest and farthest locations from the break, as shown in Figure 11.

Under these conditions, the inner surface of the CBS is thus subject to a thermal "shock," potentially causing concrete dehydration, water vaporization, and restrained thermal expansion–induced stress of the concrete region that was previously damaged by in-service irradiation.

[1] An earthquake that could be expected to affect the site of a nuclear reactor but for which the plant's power production equipment is designed to remain functional without undue risk to public health and safety.

[2] Maximum earthquake potential for which certain structures, systems, and components that are important to safety are designed to sustain and remain functional.

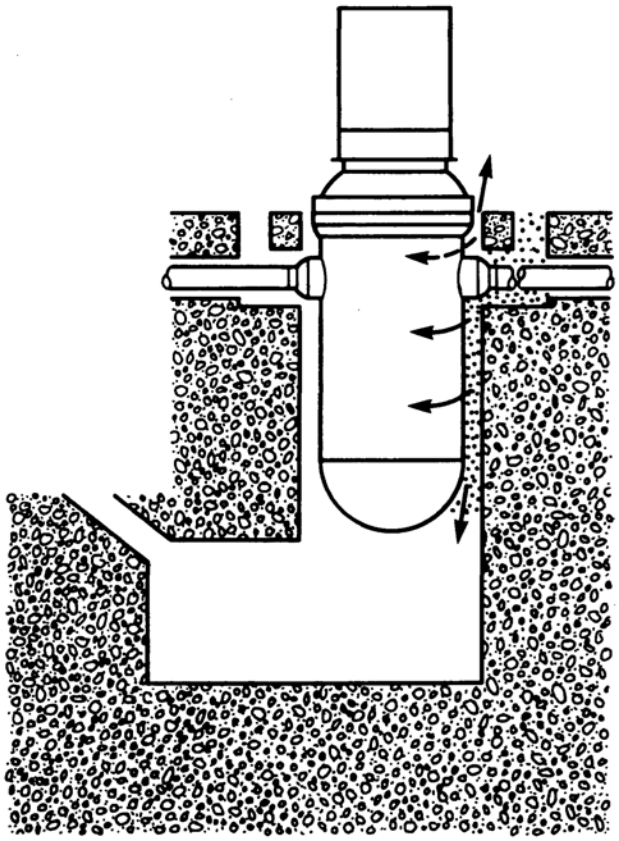

Figure 11. Pressurization of reactor annulus per NUREG-0609 [44].

Subcooled Blowdown Loads

> *As coolant discharges from the pipe break, a depressurization wave will travel from the break point into the vessel, causing unbalanced loads in the RPV and its internals. These loads are called LOCA blowdown loads. As this decompression wave enters the reactor vessel and travels down the vessel-to-barrel annulus [see Figure 12], it will cause the core barrel to deflect sideways toward the side of the decompression wave due to differential pressures acting on the two sides of the core barrel. This sideways deflection of the core barrel will create horizontal and vertical compressive forces on the reactor vessel supports and reactor internals. Such transient differential pressures, although of short duration, could place a significant load on the reactor vessel supports and reactor internals* [22].

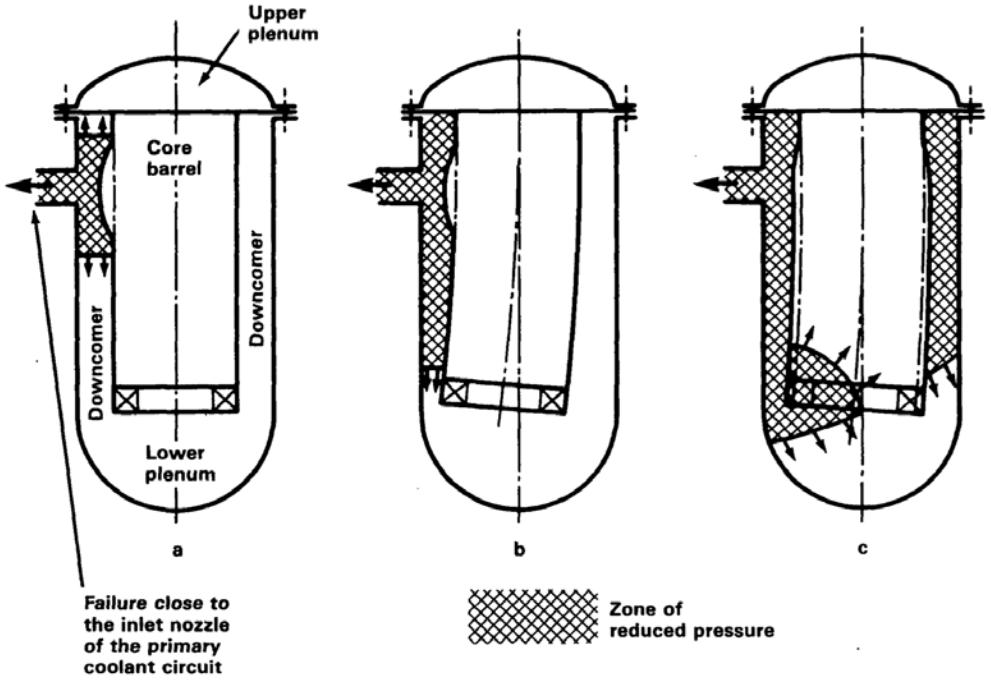

Figure 12. Example of asymmetrical internals load from NUREG-0609 [44].

Jet Thrust

At the pipe break location, a steam and water mixture is expelled, creating an axial thrust force that acts on the pipe. For PWRs, these breaks could be on the order of 75 cm (30 in) in diameter. Figure 13 shows the pipe jet thrust load acting on the reactor vessel and the reactor vessel supports at the location of the pipe break.

2.4 LOAD CASES CONSIDERED IN THIS ANALYSIS

2.4.1 Symbols and Variables

Table 2 summarizes the symbols and variables used throughout this section of the report; these definitions are applied consistently in the load combinations presented herein. Each symbol corresponds to a specific physical load mechanism or category defined by applicable nuclear codes and standards [46–49].

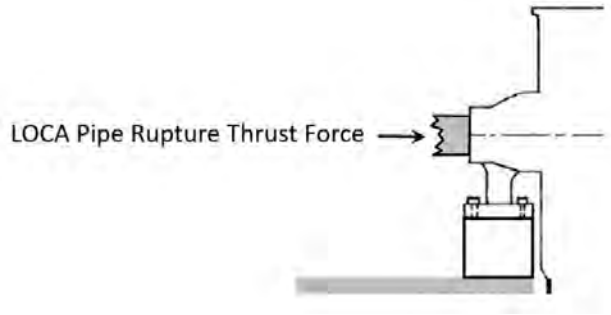

Figure 13. LOCA pipe rupture thrust force from NUREG-0609 [22].

2.4.2 LOCA Loads

A LOCA represents a design-basis accident that induces multiple transient and dynamic load mechanisms on the RPV supports and CBS, in addition to persistent operational loads. In accordance with [46, 47], all relevant effects must be combined with appropriate load factors to verify structural integrity and safety-related function. Structural components in proximity to the break location are subjected to a combination of jet impingement forces, pressure wave transients, thermal shocks, and sub-compartment pressurization. These load components must be incorporated into evaluations of the reactor cavity concrete, anchorage systems, and support structures.

Three principal transient load mechanisms are identified in [44]:

1. Temperature and pressure increase in the reactor cavity and containment building (P, T''; Table 2),
2. Jet thrust forces at the break location (M),
3. Differential pressure forces from decompression waves within the reactor internals (blowdown loads).

The evaluation of these mechanisms requires consideration of material behavior under combined effects, construction tolerances, inspection protocols, and redundancy in load paths. Engineering judgment, supported by validated computational models and experimental evidence, is essential to confirm compliance with NRC regulatory requirements [48, 49].

Pressurization and Heating of the Reactor Cavity (P, T'')

Steam release into the annulus between the RPV and the CBS creates transient pressurization and thermal loading on the inner surface. Alnaggar et al. (2023) approximate a uniform distribution in the annulus, producing time-dependent P and T'' [45]. However, NUREG-0609 notes that break asymmetry may cause differential conditions, with higher loads near the rupture and delayed peaks at the far side [44]. These conditions can induce thermal shock, concrete dehydration, pore water vaporization, and restrained expansion in irradiated concrete regions, potentially reducing tensile capacity [50].

Thermal shock introduces significant tensile stresses due to steep gradients between the rapidly heated surface and the cooler concrete interior. This stress can be approximated as

$$\sigma_{\text{th}} = E_c \cdot \alpha \cdot \Delta T\,, \tag{5}$$

where E_c is the modulus of elasticity of concrete, α is the coefficient of thermal expansion, and ΔT is the surface-to-core temperature differential. For $E_c = 30$ GPa, $\alpha = 1.0 \times 10^{-5}$/K, and $\Delta T = 150$ K, this yields $\sigma_{\text{th}} \approx 45$ MPa—far exceeding the tensile capacity of normal concrete. Mohammed et al. [51] reviewed explosive spalling behavior in heated concrete and reported that thermal stresses, in conjunction with pore pressure from steam, frequently result in spalling within minutes of exposure.

Table 2. Symbols and variables used throughout the LOCA, seismic, and combined load discussions.

Symbol	Type	Definition and application
D	Persistent	Dead load: self-weight of CBS, RPV, supports, and permanent appurtenances. Acts continuously on structural elements and support interfaces.
L	Operational	Live load: maintenance and handling loads (for example, overhead or traveling crane effects).
L'	Persistent	Dead weight of attached equipment, piping, and cable trays.
F	Operational	Hydrostatic load from the refueling cavity when flooded.
T	Persistent/Transient	Normal operating thermal load from heat-up and cool-down cycles; restraint effects in liners, anchors, and shoes.
P	Accidental transient	LOCA compartment pressure differential on reactor cavity surfaces; see Figure 11.
M	Accidental transient	Jet thrust and internal missile loads; see Figure 13.
Q	Accidental transient	Equipment or pipe accident load not otherwise captured by M or P.
A	Accidental/Operational	Transient live load that may be present during accident sequences or operational states.
E	Environmental	Seismic inertial load due to SSE or OBE.
T''	Accidental transient	LOCA-induced thermal load associated with P during hot steam impingement and cavity heating; see Figure 11.

Subcooled Blowdown Loads

A decompression wave propagates from the break into the RPV, producing unbalanced differential pressures across the core barrel. This causes lateral deflection toward the decompression side, generating horizontal and vertical forces on supports and internals (Figure 12). These short-duration forces, although smaller than seismic inertia loads, may still reach 50–100 kN [22]. While they do not directly load the CBS, they act through internals and supports, contributing to limit states related to anchor tension, base slab shear, and bond loss.

Jet Thrust and Internal Missiles (M)

Circumferential breaks in high-energy piping can produce jets of steam–water mixture that generate axial thrust on the pipe and impinge on nearby structures (Figure 13). For PWRs, design-basis breaks may be up to 75 cm in diameter. Jet thrust imparts both horizontal and vertical forces to RPV supports. Pipe rupture may also release internal missiles requiring evaluation per ASME [46].

The primary mechanical force generated by a LOCA is the jet thrust, which can be approximated as:

$$F_{jet} = K \cdot p_0 \cdot A_{break}\,, \tag{6}$$

where p_0 is the internal pressure prior to rupture, A_{break} is the cross-sectional area of the break, and K is a dimensionless coefficient representing momentum amplification due to two-phase effects. Regulatory guidance suggests using $K = 1.3$ for saturated steam or subcooled water breaks [9]. Later in this report, a 2A cold-leg LOCA case using RELAP5-3D is analyzed and peak jet forces of approximately 6.0 MN are achieved. These forces act both at the break location as a reaction and as impingement loads if directed toward the CBS or supports.

Sub-Compartment Pressurization

RELAP5-3D simulations herein indicate that the reactor cavity may experience transient internal pressures up to 5.5 MPa during early blowdown. These pressures act radially on cavity walls, floors, and embedded supports, producing outward loads that must be checked against flexural and shear capacity of the CBS.

Governing LOCA-Only Load Combination

Following Biwer et al. [22], the governing LOCA-only load combination is:

$$U = (1.0 \pm 0.1)(D + T) + 1.25(P + M + Q + A + L') + T'' \tag{7}$$

where the terms are defined in Table 2. Deterministic bounding combinations and time-history analyses are employed to ensure sufficient capacity under jet, pressure, and thermal loads. These accident load terms are modeled in accordance with ACI 349-13 and ASME Section III protocols [46, 47].

Overall, the LOCA load environment includes intense, short-duration transients from multiple sources. Proper evaluation requires a comprehensive framework that integrates deterministic design equations, dynamic simulations, and experimental validation to maintain safety margins for the RPV supports and CBS.

2.4.3 Seismic Loads

Seismic demand for the CBS and the RPV support system is governed by the SSE and, where applicable, the OBE. Seismic excitation represents a critical design-basis load case for nuclear structures. Both horizontal and vertical ground motions generate inertial forces in structural systems and equipment, and the severity of the seismic input is defined through these two primary events.

The OBE corresponds to an event under which the facility is expected to continue operation without interruption, typically associated with ground accelerations of 0.1–0.2g. The SSE represents the maximum considered seismic event, under which the facility must safely shut down without loss of structural or containment integrity, generally associated with ground accelerations ranging from 0.3g to 0.5g [52]. Ground motions are represented by three orthogonal components with corresponding horizontal and vertical response spectra that define peak accelerations as a function of natural period.

Static Equivalent Seismic Loads

The horizontal inertia force induced by seismic motion is typically estimated using a base shear formulation:

$$F_h = A_h \cdot W\,, \tag{8}$$

where F_h is the horizontal base shear, A_h is the horizontal peak ground acceleration normalized to gravity, and W is the total structural or equipment weight. In the design file for the RPV support system, this static approach was applied using a nominal horizontal SSE acceleration of 0.5g [43]. For a structure with W = 10 MN, the resulting base shear is F_h = 5 MN.

A similar approach is used for vertical seismic effects:

$$F_v = A_v \cdot W\,, \tag{9}$$

where A_v is the vertical acceleration component. Design standards such as ASCE 4 and NRC RG 1.60 recommend $A_v = 0.67A_h$ in the absence of site-specific data [52]. However, conservative assumptions in some design cases adopt $A_v = A_h = 0.5g$ to account for near-fault effects and vertical ground motion amplification, as applied in the simplified RPV load assessment [22, 43].

Rigid Body Assumption

In this method, the RPV and CBS are modeled as rigid bodies subjected to identical accelerations at the base. The total seismic force on the RPV, represented as a lumped mass at its center of mass, is given by:

$$F = M_{\text{RPV}} \cdot S_a, \tag{10}$$

where M_{RPV} is the effective mass of the RPV and S_a is the spectral acceleration.

With respect to seismic acceleration, Hong (1993) reported a safe shutdown acceleration of $0.2g$, while other analyses indicated maximum response accelerations up to $0.36g$ at the support level [53]. A conservative design may assume $0.5g$, with extreme cases applying a factor of safety of 2, corresponding to $1.0g$.

Dynamic Analysis and Soil-Structure Interaction Effects

While static equivalent methods are useful for scoping evaluations, rigorous seismic analysis typically involves dynamic techniques such as response spectrum or time-history analysis. Modal response spectrum analysis accounts for higher mode contributions and damping effects, providing a more realistic internal force distribution. For the CBS, which exhibits significant stiffness and mass, higher mode responses can be non-negligible. Dynamic soil-structure interaction modeling is often necessary for embedded or partially embedded components.

The dynamic characteristics are determined from a three-dimensional finite element model that captures CBS geometry, penetrations and openings, liner plates, and the stiffness and connectivity of RPV supports, anchors, and embedments. Soil-structure interaction is included where required by the licensing basis; in-structure amplification is accounted for using floor response spectra at equipment and anchorage locations. Mode shapes and frequencies are extracted and combined by either the square-root-of-sum-of-squares or complete quadratic combination method. Horizontal and vertical components are combined by standard orthogonal rules to obtain total seismic effects on members and connections.

Limit States and Failure Modes

The assessment employs nonlinear dynamic modeling of the CBS and identifies potential structural failure modes such as shear cracking and local crushing at the base of the RPV support zone. In particular, the “CBS shear failure due to lateral seismic load” limit state is highlighted as a governing case under horizontal SSE loading. Anchor pullout and pedestal rocking are also considered key performance concerns. The applied base shear demand in these evaluations is consistent with the simplified estimation methodology, but finite element analysis is used to resolve stress concentrations and time-dependent amplification.

Seismic accelerations also influence vertical support and anchorage systems. Vertical motion can transiently reduce contact force at supports, potentially initiating uplift or loss of shear friction resistance. This is particularly critical for RPV skirts and base slab interfaces. RPV base slab punching and shear are governing failure modes under combined vertical load and horizontal rocking. High-fidelity nonlinear simulations, including cracked concrete behavior and dynamic stiffness degradation, are required to confirm the adequacy of safety margins.

Anchorage design and verification consider concrete breakout, pullout, pry-out, steel strength, and interaction with liner plates or embedded steel. Clearances at seismic gaps and around penetrations are checked to preclude contact and secondary impact. For support shoes and bearing interfaces, analyses demonstrate that frictional and mechanical restraint accommodate thermal movements while sustaining seismic shear and uplift without loss of support.

Governing Seismic-Only Load Combination

A representative seismic-only load combination consistent with examples for severe environmental loading during normal operation, as discussed in Biwer et al. [22], is

$$U = 1.25(D + L' + T + A + E) \tag{11}$$

where:

- D – dead load,
- L' – dead weight of attached equipment and piping,
- T – normal operating thermal load,
- A – operational live loads present during the seismic event,
- E – seismic inertial load due to SSE or OBE.

This combination captures the dominating inertial effects together with persistent service loads. Acceptance checks verify strength and serviceability at critical sections of the CBS, anchors and embedments at the liner and support interfaces, and the RPV support components. Evaluation includes demand-to-capacity ratios for axial force, shear, and bending; anchor concrete limit states; and deformation compatibility. When nonlinear procedures are used, hinge formation, rotation limits, and cumulative plastic demands are demonstrated to remain within acceptance criteria.

Summary

In summary, the SSE dominates seismic structural design requirements, with the OBE generally serving as a serviceability check. Simplified acceleration-based load models are useful for bounding analysis but must be supplemented with modal and time history methods for critical features. Vertical accelerations must be considered explicitly for anchorage and base shear evaluations, especially where combined tension and shear govern performance.

2.4.4 Combined LOCA and Seismic Loads

Although design-basis events such as LOCAs and SSEs are typically considered separately due to the low probability of joint occurrence, structural evaluations increasingly incorporate scenarios in which these extreme loads occur in combination. Such a combination may result from a seismically induced pipe rupture or from closely sequenced events during beyond-design-basis conditions. The potential interaction of thermal, mechanical, and dynamic effects presents a highly demanding structural load case.

In a combined LOCA and SSE scenario, the structural system must simultaneously resist inertia forces from seismic ground motion and internal forces from pressure and thermal gradients. For the RPV support system, the key loads include base shear from horizontal acceleration, uplift and bearing from vertical acceleration, and thermal plus mechanical loads from the LOCA jet and cavity pressurization. Design guidelines such as ACI 349-13 and ASME Section III allow full-load combination for faulted conditions. A conservative representation is expressed as

$$U_{\text{combined}} = D + E + P + T + M\,, \tag{12}$$

where D is dead load, E is seismic load (including horizontal and vertical components), P is LOCA-induced internal pressure, T is thermal shock-induced stress, and M is mechanical shock or jet force.

When a LOCA coincides with an SSE, peak demands from P, T'', M, Q, and E may occur in close succession. Figure 11–Figure 13 illustrate the governing mechanisms. Conservative combination is required by the ASME [46] and American Concrete Institute [47] to ensure that safety-related functions are preserved.

Governing Combined Load Combination

From Biwer et al. [22], the governing combined load case may be written as

$$U = (1.0 \pm 0.1)(D + T) + 1.25(P + M + Q + A + L' + E) + T'' \,, \tag{13}$$

where Q represents blowdown loads, and L' represents attached equipment and piping weight. Verification must confirm that the CBS and RPV supports maintain strength and serviceability considering nonlinear dynamic effects, potential sliding at support shoes, and local bearing stresses in concrete near anchors and pedestals. This evaluation requires consideration of material behavior under combined effects, construction tolerances, inspection protocols, and redundancy in load paths. Engineering judgment, supported by validated computational models and experimental evidence, is essential to confirm compliance with NRC regulatory requirements [48, 49].

Load Phasing and Interaction Effects

Time-dependent load phasing introduces complexity into combined evaluations. The pressure spike from a LOCA typically occurs within the first second after rupture [22], whereas seismic motion can extend over tens of seconds with multiple peaks. If a seismic event initiates a pipe break, the pressure and thermal loads could superimpose on an already dynamically oscillating structural system. In such cases, demand must be evaluated during the most critical overlap window.

Anchorage and Support Behavior

Anchorage systems are particularly vulnerable in combined LOCA+SSE scenarios. Seismic motion induces alternating tension and shear in anchor bolts, whereas LOCA-induced thermal expansion and pressure gradients generate sustained axial loads. Combined demand in tension–shear space can be represented by an interaction equation:

$$\left(\frac{T}{T_{\text{ult}}}\right)^m + \left(\frac{V}{V_{\text{ult}}}\right)^n \leq 1 \,, \tag{14}$$

where T and V are axial and shear demands, T_{ult} and V_{ult} are ultimate capacities, and (m, n) are interaction exponents typically taken as 1.0 or 2.0 depending on the anchor type and applicable code provisions. Nonlinear behavior such as ratcheting, bond degradation, or pry-out must also be considered if anchors are embedded in cracked or irradiated concrete.

Deterministic vs. Probabilistic Assessment

While deterministic analysis conservatively assumes full simultaneity of maximum loads, probabilistic safety assessments (PSAs) permit load factor reduction based on conditional probability. For instance, PSA may justify scaling LOCA loads when combined with SSE if the co-occurrence probability is sufficiently low [22]. However, such reduction requires validation through fault tree and hazard modeling. In practice, design conservatism often prevails, and full combinations are used in critical evaluations.

The Biwer (2021) study emphasizes that combined scenarios, while rare, are not negligible in probabilistic risk evaluation [22]. Structural margin degradation due to prior irradiation or thermal preloading exacerbates combined effects. The use of high-fidelity finite element models incorporating concrete damage plasticity, temperature-dependent properties, and dynamic load phasing is recommended for critical combined assessments.

Summary

In summary, although simultaneous LOCA and seismic events are beyond the design basis in most licensing frameworks, their combination represents an envelope case for structural demand. Structural resilience in such scenarios is a key attribute of defense-in-depth, and margin assessments under combined loading are essential to support long-term operation strategies.

3. SIMULATION OF LOCA USING RELAP5

Reliable prediction of reactor cavity over-pressurization following a postulated LOCA is fundamental for safety analyses that concern both near-term mechanical loads and long-term degradation mechanisms in shielding concrete. The reactor cavity for a three-loop PWR is an annular, highly confined volume bounded laterally by the CBS, below by a reinforced foundation slab, and above by the refueling cavity. In the first instants after a postulated break, the cavity experiences a rapid pressure excursion driven by choked discharge at the break plane, steep pressure gradients along tortuous flow paths, and strong azimuthal/axial asymmetries caused by geometric obstructions and branch connections to neighboring rooms. Capturing these features with sufficient temporal and spatial fidelity is a prerequisite for deriving structurally meaningful loads, for quantifying jet impingement forces, and for performing sensitivity and uncertainty evaluations of parameters that govern the response.

To address this need, a plant-scale thermal hydraulic model of a generic three-loop PWR was constructed using RELAP5-3D. The model couples a multidimensional representation of the reactor cavity to complete primary and secondary system nodalizations, enabling consistent system-to-containment interactions during the blowdown. The overarching objectives are threefold: first, to resolve pressure-wave propagation within the cavity and adjacent compartments with adequate resolution to characterize peak loads and their decay; second, to furnish boundary conditions at the break plane—namely pressure, temperature, and mass flux—that support evaluation of jet impingement loads using accepted guidance; and third, to provide a computational platform for efficient sensitivity and uncertainty studies spanning break size, location, and discharge modeling assumptions. The sections that follow present a concise code overview, the geometric context and nodalization strategy for the reference plant, and detailed results for double-ended guillotine break (DEGB) and 1A break scenarios together with targeted sensitivities and validation comparisons. Break sizes are expressed relative to the cold-leg pipe flow area ($A = 0.383$ m^2); thus, a 1A case corresponds to a guillotine break of one cold leg, a 2A case to a DEGB with twice that area, and fractional cases (e.g., 0.5A, 0.25A) to smaller postulated openings

3.1 RELAP5 CODE OVERVIEW

The system analyses were performed with RELAP5-3D, which is developed at Idaho National Laboratory and supported by US Department of Energy (DOE), the NRC, and programs such as the International Code Assessment Program, Code Applications and Maintenance Program, and the International RELAP5 Users Group [54]. The code solves non-equilibrium, two-fluid, two-component conservation equations for mass, momentum, and energy, allowing explicit treatment of vapor, liquid, and non-condensable gases. Closure correlations provide models for interfacial friction, heat transfer, wall drag, and phase change phenomena, while special-purpose options represent critical flow, critical heat flux, and counter-current flow limitation. For applications where three-dimensional recirculation and anisotropic wave propagation are important, RELAP5-3D offers a multidimensional hydraulic component (`multid`) that resolves axial, radial, and azimuthal discretizations within a single control volume network.

A postulated instantaneous DEGB of an RPV nozzle or of a hot/cold leg introduces strong spatial asymmetries in pressure and mass flow distributions throughout the containment [44]. Accurate simulation therefore requires both appropriate discharge modeling and a nodalization that represents the principal flow paths linking the cavity to steam generator enclosures, the refueling cavity, and lower compartments. In this work, the nodalization divides the plant into connected control volumes and junctions, where break boundary conditions are applied with valve and branch components and the cavity is represented by stacked `multid` regions. The use of three-dimensional components in the cavity enables representation

of azimuthal wave travel, timing offsets between sensor locations, and amplitude attenuation along the vertical stack. This capability, combined with realistic containment connectivity, allows direct extraction of differential pressures across the CBS and around the RPV nozzle zone that are consistent with the system's transient mass and energy balances.

3.2 GENERIC 3-LOOP PWR AND RELAP5-3D NODALIZATION

Publicly available information for a representative Westinghouse three-loop large dry containment establishes the geometric context for the reactor building. As illustrated in Figure 14, the RPV resides in an annular cavity enveloped by the CBS, beneath the refueling cavity, and above the foundation slab. The principal compartments are summarized in Figure 15, which identifies the steam generator rooms and auxiliary spaces that exchange flow with the cavity. These references guide the definition of control volumes, inter-compartment openings, and elevation relationships used in the model.

Hot- and cold-leg penetrations provide direct communication between the nozzle zone and the steam generator rooms, while additional openings connect the cavity to the refueling cavity, the residual heat removal room, and lower compartments. To supplement incomplete geometric data, nodalization diagrams for the Beaver Valley three-loop plant in Figure 16–Figure 18 are used as a proxy for flow areas and volumes when explicit numbers are not available. This approach ensures that the modeled connectivity reflects realistic bypasses and recirculation paths during blowdown, which strongly influence pressure equalization times and differential load distributions. The vessel geometry in Figure 19 sets the nozzle elevations and the height of the cylindrical section below the nozzles; the perspective view in Figure 20 highlights the bioshield thickness and niches housing vessel supports. The cavity is highly confined: the annular gap is 0.082 m between insulation and CBS and 0.171 m from vessel outer radius to CBS inner radius. Key dimensions and volumes used in the model are tabulated in Table 3, and initial containment conditions are taken as dry air near 1 atm and 20 °C.

The RELAP5-3D model blends an existing H. B. Robinson nodalization [55] with a new multidimensional cavity and containment representation. The lower cavity is a `multid` component (ID 48) connected upward to the annular cavity region (ID 50), which in turn connects to the nozzle-zone `multid` (ID 52). The refueling cavity is represented by a top `multid` (ID 54). Radial branches link the nozzle zone to one-dimensional components that model the hot- and cold-leg tunnels leading to the steam generator rooms. The break is represented by dedicated valves on cold leg A or hot leg B, with a loop isolation valve that is closed upon LOCA initiation, thereby imposing the intended boundary conditions. Containment connectivity is implemented with branch components and junctions as summarized in Figure 21. The cold-leg-A break representation is shown in Figure 22. The three-dimensional meshing strategy in Table 4 employs uniform 30° azimuthal sectors to resolve azimuthal propagation and differential measurements, while axial and radial partitions align with geometric discontinuities such as the nozzle zone and cavity floor. The azimuthal layout is depicted in Figure 23. Primary and secondary side discretizations are provided in Figure 24–Figure 26.

3.3 RESULTS

Two initiating events are analyzed: an instantaneous 2A DEGB of cold leg A and an instantaneous 1A break of cold leg A used as the reference medium-break case. Quantities of interest are pressure histories in the nozzle zone, annular cavity, lower cavity, refueling cavity, and containment; differential pressures around the RPV and across the CBS; temperature responses in major volumes; mass flow rates at the break; and jet impingement forces. Jet force F_b is calculated using Equation 15 [10].

$$F_b = \frac{G_e^2 A_e}{\varrho_e g_c} + A_e(P_e - P_{amb}), \tag{15}$$

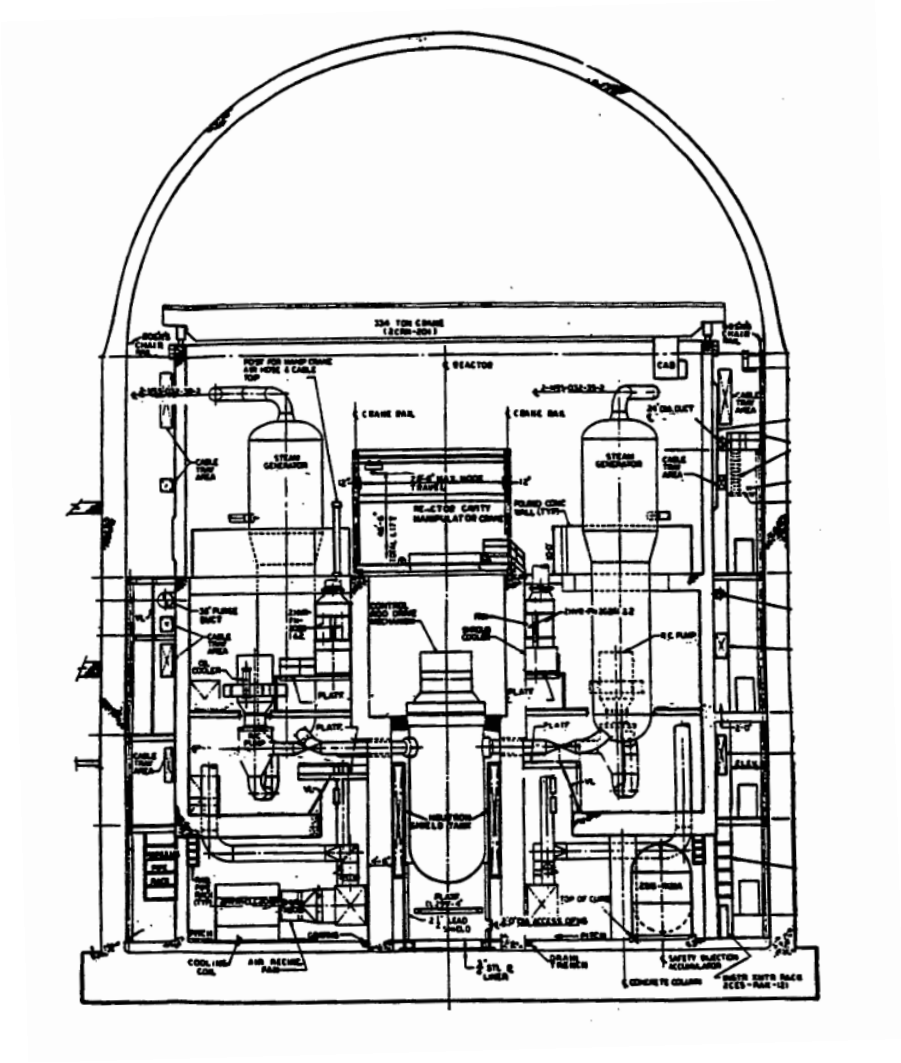

Figure 14. Three-loop containment cross-section [15].

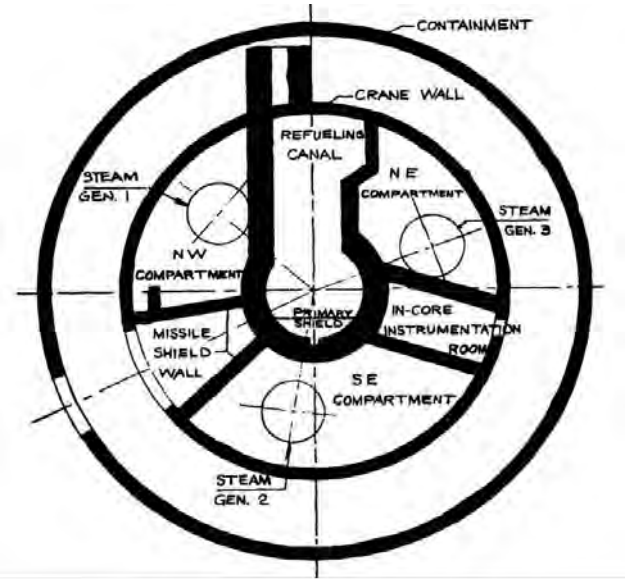

Figure 15. Reactor building compartment arrangement [56].

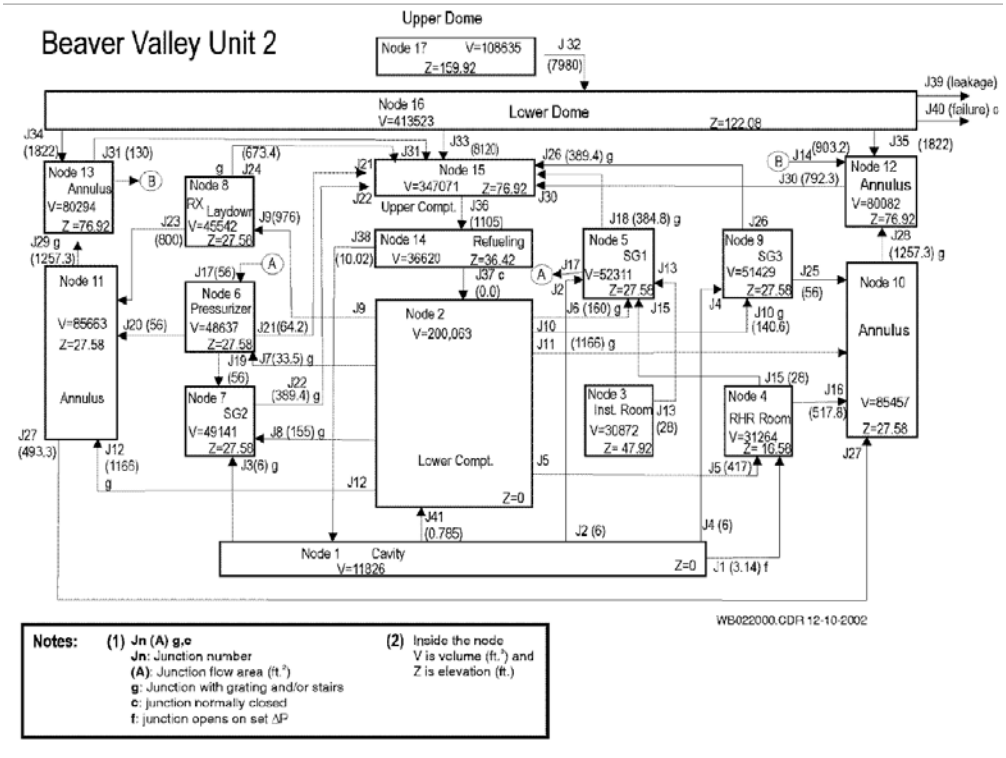

Figure 16. Example compartment connectivity for a three-loop plant [57].

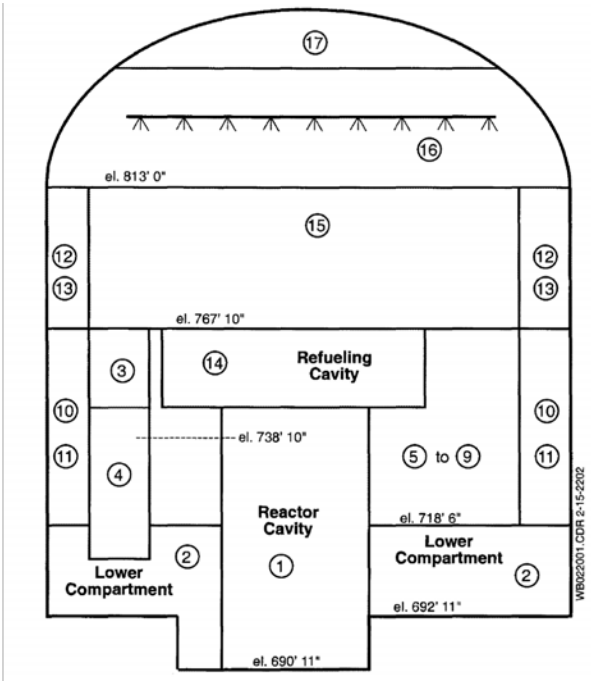

Figure 17. MAAP-based nodalization, front view [57].

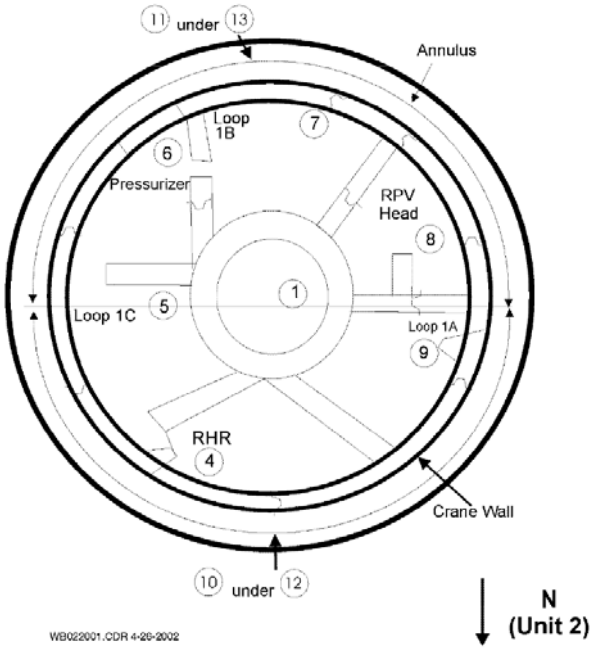

Figure 18. Top view of compartment nodalization [57].

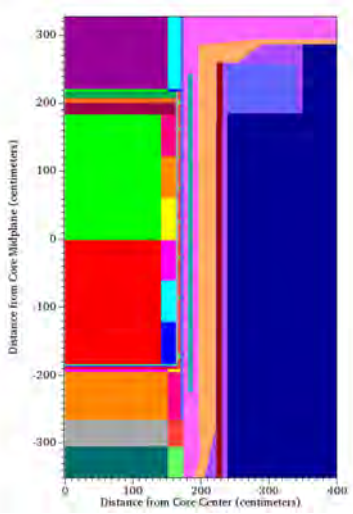

Figure 19. RPV geometry and cavity annulus [23].

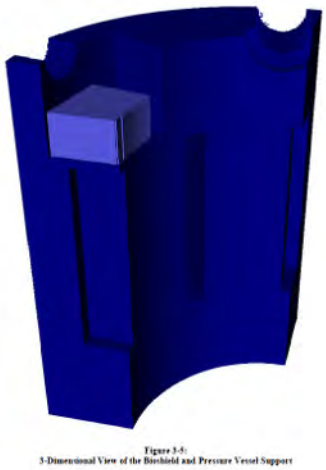

Figure 20. Perspective of cavity and bioshield [23].

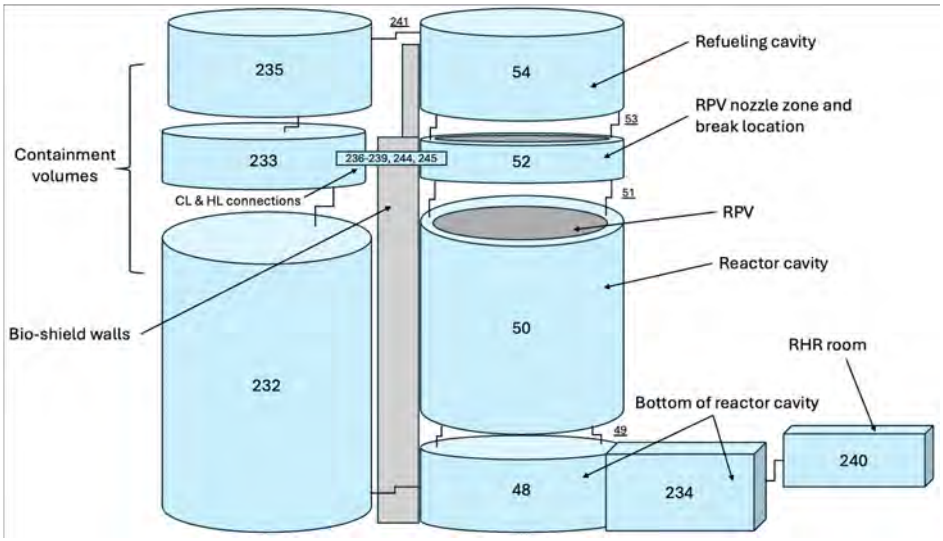

Figure 21. Containment and cavity nodalization.

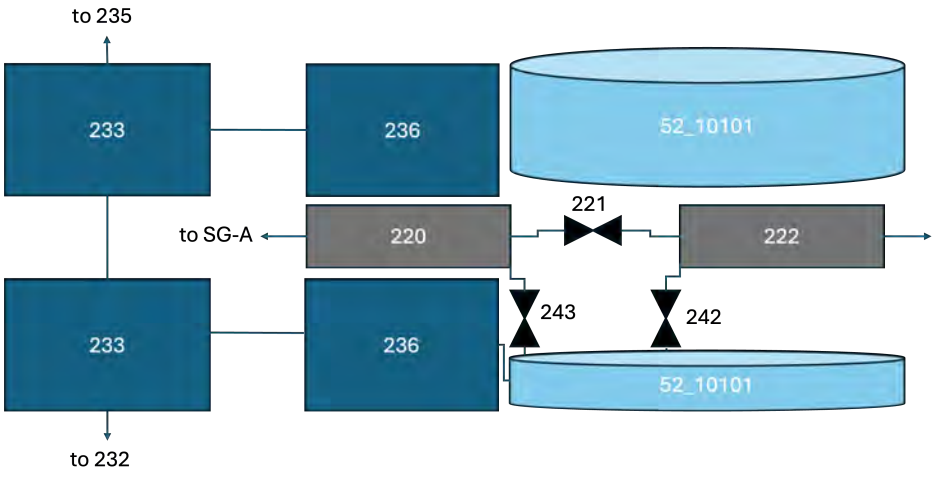

Figure 22. Cold-leg-A break representation.

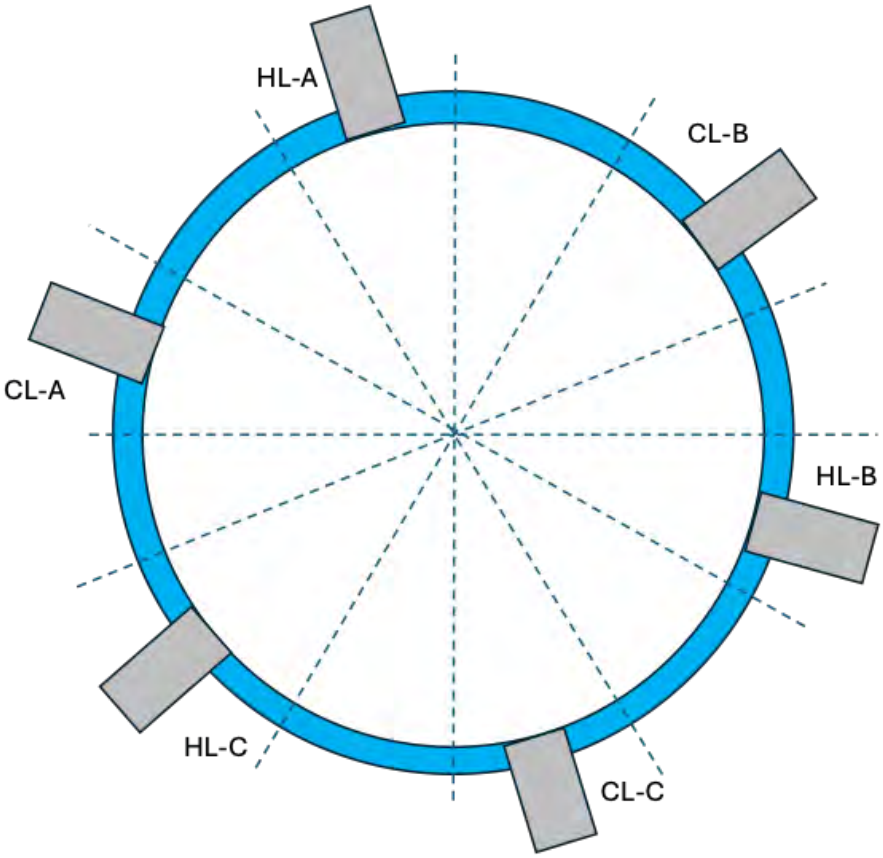

Figure 23. Azimuthal discretization of the cavity.

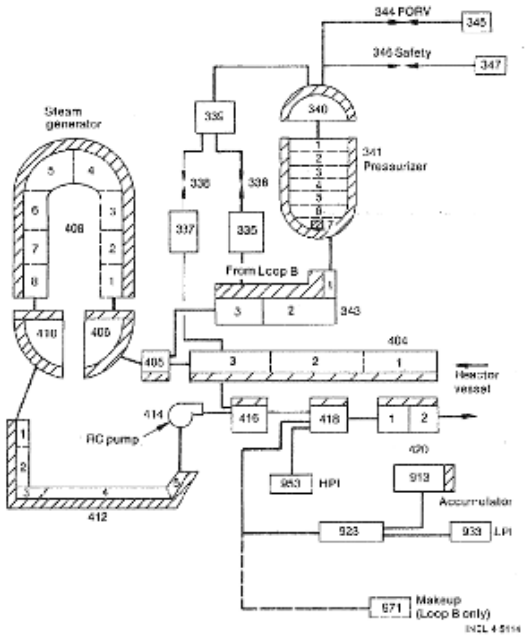

Figure 24. Primary-side nodalization.

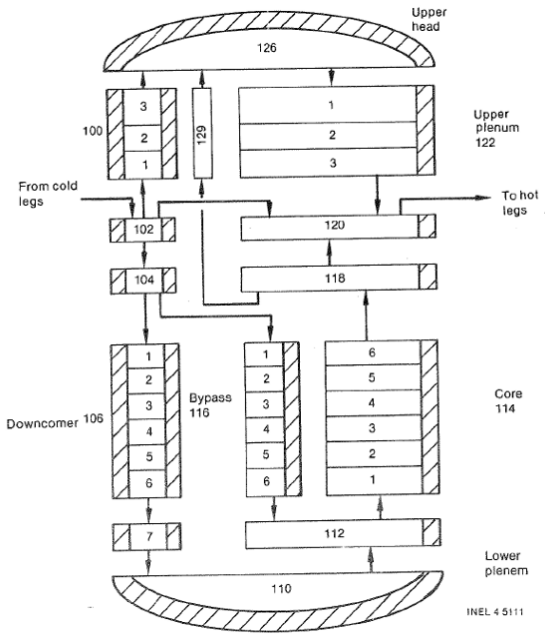

Figure 25. RPV nodalization.

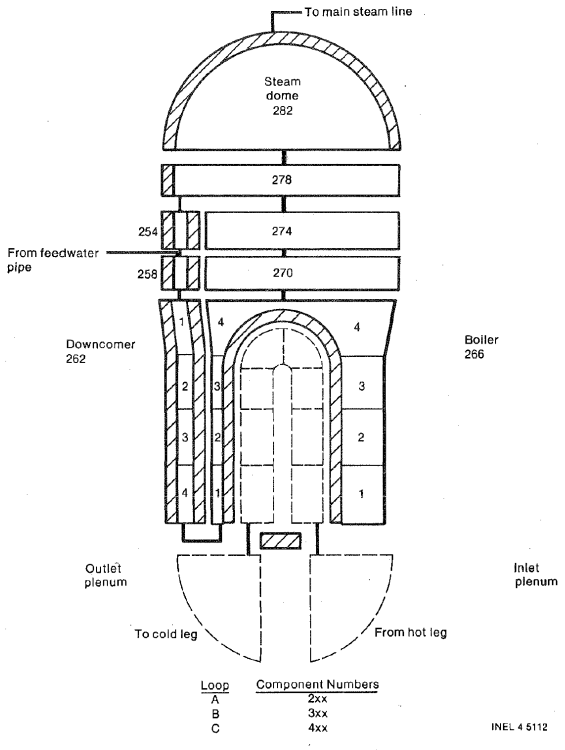

Figure 26. Steam generator nodalization.

Table 3. Dimensions and volumes used for cavity modeling.

Parameter	Value (SI)	Value (Imperial)
Reactor cavity gap (RPV OR to CBS IR)	0.171 m	0.561 ft
Effective reactor cavity gap (RPV insulation OR to CBS IR)	0.082 m	0.268 ft
RPV cylindrical part height below the nozzles	5.400 m	17.717 ft
RPV lower plenum height	1.750 m	5.742 ft
CBS thickness	1.612 m	5.290 ft
Bottom reactor cavity height	3.250 m	10.666 ft
Bottom reactor cavity diameter	5.020 m	16.471 ft
Refueling cavity height	6.500 m	21.330 ft
RPV nozzle zone height	2.301 m	7.551 ft
Cold leg diameter	0.699 m	2.292 ft
Flow area between RPV cavity and SG compartments	1.690 m^2	18.195 ft^2
Flow area between RPV cavity and RHR room	0.290 m^2	3.122 ft^2
Reactor cavity net free volume	335 m^3	1.18×10^4 ft^3
Refueling cavity net free volume	1,037 m^3	3.66×10^4 ft^3
Containment net free volume	57,000 m^3	2.01×10^6 ft^3

Table 4. Three-dimensional meshing of cavity `multid` components.

Modeled part	Component ID number	Radial mesh	Azimuthal mesh	Axial mesh
Lower part of reactor cavity	48	4	12	5
Reactor cavity	50	1	12	7
RPV nozzle section	52	1	12	5
Refueling cavity	54	9	12	7

where G_e is the mass flux, A_e the break area, ϱ_e the density, g_c the gravitational constant, P_e the pressure at the break plane, and P_{amb} the ambient pressure in the receiving compartment.

3.3.1 2A LOCA

As illustrated in Figure 27, the nozzle-zone pressure exhibits an immediate, high-amplitude spike at $t = 0$ caused by choked discharge and the resulting compressive wave. Figure 28 resolves the first 10 s, revealing steep rise, early oscillations, and partial reflections into the opposite hot-leg region (HL-B). The annular cavity responds with lower peaks and mild azimuthal timing offsets due to circumferential wave travel and geometric obstructions; this behavior is evident over the full transient in Figure 29 and during the initial 10 s in Figure 30. The lower cavity and refueling cavity, as illustrated in Figure 31, show attenuated spikes, reflecting the damping effect of the vessel skirt, floor recesses, and restricted inter-compartment openings. The containment-wide pressure, as shown in Figure 32, increases gradually toward an asymptote because sprays, fan coolers, and heat structures are not modeled, so long-term removal mechanisms are absent.

Differential pressures quantify load non-uniformity. Around the nozzle zone, Figure 33 indicates peak differentials approaching 33 bar within the first 10 s as counter-propagating waves from the two azimuthal directions superpose. In the annular region below the nozzles the differentials are substantially lower, as shown in Figure 34, consistent with both radial distance from the source and flow redistribution toward connected compartments. Across the CBS, Figure 35 shows a transient differential near 40 bar, which decays as the containment equalizes. Temperature histories in Figure 36 demonstrate short-term heating of the cavity and containment as high-enthalpy two-phase fluid is discharged. The break mass-flow histories

in Figure 37 follow the expected pattern of an initial surge at high upstream pressure followed by decay as the primary depressurizes and containment pressurizes. The jet impingement force in Figure 38 peaks near 6.03 MN, consistent with the governing expression and the large break area.

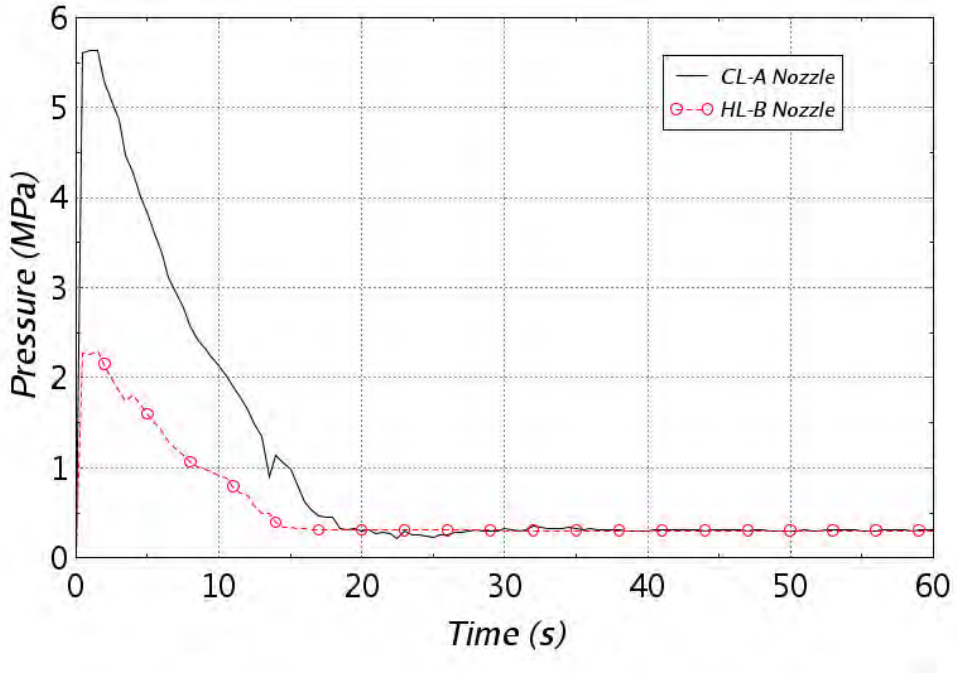

Figure 27. Nozzle-zone pressure, 2A DEGB.

3.3.2 1A LOCA – Reference Case

The 1A cold-leg-A break serves as the reference medium-break configuration. Relative to the 2A DEGB case, peak pressures in the nozzle zone and annular cavity are reduced because the smaller discharge area lowers the initial mass flux and compressive wave amplitude. The early-time nozzle-zone and annular responses are shown in Figure 39 and Figure 40. The ranking of differentials follows the 2A trend: the largest values occur near the nozzle elevation where counter-propagating waves intersect, as shown in Figure 41; lower values are observed in the annular region below, as illustrated in Figure 42; and high but reduced differentials occur across the CBS, as shown in Figure 43. Temperature evolution (i.e., Figure 44) and jet impingement force (i.e., Figure 46) are qualitatively similar to the 2A case, with maxima reflecting the interplay of upstream depressurization and compartment pressurization. The break mass-flow history for 1A is provided in Figure 45.

3.3.2.1 Sensitivities on 1A LOCA Case

Critical-flow modeling and break location were varied to evaluate robustness. Replacing the default Ransom–Trapp model with the Henry–Fauske option increases the predicted early-time nozzle-zone pressure, as shown in Figure 47, and slightly elevates the differential across the CBS, as illustrated in Figure 48, reflecting a larger effective discharge coefficient under the same boundary conditions. Relocating the break to hot leg B, the pressurizer loop, redistributes the wave paths relative to the cavity openings and reduces the load on the cavity and CBS as shown in Figure 49 and Figure 50. Quantitative comparisons of peak cavity pressures for these sensitivities are given in Table 5.

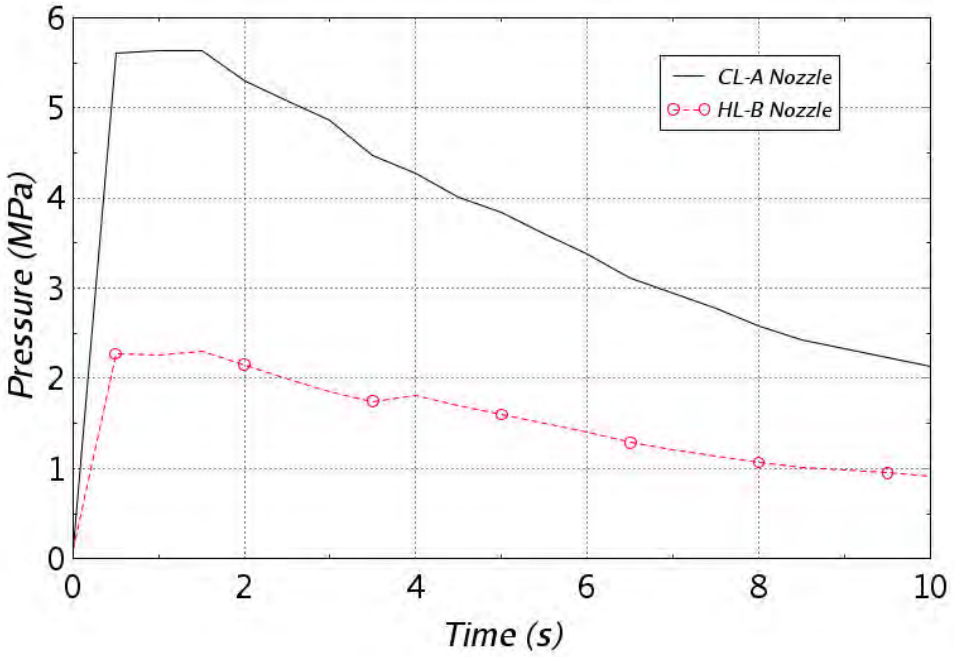

Figure 28. Nozzle-zone pressure, first 10 s, 2A DEGB.

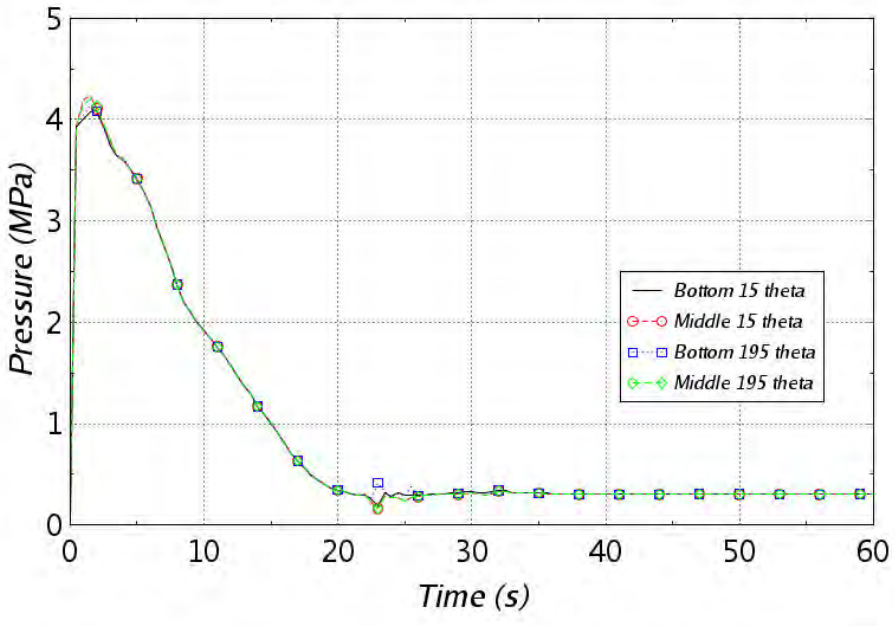

Figure 29. Annular cavity pressure, 2A DEGB.

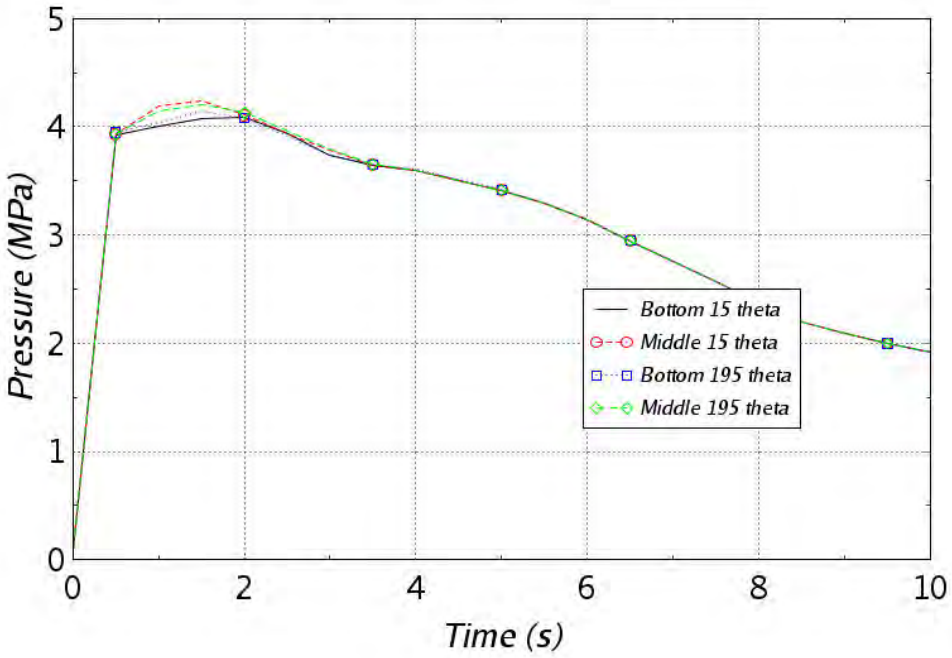

Figure 30. Annular cavity pressure, first 10 s, 2A DEGB.

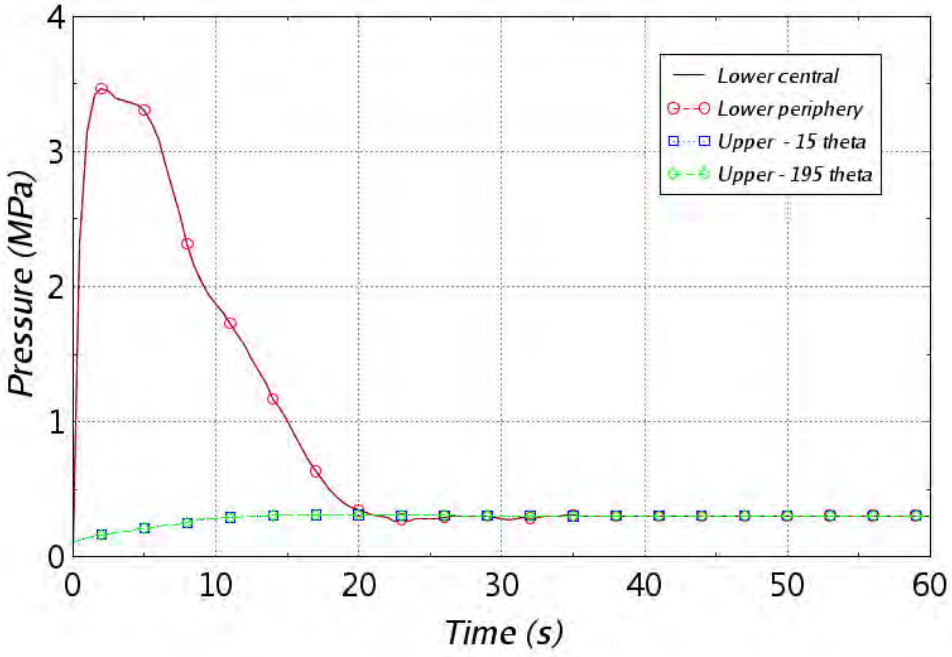

Figure 31. Lower cavity and refueling cavity pressures, 2A DEGB.

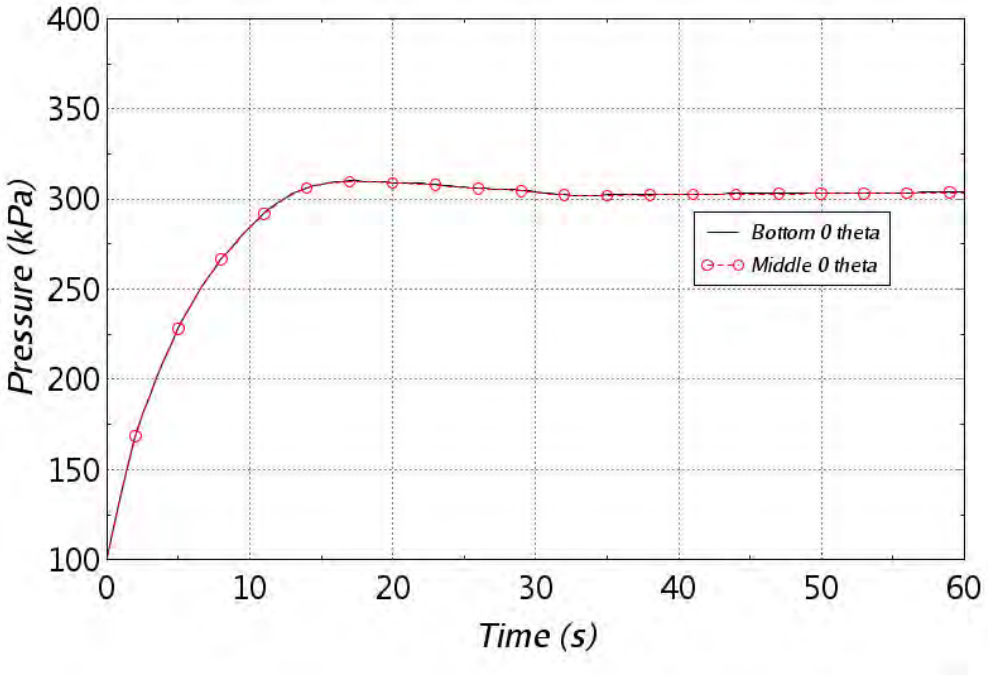

Figure 32. Containment pressure, 2A DEGB.

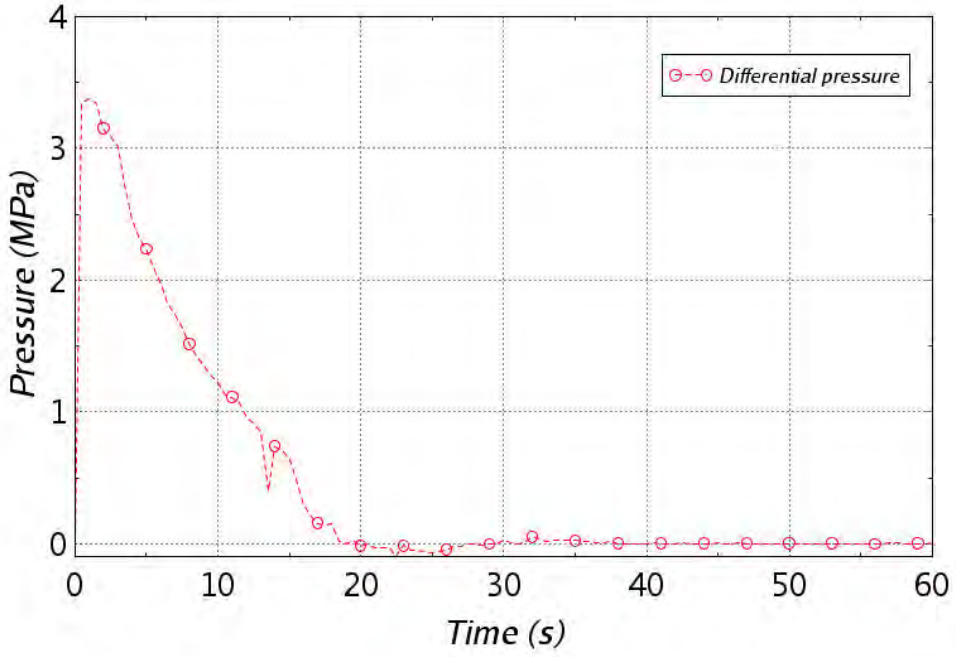

Figure 33. Differential around nozzle zone, 2A DEGB.

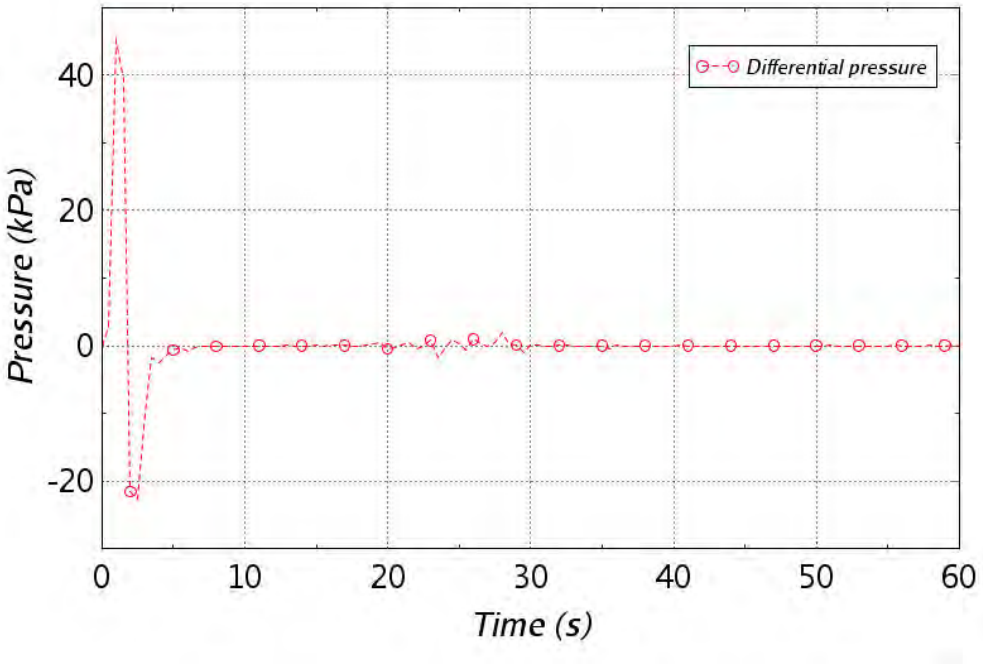

Figure 34. Differential in annular region, 2A DEGB.

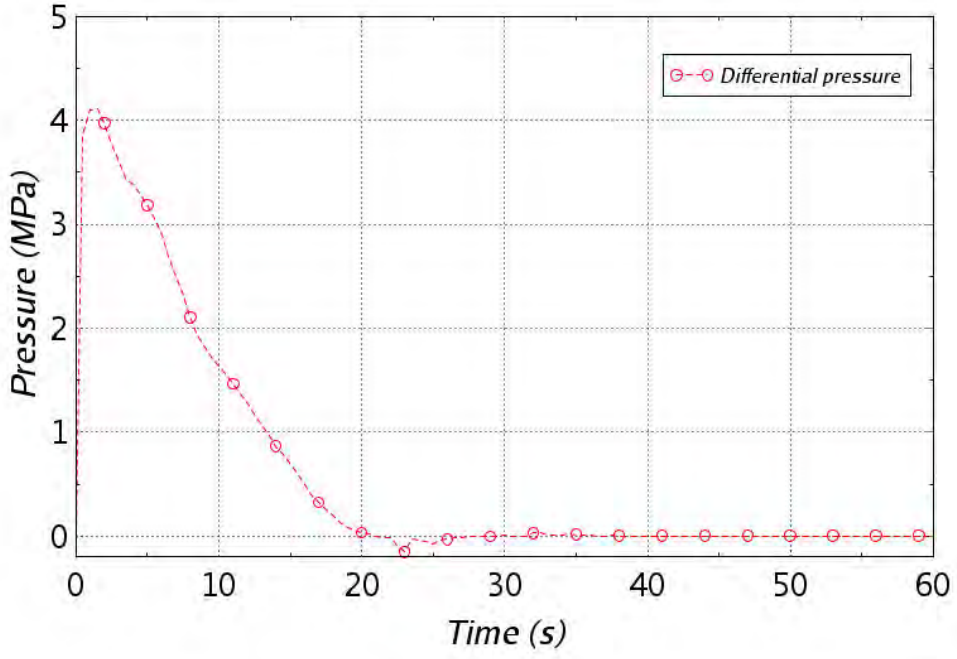

Figure 35. Differential across CBS, 2A DEGB.

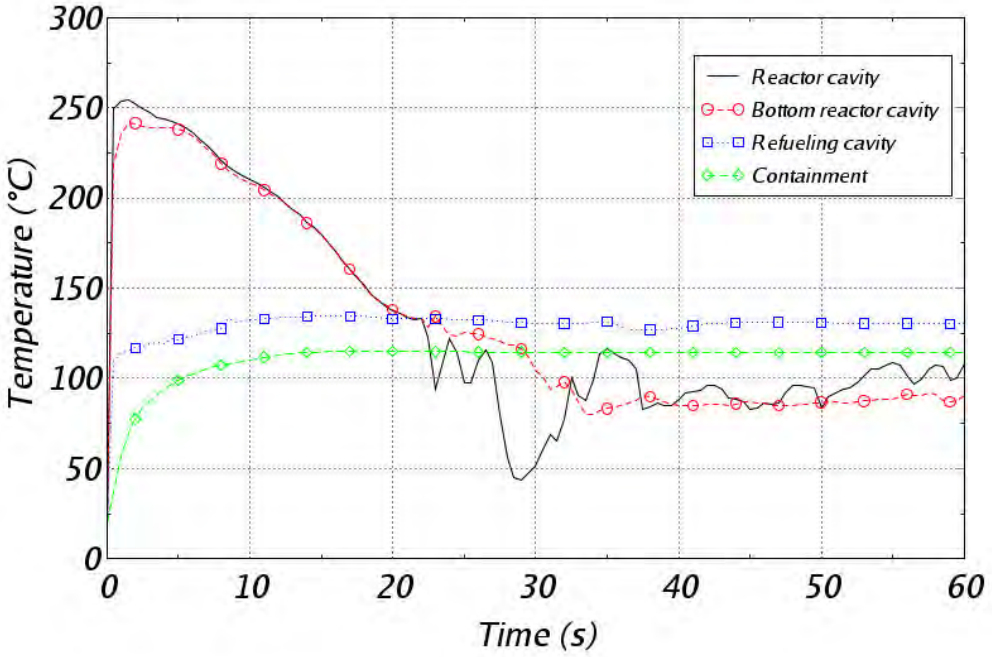

Figure 36. Temperatures in cavity and containment, 2A DEGB.

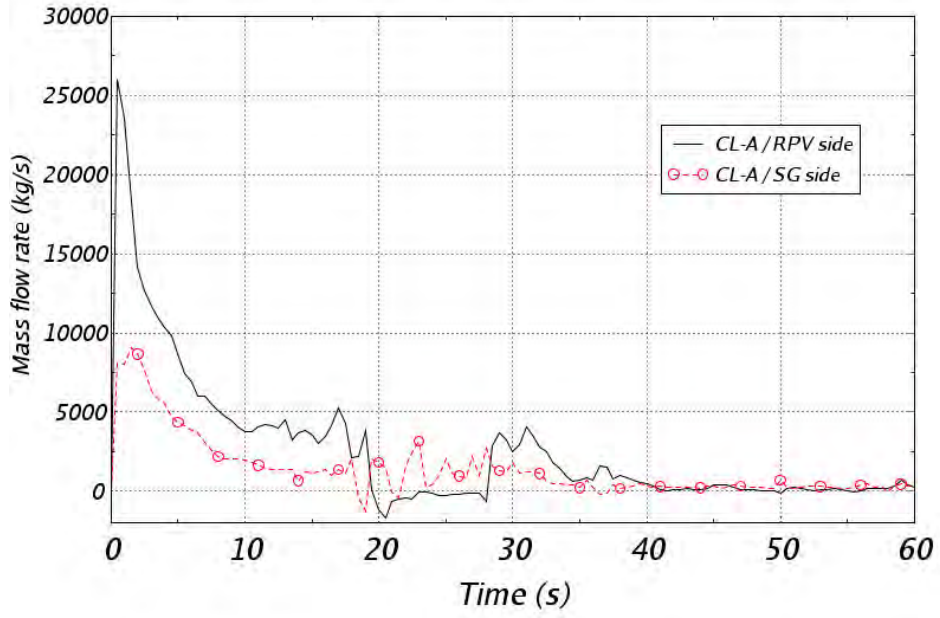

Figure 37. Break mass flow rates, 2A DEGB.

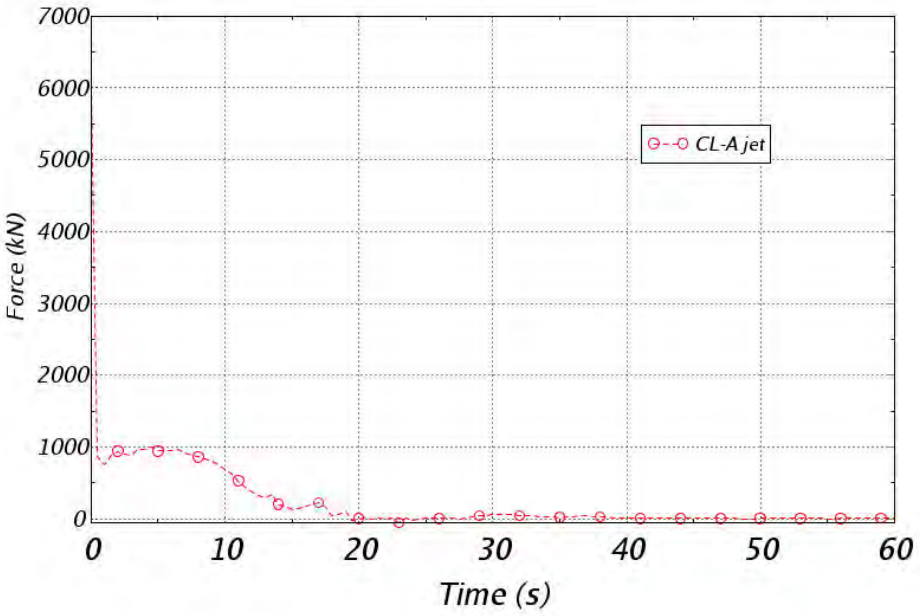

Figure 38. Jet impingement force, 2A DEGB.

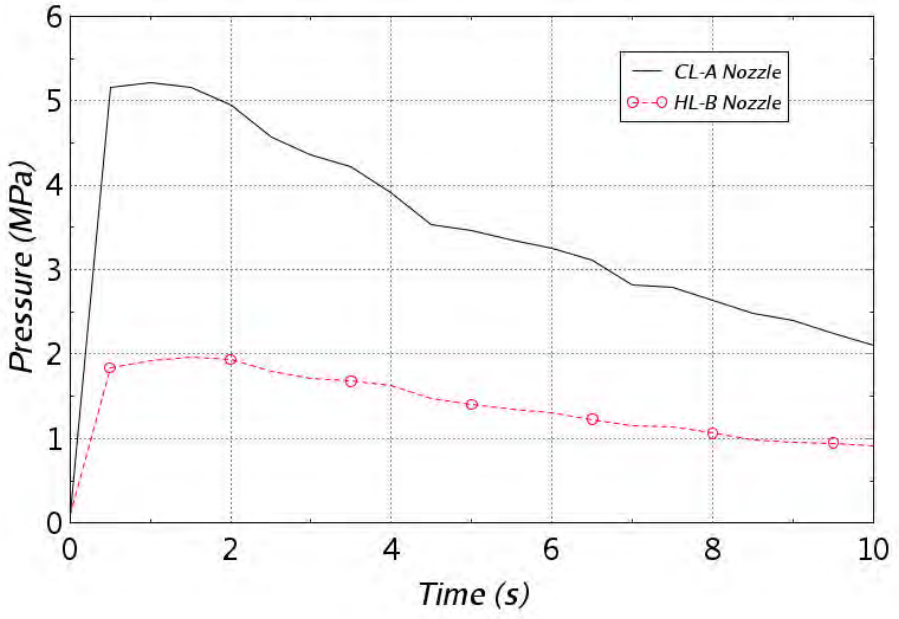

Figure 39. Nozzle-zone pressure, first 10 s, 1A reference.

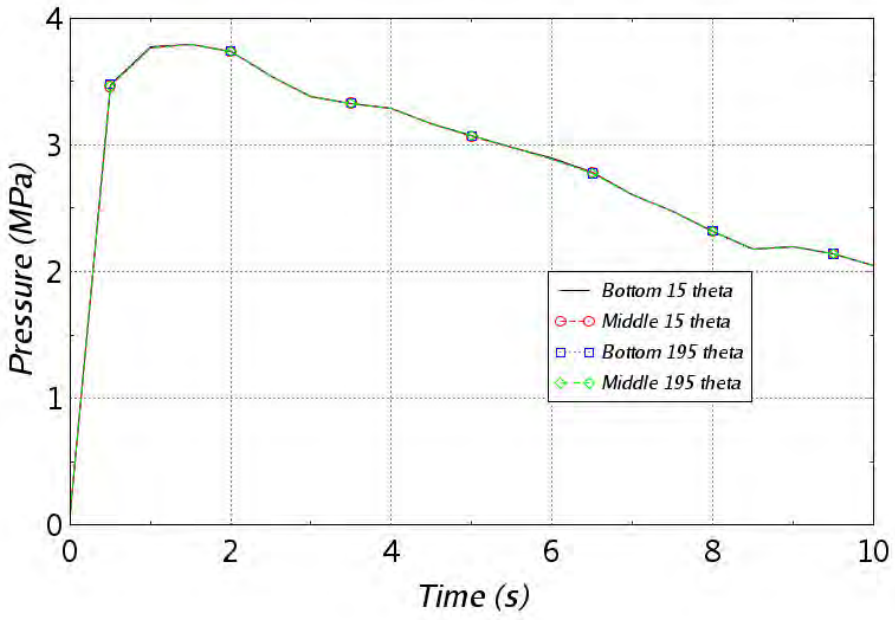

Figure 40. Annular cavity pressure, first 10 s, 1A reference.

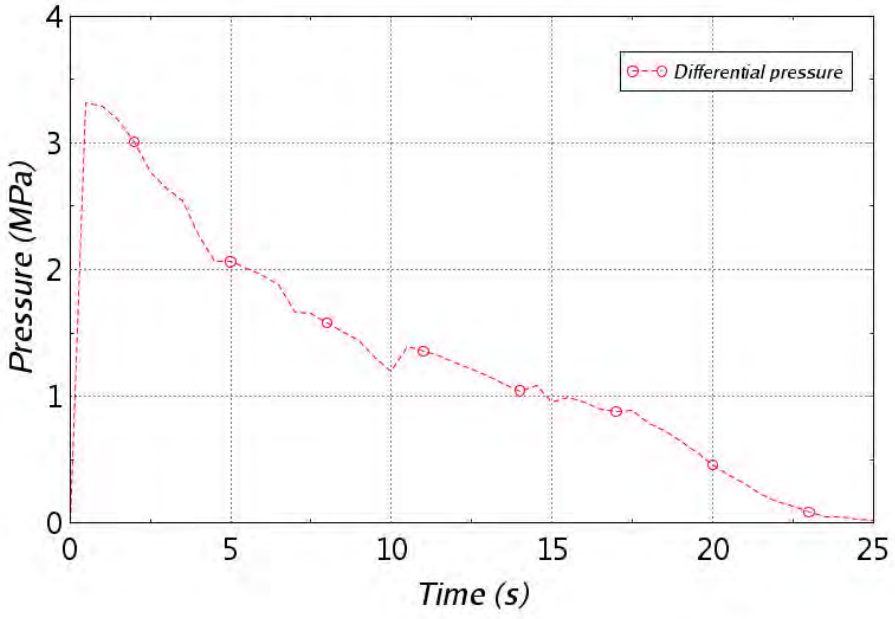

Figure 41. Differential around nozzle zone, 1A reference.

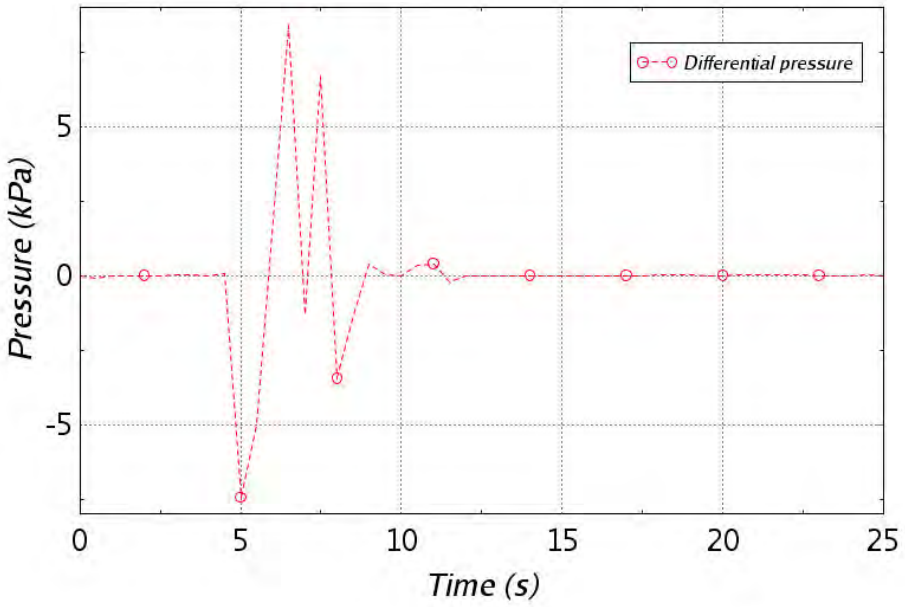

Figure 42. Differential in annular region, 1A reference.

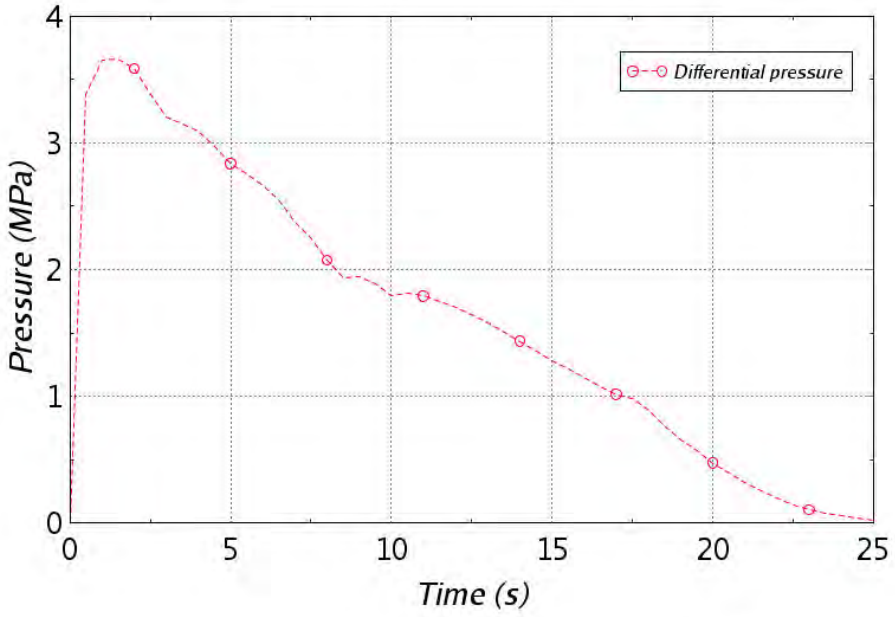

Figure 43. Differential across CBS, 1A reference.

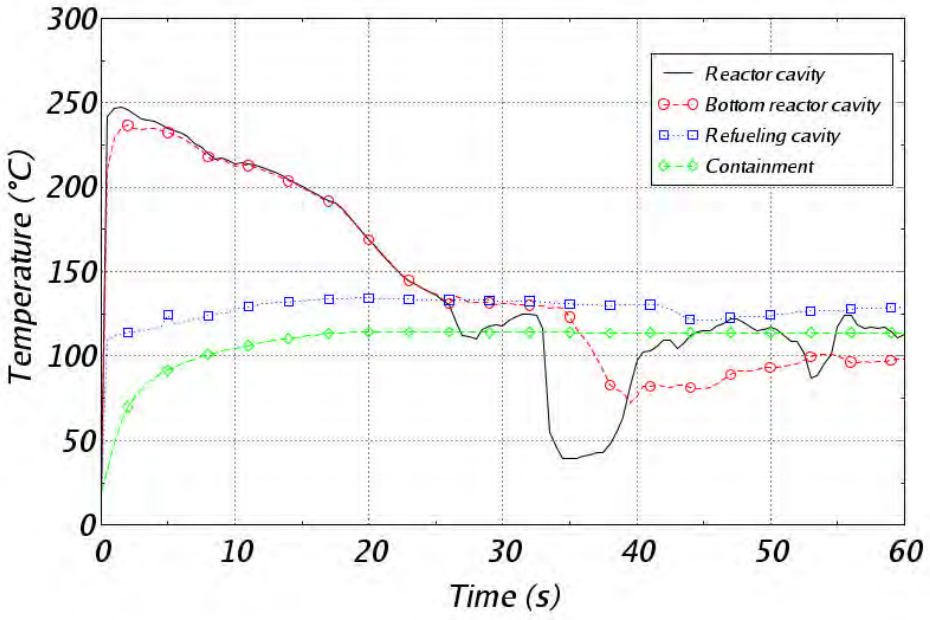

Figure 44. Temperatures in cavity and containment, 1A reference.

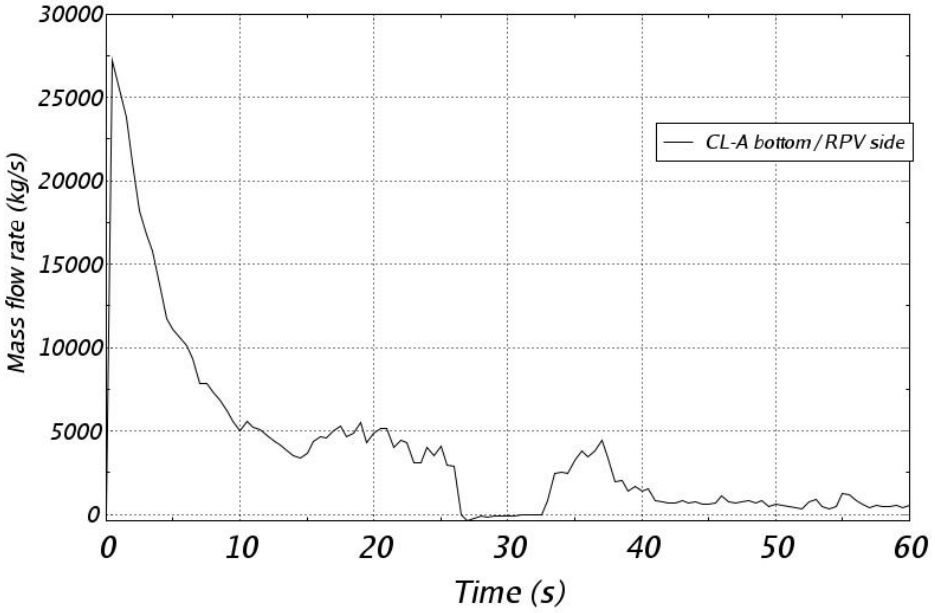

Figure 45. Break mass flow rate, 1A reference.

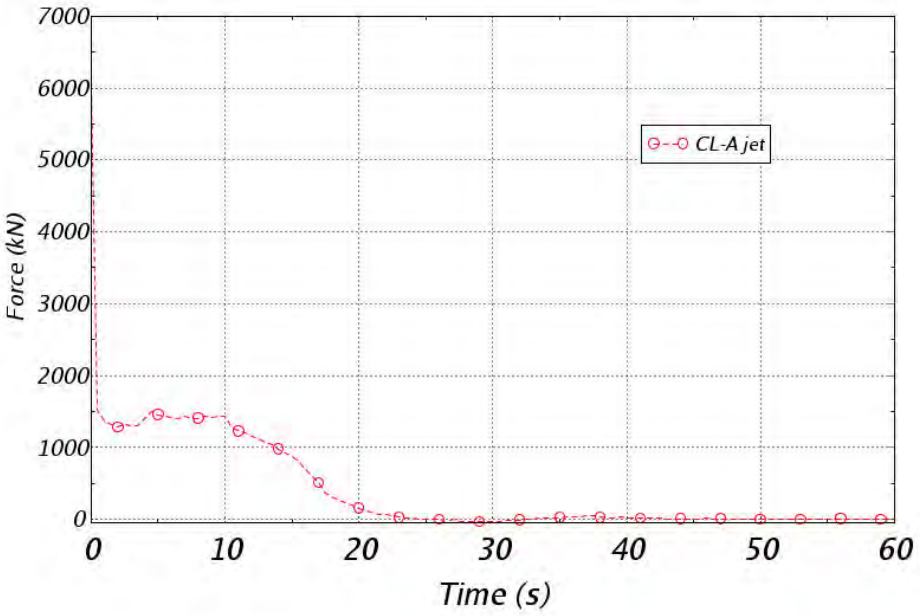

Figure 46. Jet impingement force, 1A reference.

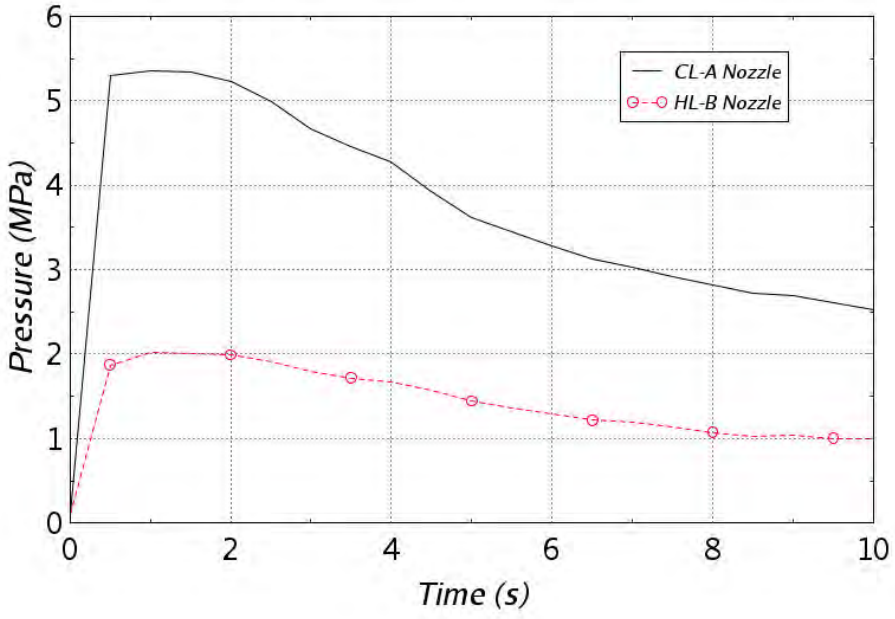

Figure 47. Nozzle-zone pressure, 1A Henry–Fauske sensitivity.

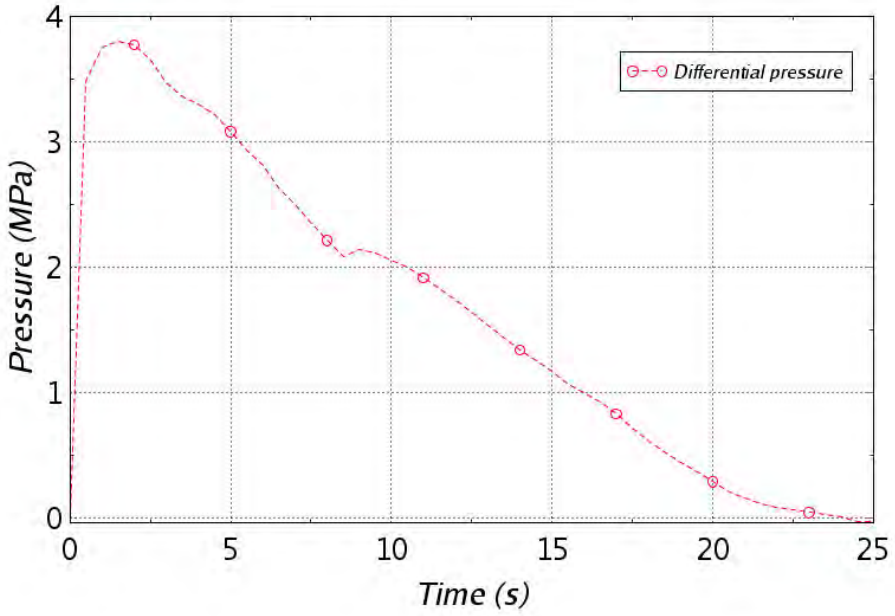

Figure 48. CBS differential, 1A Henry–Fauske sensitivity.

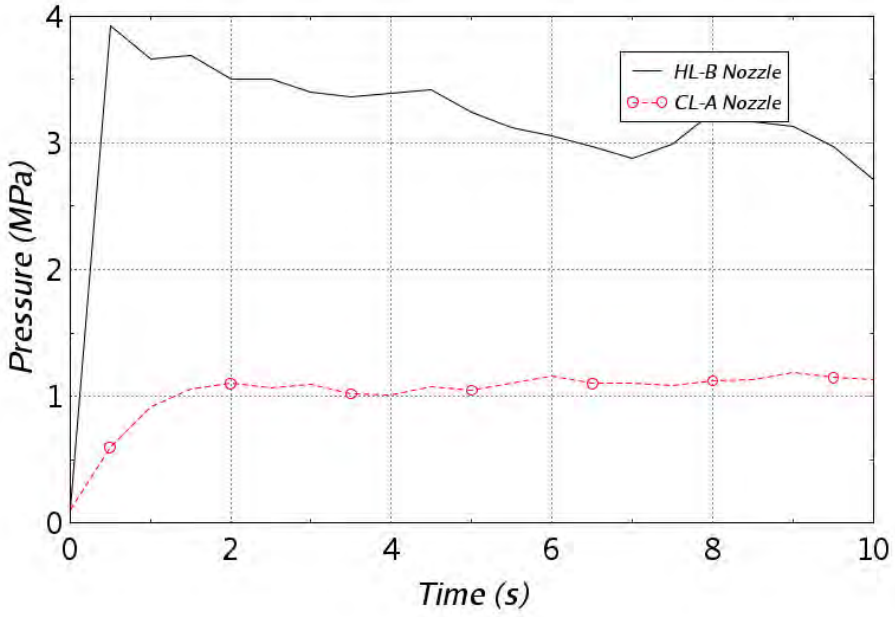

Figure 49. Nozzle-zone pressure, 1A hot-leg-B sensitivity.

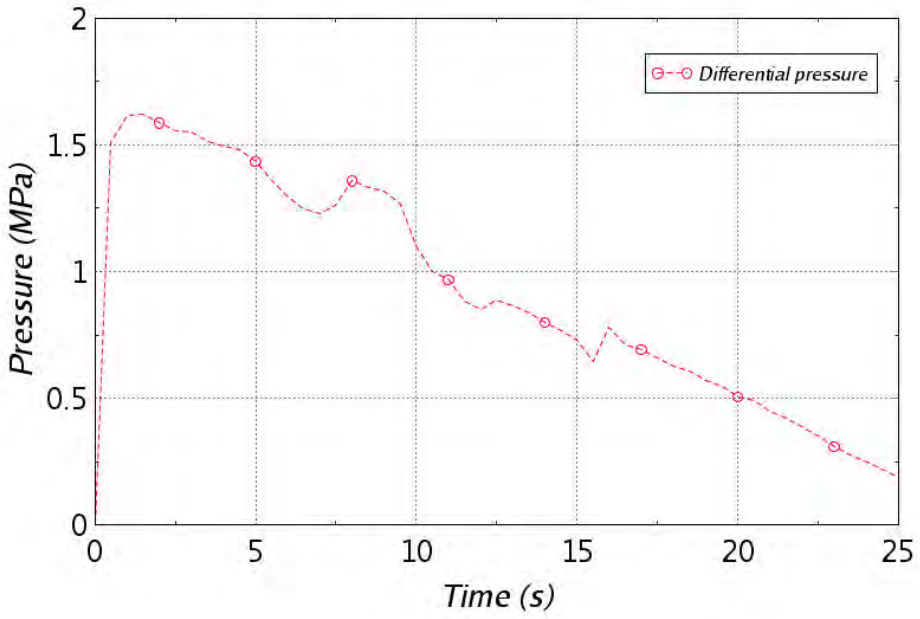

Figure 50. CBS differential, 1A hot-leg-B sensitivity.

Table 5. Sensitivities on 1A LOCA case.

Case	Cavity peak pressure	
	(MPa)	(psi)
Reference	5.21	756
Henry–Fauske model	5.37	779
Hot-leg B	3.92	569

3.3.2.2 Sensitivities on Break Area

Break-area scaling directly influences wave amplitude and discharge momentum. Table 6 reports the monotonic increase of peak cavity pressure with area for 0.25A, 0.5A, 1A, and 2A cases; Table 7 shows the corresponding near-linear scaling of maximum jet impingement force consistent with the governing expression. The functional dependence of peak pressure on area is plotted in Figure 51. To externally benchmark these predictions, Figure 52 compares the RELAP5-3D results against historical MULTIFLEX calculations from the CLOUD program [16]; the agreement is acceptable given differences in model geometry and methods.

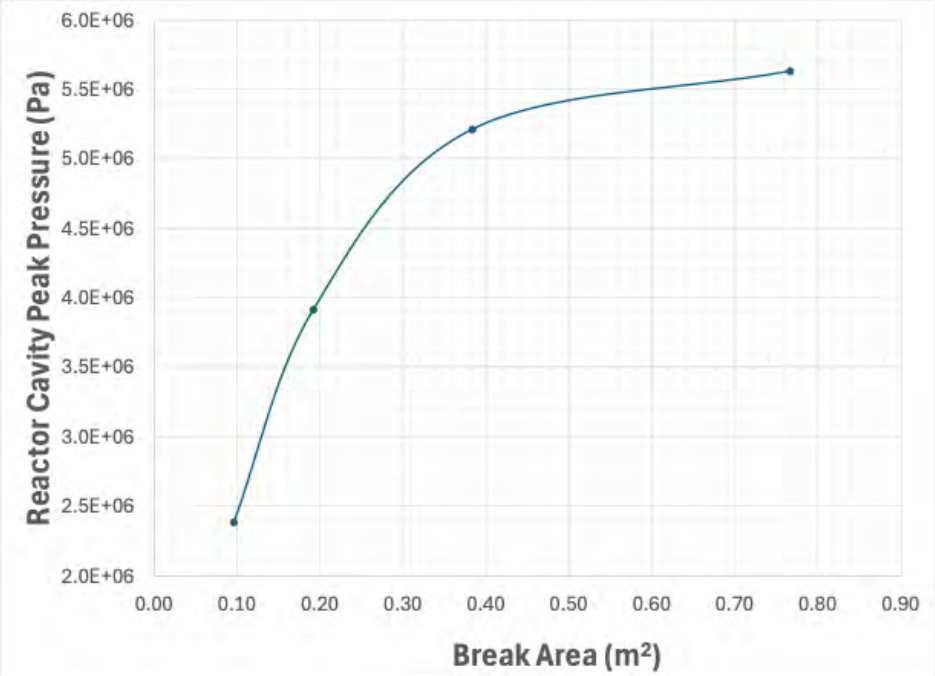

Figure 51. Peak cavity pressure vs. break area.

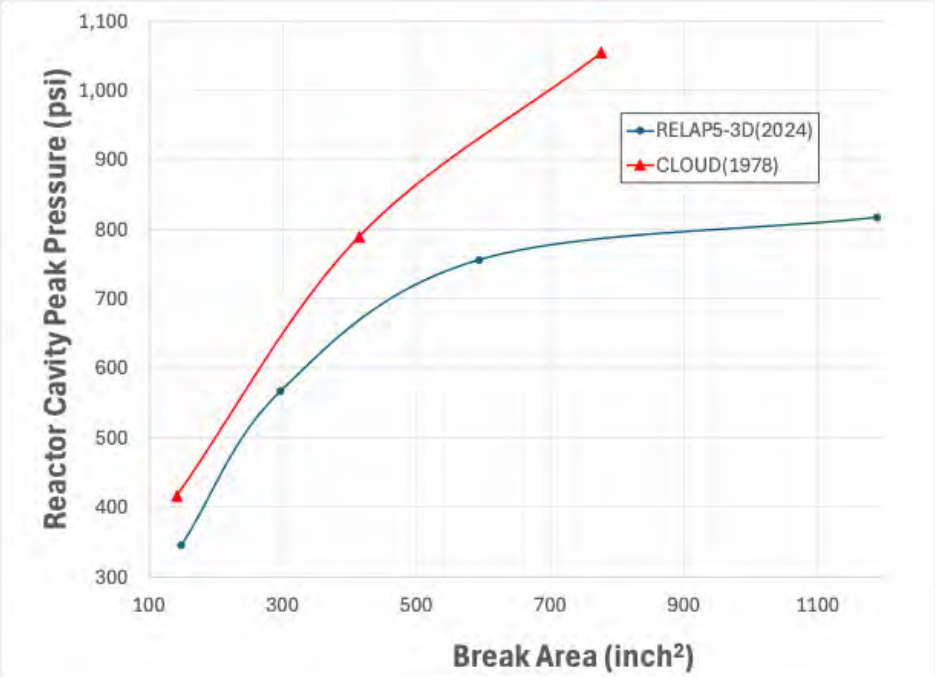

Figure 52. Validation against CLOUD (MULTIFLEX) [16].

Table 6. Sensitivities on the break area.

Case	Cavity peak pressure	
	(MPa)	(psi)
DEGB 2A (0.766 m^2)	5.63	817
Reference 1A (0.383 m^2)	5.21	756
0.5 A (0.192 m^2)	3.91	567
0.25 A (0.0958 m^2)	2.38	345

Table 7. Maximum jet impingement force.

Case	Maximum jet impingement force (MN)
DEGB 2A (0.766 m^2)	12.06
Reference 1A (0.383 m^2)	6.03
0.5 A (0.192 m^2)	3.01
0.25 A (0.0958 m^2)	1.51

4. STRUCTURAL SIMULATION OF CBS UNDER ACCIDENTAL LOADING

4.1 PRINCIPLES

The assessment of the CBS subjected to in-service irradiation includes three successive steps.

1. *Irradiation fields*. Estimates of the neutron and gamma radiation levels are the main operating factors affecting the properties of concrete. The radiation fields in the CBS vary according to height, azimuth, and depth because of the dissymmetry of the fuel core design and the attenuation caused by concrete and embedded steel elements. Determination of the radiation fields relies on the following:

    - Extrapolation from irradiation exposure in the RPV using analytical attenuation in the concrete [58]. This approach is generally limited to the radial projection at the fuel core mid-elevation.

    - Simulation of the irradiation transport using established codes such as Monte Carlo N-Particle (MCNP), SCALE, and Virtual Environment for Reactor Applications (VERA)-shift [21, 29], to name a few. Concrete is mostly made of calcium, silicon, oxygen, and hydrogen. Hydrogen is present in the concrete mix from the batching water, which partly combines with the cement oxides to form hydrates (chemically bound water). However, a remaining fraction of the original water remains in the form of adsorbed or free water in the capillary pores. This water can be subject to transport in liquid or gaseous forms because of unbalanced hygral equilibrium (i.e., drying). This phenomenon occurs in unlined CBSs because of the reactor cavity's temperature, relative humidity, and convection caused by venting. When the CBS design includes a metal liner, the moisture remains trapped in the wall. In addition, irradiation leads to water radiolysis, eventually forming di-hydrogen and di-oxygen [59, 60]. The radiochemistry of water in cementitious systems and the transport of radiolytic gas through convection and diffusion are complex and not well characterized to date. Because of the high cross section of hydrogen, this element is a significant contributor to the attenuation of fast neutron transport in concrete. Ideally, irradiation and moisture or gas transport should be coupled. This is currently not the practice. More commonly, uncertainties in moisture content are mitigated by studying the effects of varied hydrogen content on neutron transport. Lower hydrogen content ("dry" concrete) evidently leads to deeper penetration of neutrons in concrete.

2. *Irradiation-induced damage*. Neutron irradiation causes expansion of the concrete aggregate. The amplitude of this RIVE depends on the mineralogy of the aggregates and the received neutron fluence. At any given moment during operation, the CBS wall is subjected to a field of internal expansion. In addition, the mechanical properties of irradiated concrete are affected by RIVE because of the formation of microcracking. Structural models of irradiated CBS can be organized in three categories.

    - Semi-analytical models [61, 62] are generally limited to 1D analysis, deriving the mechanical stress and strength profiles along the radial direction using finite difference methods. The analysis is generally conducted at the location of the highest surface fluence—at the fuel core's mid-elevation and the azimuth of the highest fluence value. These methods benefit from fast computation time, which makes it possible to run parametric and probabilistic analyses. The limitations of these methods are their inability to account for structural damage caused by excessive stress and the inaccuracies associated with approximate boundary conditions. In the following discussion, this method is referred to as *1D-semi-analytical model (SAM).*

- Mesoscale discrete models [28, 63] such as rigid-body spring model (RSBM) or the LDPM are advantageous in that they explicitly represent the mesostructure of concrete formed by coarse aggregates ($\gtrapprox$ 4 mm, the "particles") embedded in a matrix of hardened cement paste and sand. Hence, the effects of irradiation such as RIVE and the irradiated Young's modulus are explicitly represented at the level of the aggregates. The loss of concrete strength results from the formation of microcracking between particles. Because of the difference between the millimetric size of the smallest particles and the metric dimensions of the CBS, a complete model of the CBS using discrete models is out of reach of computational resources that utilize multithreaded processors or even medium-sized clusters. Hence, published simulations of irradiated CBS using mesoscale models are limited to representative angular sectors.
- Finite element models [26, 64–66] provide a main advantage through finite element analysis (FEA), generating a full representation of the CBS geometry, including the presence of reinforcement. Finite element models remain computationally intensive for full 3D simulations.

3. *Residual bearing capacity*.

   The final stage of assessing an irradiated CBS involves quantifying its residual bearing capacity (i.e., its remaining structural resistance to applied loads after accounting for irradiation-induced degradation). This assessment is critical for determining whether the CBS can continue to fulfill its protective and load-bearing functions throughout the remaining operational life of the facility or during post-operational phases such as decommissioning.

   RIVE and microcracking significantly alter the mechanical properties of concrete. These changes affect compressive and tensile strength, modulus of elasticity, fracture toughness, and long-term creep behavior [67, 68]. As the neutron fluence increases, these properties progressively deteriorate, potentially compromising the structural integrity of the CBS.

   Residual capacity assessments typically consider the following mechanical properties as functions of neutron fluence and irradiation temperature:

   - Compressive strength reduction, commonly correlated with aggregate expansion and matrix cracking [67, 69].
   - Modulus of elasticity degradation, resulting in increased deformation under service loads [68].
   - Reduction in tensile and flexural strength, which governs cracking resistance and serviceability limits [69].
   - Fracture energy decline, impacting post-cracking behavior and resistance to localized failure [68].
   - Altered creep behavior, especially relevant for aged irradiated concrete subjected to sustained loads [70].

   Several approaches exist for estimating residual capacity:

   - Empirical degradation models derived from irradiated material testing campaigns (e.g., [68, 69]) are used to correlate material property reductions with neutron fluence and temperature exposure. These models serve as input for structural analyses to evaluate capacity under combined axial, flexural, and shear loading conditions.

- Sectional analysis methods, particularly in regions of high neutron exposure (e.g., azimuth and elevation corresponding to peak fluence), may be applied to estimate moment-curvature relationships and load-deflection behavior [67]. These analyses require calibrated material stress-strain curves for irradiated concrete and reinforcement, incorporating tension stiffening and confinement effects if applicable.
- Nonlinear finite element models, when available, can directly simulate the degraded mechanical response of the CBS using advanced constitutive laws that incorporate irradiation damage parameters [70, 71]. These models often include strain-softening behavior of cracked concrete, reduced confinement effectiveness due to degraded transverse reinforcement or expansion-induced de-bonding, and time-dependent creep and shrinkage, especially in unlined walls where moisture transport is still active.
- Limit state evaluation is also performed to assess whether the irradiated CBS retains sufficient strength to resist design-basis loads (e.g., seismic excitation, LOCA-induced pressurization, or post-shutdown thermal gradients) [70, 71]. This typically involves checking both ultimate limit states (i.e., verifying capacity against collapse under maximum credible loads) and serviceability limit states (i.e., ensuring deflections and cracking remain within acceptable bounds under normal operating conditions).

In some instances, the residual bearing capacity may be assessed probabilistically, incorporating uncertainties in irradiation dose, material degradation rates, geometry, and loading. Such approaches are often implemented via MCSs or within structural reliability frameworks [68]. The reliability index can then be computed to quantify safety margins against failure, with target values established by regulatory guidance.

Ultimately, the evaluation of residual bearing capacity informs decision-making regarding:

- The continued use of the CBS in its current state,
- The need for repair, reinforcement, or protective liner retrofits,
- The schedule and scope of decommissioning activities, especially if large-scale concrete removal or handling of irradiated materials is involved.

This assessment is essential for ensuring the CBS continues to perform its critical shielding and structural support functions under the combined effects of irradiation aging and applied loads [67, 68].

As explained in Le Pape et al. [63], the varied aging structural model of the CBS was subjected to in-service irradiation using different modeling strategies (semi-analytical, finite element, discrete approach), all leading to similar conclusions:

1. Irradiation-induced damage in concrete is caused by two concurrent mechanisms: (1) *intrinsic* damage caused by formation of voids and cracking in the concrete constituents, as observed on a concrete specimen subject to free expansion, and (2) the *structural* damage caused by excessive stresses in the region subject to high fast-neutron fluence toward the reactor cavity. These excessive stresses occur in the vertical and orthoradial directions and are caused by structural constraints associated with the cylindrical geometry of the CBS and the attenuation profile of fast neutrons moving radially toward the back of the CBS.
2. Although the damaged depth varies from one model to another because of differences in the parameters used in the RIVE, damage, and creep constitutive laws, all models indicate that the damage extends to or beyond the location of reinforcement. This observation leads to questions about the integrity of the steel–concrete bond during accident conditions.

3. Cracks open mainly along the unrestrained radial direction in the region located near the reactor cavity. Crack opening width decreases with the CBS radius: larger cracks occur near the CBS surface, and minimal cracking occurs at or beyond the reinforcement location.

4.2 IN-SERVICE DAMAGE DEPTH

Estimation of the damage depth at the fuel's mid-core elevation is central to the assessment of the in-service structural performance of the CBS. As discussed in the previous section, three methods can be employed to this end: FEA [26], a mesoscale discrete method such as the LDPM [63], and a 1D semi-analytical model [62]. The computational resources and time required to complete a single simulation using each of these methods differ substantially. When either FEA or the LDPM is used, several days are needed to complete a simulation on a multi-node cluster and a multi-threaded workstation, respectively. A single 1D semi-analytical simulation is completed within a few minutes on a personal computer. Hence, the 1D semi-analytical approach makes it possible to conduct large parametric—for example, based on the effects of the concrete's chemical composition—and probabilistic studies. However, to date, the 1D semi-analytical approach has not yet been validated against the results obtained more recently using finite element method (FEM) and the LDPM. This topic is addressed in the next section.

4.2.1 Comparison between FEM, LDPM, and 1D Semi-Analytical Methods

The three models differ in their nature, constitutive models, and boundary conditions.

- FEM and 1D-SAM consider concrete as a homogeneous material and assume a continuum description of concrete structures. Instead, the LDPM explicitly represents the coarse aggregate distribution and model discontinuities caused by cracking.
- The 1D-SAM accounts only for the *intrinsic* irradiation-induced damage, meaning the loss of mechanical properties caused by microcracking. The FEM includes both *intrinsic* irradiation-induced damage and *structural* damage following the isotropic damage model proposed by Mazars and Pijaudier-Cabot [72]. The LDPM addresses *intrinsic* irradiation-induced damage by reducing the Young's modulus of the irradiated aggregate and accounting for microcracking in the mortar, which arises from microstructural heterogeneity and differential expansion between adjacent aggregates. Additionally, *structural* damage is represented at the level of the mortar.
- The boundary conditions (BCs) in the vertical direction assume no deformation or homogeneous deformation for the 1D-SAM and the LDPM, respectively. The BCs of a representative wedge cut-out from the CBS at the fuel's mid-core elevation are mixed deformation and stress conditions resulting from the structural response of the entire CBS subject to a nonuniform field of fluence.
- A similar comment can be made about the BCs in the orthoradial direction which are assumed axisymmetric for the 1D-SAM and the LDPM.

Nevertheless, the noted variations in BCs only moderately affect the mechanism underlying the formation of damage, which is governed by RIVE-induced unconfined expansion in the radial direction near the reactor cavity.

In the following itemized analysis, the different models were run with comparable conditions:

- The fast neutron flux profile was obtained from irradiation transport using the VERA-Shift code [26].
- The temperature ranges from 65 °C at the inner radius to 40 °C at the outer radius.

- Aggregate RIVE was calculated assuming a quartz content of 92% and a RIVE model derived from Bykov et al. [73] (see equations in [24]). Concrete RIVE was obtained using comparable homogenization rules in the LDPM and 1D-SAM.
- The loss of the Young's modulus of irradiated aggregate and concrete assumes empirical relations derived from post-irradiation measurement of the Con-A concrete and GA(F) aggregate specimens provided by the Japan Concrete Aging Management Program (JCAMP) [27, 32].
- The unirradiated tensile and compressive strengths of concrete are similar in all simulations.
- No concrete shrinkage was considered.

Figure 53 presents the results of previous simulations obtained using the LDPM and FEM. Within the damaged depth, the damage profiles are much sharper (solid lines) than the profiles obtained from the finite element simulation using Grizzly (dashed lines). Whereas the maximum damage value at the surface of the CBS gradually increases with the operation time, its value is always higher in the interpretation of the LDPM simulations. In the LDPM simulation, the RIVE value near the surface of the concrete creates a delamination of cement paste located between the liner and the first layer of aggregates, as well as spalling of the aggregates located in the immediate nearby region. In the finite element model, the heterogeneities created by aggregates of varied sizes are not represented. Thus, the induced microcracking is not represented either.

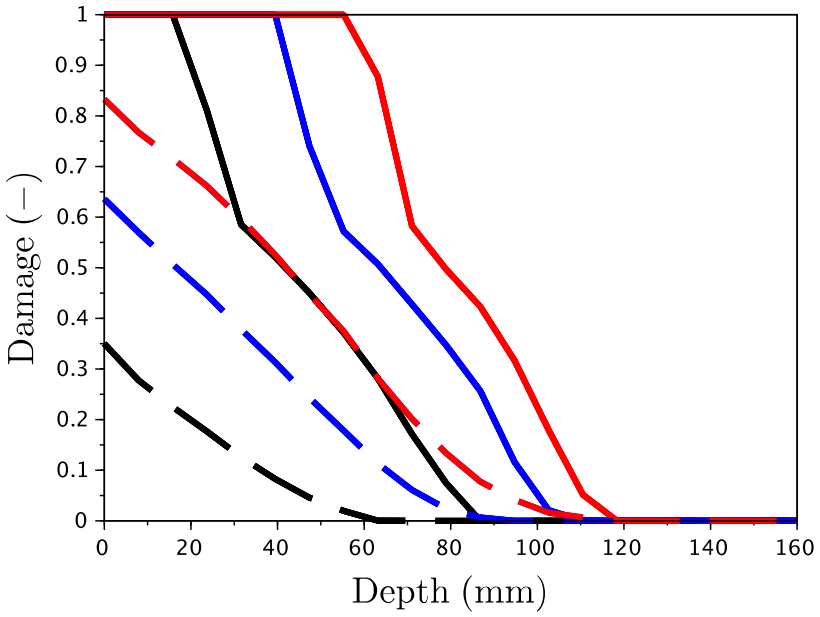

Figure 53. Comparison of the damage profile in the CBS obtained using the LDPM (solid lines) and FEM (dashed lines) at 40, 60, and 80 years of operation (in black, blue and red, respectively).

The damage depth corresponds to the maximum depth at which damage is strictly positive. These damage depths are plotted against the fast neutron fluence at the surface of the concrete in Figure 54. Note that the results presented here are representative only for ordinary concrete, in which the aggregate is almost exclusively composed of quartz ([Qz] = 92%). The blue diamond and red square markers correspond to the damage depths obtained by the LDPM and FEM, respectively. The dashed and solid lines correspond

to the damage depths obtained using 1D-SAM simulation. The dashed line represents the damage criterion related to excessive biaxial compression, whereas the solid line corresponds to the damage criterion associated with excessive radial deformations. Notably, the deformation-based criterion shows a strong correlation with the FEM-based results. In contrast, the stress-based criterion fails to capture damage resulting from the formation of cracks caused by RIVE unconfined in the radial direction and confined in the vertical and orthoradial directions as indicated by the red regions in Figure 55. However, this criterion should not be dismissed entirely because it may be more conservative in situations where the quartz content—and hence the RIVE amplitude—is significant.

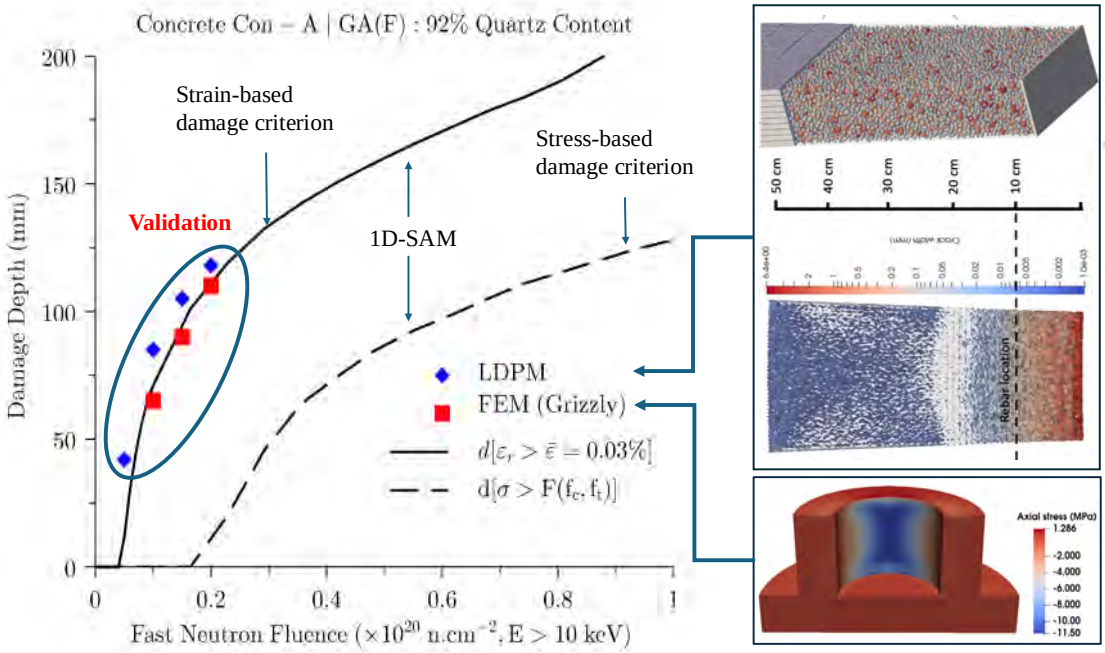

Figure 54. Damage depth in the CBS with increasing fast neutron fluence at the surface of the concrete. Comparison of the LDPM, FEM, and 1D-SAM simulations.

In conclusion, estimates of the damage depth caused by in-service irradiation of the CBS at the elevation of the fuel's mid-core can be obtained using the 1D-SAM. This approach is computationally inexpensive and thus makes it possible to run varied scenarios, including study of extended operational duration and the role of varied mineral composition of the concrete aggregate. The effects of mineralogy on damage depth are not the specific subject of this report. However, some results obtained from previous research on igneous or magmatic rocks are presented here to provide ranges of damage depths at varying operation durations. In a previous report [74], the estimated damage depth was obtained using a stress-based criterion. Here, the results are presented using a strain-based criterion.

The formation of igneous rocks depends on the thermodynamic equilibrium of mineral phases associated with the cooling of magma. From a single parental magma, all the various types of igneous rocks can be derived following the so-called Bowen series [75]. The common minerals of igneous rocks can be classified into two series: a continuous reaction series of feldspars, and a discontinuous reaction series of ferromagnesian minerals (olivine, pyroxene, hornblende, biotite). The second reaction series is characterized by a gradual coordination of silicate tetrahedra, progressing from isolated silicates to chain silicates to sheet silicates, and finally to framework silicates.

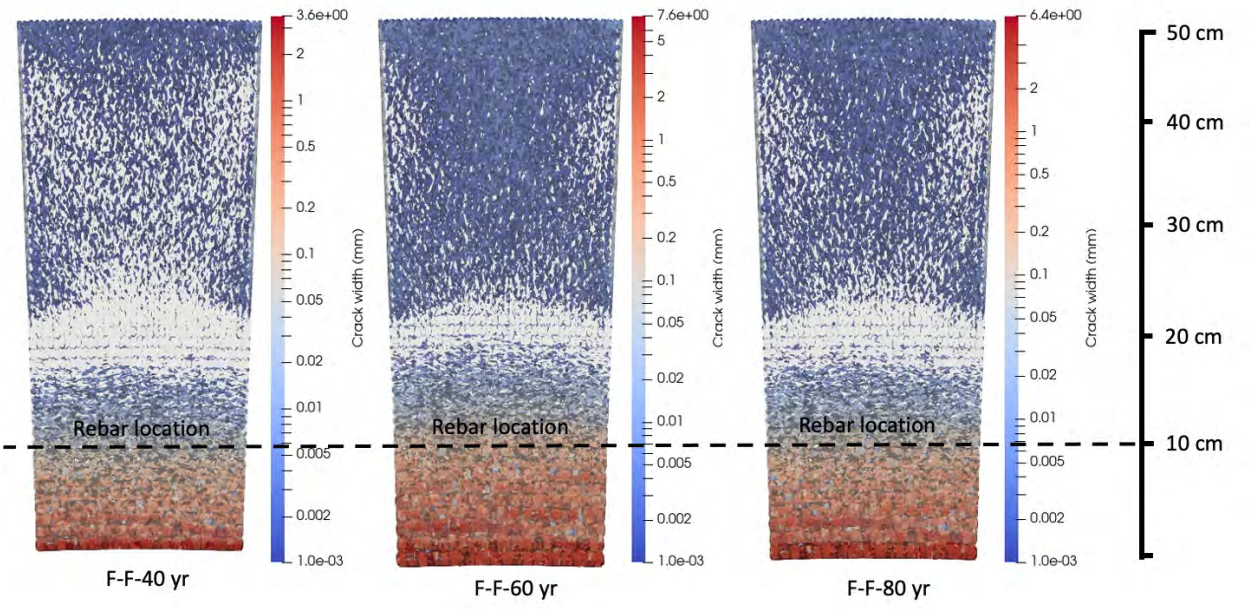

Figure 55. Crack opening map (top view) using the LDPM [27].

The RIVE susceptibility of silicates is correlated with the Goldich series [24]—Figure 56—which describes the tolerance of silicates to weathering [76]. The Goldich series is essentially the reverse of the Bowen series. Using the Bowen series, the compositions of various igneous rocks can be determined (Figure 57). The names of the rocks are given according to their silicate proportions.

Note that in this study, the distinction between intrusive (plutonic) and extrusive (volcanic) igneous rocks is ignored. Although comparable mineral compositions can be found between intrusive and extrusive rocks, the faster cooling rate of extrusive rocks leads to the formation of smaller grains compared to those in intrusive rocks. In the proposed model, the effects of grain size on the irradiated properties of the rocks are not considered. In Figure 57, the names of the rocks are given first for the intrusive form and then for the extrusive form: for example, granite (intrusive), and rhyolite (extrusive).

Using the information provided in Figure 56, it can be inferred that ultramafic igneous rocks, which contain mostly isolated and chain silicates, are likely to be less susceptible to RIVE than felsic igneous rocks, which contain framework and sheet silicates. This expected result is confirmed by the simulation. Figure 58 shows the calculated RIVE values for various igneous rocks following the compositions presented in Figure 57. The vertical axis corresponds to increasing fast neutron fluence. All simulations presented in Figure 58 were run at 45 °C. Interestingly, the RIVE of intermediate and mafic igneous rocks (the middle portion of the color map) is lower than the RIVE of both felsic and ultramafic igneous rocks.

Finally, Figure 59 presents the calculated irradiation-induced damage depths in the CBS for the various igneous rock compositions. The simulations were conducted using the 1D-SAM model presented in the appendix. The observations from Figure 59 and Figure 58 show a qualitative correlation between the RIVE and the irradiation-induced damage depth. The most susceptible igneous rock is granite (rhyolite). The corresponding irradiation-induced damage depths are approximately 10 cm, 15 cm, and 19 cm at fast neutron fluences of 2×10^{19}, 4×10^{19}, and 8×10^{19} n.cm^{-2} ($E > 10$ keV), respectively.

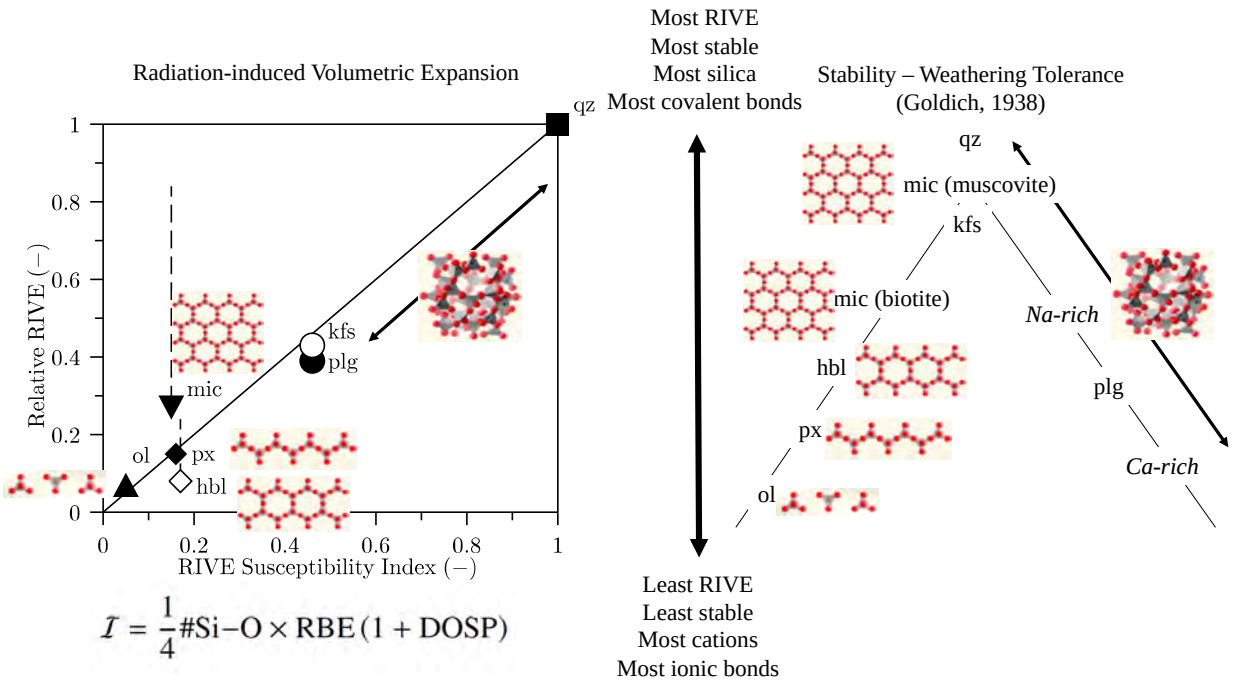

Figure 56. Correlation of the RIVE susceptibility index, $\mathcal{I}$, and the relative maximum volumetric expansion normalized by that of quartz (17.8%) for different groups of minerals. Shown are hornblende (hbl), potassium feldspar (kfs), micas (mic), olivine (ol), (data limited to high-magnesian olivine), plagioclase (plg), pyroxene (px), and quartz (qz) [77]. Vertical dashed lines indicate the uncertainty of the maximum RIVE expansions (left), and Goldich series showing the tolerance of silicates against weathering (right). Reproduced from [24].

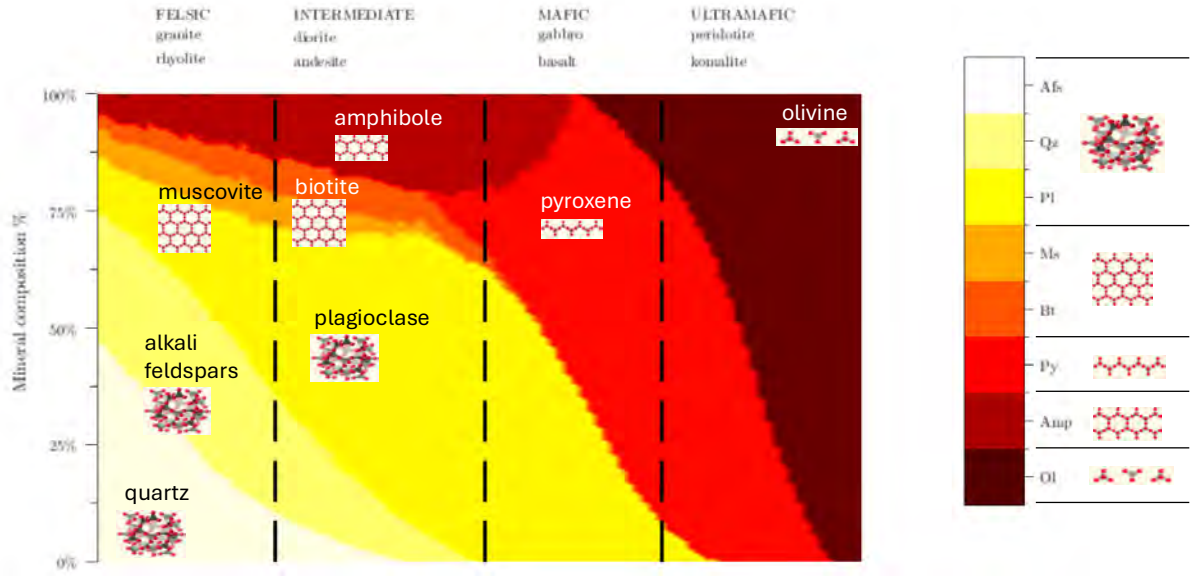

Figure 57. Mineral compositions of igneous rocks.

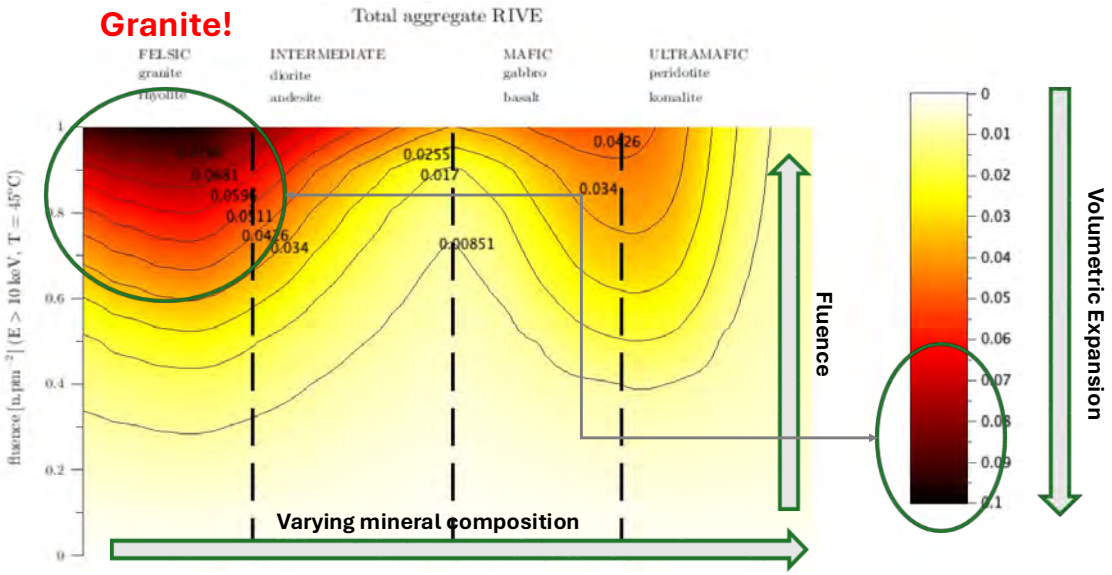

Figure 58. Calculated RIVE of varied igneous rocks with increasing fast neutron fluence at a temperature of 45 °C.

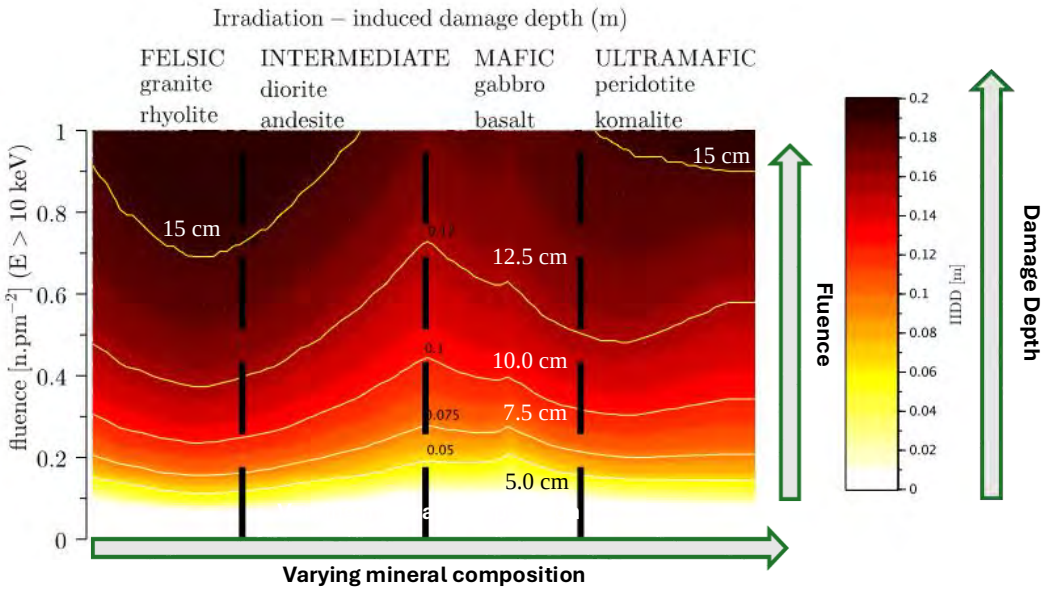

Figure 59. Calculated irradiation-induced damage depth of varied igneous rocks with increasing fast neutron fluence.

4.3 LOCA EFFECTS ON CBS DAMAGE

In this section, the thermo-mechanical effects of LOCAs on CBS damage are studied. LOCAs cause vapor release in the reactor cavity with increased pressure and temperature.

4.3.1 Cavity Pressure

Because CBS geometry can be modeled as a thick cylindrical structure, the pressure-induced stress field in the undamaged concrete can be approximated from:

$$\sigma_\theta = p\frac{r_a^2}{r_b^2 - r_a^2}\left(1 + \frac{r_b^2}{r^2}\right) \tag{16}$$

and

$$\sigma_r = p\frac{r_a^2}{r_b^2 - r_a^2}\left(1 - \frac{r_b^2}{r^2}\right), \tag{17}$$

where r_a and r_b are the inner and outer radii of the CBS, and p is the LOCA-induced pressure relative to the atmospheric pressure. This pressure exerts compression in the radial direction and tension in the orthoradial direction. The maximum value of $|\sigma_r|$ is p at the inner surface of the CBS. The maximum value of σ_θ is equal to $p(r_b^2 + r_a^2)/(r_b^2 - r_a^2)$. For example, assuming values of 2.4 m for the inner radius and a CBS wall thickness of either 1 m or 2 m, $\sigma_\theta(r_a)$ equals $\sim 3.00p$ or $\sim 1.85p$, respectively. Thus, depending on the value of p, the orthoradial stresses may exceed the tensile strength of the concrete. As a result, the structural integrity of the CBS may partly depend on the presence of hoop reinforcement and the ability to transfer loading from the concrete to the bonded reinforcing bars.

Equations (17) and (16) are valid under the assumption that the elastic properties of the concrete are uniform within the CBS, and therefore they apply before the onset of irradiation-induced damage

during service. However, it is important to note that the cavity pressure produces tensile orthoradial stresses, whereas irradiation-induced orthoradial stresses are compressive. As a result, during LOCA, the pre-existing orthoradial stresses may be relaxed.

4.3.2 Accidental Temperature

The release of vapor increases the temperature in the reactor cavity. During the LOCA, the temperature profile in the CBS evolves over time as a function of the reactor cavity temperature history and heat conduction through the wall. This type of transient has been studied using the LDPM [45]. For the sake of illustration, the model is reproduced in Figure 60. Further details can be found in the referenced technical report [45].

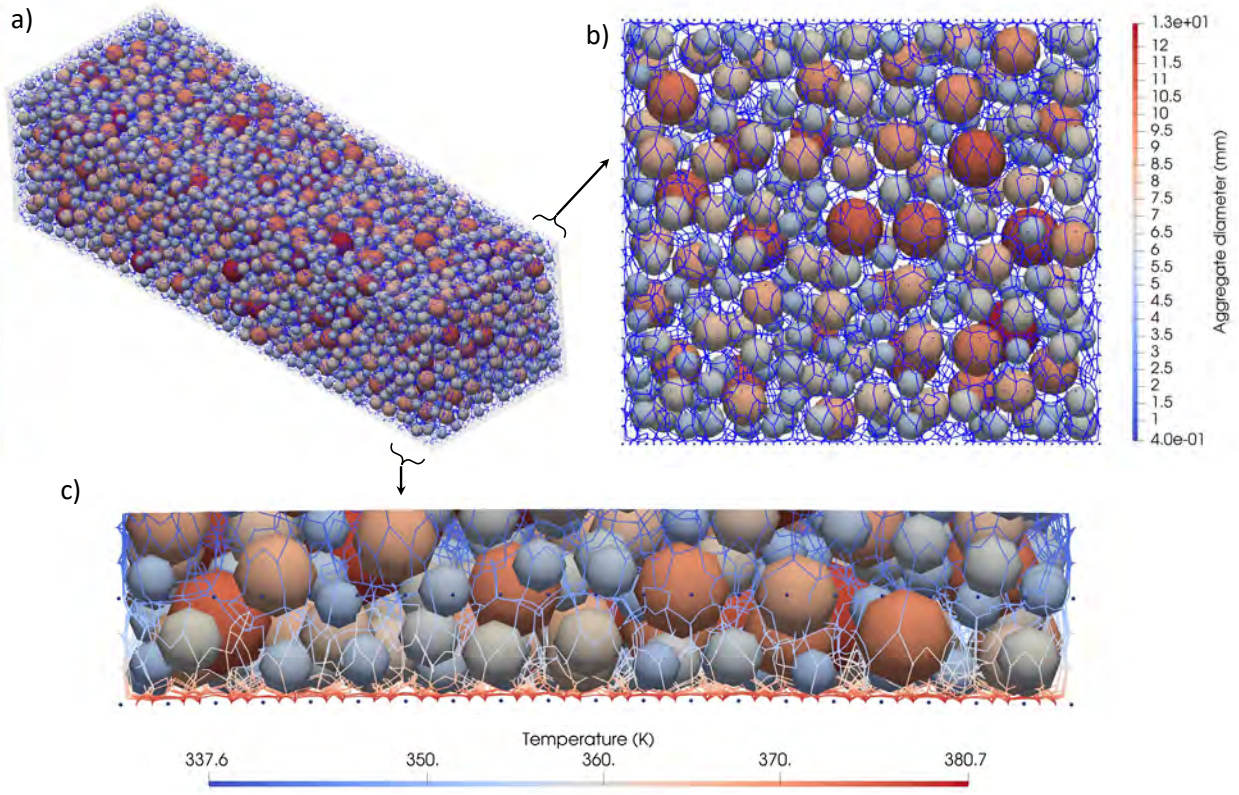

Figure 60. Heat diffusion conduit network surrounding LDPM concrete particles. (a) the full 300 mm sector system with conduits colored in blue, and aggregates colored based on their diameters, (b) front view of a slice of the first 20 mm from the inner surface, (c) top view of the same slice with the diffusion network colored according to temperature gradient during the early LBLOCA thermal shock peak.

4.3.3 Models

The modeling strategy adopted to estimate the additional damage depth caused by a LOCA is similar to that used to determine the in-service irradiation-induced damage depth at the fuel mid-core elevation. The LDPM simulation results presented in [45] serve as baseline data. The Alnaggar, Choi, and Le Pape study was performed to obtain an understanding of the effects of thermal exposure during LOCA on the depth of cracking and degree of damage of the CBS at different ages, thus accounting for RIVE effects. Three LOCA scenarios were considered, starting with no RIVE (pristine control case, assuming no

irradiation-induced degradation) and RIVE-induced degradation after 20 and 40 years of operation. The simulations were performed in three steps:

1. The in-service irradiation depth was calculated assuming that the neutron attenuation profile did not vary over time, thus ignoring the possible effects of core or internal design changes. The single input parameter was the fast neutron fluence at the surface of the concrete. RIVEs were determined from the fluence and in-service temperature profiles. The induced cracking and damage in the CBS sector were obtained from the mechanical simulations using the LDPM.
2. A thermal shock caused by a LOCA was applied to the surface of the concrete. The transient temperature profiles were calculated using the LDPM's heat transfer simulation. (See the temperature profile in Figure 61).
3. The mechanical response of the irradiation-induced pre-damaged CBS sector to the thermal expansions caused by the LOCA was calculated to determine the increase in damage depth.

Thus, these computationally intensive simulations yielded three damage depths that were used as benchmark data points to be compared with a 1D-SAM.

1D-SAM relies on linear simulation principles, even though the concrete properties vary with exposure to neutron irradiation. Hence, loading can be superimposed into a single simulation to account for irradiation-induced RIVE, LOCA-induced temperature increase, and LOCA-induced pressure in the reactor cavity. For the sake of comparison with the LDPM, pressure is ignored at this stage.

The LOCA-induced temperature profiles vary over time, starting with a spike (black line in Figure 61, temperature vs. depth plot) at the surface of the concrete when subjected to steam release in the cavity, evolving into quasi-linear profiles after a few hours (turquoise, green, and magenta lines in Figure 61, temperature vs. depth plot).

In the 1D-SAM simulation, only a linear temperature profile was considered as an approximation of the temperature profile at approximately 1 hour after the start of the LOCA. The main plot in Figure 61 shows the evolution of the damage depth caused by a combination of irradiation and LOCA loading with an increasing fast neutron fluence at the surface of the concrete. The same stress-based (dashed line) and strain-based (solid line) criteria are used to interpret the 1D-SAM results and to compare them with the LDPM results (blue diamonds) which model a LOCA occurring after 0, 20, and 40 years of operation. The agreement between the LDPM and 1D-SAM provides reasonable assurance that the simplified model can be employed to conduct parametric studies.

Thus, 1D-SAM simulations could be expanded to account for varying temperature and pressure in the reactor cavity during a LOCA. The modeled temperature increase and pressure during a LOCA range from 15 °C to 40 °C and from 0 to 1 MPa, respectively.[3] In-service irradiation was considered for six different fast neutron fluences at the surface of the concrete: 0.5×10^{19}, 1×10^{19}, 2×10^{19}, 4×10^{19}, 7×10^{19}, and 10×10^{19} n.cm^{-2} ($E > 10$ keV). The results of the 216 simulations are summarized in Figure 62. Each colored heat map corresponds to a specific irradiation condition. All maps show the same qualitative trends. Note that the range of values varies from one heat map to another; refer to the contour line values on each map for clarification. The highest LOCA-induced damage depth occurs at the highest temperature increase and lowest pressure in the cavity because temperature increase and pressure in the cavity contribute to opposite mechanical effects in the concrete region near the reactor cavity. Temperature increase and irradiation-induced expansion cause the development of biaxial compression in the concrete, whereas pressure in the cavity creates tension in those directions. Within the range of modeled temperature

[3] Simulated pressure values: 0, 0.1, 0.25, 0.5, 0.7, and 1.0 MPa. Simulated temperature increase values: 15, 20, 25, 30, 35, and 40 °C.

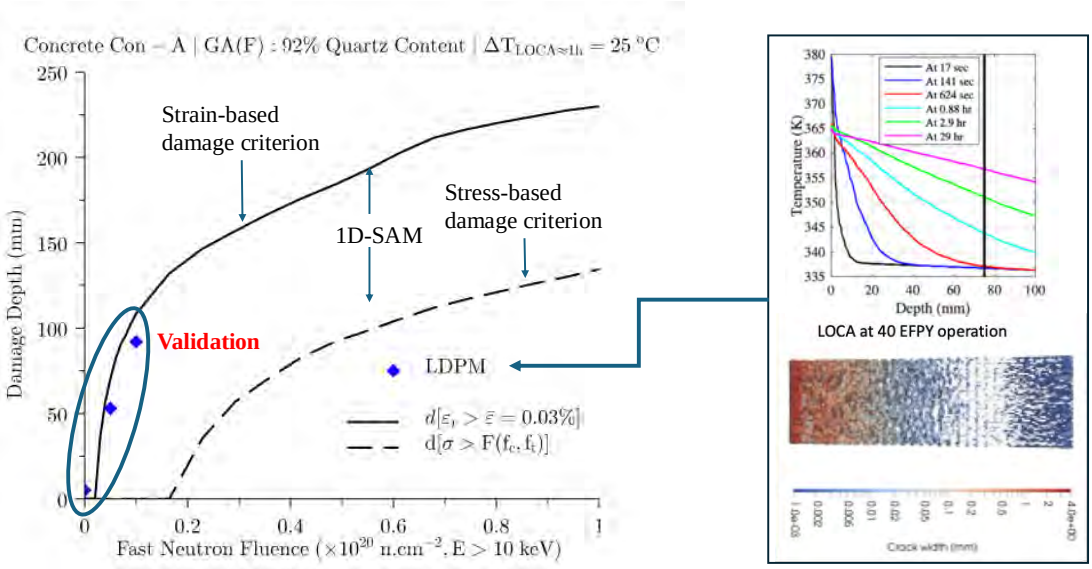

Figure 61. LOCA-induced damage depth in the CBS with increasing fast neutron fluence at the surface of the concrete. Comparison between the LDPM and 1D-SAM simulations.

increase and pressure, the variation in LOCA-induced damage depth is approximately 30 mm for each in-service irradiation value. The main variation in damage depth is caused by in-service irradiation. Figure 63 shows the evolution of the damage depth with increasing fast neutron fluence, comparing the effect of in-service irradiation alone (black line) and the combined effects of in-service irradiation and LOCA (red line: average values). The increase in damage depth caused by LOCA is approximately 25 mm, independent of in-service irradiation, and it extends to an additional 40 mm in the worst-case scenario.

The CBS is a safety-significant, heavily reinforced concrete structure that performs both radiological and structural functions throughout plant life. Its principal role is the attenuation of fast neutron and gamma radiation emanating from the reactor core to levels acceptable for personnel and equipment protection, while simultaneously providing geometric stability and load transfer for the surrounding containment systems. Because the CBS is continuously exposed to an irradiation environment whose intensity and spectrum vary in space and time, long-term changes in material behavior and structural performance must be assessed using a systematic, physics-informed approach.

Irradiation effects in concrete originate from the coupled influence of fast neutrons and ionizing photons on the cement paste and aggregate phases. Fast neutrons displace atoms, disrupt crystalline lattices, and can induce volumetric instability in susceptible aggregates; gamma rays deposit energy through ionization, producing localized heating and radiolysis of bound water within the hydrated cement matrix. These mechanisms collectively alter modulus, strength, creep, shrinkage, permeability, and fracture characteristics. The magnitude of degradation is governed not only by the fluence and dose, but also by the local spectrum, temperature, moisture state, and mixture composition.

The spatial distribution of the irradiation field inside the CBS is inherently nonuniform. Axial variations arise from differences in neutron leakage along the height of the core; azimuthal variations reflect core

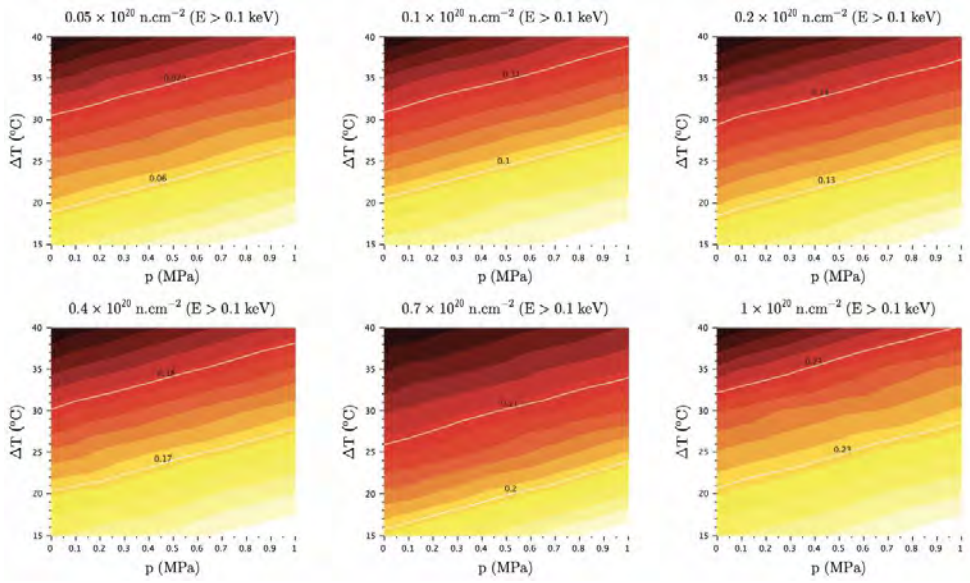

Studied range
ΔT_{1h}: +15 to +40°C
p: 0 to 1 MPa

Limited effect of the range of pressure and temperature on the damage depth increase.

Main factor: in-service irradiation

Figure 62. LOCA-induced damage depths at varied in-service fast neutron exposures as well as varied pressure and temperature increases in the reactor cavity during a LOCA.

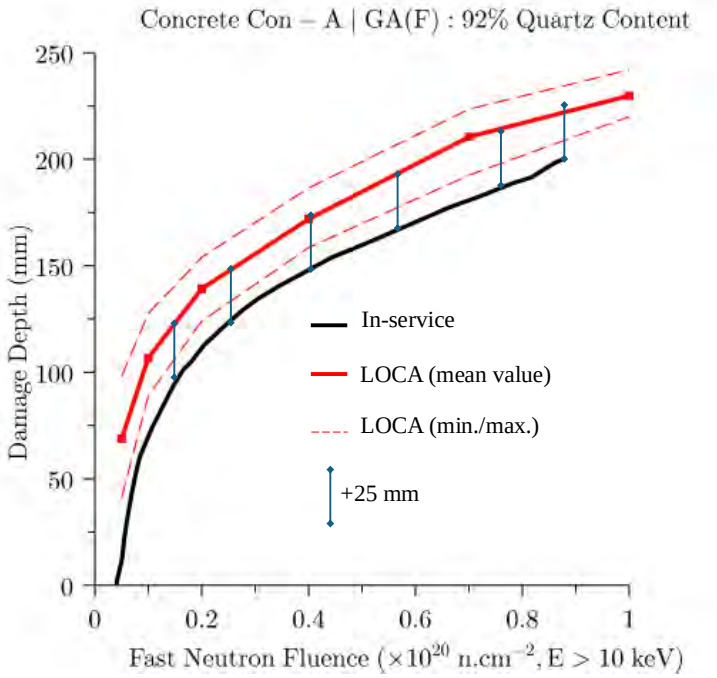

Figure 63. Combined in-service irradiation and LOCA effects on the damage depth.

loading asymmetry and localized shielding; and depthwise gradients are driven by attenuation through the concrete thickness and by embedded steel, liners, and penetrations that perturb transport. Accurate field quantification is therefore the precursor to any credible prediction of serviceability and residual capacity.

Two complementary approaches are typically used to characterize the irradiation field. The first is analytical extrapolation from surveillance measurements near the RPV, with semi-empirical attenuation functions applied to estimate conditions within the shield wall [21, 26, 28, 29, 58–66]. The second is high-fidelity neutron and photon transport simulation using codes such as MCNP, SCALE, or the VERA-shift suite to resolve three-dimensional flux and dose distributions in plant-specific geometry [21, 26, 28, 29, 58–66]. Transport results provide boundary conditions for thermo-mechanical analysis and enable mapping between exposure histories and material property evolution.

Concrete composition strongly influences the irradiation response. Hydrogen, primarily introduced via mixing water and present in hydrates such as calcium–silicate–hydrate, moderates neutrons and participates in radiolytic reactions. Calcium- and silicon-bearing phases are susceptible to irradiation-induced disorder, which reduces stiffness and can alter thermal expansion. Carbonate aggregates can experience decarbonation under sustained gamma heating. Understanding these constituent-level interactions is essential for predicting macroscopic changes in stiffness, strength, and fracture resistance across the CBS wall thickness.

4.4 MODELING METHODOLOGIES

Predicted damage depths under LOCA conditions from both SAM and the LDPM are compared in Figure 61, validating the semi-analytical method against detailed mesoscale simulation. The meso-scale LDPM framework and its discretization are depicted in Figure 60, showing polyhedral cell tessellation and contact facets governing fracture evolution. Figure 57 details the compositional variability of igneous aggregates, which plays a decisive role in governing irradiation response. Depth-wise comparisons of predicted damage using the LDPM, FEM, and the 1D semi-analytical model are shown in Figure 54, confirming convergence among the approaches for representative loading conditions.

4.5 SEISMIC EFFECTS ON CBS DAMAGE

Seismic demand is characterized using site-specific response spectra or acceleration time histories that are compatible with probabilistic seismic hazard analyses for the plant location. Input motions are propagated to the foundation level through soil columns or half-space models, and soil–structure interaction is represented using impedance functions or direct finite element coupling with nonlinear constitutive behavior for the near-foundation soil. Damping is modeled using a combination of material hysteresis and Rayleigh components calibrated to small- and large-amplitude response.

Analyses resolve the distribution of stresses, strains, and crack indices across the CBS, with attention to re-entrant corners, penetrations, and liner discontinuities where stress concentrations develop. Cyclic loading is tracked to identify initiation and stabilization of crack widths, potential bar slip at lap splices and anchorages, and yielding of reinforcement in ductile detailing regions. Capacity reduction factors are derived by reanalyzing the seismically damaged state under service loads, quantifying the loss of effective stiffness and strength.

Where appropriate, bidirectional and vertical components of seismic input are applied simultaneously to capture coupling effects. High-frequency content is examined for potential resonance with local modes of stiff components, while long-period components are evaluated for global drift and rocking. The resulting damage maps identify zones susceptible to microcracking, spalling near the inner face, and interface shear at liner–concrete boundaries.

4.6 COMBINED LOCA AND SEISMIC LOAD EFFECTS ON CBS DAMAGE

Combined hazard scenarios consider simultaneous or sequential occurrence of LOCA and seismic events. Thermal cracking and stiffness degradation produced during the LOCA transient can elevate stress concentrations and reduce ductility just prior to or during seismic shaking. Conversely, seismic-induced cracking can increase permeability and modify thermal gradients during LOCA transients. Numerical simulations therefore superimpose mapped pressure and temperature histories with ground motion time series, respecting proper phasing for worst-case combinations.

Interaction effects are evaluated by comparing stress invariants, crack opening indices, and energy dissipation between single-hazard and multi-hazard analyses. Worst-case damage zones frequently occur at structural discontinuities, around penetrations, and where reinforcement is curtailed or anchored. Residual capacity is quantified by subjecting the post-event damaged configuration to service and design-basis loads and comparing global stiffness, drift capacity, and margin to demand against undamaged baselines.

The comparative results across the three loading scenarios are summarized in Table 8.

Table 8. Comparative summary of residual capacity under LOCA, Seismic, and Combined loading conditions.

Loading Scenario	Primary Effects	Damage Characteristics	Residual Capacity Reduction
LOCA	Rapid pressurization, elevated temperature, jet thrust	Cracking, spalling, thermal gradients, stiffness loss	Moderate to High
Seismic	Dynamic acceleration spectra with SSI	Stress redistribution, localized cracking, reinforcement yielding	Moderate
Combined LOCA + Seismic	Thermo-mechanical + dynamic interaction	Amplified cracking, stress concentration, accelerated propagation	High to Severe

4.7 SUMMARY AND CONCLUDING REMARKS

The assessment establishes coherent links between plant-specific irradiation fields and material property evolution, as well as between accident and seismic demands and structural performance metrics. Irradiation progressively modifies the mechanical response of concrete and reinforcing steel, influencing stiffness, strength, and fracture resistance. The LOCA transient imposes rapid thermo-mechanical loading that triggers cracking and spalling; seismic excitation redistributes demand cyclically and may activate reinforcement yielding and liner–concrete interface slip. When combined, these hazards amplify one another, creating the most severe damage patterns and the largest reductions in residual capacity.

The integrated modeling framework described herein—which combines FEA for global response, the LDPM for mesoscale fracture, and 1D-SAM for rapid screening—enables cross-validated predictions of damage depth, crack topology, and post-event performance. Results guide targeted detailing, inspection, and mitigation strategies, including reinforcement anchorage improvements, interface treatments, and thermal protection measures. The methodology provides a defensible basis for safety evaluations, life-extension studies, and planning for outage inspections and decommissioning.

5. STRUCTURAL SIMULATION OF RPV SUPPORTS UNDER ACCIDENTAL LOADING

This section provides an analysis of the bearing capacity of a generic RPV shoe-type support system, with a focus on the resistance of the anchor group system embedded in concrete and subjected to in-service irradiation.

5.1 GEOMETRY

A study of a shoe-type support is presented in this report. Specific design may vary from one reactor to another.

> *Per system design requirements, the RPV supports must restrict movement of the RPV under all design loading conditions. At the same time, the RPV must be allowed to expand and contract under varying temperature conditions. A 'shoe' interface, also referred to as a 'saddle,' is used under the inlet and/or outlet nozzles or under load brackets between nozzles; the shoe restricts vertical and tangential movement, but allows radial thermal growth of the RPV. The loadings on the shoe are transferred to the underlying support system. The shoe is anchored to the top of the biological shield wall (i.e., either sitting directly on the top surface or set in a recess on the top surface). The shoes are attached to metal weldments. These designs incorporate some type of air or water cooling to minimize heat transfer to the underlying concrete. Some designs incorporate taller vertical plates that allow for better air cooling, but place the load-bearing baseplate of the weldment on the concrete, closer to the higher radiation fields at the beltline of the RPV* [22].

In this study, a generic shoe-support design inspired by Farley's design was analyzed. The details of Farley's support system are presented in Figure 8, p. 17. Additional details of the shoe box design are shown in Figure 64.

The description of Farley's support system is provided in [37]:

> *The reactor pressure vessel (RPV) rests on six steel supports which are located underneath the RPV nozzles. There are six supports; one support for each of the three hot leg nozzles and one support for each of the three cold leg nozzles. Each nozzle support consists of two parts, one part (the upper part) which is attached to the nozzle and the lower part which supports the upper part and is in turn supported by the concrete primary shield wall. The lower part is anchored into the concrete primary shield wall. The upper part is allowed to slide on the lower part to allow for thermal expansion of the RPV. The load path from the RPV is the nozzle support upper part through the lower part to the concrete surface. The gross cross-sectional area of the primary shield wall is approximately 835 square feet, as compared to sum of the footprint areas of the six supports, which is approximately 76.6 square feet. Based on these areas, the supports occupy less than ten percent of the cross-sectional area of the primary wall.*

5.2 LOADING

The maximum loads induced in PWR vessel supports are those from the combined effects of postulated pipe ruptures (i.e., LOCAs), SSEs, and other loads per the licensing basis.

Both LOCAs and earthquakes involve complex dynamic loading and structural analysis, including thermohydraulics, fluid–structure interaction, and soil–structure interaction. To derive the loading

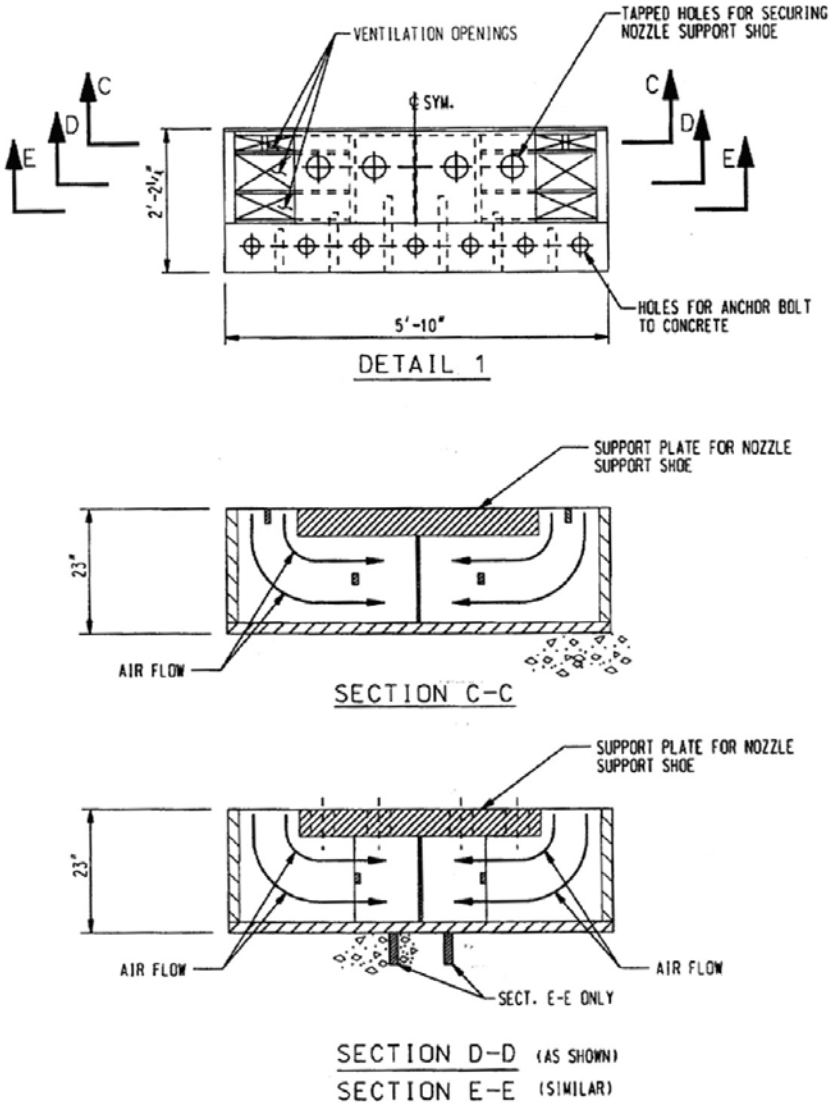

Figure 64. Farley Units 1 and 2 reactor vessel support box detail.

conditions exerted on the RPV support structures, thermohydraulics and structural models are used, including the reactor's main components—the reactor vessel, steam generators, the reactor coolant pump, main coolant piping [78]; the main concrete structural components—the CBS and concrete containment building (CCB); and a refined description of the reactor internals and core assemblies, as well as the reactor vessel supports. In the work documented herein, the objective was to assess the bearing capacity of a shoe-type support system and the possible effects of irradiation on that system. Realistic loading scenarios are considered based on published information available in the literature and as informed by best judgment.

5.2.1 LOCA

Cloud [16] provides time-dependent loads at the RPV support locations for a Westinghouse four-loop PWR. Break locations were postulated in the reactor coolant loop using the methods and criteria outlined in WCAP-8082 [79]. Figure 65(a) shows the vertical and horizontal forces at the support under the broken nozzle. Note that the intervals where the vertical force is zero indicate lift-off during these periods. Because of the unilateral boundary conditions in the support system and the downward movement of the vessel's centerline (Figure 66), the vertical load at the support near the break varies from 0 (lift-off) to compression, with a maximum value of approximately 1.1×10^6 pounds (~5 MN). At the opposite support, no lift-off is observed, and the vertical compression ranges between approximately 0.8 and 13 MN as the vessel rocks on its supports (Figure 66). The horizontal load at the support located at the broken nozzle is directed toward the CBS's back wall, opposite the concrete edge near the cavity. The horizontal load shows an initial spike around 2.8×10^6 lb (~12.7 MN), followed by variations around an average value of about 6.75 MN. The horizontal load at the nozzle opposite the break is not reported in [16]. Nevertheless, because of the vessel's rocking motion, it is assumed that the horizontal load at this location may be directed toward the edge of the concrete, toward the reactor cavity. "Generally, the peak horizontal loads and peak vertical loads do not occur at the same support. The largest vertical load occurs beneath the nozzle on the opposite side from the broken nozzle, and the peak horizontal load occurs on the supports that are mostly perpendicular to the broken nozzle" [22].

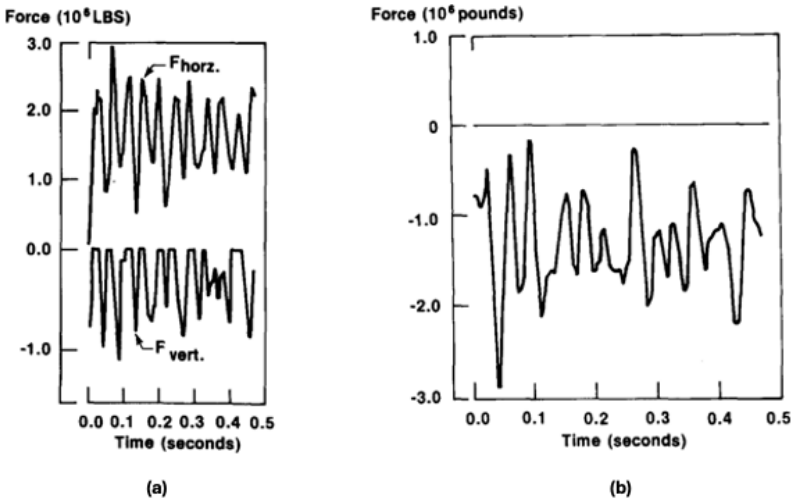

Figure 65. LOCA-induced time-dependent load at (a) the broken nozzle support and (b) the support opposite the broken nozzle [16].

The peak horizontal load values provided by Cloud [16] appear to be higher than the estimated jet

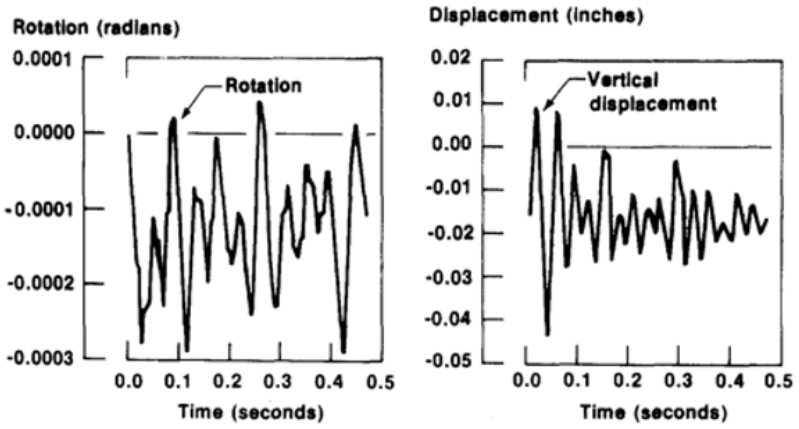

Figure 66. LOCA-induced time-dependent rotation and vertical displacement of the RPV centerline [16].

impingement thrust calculated using RELAP5-3D (see Table 7), although these values are comparable to the average horizontal loads provided by Cloud [16].

5.2.2 SSE

As explained in Section 2.4.3, full analysis of the RPV and CBS under seismic loading requires plant-specific data for the design under consideration—along with a complex analysis of the reactor system's response to a hypothetical earthquake, including site-specific data, soil–structure interaction, and reactor component design. Because the main objective of this part of the analysis is to determine the effect of irradiation-induced degradation on the support load-bearing capacity, the assumed simplification of considering both the RPV and the CBS as rigid bodies allows for simple calculation of the seismic load demand, especially in the horizontal direction. This is the approach considered here.

5.3 SUPPORT SYSTEM CAPACITY

5.3.1 Anchorage Failure Modes

The shoe support system relies on a steel plate to transfer the vertical downward force exerted by the RPV and nozzle system, as well as seven long anchors (diameter $2\frac{3}{4}$ in. [$\sim$ 7 cm], approximate length 2 ft [$\gtrsim$ 60 cm]) to transfer shear force to the CBS wall. The anchor centers are aligned at a distance of $23\frac{3}{4}$ in, which is also close to 60 cm. The height of the support box for the nozzle is 23 in. Hence, the horizontal force creates a bending moment at the location of the interface between the bottom steel plate and the supporting concrete.

The presence of reinforcement through the thickness of the concrete below the support plate plays an important role in the shear strength of an anchor group near a concrete edge [18, 20]. However, it is helpful to examine the independent contributions of concrete and steel to load resistance. In the following sections, analytical and computational evaluation of the load carrying capacity of the support shoe are presented.

Different failure modes can be hypothesized (see Figure 67 for details):

Concrete edge failure develops from the external anchors toward the edge of the concrete. The angle between the concrete edge and the fracture is approximately 30 degrees [19]. In the absence of reinforcement, the shear capacity is governed by the geometry of the fracture surface and the shear strength of plain concrete. A similar fracture mode can occur with stirrups, which significantly increase the shear capacity of the anchored system [18].

Stirrup failure (yielding) may occur when the tensile stress in the reinforcing bars is exceeded.

Concrete crushing may also occur beneath the box's bottom steel plate. This effect is aggravated by the bending moment caused by the horizontal force applied at the top of the shoe box. If only plain concrete is considered, then the compression stresses under the plate near the concrete edge may lead to a wedge-type fracture toward the cavity. To reach concrete failure by crushing, reinforcement tying the hypothetical wedge is needed.

Pry-out failure may occur as the result of a rotation of the anchor.

The irradiation-induced damage may affect a portion of the concrete located directly under the support plate near the reactor cavity.

The effects of irradiation on the concrete located below the support system depend on its elevation relative to the elevation of the fuel at mid-core.

5.3.2 Analytical Expressions for Each Failure Mode

Notations

A_s: area of a single reinforcement bar
a: bottom steel plate width (hoop direction)
b: bottom steel plate length (radial direction)
c: horizontal distance of the anchor bolts to the concrete edge
c': horizontal distance of the anchor bolts to the bottom steel plate edge
c_1: concrete cover (to center)
d: embedded depth of the anchors
δ: irradiation-induced depth
f_c: concrete compressive strength (cylinder)
$f_{c,c}$: concrete compressive strength (cube)
f_y: steel yield strength
ϕ_s: reinforcement diameter
s_t: reinforcement spacing

5.3.2.1 Concrete Edge Failure

Plain Concrete

The hypothetical shear failure mode only accounts for the effects of the horizontal load H. The assumed failure occurs along three planes: one horizontal plane located at the elevation of the bottom of the anchors, and two lateral outward planes. The three shear planes form a trapezoidal prism sloping toward the reactor cavity. The lateral planes meet the concrete edge at an estimated distance of approximately $1.5c$ [19]. See Figure 68 for details. The back of the prism fails in tension. Denoting τ_s and f_t, the shear and tensile strength of plain concrete, the shear capacity reads: $\bar{V} = f_t ad + \tau_s \left(\sqrt{13} cd + ac + \frac{3}{2} c^2 \right)$. Assuming that τ_s is approximately 3 MPa, neglecting the contribution of tension resistance, and considering that $c \simeq h \simeq 0.6$ m, the edge failure shear resistance of this anchored system is approximately 8.75 MN considering only the plain concrete contribution.

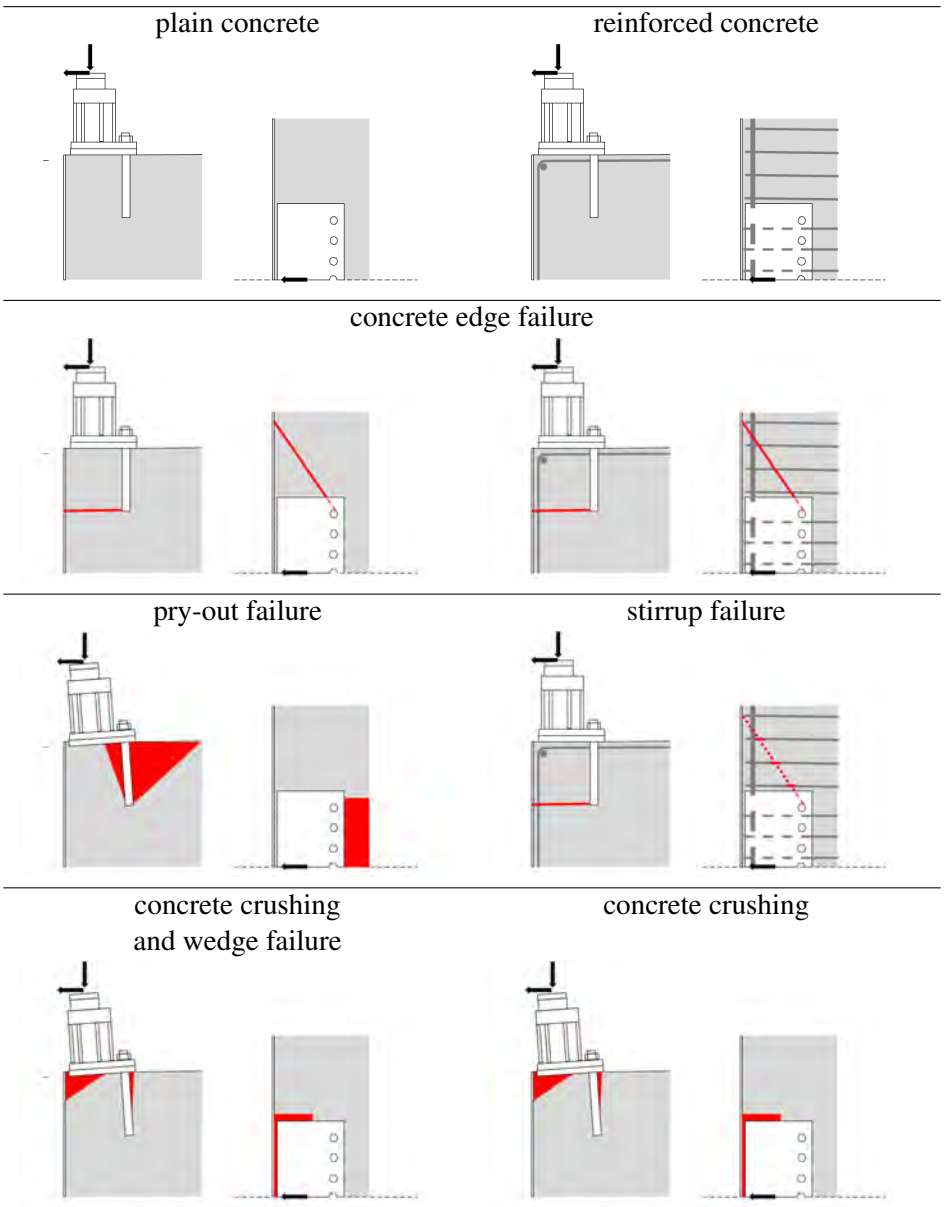

Figure 67. Hypothetical failure modes of the (reinforced) concrete below the nozzle shoe support.

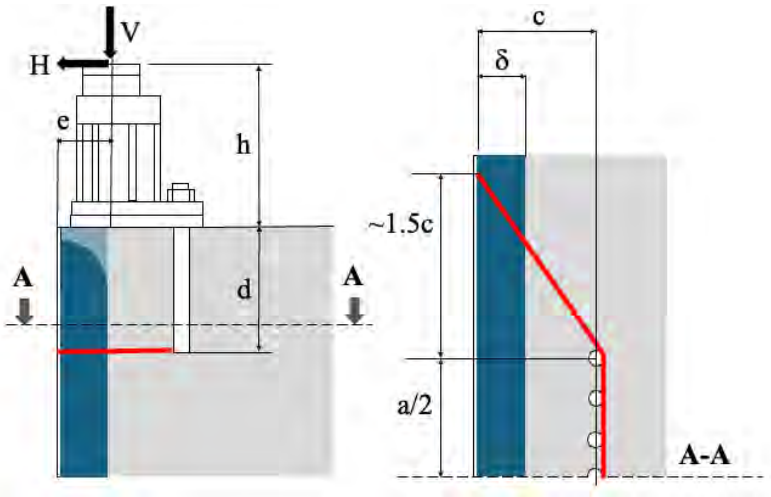

Figure 68. Concrete edge failure (red) and in-service irradiation damage (blue).

Assuming that irradiation-induced damage causes the formation of a damage depth (δ) considered constant in the region of the edge failure, the variation of shear capacity evolves linearly with δ when the tensile resistance of the back plane is not considered: $\frac{\Delta \bar{V}}{\bar{V}} = -\frac{\delta}{c}$

The presence of reinforcements is necessary to provide resistance in the concrete supporting the shoe-type support system. The details of the reinforcement are not known to date. Therefore, only a theoretical analysis can be presented at this time. Details are provided in the paragraph below.

Reinforced Concrete

The contribution of the horizontal bars to the resistance of the wedge failure is the sum of the hook and bond capacities for each bar crossing the failure plane. The hook capacity depends on the location (l) of the failure crack relative to the hook, specifically relative to the concrete cover of the vertical reinforcement, denoted as c_1. According to Sharma et al. [19], "Any stirrup that is not intercepted by the crack or whose anchorage length in the assumed breakout body is $\leq 4\phi_s$ does not contribute toward the load carrying capacity of the anchorage." For illustration, assuming that the concrete cover is approximately 7 cm and the bar diameter is 25 mm, if the crack intercepting the rebar is located less than $7 + 2.5 \times 4 = 17$ cm from the concrete edge, then it does not contribute to the anchor capacity.

The hook contribution of each bar is determined by $N_{hook} = \Psi_1\Psi_2\Psi_3 A_s f_y \, (f_{c,c}/30)^{0.1}$, where Ψ_1 accounts for the influence of the reinforcement position relative to the crack, and Ψ_1 is equal to 0.95 for position *1* and 0.16 for position *2* (see Figure 69 for explanation), Ψ_2 accounts for the influence of the diameter, $\phi_{s,\text{hoop}}$, of the hoop bar forming the hook located at the edge reinforcement as given by $\Psi_2 = \left(\frac{\phi_{s,\text{hoop}}}{\phi_s}\right)^{3/2} \leq 1.2$, Ψ_3 accounts for the influence of the bond length, l_1, and is given by $\Psi_3 = (l_1/c)^{2/5}(10/\phi_s)^{1/4}$. $f_{c,c}$ is the mean compressive strength of concrete obtained using 150 mm cubes. The ratio of the compressive strength of concrete from cylinder to cube specimens can be approximated as $f_c/f_{c,c} \sim 0.8$.

The contribution of the bond of one bar is given by $N_{\text{bond}} = \pi(l_1 - 4\phi_s)\phi_s\bar{\tau}_b$, where $\bar{\tau}_b$ is the mean bond strength between the concrete and the bar.
$\bar{\tau}_b$ is approximately twice the value of the design's bond strength.

The total anchor group capacity is the sum of the hook and bond resistance of the contributing bars that tie the cracking planes. The specific total anchor group capacity depends on the geometry of the

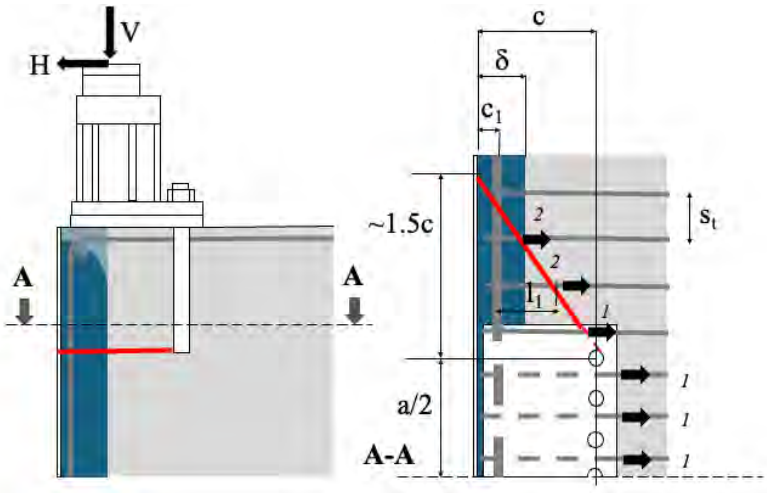

Figure 69. Concrete edge failure of reinforced concrete (red) and in-service irradiation damage (blue).

support system and the steel and concrete properties. For the sake of illustration, a calculation is presented assuming the following values:
Steel yield strength (f_y): 414 MPa (grade 60).
Concrete compressive design strength (cylinder, f_c): 25 MPa. The corresponding compressive strength obtained on cube specimen ($f_{c,c}$) is approximately 30 MPa.
Steel–concrete bond strength (τ_b): 5 MPa. Reinforcement spacing: 25 cm (approximately 10 in., which is also the spacing between the anchors).
Reinforcement diameter (all directions): 25 mm.
Concrete cover to the hoop reinforcement center: 7 cm.
Layers of rebar in the height of the wedge: 3 (spacing 25 cm).
Note that these values are hypothetical and need to be established from construction drawings that are not readily available at this date. For each layer, after calculation, the total capacity is 9.3 MN.

The possible effects of the irradiation-induced damage depth on the anchor group capacity for this failure mode are as follows:
(1) If the damage depth exceeds the location of the hook, then the contribution of the hook capacity should not be considered. The calculation hypothesis provided above implies a reduction of the total anchor group capacity of $\approx -40\%$ if the damage depth at the elevation of the contributing reinforcing bars reaches or exceeds approximately 7 cm.
(2) The bond capacity will also be affected if the irradiation-induced damage depth exceeds the location of the hook because it will reduce the bond length denoted l_1.

It is important to note here that this analysis is based on simplified assumptions of the location and morphology of the formed cracks and final crack surface. It also assumes that all hooks crossing the crack contribute the same full yield strength. In the following section, a detailed computational simulation with and without reinforcement will examine these assumptions.

5.3.2.2 Concrete Crushing

Pure Flexural Mode

In pure flexure, only the effect of the horizontal load on the bending moment is considered. The resisting bending moment is estimated by $\bar{\mathcal{M}}_r = 0.8\Psi f_c b x(c' - x/2)$, where f_c is the compressive strength of concrete,

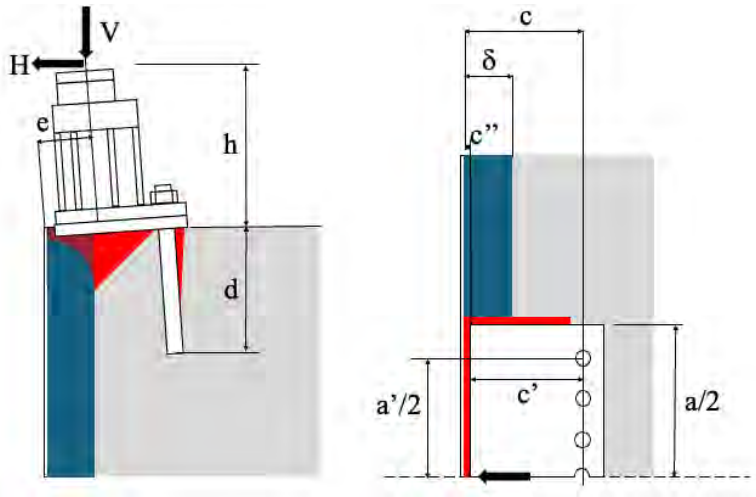

Figure 70. Concrete crushing failure (red) and in-service irradiation damage (blue).

and bx is the area under the plate subject to compression. The value of x is determined assuming that the deformation field under the plate is linear and that the maximum allowable compression strain in concrete is $\varepsilon_{c,u} = 0.35\%$. The balance of forces[4] between the anchors in tension and the concrete in compression leads to $x \sim 0.4$ m. The value of $\bar{\mathcal{M}}_r/h$ is ~ 6.24 MN.

The irradiation-induced damage depth reduced the load transmission area under the bottom plate of the support shoe box. Assuming a maximum damage depth of 20 cm, the value of $\bar{\mathcal{M}}_r/h$ is reduced to 2.9 MN. The horizontal load capacity for intermediate values of irradiation-induced damage depth is provided in the summary presented at the end of this chapter. The anchors remain in the elastic regime for all studied cases.

5.3.2.3 Pry-Out Failure

The study of the pry-out failure mode depends mainly on the formed pry-out crack surface, which is controlled by loading and CBS geometry in the case of plain concrete; for reinforced concrete, it also depends on the bond and interaction among concrete, rebar, and hooks. Therefore, pry-out failure was studied using the LDPM, as detailed in the next section.

5.4 SUPPORT SYSTEM SIMULATIONS WITH LDPM

5.4.1 LDPM Overview

The LDPM is a 3D mesoscale modeling approach for concrete and other quasibrittle materials that was developed by Cusatis et al. in 2010–2011 [80, 81]. The LDPM represents concrete as an assembly of discrete particles (i.e., coarse aggregate pieces) interconnected by lattice springs or facets, which model the mortar between aggregates [82]. The internal structure is generated by packing particles into concrete, followed by Delaunay tetrahedralization to form polyhedral cells [82]. Each cell facet acts as a potential crack plane that is governed by micro-level vectorial stress–strain relationships for normal and shear interactions [82]. This framework explicitly captures concrete heterogeneities and discrete cracking and thus offers a more realistic alternative to continuum models, which smear out cracks.

[4] $0.8\Psi f_c bx = nE_s\varepsilon_s A_s$ with n the number of anchors and E_s the Young's modulus of steel. The tensile strain in the steel anchors is determined by $\varepsilon_s = \varepsilon_{c,u}(c' - x)/x$.

The LDPM combines earlier lattice and discrete particle models into a unified 3D framework [80]. Its nonlinear constitutive laws capture key micro-mechanical actions: normal tension, compression, shear with friction, and crushing under high confinement. Tensile microcracking, frictional slip, and plastic compaction emerge naturally within the LDPM, allowing it to simulate a wide range of behaviors—from brittle fracture to ductile hardening—using a single set of micromechanical parameters [81].

5.4.1.1 Advantages and Mechanisms of LDPM

The LDPM excels in representing the fundamental failure mechanisms of concrete, including tensile cracking, crack propagation, shear-induced dilation, and compressive crushing. For example, the LDPM replicates distributed microcracks under tension or bending that coalesce into realistic macroscopic cracks, as well as lateral expansion and axial splitting under uniaxial compression. Under multiaxial confinement, the model transitions naturally from a cracking-dominated response to strain-hardening behavior, consistent with experimental observations [81, 83]. These capabilities arise directly from the LDPM's discrete structure, requiring no ad hoc adjustments for different stress states.

A key strength of the LDPM is its ability to incorporate material heterogeneity, which is critical for capturing phenomena like size effects. Properties such as aggregate size and distribution are explicitly modeled, allowing natural transitions between distributed cracking in larger specimens and localized failure in smaller ones [84]. Extensions of the LDPM, such as LDPM-F for fiber-reinforced concrete and ASR-LDPM for simulating alkali–silica reaction (ASR), demonstrate its versatility in addressing complex physical phenomena [85–87].

5.4.1.2 Comparison with FEA

Unlike standard FEA, which treats concrete as a homogeneous continuum with smeared cracks, the LDPM explicitly models its discrete mesostructure. In FEA, damage and cracks are often introduced through smeared damage laws or cohesive elements, requiring careful calibration and regularization. The LDPM, on the other hand, generates cracks inherently through the breaking of facet connections between particles, resulting in realistic crack patterns driven by concrete's inherent heterogeneity [83]. For instance, the LDPM naturally captures phenomena such as size effects, stochastic strength variation, and crack path tortuosity, which are challenging for conventional FEA to replicate.

While the LDPM is computationally more intensive, recent advances in multiscale modeling and coarse graining have made it feasible for larger scales by combining LDPM insights with continuum FEA [88, 89]. The LDPM is most suited for highly detailed fracture simulations, whereas FEA remains advantageous for large-scale elastic analysis.

5.4.1.3 Applications of LDPM in Nuclear Concrete Structures

Concrete's critical role in nuclear infrastructure—such as biological shielding, reactor supports, and containment structures—makes the LDPM an invaluable tool. The LDPM has been applied to a range of nuclear-specific challenges, including the following.

- Biological Shield Walls:
  The LDPM has been used to study neutron irradiation-induced damage, where aggregate expansion and microcracking are modeled explicitly. This approach provides insights into damage gradients and residual strength that continuum models struggle to capture [90].
- Reactor Supports:
  LDPM simulations of ASR show how microcracking from ASR expansion reduces stiffness and strength, directly informing assessments of nuclear reactor supports [86].

- Containment Structures:
  For impact and blast scenarios, the LDPM has accurately predicted crater formation, spalling, and fragmentation under extreme loads, outperforming FEA in capturing complex fracture dynamics [91].
- Long-Term Aging:
  The LDPM coupled with creep and shrinkage formulations has been used to simulate long-term deformations, offering mechanistic insights into aging effects on nuclear concrete structures [92].

These applications highlight the LDPM's strength in addressing extreme and coupled deterioration mechanisms, providing higher accuracy and fidelity than traditional methods.

5.4.1.4 Summary

The LDPM offers a fundamentally different approach to modeling concrete than FEA, treating it as a composite of discrete particles that enables detailed simulations of microstructural failure mechanisms. This makes it uniquely capable of capturing size effects, heterogeneity, and realistic crack patterns [81, 83]. While computationally demanding, its predictive power has been demonstrated in a range of scenarios, including nuclear infrastructure, where traditional FEA often falls short [90, 91]. With ongoing developments in multiscale techniques, the LDPM is poised to remain a leading tool for understanding and engineering concrete's complex behavior.

Additional information regarding the LDPM can be found in Le Pape et al. [74].

5.4.2 Push-Over Analysis of the RPV Support Shoe Using the LDPM

Similarly to the analytical analysis of failure documented in the previous section, a detailed analysis was performed using the LDPM. Two cases were analyzed to understand the contribution of concrete and steel independently. However, data about the system reinforcement and dimensions are unclear and lack detail. The team had to depend on very old drawings with limited details. Therefore, best engineering judgment and simplifications of the reinforcement were used to generate a reasonably representative reinforced concrete model. In addition, due to the high computational cost of the LDPM, some simplifying assumptions were also made. Those assumptions are as follows.

1. Symmetry boundary conditions are assumed, so only one half of the support was simulated.
2. To limit computational cost, only 45° angle of the CBS was considered.
3. The support block and anchors were simulated using tetrahedral finite elements with elastic steel properties. As explained later, this assumption is needed to bypass the initial plastic failure observed in the shoe block itself at low horizontal loads.
4. The LDPM was used to simulate the concrete around the support block, and the remainder of the wedge was simulated using tetrahedral finite elements with elastic concrete properties. For the simulations with only plain concrete (no reinforcement), a smaller LDPM domain was used given that the expected concrete damage will be more localized. For the reinforced concrete cases, rebar and hooks transfer the load farther away from the anchorage system; therefore, the LDPM domain was extended.
5. To reduce computational costs, the effects of irradiation on concrete damage were considered by neglecting the contribution of (deleting) the innermost LDPM elements within 10, 15, and 20 cm from the inner surface of the CBS facing the RPV cavity.

6. A very coarse concrete mix design was used in this model; it consists of a maximum aggregate size of 50 mm and a minimum aggregate size cutoff at 25 mm. Details of the model calibration are presented next.
7. CBS reinforcement is not exactly the same as in the real plant, but it was chosen to be as close as possible based on the limited drawings that were obtained.
8. For the reinforced concrete case, the reinforcement was simulated using 1D beam elements with an idealized elastic–perfectly plastic constitutive model as is typically done in reinforced concrete design. Once a rebar reaches its yield strength, the system is considered to have reached failure.

5.4.2.1 Model Calibration

Because material data are limited and only the compressive strength is known, the same procedure detailed in Alnaggar and Bhanot [93] was used here. Assuming actual $f_c = 30$ MPa and using [11], estimates of elastic modulus $E_c = 25,907$ MPa and splitting tensile strength $f_{sp} = 3.0672$ MPa can be obtained. For a normal concrete with a Poisson's ratio of 0.19, LDPM elastic parameters can be computed following Cusatis et al. [80], which gives $\alpha = 0.25$ and $E_0 = 40,040$ MPa. To determine strength parameters, it is first assumed that the mesoscale tensile strength is equal to the splitting tensile strength $\sigma_t = f_{sp} = 3.0672$ MPa. Then, the tensile characteristic length l_t is to be calculated from the mesoscale fracture energy G_t, which was shown to be equal to the initial fracture energy G_f [93]. Using a maximum aggregate size of $d_a = 50$ mm, a water-to-cement ratio of $w/c = 0.5$, and $f_c = 30$ MPa, the initial fracture energy can be estimated following Bažant and Becq-Giraudon [94], giving $G_f = 33.579$ N/m. This gives $l_t = 285.82$ mm. It only remains to calibrate the mesoscale shear strength σ_s using simulations of uniaxial compression tests of standard 6×12 in. cylinders. Given the coarse aggregate size used, four randomly generated cylinders were simulated, and $\sigma_s = 11.87$ MPa was calibrated to achieve an average of $f_c = 30$, as shown in Figure 71.

5.4.2.2 Push-Over Analysis under Horizontal Loads Only

Plain concrete analysis

The model geometry is shown in Figure 72. The gray-colored part represents the LDPM domain and is shown partially transparent to reveal the internal idealized spherical aggregate. Here, the LDPM domain is extending 91.44 cm (3 ft) radially behind the block and 152.4 cm (5 ft) below the bottom of the support block (91.44 cm or 3 ft below the tips of the anchors). The support block and anchors are colored red, and the remaining volume of the simulated CBS wedge is colored blue. Concrete above the elevation of the base plate was neglected because it is far away from the anchors and would contribute very small forces if not reinforced.

To perform the push-over analysis, a monotonically increasing horizontal load was applied to the top of the support plate. The failure surface is a combination of pry-out and concrete edge failure, where the anchors form a concrete cone that initiates a crack surface starting at the anchor tip and propagating to the surface. Because of the compression from the edge of the support block on the interior edge of the CBS, the crack propagates nearly horizontally under the block zone. The estimated peak load in this case is approximately 3.26 MN. At this peak load, Figure 73 shows the system colored by the displacement magnitude. Crack traces can be seen in Figure 74. The formed crack surface is shown in Figure 75. At this peak load, while anchors are under significant tension caused by support block rotation, none of the anchors yield, as illustrated by the von Mises stress distribution shown in Figure 76, where the color bar's upper limit is 414 MPa, which is the steel yield strength (Grade 60). This indicates that as long as the 2 ft length of the anchors is adequate for full development, then the resulting peak load and failure mode can be considered realistic. However, as can be seen from the same figure, the web plate under the large

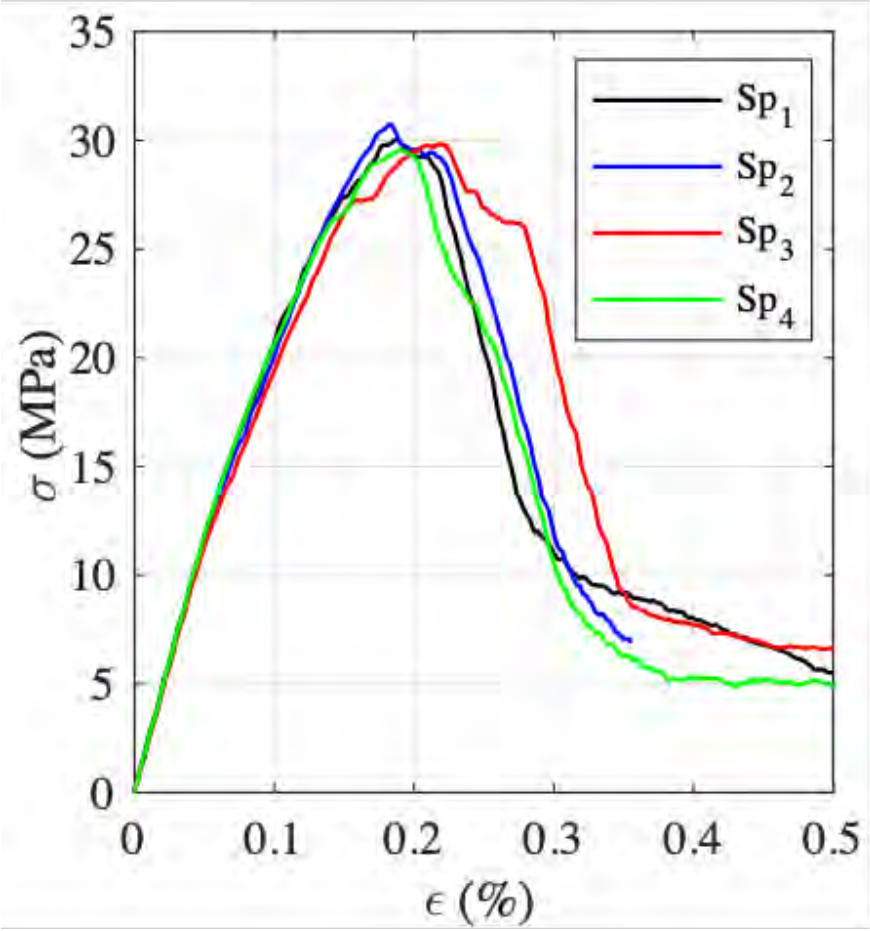

Figure 71. Calibrated uniaxial compressive response of four 6×12 in. cylinders.

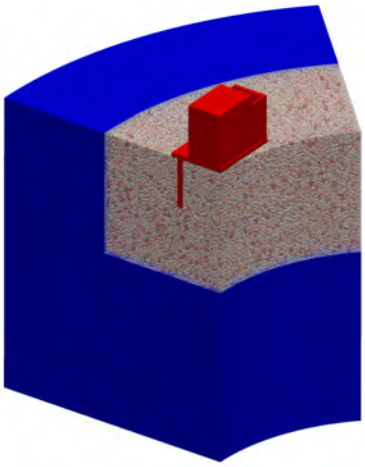

Figure 72. A 45° wedge model of the CBS showing LDPM (opaque gray) with internal aggregate, along with the support block (red) and the surrounding elastic concrete (blue).

support block is yielding at the connection with the base plate attached to the anchors. Also, yielding is observed at different connections with the web plates and the top block. This is why the support block is simulated using an elastic constitutive law rather than accounting for its plastic deformations. It is assumed here that either the support block design for lateral loads used a simplified analysis rather than full 3D analysis, or that the drawings for the support block do not include all details. Regardless of the explanation, the main objective of this report is to investigate the effects of irradiation on the system capacity, which would be governed by the concrete and reinforcement around the anchorage. Thus, failure modes that are independent of the concrete damage were neglected.

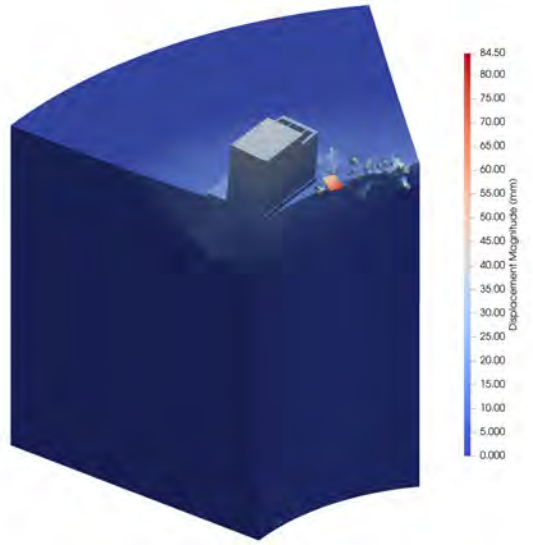

Figure 73. CBS wedge displacement at a peak horizontal load of 3.26 MN without applied vertical loads.

To account for irradiation-induced damage effects in a simplified manner, the innermost LDPM elements are neglected. This is done here solely to reduce the computational cost and to provide insight into the possible conservative failure mechanisms. Three explicit damage depths are simulated, including 10, 15, and 20 cm from the inner surface of the CBS facing the RPV cavity, as shown in Figure 77.

The partial loss of support under the support block results in an increase of its rotation. Although more cracking and damage around the support block can be observed, the mode of failure is still dominated by pry-out. This is expected because the lost elements shorten the lever arm between the compression zone under the support block and the anchors, causing higher tensile forces in the anchors and higher compression under the plate at the same horizontal force. Crack traces on the wedge surface, as well as the internal crack surface, are shown for the 20 cm damage depth case in Figure 78. Similar crack patterns were observed for 10 cm and 15 cm damage depths. The horizontal peak load capacities for all push-over cases without applied vertical loads are presented in the first column of Table 9.

Reinforced Concrete Analysis

While reinforcement details were not clear from the provided drawings, engineering judgment was employed to extract the most representative reinforcement detailing. The model geometry is shown in Figure 79. The gray-colored part represents the LDPM domain and is shown partially transparent to reveal the internal reinforcement. Here, the LDPM domain represents all the CBS thickness at the support block

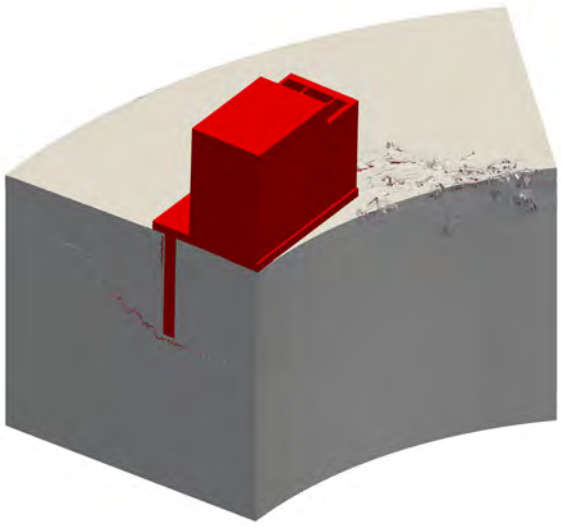

Figure 74. CBS wedge crack traces on the surface at a peak horizontal load of 3.26 MN without applied vertical loads.

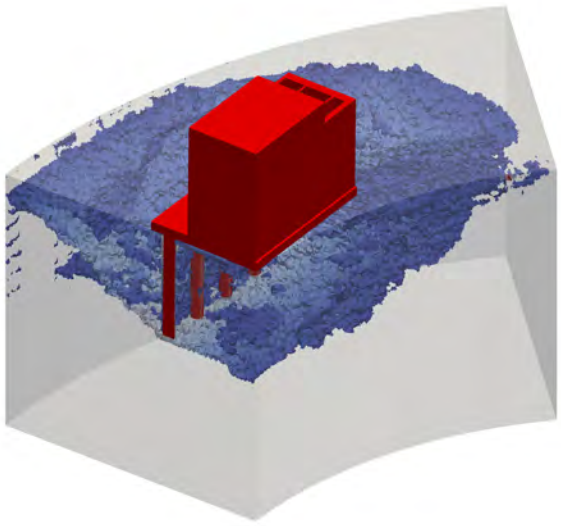

Figure 75. CBS wedge crack surface at a peak horizontal load of 3.26 MN without applied vertical loads.

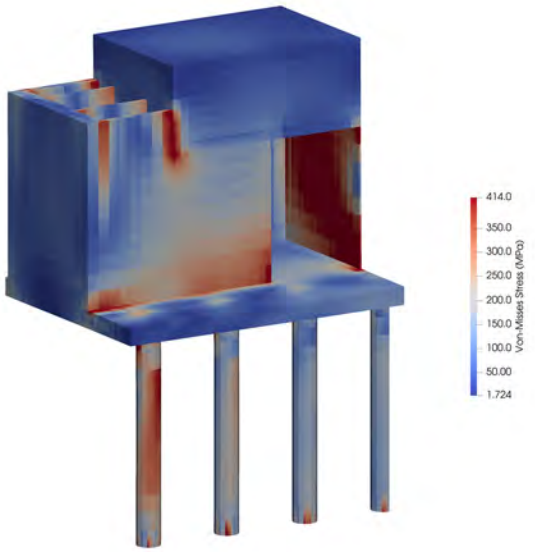

Figure 76. von Mises stress distribution within the support block showing no yielding of the anchors at a peak horizontal load of 3.26 MN without applied vertical loads.

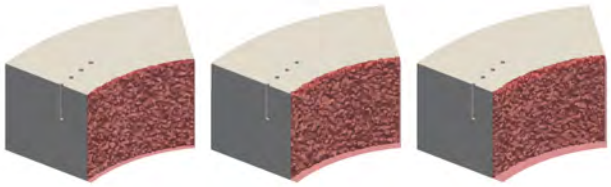

Figure 77. LDPM model geometry showing the removed elements (opaque red) to represent damage depths of 10 cm (left), 15 cm (middle), and 20 cm (right).

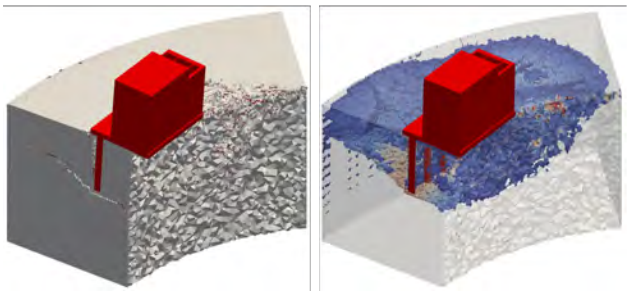

Figure 78. CBS wedge with 20 cm damage depth showing crack traces on the surface (left) and interior crack surface (right) at a peak horizontal load of 2.06 MN without applied vertical loads.

level and extends 114.3 cm (3.75 ft) below the bottom of the support block (53.34 cm or 1.75 ft below the tips of the anchors). The cooling pipe is also considered in the model. The support block and anchors are colored red, and the remaining volume of the simulated CBS wedge is colored blue.

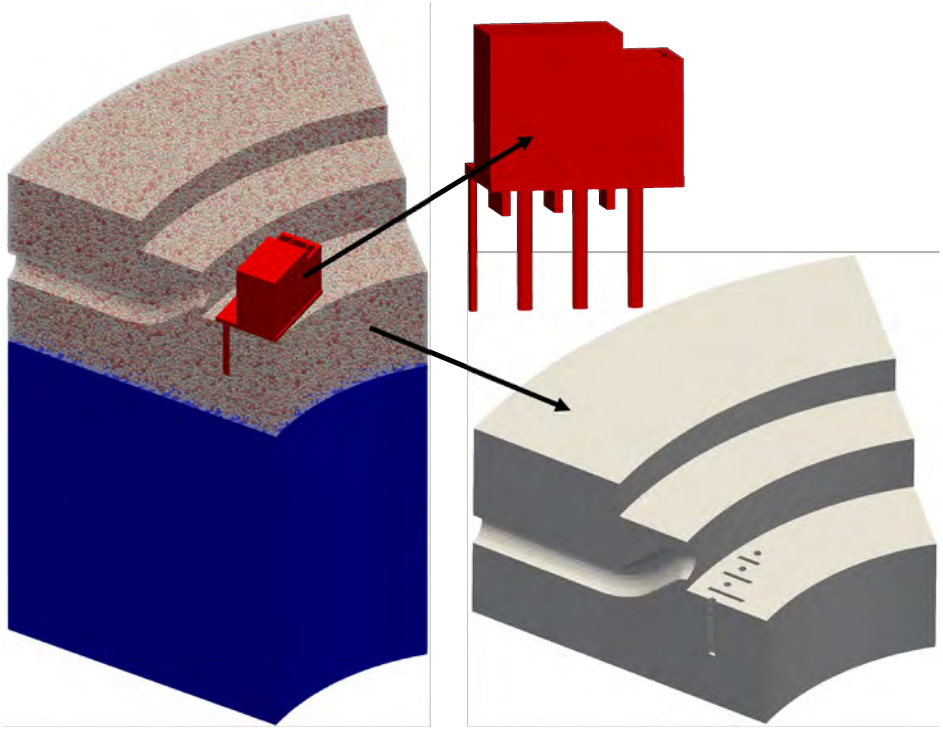

Figure 79. A 45° wedge model of the CBS for simulating the reinforced concrete cases showing LDPM (opaque gray) with internal aggregate, along with the support block (red) and the surrounding elastic concrete (blue).

Reinforcement details are shown in Figure 80 showing a top view and two radial planes that show the full depth and filling stirrups. The stirrup planes alternate at 1.5° apart radially. Based on the dominant rebar size in the drawing (#18 with 28.665 mm diameter) the reinforcement ratio ρ_s in the horizontal direction and the vertical direction below the support block is 1.6% which is a very reasonable value. In the following simulations, ρ_s = 0.8% is also considered to evaluate the effect of reinforcement ratio on load carrying capacity.

By studying the push-over analysis results of the pristine reinforced concrete case, the first observation is that any reinforcement increases the horizontal load capacity as expected. This means that the support block and its anchors would be exposed to higher loads. Again, simulating the support block using elastic constitutive laws allowed for studying the failure modes beyond the support block itself. This exercise is important in determining the ultimate failure mechanism as well as in providing an understanding of how to enhance and strengthen the system. Nevertheless, by monitoring the block anchors von Mises stress, the peak capacity for anchor yielding failure can be determined.

It is important to mention here that the failure occurs gradually, and the different modes engage at different levels of loading. Figure 81 shows the different stages of failure observed under horizontal push-over loading for the pristine case (no irradiation damage) with ρ_s = 1.6%. First, the concrete behind the anchors and shear lugs cracks, along with the concrete below the base plate. Limiting the maximum crack opening to 100 μm (crack openings visible to the naked eye), the first visible crack occurs only

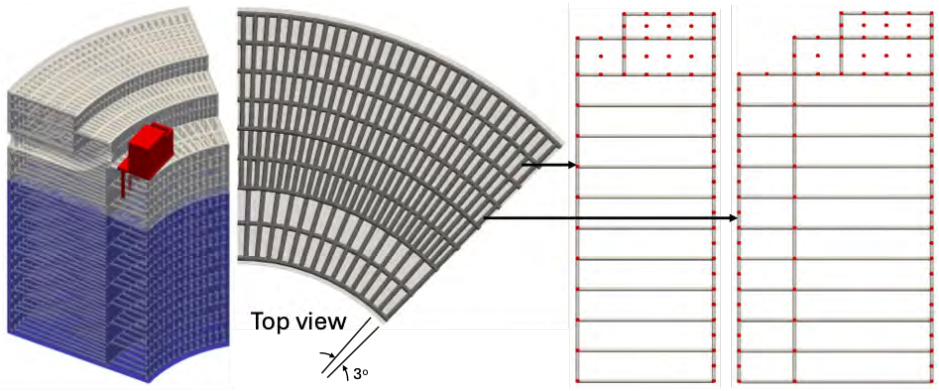

Figure 80. Details of the reinforcement used in the 45° wedge model of the CBS for simulating the reinforced concrete cases showing the alternating reinforcing stirrups (gray) and locations of radial rebar (red).

at 0.64 MN. Although this is not a critical case, it ultimately leads to the failure of stirrups that bridge the crack, just as the assumption in analytical analysis states. Next, the center anchor yields at 2.08 MN (Figure 81a). Note that this load is lower than the peak load of the plain concrete case because the increased confinement of the reinforcement forces the anchor to transfer more load at less horizontal force. At 3.68 MN of horizontal force, the outermost anchor also starts to yield (Figure 81b). The third anchor from the edge (second from the center) yields at 4.48 MN (Figure 81c). Next, the ultimate failure mode—stirrup yielding—initiates, which occurs at 8.32 MN (Figure 81d). Note that at this point the concrete cracks are much more developed, with crack openings up to 2.22 mm. (Figure 81e) shows the details of concrete cracked surface colored between 0.1 mm up to 1 mm, so all cracks in red are larger than 1 mm. The observed cracks represent a combination of pry-out failure (the large crack that forms under the anchors tip) and anchor cone failure (the cracks initiating above the pry-out crack). The reason for both modes initiating at the same time is the ability of reinforcement to confine concrete, allowing for different localized and global modes of failure to initiate within the concrete around the rebar. Note also that some small cracks started to form at the tip of the support block on the innermost surface of the CBS, indicating the initiation of concrete crushing. Continuation of the push-over analysis beyond this point provides a prediction of the progressive collapse, but based on the standard definition of failure limit states, no further load carrying capacity increase should be considered because the onset of reinforcement yielding should be the ultimate limit of strength. However, it is acknowledged that the structure will have additional bearing capacity as more stirrups will start to engage and yield as the load continues to increase but at the expense of excessive deformation and cracking. For example, continuing up to 13 MN as shown in (Figure 81f), a much more pronounced pry-out surface can be observed, and it can be seen that more concrete crushing is occurring under the tip of the plate. This crushing is a contributing factor to the reduction in the horizontal load carrying capacity for the irradiated cases. The reason that the structure is still carrying loads here is because of the progressive yielding of the stirrups at the support block area. This represents a significant difference between the analytical simplified solution and the detailed modeling. In the analytical solution, the capacity is based on assuming that all stirrups crossing the formed concrete crack are yielding, which would give an unrealistic load capacity. In the detailed model here, stirrups closer to the center of the block yield first. Nevertheless, in both cases, a significant concrete cracking is observed in both Figure 81e and f.

In order to simulate irradiation effects, the same procedure was followed: to remove the concrete thickness corresponding to the damage depth. Because the concrete cover is 75 mm (3 in.), it is important to

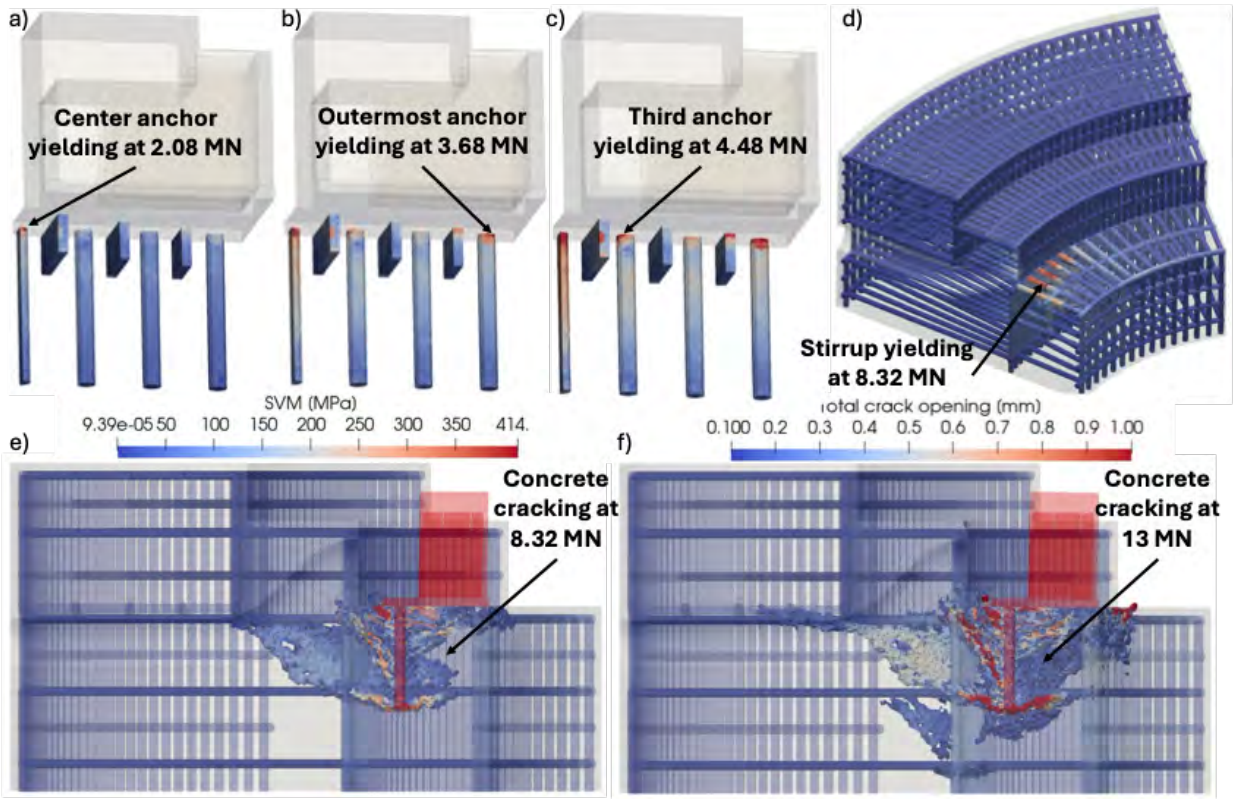

Figure 81. LDPM simulation of the progressive failure of the shoe support under horizontal loads only with ρ_s = 1.6% without irradiation damage.

investigate the effect of a concrete damage thickness that is smaller than the cover. Therefore, for the reinforced concrete cases, irradiation depths considered were 5 cm, 10 cm, 15, cm, and 20 cm, as shown in Figure 82. As shown in the figure, removing 5 cm still maintains rebar inside concrete; however, for all cases above 5 cm, the rebar is exposed.

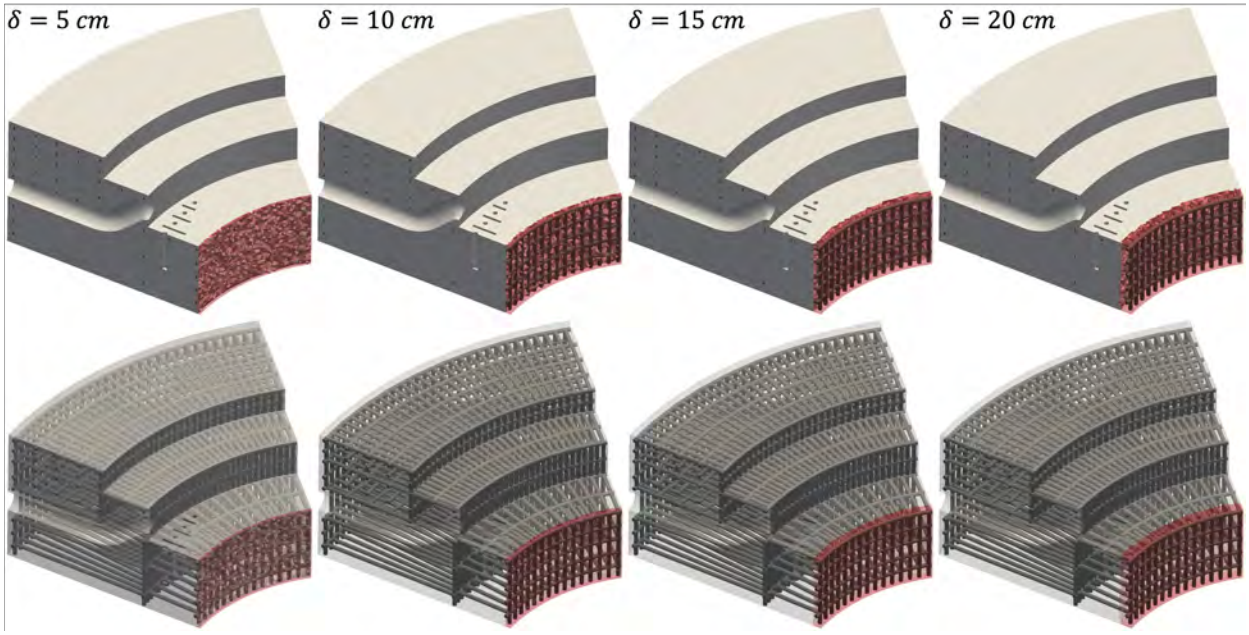

Figure 82. LDPM model geometry showing the removed elements (opaque red) to represent damage depths of 5 cm, 10 cm, 15 cm, and 20 cm.

Cracking for each damage depth and $\rho_s = 1.6\%$ is shown in Figure 83. It can be concluded from the figures that the mode of failure is the same, a combined anchor cone failure with pry-out. For all cases, one can still see concrete crushing at the edge of the plate too but this is less pronounced. Nevertheless, irradiation-induced damage that resulted in shortening the concrete under the base plate of the support block obviously contributes to the reduction of the lever arm between the compression zone under the base plate and the tension in the anchors resulting in more loads on the stirrups. The effects of irradiation are not small since the capacity was reduced to 6.56 MN down from 8.32 MN which is a 21% reduction. The horizontal load capacity for each case is listed in the fifth column of Table 9.

Additionally, to further investigate reinforcement effects, the same simulations of the damage depth were performed for $\rho_s = 0.8\%$, which represents a minimum reinforcement case. Similarly, here, the observed mode of failure is the same combination, but because less reinforcement ratio is simulated, stirrups yield at a lower load across all damage depths. Thus, the horizontal load carrying capacity is lower at each case, as listed in the third column of Table 9.

5.4.2.3 Push-Over Analysis under Vertical and Horizontal Loads

Plain Concrete Analysis

Here, a vertical load of 5.0 MN representing the vertical reaction of the RPV is first applied to the top of the support block. Then, a monotonically increasing horizontal load is applied to the top of the support block in a manner similar to that applied in the case without vertical loads. The failure surface is similar to the previous case, showing a combination of pry-out and concrete edge failure where the anchors form a concrete cone that initiates a crack surface starting at the anchor tip and propagating to the surface. The

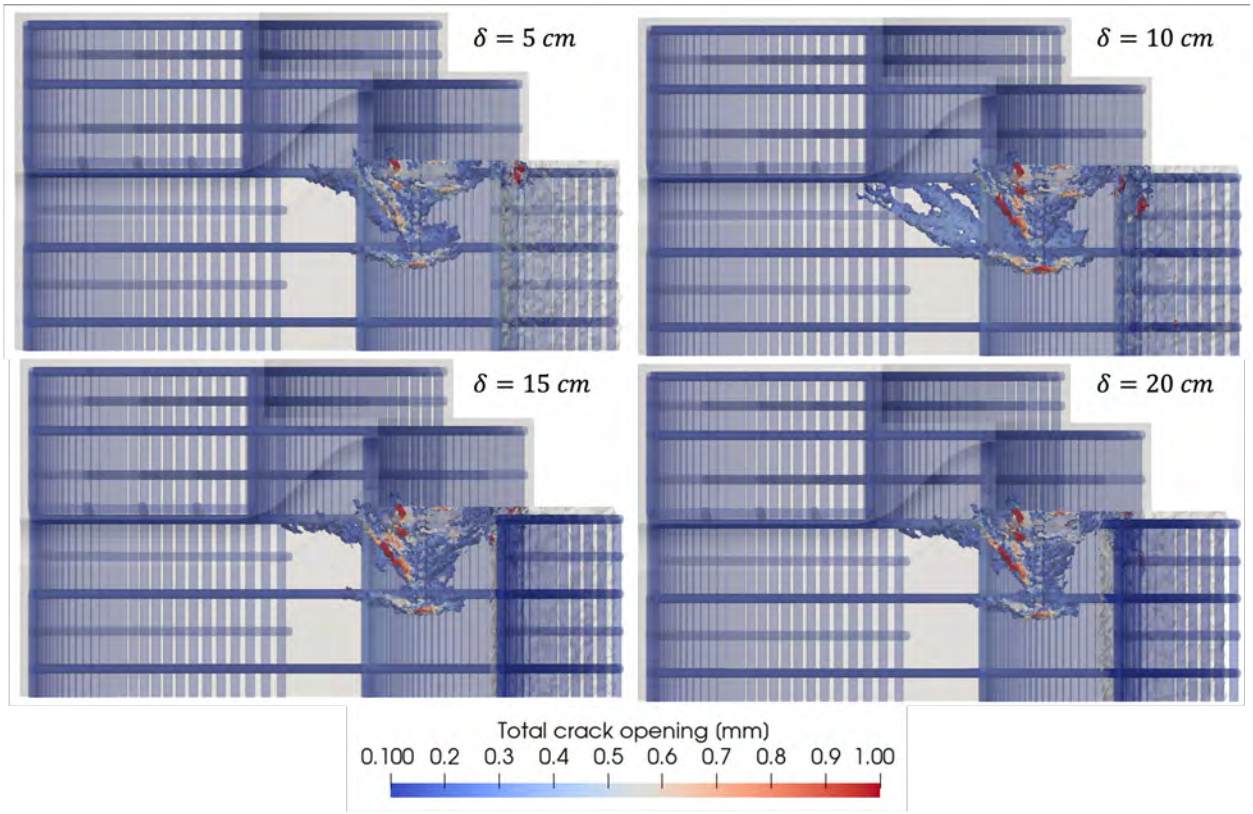

Figure 83. Cracking pattern at the onset of stirrups yielding for damage depths of 5 cm, 10 cm, 15 cm, and 20 cm.

main difference here is that the presence of an additional vertical load increases the compression zone under the support block and also increases the concrete's internal friction. This is why the simulations show a higher peak load capacity of 4.25 MN as compared to 3.26 MN without vertical loads. The increase of horizontal load capacity can be understood by observing that the compression from the edge of the support block (increased by the combination of bending and vertical loads on the interior edge of the CBS) increases friction along the crack which in turn propagates nearly horizontally under the block zone. At this peak load, Figure 84 shows the system colored according to the displacement magnitude, Figure 85 shows crack traces on the wedge surface, and Figure 86 shows the formed internal crack surface. These figures show that the additional compressive force prevented the horizontal crack that initiated at the anchor tip from fully propagating to the internal CBS surface. Instead, an additional vertical crack propagated also at the anchors' tips. This is because the support block is attached better to the concrete block beneath it, and the blocks tend to move together.

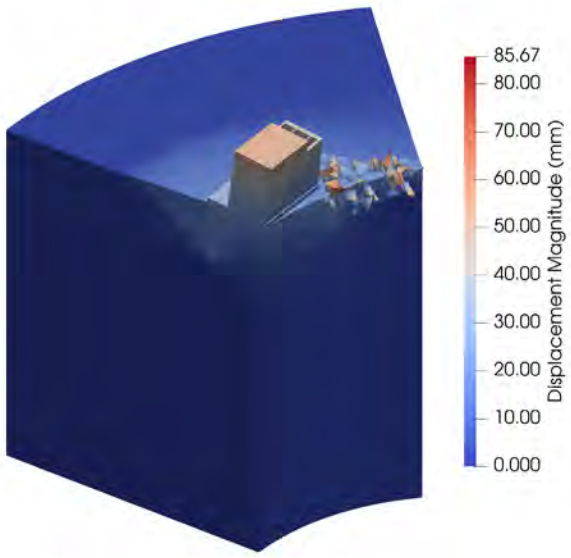

Figure 84. CBS wedge displacement at a peak horizontal load of 4.25 MN with applied vertical loads.

The effects of irradiation were simulated in a similar manner by removing the innermost LDPM elements, and the results show similar trends in terms of preventing the propagation of a horizontal crack beneath the support block and initiating a vertical crack at the tips of the anchors. Figure 87 shows surface and interior cracks for the 20 cm damage depth case under vertical loads, thus illustrating the observed cracking trends. Note that crushing under the support block can be observed. However, the compression-induced vertical crack suggests that an extended concrete volume participated in resisting the lateral loads, which explains the higher horizontal load capacity of 2.61 MN compared to 2.06 MN for the same damage depth without vertical loads. The horizontal peak load capacities for all push-over cases with applied vertical loads are presented in the second column of Table 9.

Reinforced concrete analysis

The presence of vertical loads with reinforcement is more complex than the case without reinforcement. Figure 88 shows the horizontal load capacity for plain concrete and reinforced concrete with both ρ_s = 0.8% and ρ_s = 1.6% with and without vertical loads. While it is obvious that vertical loads increase the

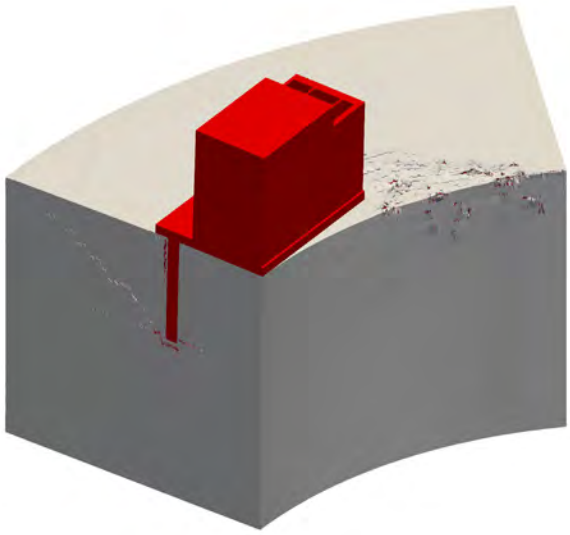

Figure 85. CBS wedge crack traces on the surface at a peak horizontal load of 4.25 MN with applied vertical loads.

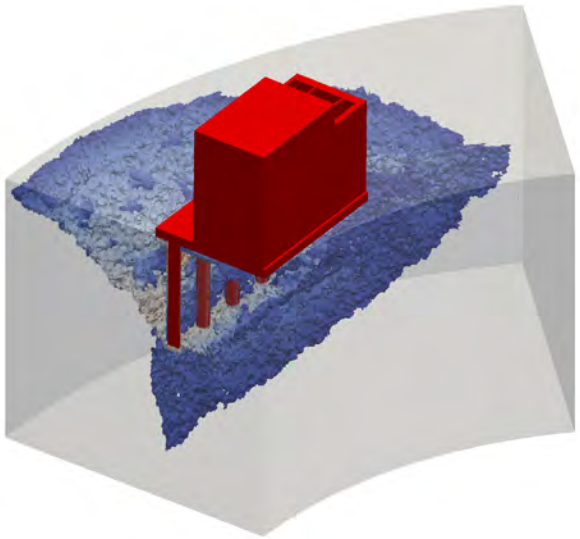

Figure 86. CBS wedge crack surface at a peak horizontal load of 4.25 MN with applied vertical loads.

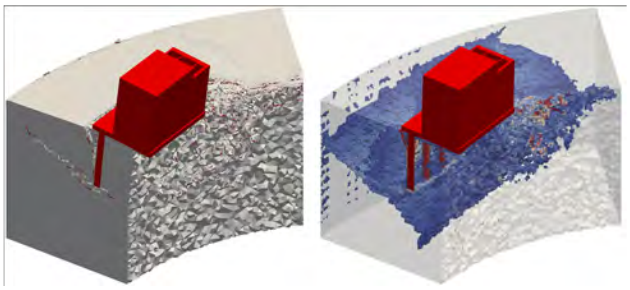

Figure 87. CBS wedge with 20 cm damage depth showing crack traces on the surface (left) and interior crack surface (right) at a peak horizontal load of 2.61 MN with applied vertical loads.

capacity in the plain concrete case, such an increase is less pronounced for the reinforced concrete cases with no irradiation damage or small damage (5 cm). For example, in the pristine case before irradiation and with ρ_s = 1.6%, the capacity increased from 8.32 MN without vertical loads to 8.64 MN with vertical loads, which is an increase of only 3.4%. However, for the 20 cm damage depth case, the capacity decreased from 6.56 MN to 6.08 MN, which is a reduction of 7.3%.

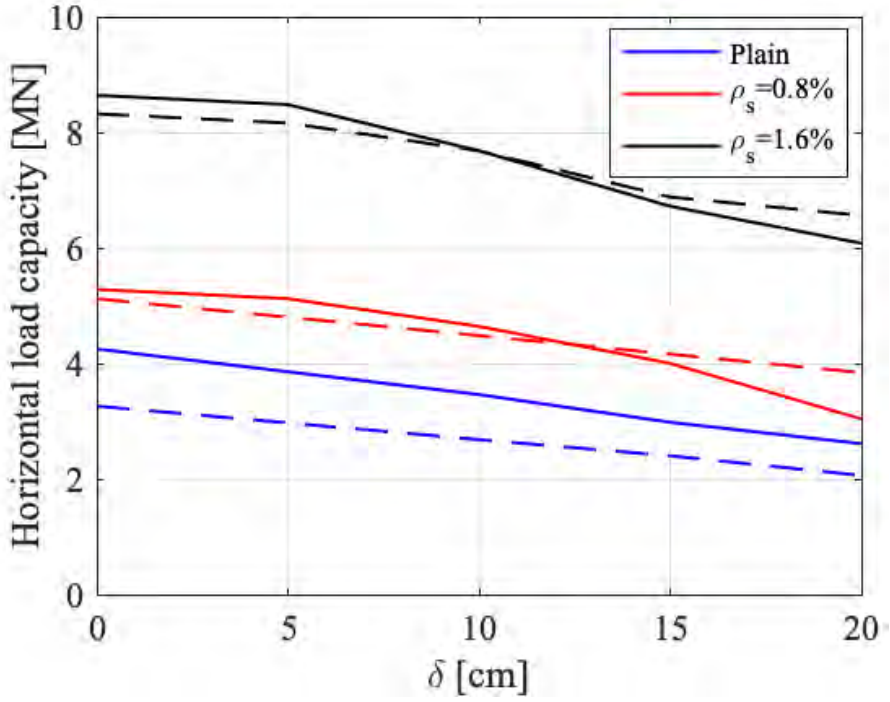

Figure 88. LDPM simulated evolution of horizontal load capacity with the irradiation-induced damage depth

This trend can be explained by the fact that vertical loads contribute to increasing compressive stresses at the edge of the support block base plate. Since degradation due to irradiation renders a specific depth of concrete nearly fully damaged, the concrete crushing failure mode becomes more pronounced. However, full crushing does not appear to occur before stirrups yield, and only partial crushing occurs. This can be observed in Figure 89, where the concrete cracking under the support block is shown for the 20 cm damage depth case and ρ_s = 1.6% with and without vertical loads at the onset of stirrups yielding for both cases. One can see that vertical loads result in more cracking at the concrete edge.

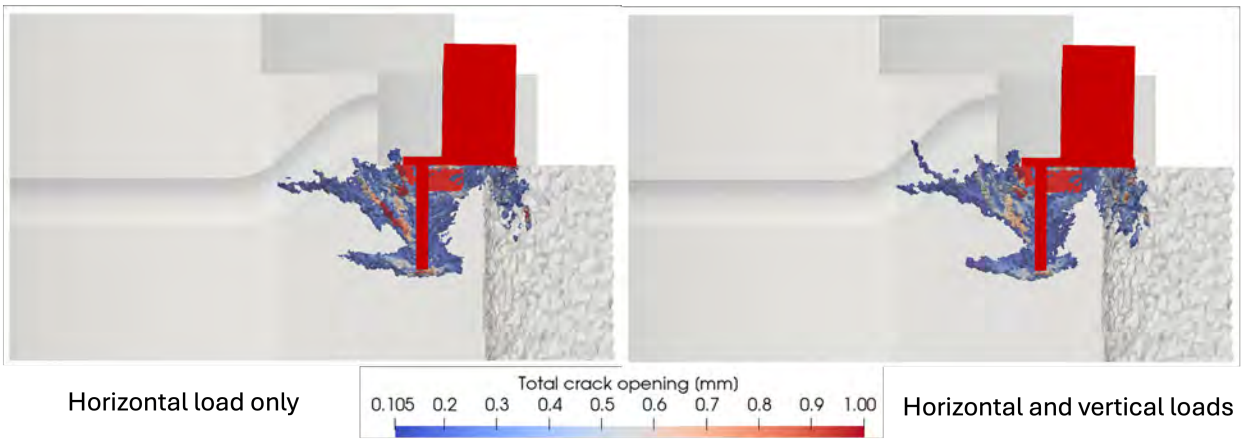

Figure 89. LDPM-simulated cracking under the support block for δ = 20 cm and ρ = 1.6% at the onset of stirrup yielding.

The same trend was also observed for ρ_s =0.8%. The horizontal load capacity corresponding to each damage depth under vertical loads for both ρ_s =0.8% and 1.6% is listed in the fourth and sixth columns of Table 9, respectively.

Table 9. Results of the LDPM simulations. Horizontal load capacity with increasing irradiation-induced damage depth

	Plain Concrete		Reinforced Concrete ρ_s=0.8%		Reinforced Concrete ρ_s=1.6%	
Damage depth (cm)	$\bar{H}(V=0)$ (MN)	$\bar{H}(V>0)$ (MN)	$\bar{H}(V=0)$ (MN)	$\bar{H}(V>0)$ (MN)	$\bar{H}(V=0)$ (MN)	$\bar{H}(V>0)$ (MN)
0	3.26	4.25	5.12	5.28	8.32	8.64
5	—	—	4.80	5.12	8.16	8.48
10	2.68	3.46	4.48	4.64	7.68	7.68
15	2.40	2.98	4.16	4.00	6.88	6.72
20	2.06	2.61	3.84	3.04	6.56	6.08

5.4.2.4 Consideration of higher concrete strength

It is expected that concrete in the CBS, especially from its inner surface, would have an increased strength due to the exposure to moderately high temperatures (55°C to 65°C). Such an increase may increase the horizontal load capacity of the support block. This was done by calibrating LDPM parameters to achieve f_c'=50 MPa following the same procedure described before. Note here that assuming such a high compressive strength is arbitrary to investigate the corresponding increase in capacity. For this purpose, simulations were performed using ρ_s = 1.6% and with vertical loads. The yield started at 9.28 MN. Comparing this with the same case but with f_c'=30 MPa (8.64 MN capacity), only an increase of 7.4% is observed in the horizontal load capacity, although the concrete strength increased by 67%. Very similar failure and cracking patterns can also be observed, as shown in Figure 90. It was expected that increasing the concrete strength is very unlikely to have a large impact because the observed mode of failure was mainly stirrup yielding, not concrete crushing.

5.4.3 Observations and Limitations of the Numerical Simulations

These numerical simulations using the LDPM provide important insights into the possible complex interactions between the support block and the CBS. For the plain concrete cases, when compared to

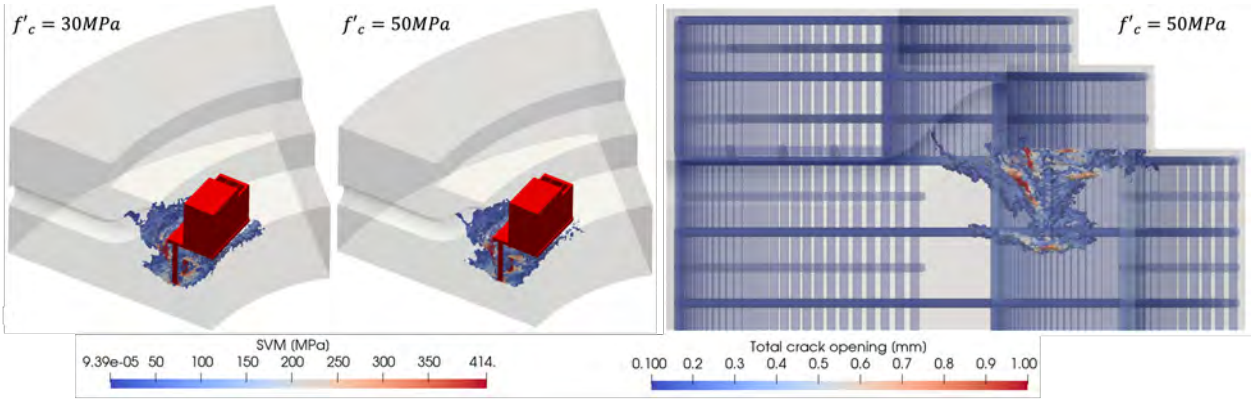

Figure 90. Comparison between crack pattern at the onset of stirrups yielding for f'_c = 30 MPa and 50 MPa.

analytical postulated failure modes, it was shown that ultimate failure is initiated by pry-out, followed by crack propagation from the tip of the anchor group. This crack propagation is nearly horizontal and reaches the inner surface of the CBS when no vertical loads are applied. When vertical loads representing the RPV vertical reaction are applied, the propagating crack becomes vertical initially, and then it branches as a result of the high compression under the support block. It is important to note that the wedge analysis with proper boundary conditions allowed for capturing the CBS ring action effects on the propagation of cracks on the sides of the support block, thus causing their surfaces to follow a curved path rather than a straight path at an angle, as had been assumed in the analytical solutions. Furthermore, for the reinforced concrete cases, details of the progression of failure were captured and show that cracking first initiates behind the support block and within the grout below its base plate. This is followed by progressive yielding of the anchors. While this is a limiting case, analysis continued (assuming that more proper anchorage could be used) to investigate the effect of irradiation of the reinforced concrete around the support block anchorage. At higher loads, stirrups crossing the formed cracks start to yield. A combination of anchor cone failure and pry-out cracking could be observed at the onset of stirrups yielding. As opposed to the analytical solution, stirrup yielding occurs gradually—meaning that not all stirrups yield at the same load. It was also shown that the vertical load will not always cause an increase in horizontal load capacity at high enough degradation due to irradiation. Finally, an investigation of the possible benefits of moderate thermal exposure of the CBS concrete by simply using a significantly higher concrete strength (50 MPa as compared to 30 MPa). The results showed a limited increase in horizontal load capacity, which was consistent with the conclusion that failure is mainly dependent on stirrups yielding—not concrete crushing. These observations show the benefits and depth of understanding that could be obtained when such high-fidelity modeling is used.

However, it must be noted that simplifying assumptions of the model and limited details about the reinforcement and the support block may lead to some differences compared to the actual system capacity. Nevertheless, it is expected that the results shown here are very well representative of the general trends of failure and are also representative of realistic reinforcement and concrete details.

5.4.4 Summary of Results

The bearing capacity of a shoe-type nozzle support system was studied, and various failure modes of plain and reinforced concrete were considered. Figure 91 summarizes the results of the analytical calculations and simulation results obtained with the LDPM for different failure modes, including plain concrete crushing, plain or reinforced concrete wedge failure, and pry-out failure (white diamonds indicate damage

without considering the vertical load, and black diamonds indicate damage considering the vertical load) as well as stirrups yielding failure for ρ_s = 0.8% and 1.6%. The red lines correspond to the jet thrust force obtained using RELAP5-3D for a full break area (1A) or a partial break area (0.5A, i.e., at 50% of the total).

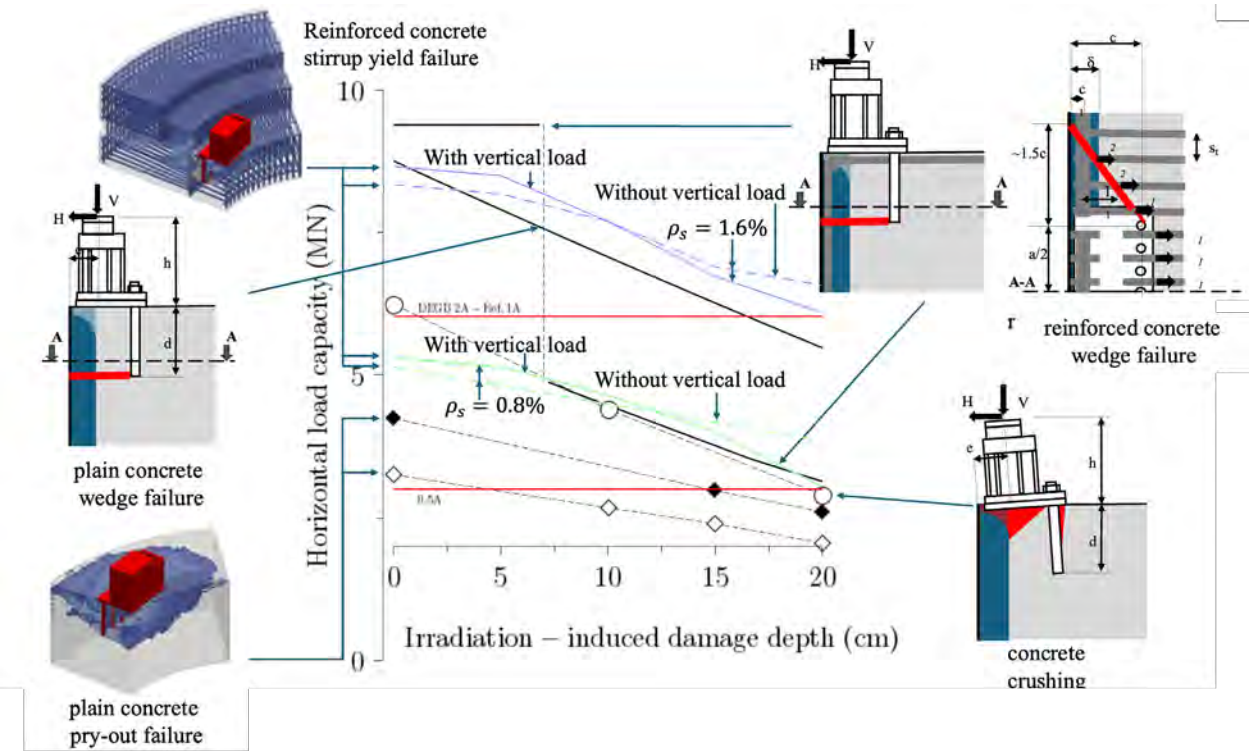

Figure 91. Evolution of the horizontal load capacity with the irradiation-induced damage depth.

The horizontal load applied to the support system depends on the actual break area, the dynamic response of the reactor system during the LOCA, and specific design details of the support system that permit relative free deformation of the nozzle. The jet thrust–induced horizontal load of approximately 6 MN at full break is considered an upper bound value. Assuming this value as the design accidental load, the structural safety margin of the unirradiated concrete is minimal for the crushing concrete mode. The presence of reinforcement (e.g., stirrups not considered in the crushing failure analytical mode) provides additional concrete confinement and resistance, thus improving the bearing capacity of the edge concrete.

The bearing capacity obtained by the LDPM, assuming plain concrete during the pry-out failure mode, is lower than that of the LOCA design load. The presence of reinforcement significantly improved the overall bearing capacity. However, it is still close to the LOCA design load.

The effects of irradiation were considered, assuming a uniform damage depth with elevation. This hypothesis is conservative. Figure 92 shows the fast neutron flux profile with height that was obtained by Remec [14] using the irradiation transport code MCNP and the corresponding irradiation-induced damage depth obtained using the 1D-SAM presented in Section 4. The profile of irradiation-induced damage depths exhibits a sharp change above approximately 1.5 m from the fuel core mid-elevation. Based on data provided in NUREG/CR-7280 [22], the blue-shaded area in Figure 84 indicates the estimated range of elevations of the support system for varied designs. Each configuration is specific to the geometry of the reactor cavity. Hence, it is conservative to assume a uniform damage depth in the concrete region bordering the cavity below the support system. With increasing damage depth, the bearing capacity of the

concrete gradually decreases for all failure modes except the analytical wedge failure mode of reinforced concrete. In this case, once the damage depth reaches the reinforcement, the hook bond resistance is considered lost; hence, a sudden drop in bearing capacity is observed. However, the bearing capacity of plain concrete mitigates this effect, ensuring sufficient bearing capacity. When compared with the detailed LDPM simulations, accurate accounting of bond losses is achieved, and, thus, a gradual change still exists. The loss of load capacity caused by irradiation-induced damage may be the limiting factor for such a support system design.

Whereas previous studies show that the irradiation-induced damage marginally affected the over-designed bearing capacity of the CBS, the coefficient of structural safety of the studied structural support system appears to be limited. The next section of this report utilizes these data and fully investigates the reliability of the system under different load combinations.

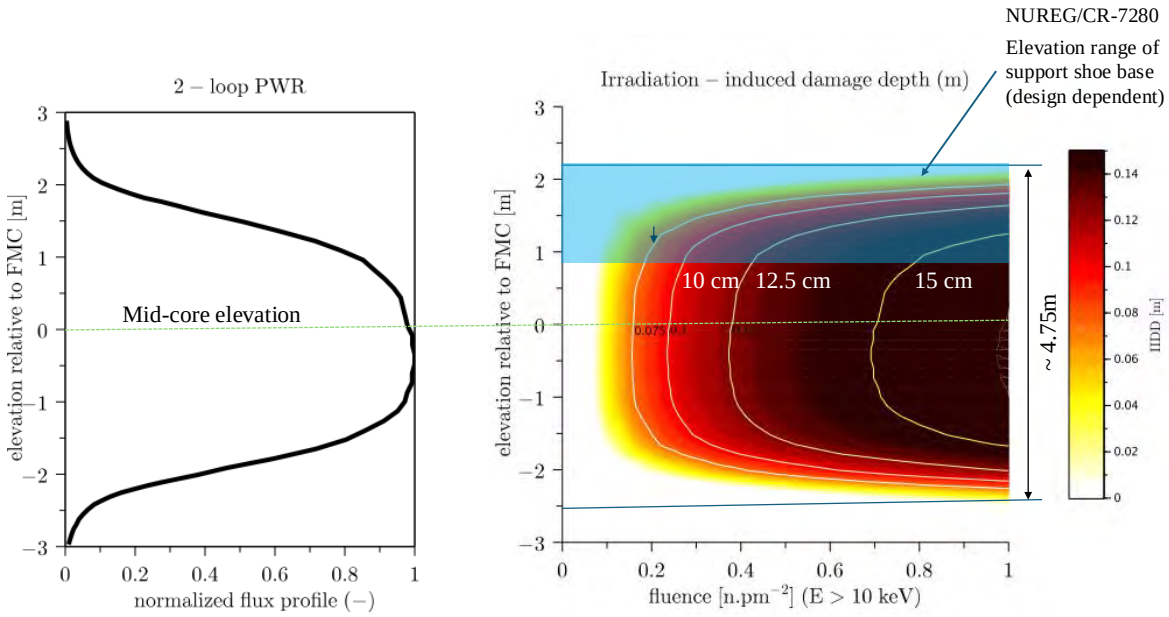

Figure 92. Fast neutron flux profile and irradiation-induced damage estimates with elevation.

The key findings and observations are summarized below.

1. **Loading Conditions**: The most demanding loading scenarios arise from the combination of large-break LOCA and safe shutdown earthquake (SSE) conditions. Time-dependent force data from Cloud [16] and methodology from WCAP-8082 [79] were used to estimate peak support reactions. Vertical loads up to 13 MN and horizontal forces exceeding 12 MN were observed at various support locations, depending on rupture direction and rocking behavior.
2. **Edge Breakout and Shear Failure**: The concrete edge breakout mechanism was characterized using a simplified shear-prism model [19] and was estimated to have a capacity of approximately 8.75 MN in plain concrete under horizontal loading. Simulations confirmed that shear failure planes initiate at anchor tips and propagate toward the edge, forming a breakout cone.
3. **Hook Anchorage and Bond Strength Degradation**: Irradiation-induced degradation of concrete adjacent to the anchors leads to loss of effective bond length and hook engagement. When the

damage depth exceeds the hook embedment, up to 40% of anchorage capacity may be lost. Partial damage depths of 10–20 cm reduce bond capacity by 8–35%, findings that are consistent with data in Biwer et al. [22] and Sharma et al. [19].

4. **Concrete Crushing in Flexure**: Horizontal loading on the shoe interface induces bending moments that produce toe crushing beneath the baseplate. The resulting moment capacity, estimated by $\bar{M}_r = 0.8\Psi f_c b x \left(c' - \frac{x}{2}\right)$, is sensitive to the compressive strength and irradiated depth of concrete. If the irradiation-affected layer overlaps the compressive zone, the crushing resistance is significantly reduced (Figure 70).

5. **Push-over Simulations**: LDPM push-over simulations captured the full response of the shoe–concrete system under increasing horizontal load, both with and without vertical preload. For the plain concrete case, results showed a peak load of 3.26 MN for horizontal-only loading, with slightly higher capacity and delayed failure when vertical confinement was included. Figure 73 and Figure 74 illustrate the displacement and crack propagation patterns. For the reinforced concrete case, a peak horizontal load corresponding to the initiation of yield in stirrups is 8.32 MN at $\rho_s = 1.6\%$. The presence of vertical preload increases this value slightly to 8.64 MN. However, for the irradiated cases, the presence of vertical preload eventually reduces the horizontal load capacity, as shown in Figure 88. It was observed that a gradual failure emerges where concrete behind the support block anchors crack first, then the support block anchors yield, and finally the stirrups bridging the cracked concrete yield one by one with the formation of anchor cone cracking failure and a pry-out crack failure as shown in Figure 81. Additionally, increasing f_c' from 30 MPa to 50 MPa did not cause a significant increase in the horizontal load capacity.

6. **Design Implications**: The analyses suggest that anchorage systems in irradiated concrete require careful evaluation of bond degradation, crushing, and edge breakout. Where anchors are embedded close to the beltline of the RPV, long-term radiation exposure can severely affect load transfer mechanisms. Anchors located deeper in the bioshield, or reinforced with confinement bars, may retain higher capacity.

7. **Modeling Considerations**: The lattice particle modeling approach used here allows for localized damage tracking, including crack path evolution and stress redistribution. The model was calibrated using standard cylinder tests (Figure 71) and validated against expected concrete behavior under flexural and shear loading.

Overall, the study demonstrates that radiation exposure, combined with dynamic and thermal loads, can lead to complex failure modes in RPV support systems. Figure 67 summarizes the primary failure mechanisms observed. Future evaluations should incorporate detailed fluence mapping, site-specific geometry, and experimental validation of radiation-modified material properties.

Where possible, mitigation measures should include the following:

- Strengthening of the shoe support above the concrete based on full 3D analysis rather than simplified analysis to account for stress concentrations.
- Use of a ring beam to connect individual shoe supports
- Use of tie backs with anchors in the concrete behind the shoe support to bypass the irradiated concrete zone
- Periodic inspection of support systems in high-dose regions

For new constructions the design of the shoe support should include the following:

- Use of tie-backs or a ring beam to distribute the load on the CBS.
- Deep embedment of anchors.
- Use of confinement reinforcement with special additional reinforcement around the shoe.
- Full shoe redesign with detailed 3D analysis under vertical and lateral loading.

These observations are relevant for both the assessment of existing reactors and the design of next-generation support systems exposed to prolonged irradiation environments.

6. PROBABILISTIC PERFORMANCE EVALUATION UNDER ACCIDENTAL LOADING

6.1 UNIFIED PROBABILISTIC FRAMEWORK

The performance of safety-related structures in nuclear power plants must be assessed with a rigor that is commensurate with the potential consequences of failure. Traditional deterministic design methods, while effective for ensuring conservative safety margins, provide limited insight into the actual probability of failure or the influence of uncertainty. A probabilistic framework addresses this gap by explicitly modeling the variability of both capacity (resistance) and demand (loads) and by quantifying the likelihood of structural limit states being exceeded.

For critical components such as the CBS and RPV supports, the distinction between resistance and applied loading forms the foundation of structural reliability assessment. By treating capacity and demand as random variables, a limit state function can be defined that separates safe from failed conditions. The probability of failure derived from this formulation provides an objective measure of reliability under different hazard scenarios.

This section outlines the theoretical basis and implementation of the probabilistic methodology. First, the roles of capacity and demand in structural reliability are clarified, along with the definition of limit states and the formal expression of failure probability. The reliability analysis procedure is then presented in a step-by-step manner, from limit state definition through uncertainty propagation and reliability index calculation. The treatment of uncertainty, including the use of LHS for efficient simulation, is described in detail. Finally, the computational models used to represent structural capacity (via LDPM simulations) and loading demands (via RELAP5 thermal hydraulic analyses and seismic code spectra) are discussed, together with the performance metrics extracted from the analysis.

This framework combines advanced physical modeling with probabilistic simulation to provide a transparent and quantitative measure of safety for CBS and RPV supports under LOCA, seismic, and combined LOCA–seismic events. The following subsections develop this methodology in detail.

6.1.1 Capacity vs. Demand in Structural Reliability

A fundamental concept in structural reliability is the distinction between capacity (or resistance) and demand (or load effect). The safety of a structure can be assessed by comparing random capacity R to random demand L, typically via a limit state function $g(\mathbf{X})$ that defines the boundary between safe and failed states [95]. For a component such as the CBS or an RPV support, an ultimate limit state can be defined as $g = R - L$, where R is the structural capacity (e.g., peak strength) and L is the applied load effect (e.g., LOCA or seismic force). Failure occurs when $g \leq 0$ (i.e., when demand exceeds capacity). The probability of failure is then $P_f = P[g(\mathbf{X}) \leq 0]$ [95]. In the simplified case $g = R - L$, this reduces to $P_f = P(R \leq L)$, the probability that the load demand surpasses the resistance capacity [95]. This formulation underpins reliability analysis and emphasizes that both R and L are treated as random variables with inherent uncertainties [95]. A clear definition of the limit state of interest (e.g., gross failure of the support or exceedance of a deformation limit) is crucial, as it delineates the boundary between acceptable (safe) and unacceptable (failed) performance. Each limit state will have an associated P_f that quantifies the risk of failure under the given loads.

6.1.2 Probability of Failure and Limit States

The probability of failure P_f is formally defined as an integral of the joint probability density of all basic variables over the failure domain. In general,

$$P_f = \int_{g(\mathbf{x})\leq 0} f_{\mathbf{X}}(\mathbf{x})\, d\mathbf{x}, \tag{18}$$

where $\mathbf{X}$ is the vector of all uncertain inputs (material strengths, loads, etc.) and $f_{\mathbf{X}}$ is their joint probability density function (PDF) [95]. When $g(\mathbf{X}) \leq 0$ defines failure, P_f represents the likelihood that the capacity-demand limit state is violated. The notion of a limit state is central: it represents a condition beyond which the structure no longer meets a specified performance criterion (e.g., collapse, loss of support function, excessive deformation). Ultimate limit states correspond to collapse or loss of load-carrying capacity, while serviceability limit states correspond to functionality or usability thresholds [95]. In this study, the main focus is the ultimate limit states for the CBS and RPV supports under extreme loading (i.e., LOCA and seismic excitation), and failure is defined as the incapacity of the support to carry the required loads. Thus, P_f for each support under each loading scenario (LOCA, seismic, or combined) can be obtained once R and L are characterized probabilistically.

6.1.3 Reliability Analysis Procedure

A structured, step-by-step reliability analysis procedure that is consistent with established guidelines was adopted herein. The procedure is as follows:

1. **Define Limit States**
   Identify the relevant limit state function $g(\mathbf{X})$ for each failure mode. For example, for gross failure of a support, $g = R - L$ where R is the support's strength (capacity) and L is the applied load effect. Distinct limit states may be considered for different failure modes (e.g., shear failure of concrete, anchor pull-out), but here the focus is on global support failure.

2. **Select Time Frame and Load Cases**
   Specify the design or evaluation scenario (e.g., single-event failure during LOCA or seismic event). In this work, three loading cases are considered: a design-basis LOCA event, a design-basis seismic event, and the combined occurrence of LOCA concurrent with the seismic event. Each case involves a different combination of demands acting on the supports. For the combined LOCA and seismic case, it can be conservatively assumed that the total demand $L_{\text{combined}} = L_{\text{LOCA}} + L_{\text{seismic}}$ acting simultaneously, consistent with a worst-case load combination [96].

3. **Identify Basic Random Variables and Distributions**
   List all uncertain input parameters that affect capacity or demand, and assign each a probabilistic model. These include material properties (e.g., concrete compressive strength, steel yield strength, etc.), geometric parameters (e.g., dimensions, clearances), and load parameters (e.g., peak LOCA pressure, seismic acceleration, etc.). For each variable, assign an appropriate probability distribution (e.g., normal, lognormal, etc.) with specified mean, variance, and any distribution truncation, if applicable. All analyses are performed with unfactored values (i.e., nominal strengths and loads without code safety factors) to realistically capture true behavior. Treatment of these uncertainties is discussed below.

4. **Propagate Uncertainties and Compute P_f**
   Use a probabilistic method (e.g., sampling or analytical) to evaluate the failure probability. In this case, MCS with LHS is employed to propagate uncertainties through the limit state. For each of N simulated realizations, a set of input parameters (R_i, L_i) are sampled from their joint distribution (using LHS for efficiency) and the limit state $g_i = R_i - L_i$ is evaluated. Then $P_f \approx \frac{1}{N} \sum_{i=1}^{N} I[g_i \leq 0]$ is estimated, where $I[\cdot]$ is the indicator of failure (1 if $g_i \leq 0$, else 0). This yields an estimate of the probability that capacity falls short of demand under the given scenario [95]. The simulation is continued until the estimate of P_f (and associated statistical error) is sufficiently stable.

5. **Calculate Reliability Index**
   Finally, compute the reliability index β, an alternative measure of safety defined as $\beta = -\Phi^{-1}(P_f)$ [97], where Φ^{-1} is the inverse standard normal cumulative distribution function (CDF). The index β

represents the number of standard deviations by which the mean safety margin exceeds zero in the case of a linear limit state with normal variables [95]. A larger β indicates a more reliable system. For small P_f, β is related one-to-one with P_f (e.g., $\beta \approx 3$ corresponds to $P_f \sim 0.0013$) [95]. This reliability index concept, first introduced by Cornell [97] and later generalized by Hasofer and Lind [98], provides a convenient single metric of safety that is independent of the particular units of R and L. The β values for each support under each load case are reported as a summary performance indicator alongside the direct probabilities of failure.

This structured approach is in line with recommendations by the Joint Committee on Structural Safety (JCSS) [95] and other reliability guidelines [99, 100]. It ensures that all important uncertainties are accounted for and that the results (e.g., failure probabilities and reliability indices) are computed in a traceable, repeatable manner.

6.1.4 Uncertainty Treatment and LHS

All inputs in the analysis are treated as random variables. Uncertainties in material strengths (e.g., concrete compressive strength f'_c, steel yield stress f_y), resistance model parameters (e.g., friction factors, anchorage capacity), and loads (e.g., peak LOCA pressure, jet thrust, seismic spectral accelerations at support frequencies, etc.) are accounted for in this approach. The choice of probability distributions and their parameters is informed by experimental data or code recommendations (e.g., concrete strength is often modeled as normal or lognormal with COV $\sim$ 10%, seismic spectral acceleration may be modeled via a lognormal distribution reflecting ground motion variability). LHS is applied to efficiently explore the multi-dimensional uncertainty space. LHS stratifies each variable's range into equiprobable intervals and ensures each interval is sampled exactly once, greatly reducing variance in the Monte Carlo estimates compared to simple random sampling for the same number of runs [101]. This is especially beneficial given the low failure probabilities of interest, which require many samples to estimate directly. By using LHS, faster convergence of P_f estimates is achieved; studies have shown LHS can save over 50% of computational effort relative to brute-force Monte Carlo for structural reliability problems [101]. In this analysis, N LHS samples are generated (e.g., typically on the order of 10^5 simulations to capture P_f levels around 10^{-3}–10^{-5} with reasonable accuracy). Each simulation involves computing the capacity and demands for one realization of the random inputs and checking the limit state. The use of variance-reduction techniques like LHS is important, given the computational expense of evaluating capacity via detailed models. Consistency checks are also conducted to ensure the LHS sample accurately reproduces each variable's marginal distribution and pairwise correlations, if any dependencies are modeled. Uncertainty propagation through this sampling yields not only estimates of P_f but also insight into the distribution of safety margins $g = R - L$ and identification of critical random variables via sensitivity analysis (e.g., using rank correlation between inputs and the failure indicator) [102]. All random variables are treated as statistically independent in this study, unless specific correlation is justified by physical reasoning; independence is a common and often conservative assumption in the absence of data, per JCSS guidelines [95].

6.1.5 Computational Modeling of Capacity and Demand

The probabilistic framework is supported by detailed computational models for both capacities (resistances) and demands (loads):

- **Structural Capacities via the LDPM**
  The load-carrying capacities of the CBS and RPV supports are determined using high-fidelity simulations based on the LDPM for concrete [80]. The LDPM is a mesoscale discrete modeling approach that explicitly simulates concrete's heterogeneous structure and can capture complex failure mechanisms such as cracking, crushing, and fragmenting under load [81]. By calibrating

the LDPM against material tests, realistic probabilistic capacity predictions are obtained. Material parameters (e.g., tensile strength, fracture energy, etc.) and geometric details are used as inputs into a LDPM non-linear analysis to compute the peak support strength R. In practice, a surrogate model or response surface would be fitted to LDPM simulation results to speed up the MCS, due to the LDPM's high computational cost. Within the analyses presented herein, the mean load-carrying capacity is taken directly from the LDPM; this mean resistance, an assumed coefficient of variation (COV), and a corresponding PDF were used herein to probabilistically characterize the resistance R. By using the LDPM, or similarly detailed FEA models, as the source of capacity data, a realistic representation of how the CBS and RPV supports would behave up to failure is incorporated, including non-linear effects, 3D stress states, and brittle or ductile failure modes [65]. This is a significant advancement beyond traditional deterministic design capacity, and it allows for the quantification of the uncertainty in capacity arising from material variability and model uncertainties.

- **LOCA Load Effects via RELAP5**
  Demands on the supports due to a postulated LOCA are obtained from system-level simulations using the RELAP5 thermal-hydraulic code. A large-break LOCA PWR scenario is modeled, including the rapid depressurization and fluid discharge following a primary pipe rupture. The code predicts time-histories of pressures and fluid forces inside the reactor cavity and containment. Of particular interest is the peak differential pressure across the CBS wall and the jet thrust on internal structures caused by the high-energy break. These pressures produce impulsive loads on the CBS and any attached supports. The RELAP5 simulations provide a distribution of LOCA loads; for example, the peak cavity pressure might have a mean of P_{LOCA} with some variability due to uncertainties in break size, blowdown rate, and modeling approximations. Jet impact forces on the RPV support structure, if the break jet impinges on it or nearby structures, are also characterized. A conservative approach is taken by using the enveloping peak loads from the RELAP5 analysis as the nominal demand, and then assigning uncertainty (e.g., $\sim \pm 10\%$) to represent variability in break location and assumptions. Notably, recent studies and leak-before-break provisions have reduced the magnitude of postulated LOCA loads in many designs, thereby eliminating extremely large pipe breaks from consideration [65]. For example, the older design-basis DEGB loads have been largely supplanted by smaller break scenarios with correspondingly lower pressure transients [65]. The load modeling reflects these updated insights: the LOCA pressure transient across the reactor cavity is sampled from a distribution truncated at a lower level than legacy design values, consistent with modern leak-before-break criteria that preclude the largest breaks [65]. This means the probabilistic LOCA demand on the CBS wall or supports is less severe, in probabilistic terms, than one might assume from past conservative design envelopes, which is a realistic refinement.

- **Seismic Demand via Code-Based Spectra**
  Seismic loads on the supports are determined using a combination of structural response analysis and code-based seismic criteria. In nuclear facilities, the SSE is the design-level seismic event, often with a return period on the order of 10^4 years. The site's design response spectrum (e.g., per US NRC Regulatory Guide 1.60 [52] or site-specific seismic hazard analysis) is used to compute forces in the CBS and RPV supports. A structural model of the supports and attached reactor system is analyzed (e.g., via response spectrum analysis or time-history analysis with appropriately generated floor motion inputs) to obtain internal forces/moments in the supports due to seismic inertia loads. Uncertainty in seismic demand arises from variability in earthquake ground motion characteristics (even for a given peak ground acceleration, spectral shape can vary) and from modeling uncertainty in the dynamic response. Herein, the peak support demand L_{SSE} is modeled as a lognormally distributed variable, where the mean value is provided by RELAP5 simulations

and a realistic COV is assumed. This approach aligns with common practice in seismic fragility analysis which often assumes lognormal distribution of structural demand given an intensity [103, 104]. For simplicity, additional inelastic response reduction factors are not applied since the focus herein is on ultimate load; instead, the support responding essentially elastically up to failure (e.g., a conservative assumption for demand calculation) is considered. The demand from the SSE is treated as an unfactored nominal value, since the goal is to assess actual failure probabilities rather than apply code safety margins.

- **Combined LOCA and Seismic Loading**
  The concurrent occurrence of a LOCA and SSE is a rare beyond-design-basis scenario, but it is included herein for completeness. In such a combined event, seismic shaking might induce a large LOCA (e.g., a seismic-induced pipe break). It is conservatively assumed that the total demand on the supports is the sum of the seismic inertial load and the LOCA pressure/jet load applied simultaneously. In reality, the worst pressures might not coincide exactly with peak inertial loads, but to envelope all possibilities, $L_{\text{combined}} = L_{\text{SSE}} + L_{\text{LOCA}}$ is considered. Design guidance often allows the square-root-sum-of-squares combination or other less conservative rules for combining independent loads [105], but using a direct sum gives a higher demand and, thus, a more cautious estimate of failure probability. Each simulation sample for the combined case draws a seismic demand and a LOCA demand from their respective distributions and sums them for the limit state check. It is worth noting that the probability of the combined scenario itself is extremely low (e.g., product of the individual event probabilities), but it is treated conditionally, assuming the scenario has occurred, and the conditional failure probability given both loadings is evaluated. This provides fragility insight for beyond-design-basis evaluations.

6.1.6 Performance Metrics

Using the above framework, several probabilistic performance metrics for the CBS and RPV supports under each loading case are evaluated:

- Capacity Exceedance Probability P_f
  This is the probability that the applied demand will exceed the structural capacity (i.e., $P_f = P(R < L)$). It directly corresponds to the failure probability for the defined limit state. P_f values, or often, $1 - P_f$ in percentage as reliability, are reported for each case. For example, if $P_f = 5 \times 10^{-4}$ under SSE loading, that indicates a 0.05% chance of failure when the structure is subjected to an SSE-level event. The P_f results allow comparison against target reliability levels; nuclear structures often target very low failure probabilities (i.e., on the order of 10^{-5} per demand cycle for SSE) to ensure high safety margins [5, 106].
- Reliability Index β
  β provides a standardized measure of safety. β alongside P_f are presented for each case, which facilitates interpretation. For instance, $\beta \approx 3.0$ for the seismic case might be compared to typical target β of approximately 3.5 used in structural code calibrations (which corresponds to $P_f \approx 2 \times 10^{-4}$) [107, 108]. A higher β in one scenario versus another indicates a relatively safer condition in terms of margin.
- Safety Margin Distribution and Reliability Sensitivity
  The MCS analysis yields distributions of the safety margin $M = R - L$ for each case. From these, the probability that a certain margin is maintained can be computed. For example, there may be a 95% probability that R exceeds L by at least X% for a given scenario. Additionally, by examining which random variables most frequently drive $g < 0$ outcomes, critical factors can be identified. For instance, if variability in concrete strength contributes most to failure probability, that could indicate the need for material quality control or retrofitting.

The outcomes of the analysis will be presented in terms of the above metrics.

6.1.7 Use of Unfactored Nominal Values vs. Code Factors

It is important to clarify that this probabilistic analysis uses unfactored loads and resistances (i.e., the actual nominal capacities and expected loads without the application of code safety factors). This approach provides an unbiased estimate of the true probability of failure. In contrast, design codes, such as ACI 349 [47] for nuclear concrete structures or ASCE 43 [5] for seismic design, employ load and resistance factor design (LRFD) formats with factored loads (amplified by load factors > 1.0) and reduced resistances (multiplied by resistance factors $\phi < 1.0$) to achieve a desired level of safety. For example, ACI 349 [47] might require applying a factor of, say, 1.2 to dead load and 1.6 to live load in design, and use a strength reduction factor $\phi \approx 0.9$ for concrete flexural capacity. These factors are calibrated so that, for typical uncertainties, the probability of failure is very low (target reliability). In fact, using a ϕ factor around 0.75–0.9 effectively shifts the nominal (mean) capacity to a lower fractile (e.g., $\phi = 0.75$ can shift the median capacity to about the 90th percentile lower bound of capacity) [109]. Similarly, code seismic load definitions often correspond to an upper fractile of actual demand (e.g., the code design earthquake may be an 84th-percentile motion in ASCE 43 [5], meaning only 20% chance actual demand exceeds it [109]). Combined, the load and resistance factors aim to ensure that the probability of failure in design is below a target (often on the order of 1% or less for design-basis events [109]). For instance, ASCE 43-05 targets an approximate 10^{-5} annual failure probability for seismic Category I structures, which translates to $\beta \approx 4$ for a 50-year period [5].

In this analysis, by *not* applying these factors, the "as-designed" reliability is effectively assessed. The use of nominal values is justified because the intent is to capture the inherent margins and explicitly calculate P_f. If the code factors were included in each simulation (i.e., artificially increase R and decrease L), every simulation would almost certainly indicate failure (since design ensures $R_{\text{nominal}} > L_{\text{nominal}}$ only after factoring). The code factors are not random; they are deterministic safety margins chosen to achieve a target reliability [107]. Instead, the uncertainties are incorporated explicitly and P_f is determined. The expectation is that the resulting P_f will align with code-intended targets if the code calibration is sound. For example, if the code's intent were a 10^{-4} failure probability for SSE, this analysis should yield roughly that order of P_f when using nominal values. Indeed, prior studies have shown that factored design approaches correspond to reliability indices on the order of 3–4 for structural components [97, 108]. In the context of the CBS/RPV supports, using nominal (i.e., unfactored) capacities which are near the mean of the capacity distribution, and nominal loads which are near an upper percentile of demand, should result in very low calculated P_f. This is verified by comparing the computed β with code target β. Notably, a commentary in a recent design guide indicated that using $\phi = 0.75$ in ACI 349 moves the design capacity to roughly the 90th percentile of the actual capacity distribution, and typical seismic design loads correspond to about the 80th percentile of actual demand, aiming for < 1% probability of unacceptable performance at the design basis earthquake [109]. This aligns with the proposed approach; the actual probability of demand exceeding capacity is determined with those distributions. If the probability is indeed on the order of 1% or less, it confirms the adequacy of the design. If it is higher, that flags a potential safety concern. By using the probabilistic approach, the safety factors' impact is effectively reverse-engineered rather than assumed, thus providing insight into where the design is conservative or whether there are hidden risks not accounted for by simplistic factoring (e.g., if multiple loads combine non-linearly or if there is correlation between material weaknesses and load effects).

6.1.8 Summary of the Probabilistic Approach

Overall, the unified probabilistic framework presented herein provides a comprehensive picture of the CBS and RPV support performance under LOCA, seismic, and combined hazards. It brings together

advanced capacity modeling (LDPM simulations) and realistic load characterizations (RELAP5 for LOCA, code spectra for seismic) in a MCS environment to quantify reliability. By doing so, it not only verifies that code-intended safety levels are met (or identifies where they might not be), but it also yields fragility information that is valuable for risk assessments and beyond-design-basis evaluations (e.g., the probabilistic risk assessment of the plant). The expected outcome is a set of reliability metrics and fragility curves that demonstrate a high level of structural safety and identify any potential weak points (e.g., if the combined load fragility has a shallow slope or low median, indicating vulnerability).

6.2 IRRADIATION-AWARE ULTIMATE STRENGTH LIMIT STATES FOR CBS AND RPV SUPPORTS

The structural integrity of the CBS and the RPV support slab in a nuclear reactor containment system is a critical component of the overall safety and performance of the facility. These structural elements are designed to withstand not only routine service loads but also extreme accident scenarios such as LOCA and SSE. Complicating this design challenge is the fact that these concrete elements are subject to long-term neutron irradiation, which introduces radiation-induced degradation mechanisms that significantly reduce their material performance. The most notable of these degradation mechanisms is RIVE, which occurs when high-energy neutrons cause siliceous aggregates to expand, inducing internal stresses, microcracking, and bond deterioration between aggregates and the cement paste matrix.

Such radiation exposure reduces the mechanical properties of concrete, including tensile strength, compressive strength, modulus of elasticity, and shear capacity. These reductions are particularly severe at fluence levels exceeding 10^{19} to 10^{20} n/cm^2, conditions that are common in CBS concrete near the reactor core over several decades of operation. To ensure that the structural assessment and safety evaluations accurately reflect this degradation, a set of ultimate strength limit states incorporating irradiated material properties has been developed. These limit states provide a formal framework for evaluating whether the structure can withstand critical loads without reaching a condition of collapse or functional failure.

Each limit state takes the general form

$$g_i = R_i - L_i, \tag{19}$$

where g_i represents the safety margin (with failure occurring when $g_i < 0$), R_i is the radiation-degraded structural resistance, and L_i is the applied load effect. This formulation allows for a direct evaluation of structural capacity versus demand in an irradiated context. The following limit states are developed in accordance with US NRC standards (e.g., SRP 3.6.1 and 3.6.2 [9]), ACI 349-13 [47], ACI 318-19 [11], and industry evaluations such as Biwer et al. (2021) [22], which specifically address RPV supports and LOCA–seismic interactions.

6.2.1 Limit State 1: CBS Surface Cracking and Spalling Due to LOCA Thermal Shock

In an ultimate strength context, failure is defined as the exceedance of the irradiated tensile strength of concrete due to thermally induced stress from a LOCA-induced transient. This formulation assumes that when the induced tensile stress exceeds the degraded tensile strength of the material, structural failure at the surface (spalling or full-thickness cracking) is possible. The governing limit state equation is:

$$g_1 = f_{ct,\mathrm{irr}} - \sigma_{\mathrm{th}} = f_{ct,\mathrm{irr}} - E_{c,\mathrm{irr}} \cdot \alpha \cdot \Delta T \tag{20}$$

where $f_{ct,\mathrm{irr}}$ is the irradiated tensile strength of concrete, $E_{c,\mathrm{irr}}$ is the irradiated modulus of elasticity, α is the coefficient of thermal expansion, and ΔT is the temperature differential across the CBS thickness. This criterion is especially applicable when RIVE effects have caused significant microstructural weakening, allowing cracks to initiate and propagate under relatively modest thermal gradients.

6.2.2 Limit State 2: Crushing Failure from Jet Impingement

During a large-break LOCA, a high-velocity steam or water jet may escape from the breached piping and impact the CBS with concentrated force. If this force is transmitted over a small area, the resulting compressive stress at the impact zone may exceed the compressive strength of the irradiated concrete. In such cases, localized crushing and potentially material ejection can occur, especially in concrete already weakened by RIVE or other irradiation-induced mechanisms. The ultimate limit state is defined as:

$$g_2 = f'_{c,\text{irr}} - \left(\frac{F_{\text{jet}}}{A_{\text{impact}}} \right) \tag{21}$$

where $f'_{c,\text{irr}}$ is the irradiated compressive strength, F_{jet} is the thrust force of the LOCA jet, and A_{impact} is the area over which the force is applied. Exceedance of this limit indicates failure due to dynamic pressure exceeding localized strength.

6.2.3 Limit State 3: Anchor Pull-Out or Yielding Under SSE

Seismic loads cause vibration and inertia in anchored equipment, leading to tension and shear in anchor bolts embedded in the CBS. Failure may occur through two primary mechanisms: steel yielding of the anchor shaft or pull-out of the anchor from the surrounding concrete. In irradiated concrete, bond degradation and reduced tensile strength lower the concrete breakout capacity. The governing limit state accounts for both potential failure modes:

$$g_3 = \min(N_{cb,\text{irr}}, A_s f_y) - T_{\text{SSE}} \tag{22}$$

where $N_{cb,\text{irr}}$ is the irradiated concrete breakout capacity, A_s is the anchor steel cross-sectional area, f_y is the steel yield strength, and T_{SSE} is the applied tensile demand from seismic action. This formulation ensures that both steel and concrete failure mechanisms are considered.

6.2.4 Limit State 4: CBS Wall Shear or Flexural Failure Due to Seismic Base Shear

During an SSE, the CBS wall is subjected to horizontal inertial forces that translate into shear and bending demands at the base of the wall. In an irradiated state, the compressive strength of the concrete $f'_{c,\text{irr}}$ is reduced, thereby lowering both its shear and flexural capacity. The ultimate strength limit state for shear failure is written as:

$$g_4 = \frac{2}{3} \cdot \sqrt{f'_{c,\text{irr}}} \cdot b \cdot d - V_{\text{SSE}} \tag{23}$$

where b is the wall width, d is the effective depth to tension reinforcement, and V_{SSE} is the seismic base shear demand. Failure occurs when this base shear exceeds the degraded shear capacity of the irradiated CBS section.

6.2.5 Limit State 5: RPV Base Slab Punching/Shear Failure under Combined Vertical Loading

In the combined scenario of LOCA-induced uplift and SSE-induced vertical acceleration, the base slab supporting the RPV may experience high vertical forces that induce punching shear failure. This is a brittle failure mechanism that initiates when the vertical force exceeds the slab's capacity to transfer load through shear to the surrounding concrete. Irradiation exacerbates this vulnerability by reducing $f'_{c,\text{irr}}$, particularly in slabs without sufficient shear reinforcement. The ultimate limit state is

$$g_5 = V_{\text{punch,irr}} - (V_{\text{LOCA}} + V_{\text{SSE}}), \tag{24}$$

where $V_{\text{punch,irr}}$ is the irradiated punching shear capacity, V_{LOCA} is the upward load from LOCA cavity pressure, and V_{SSE} is the vertical inertial load from seismic excitation. This is often a governing limit state under beyond-design-basis load combinations.

6.2.6 Summary of Irradiation-Aware Ultimate Strength Limit States

Table 10 contains a summary of all five limit states considered in this analysis.

Table 10. Summary of irradiation-aware ultimate strength limit states.

ID	Failure Mode	Degradation Mechanisms	Analytical Formulation	Sources
1	Surface cracking and spalling due to LOCA thermal shock	Irradiation-induced tensile strength loss + LOCA thermal gradient	$g_1 = f_{ct,\text{irr}} - E_{c,\text{irr}} \cdot \alpha \cdot \Delta T$	[9, 22, 47]
2	Localized crushing from LOCA jet impingement	Irradiation-induced compressive strength loss + LOCA jet thrust	$g_2 = f'_{c,\text{irr}} - \frac{F_{\text{jet}}}{A_{\text{impact}}}$	[9, 22, 47]
3	Anchor failure (steel yielding or pull-out under SSE)	Irradiation-induced bond degradation + Seismic inertial tension	$g_3 = \min(N_{cb,\text{irr}}, A_s f_y) - T_{\text{SSE}}$	[9, 22, 110]
4	CBS wall shear or flexural failure under SSE base shear	Irradiation-induced compressive strength reduction + Seismic shear demand	$g_4 = \frac{2}{3}\sqrt{f'_{c,\text{irr}}}\, b\, d - V_{\text{SSE}}$	[9, 11, 47]
5	RPV base slab punching shear failure under combined LOCA uplift and SSE vertical load	Irradiation-induced reduction in punching shear capacity + Combined vertical demands	$g_5 = V_{\text{punch,irr}} - (V_{\text{LOCA}} + V_{\text{SSE}})$	[9, 11, 22]

6.2.7 Ultimate vs. Serviceability Limit States

While the above formulations define failure based on ultimate strength thresholds, it is often more informative to evaluate damage progression through serviceability limit states, especially for modes that do not immediately threaten global structural stability. For example, cracking or spalling that does not expose reinforcement may not compromise safety but could necessitate inspection or repair. Transitioning Limit States 1 and 2 to serviceability criteria allows modeling of acceptable performance degradation without

invoking immediate structural failure. This approach aligns with the philosophy of performance-based design and supports life-extension decisions for irradiated containment structures.

Alternative Formulations for Limit States 1 and 2

Initial formulations of Limit States 1 and 2 were based on direct comparisons between load effects (stress or pressure) and irradiated material strengths. While mechanically valid, this approach introduces numerical behavior that may produce unrealistically high probabilities of failure, even for reasonably conservative input values. This section provides a detailed explanation of the issues with the original formulations and presents revised alternatives that are more suitable for structural reliability analysis.

Issue with Limit State 1: Overconservative Stress Comparison

While strength-based limit state 1, as shown in 20, is dimensionally consistent, this equation assumes that any instance where thermal stress exceeds irradiated tensile strength results in failure. However, due to the inherently low tensile strength of irradiated concrete ($f_{ct,\text{irr}} \sim$ 1.5–2.5 MPa) and the relatively high elastic modulus ($E_{c,\text{irr}} \sim$ 20–30 GPa), even moderate LOCA-induced temperature gradients (e.g., $\Delta T \sim$ 100–150 K) yield thermal stresses on the order of 20–30 MPa. This consistently results in negative g_1 values, suggesting extremely high failure probabilities, which do not reflect actual structural performance or design intent.

To better reflect actual structural performance, an alternative formulation defines failure in terms of cracking depth exceeding a critical limit (e.g., rebar cover):

$$g_1 = d_{\text{crit}} - d_{\text{spall}} \tag{25}$$

where d_{spall} is the estimated cracking or spalling depth from LOCA-induced thermal shock, and d_{crit} is the allowable depth (e.g., 25–50 mm). This allows the reliability model to distinguish between superficial thermal damage (acceptable) and functionally significant cracking.

Issue with Limit State 2: Overconservative Jet Pressure vs. Strength

Strength-based limit state 2, as shown in 21, assumes that the full LOCA jet thrust is uniformly applied over a small impact area. In practice, this results in average contact pressures (e.g., 30–80 MPa) that far exceed irradiated concrete compressive strengths (e.g., 20–30 MPa), leading to extremely high P_f values. However, localized crushing from a brief jet pulse does not typically compromise the structural integrity of massive concrete elements such as the CBS.

The alternative formulation evaluates whether the jet physically penetrates the concrete to a depth that threatens functional capacity:

$$g_2 = d_{\text{crush,crit}} - d_{\text{jet}} \tag{26}$$

where d_{jet} is the estimated penetration or crushing depth due to jet force, and $d_{\text{crush,crit}}$ is the maximum allowable depth of damage. This approach accounts for duration, material heterogeneity, and transient effects, and aligns better with empirical and simulated behavior from Biwer et al. (2021) and NRC SRP 3.6.2 guidance [9, 22].

6.3 COMPUTATIONAL APPROACH FOR RELIABILITY ANALYSIS

The mathematical basis for this study involves defining limit state functions $g(X) = R - L$, where R is the capacity and L is the load. Failures occur when $g(X) \leq 0$, and the probability of failure P_f is calculated across various limit states. To address the inherent uncertainty in both R and L, each is modeled as a random variable following certain probability distributions, consistent with recommendations in JCSS [95] and other probabilistic nuclear design standards [47, 52, 53]. This probabilistic framework integrates advanced structural simulations with probabilistic sampling techniques, such as LHS, to achieve efficiency and accuracy in evaluating failure probabilities across five limit states. The results are then analyzed in terms of probabilities of failure P_f and reliability indices β.

6.3.1 Input Parameters

6.3.1.1 Capacity Estimation

The resistance or capacity of the CBS and the RPV supports under various loading conditions is derived from mesoscale high-fidelity simulations using the LDPM. As previously documented in the report, these simulations capture the degradation of mechanical properties in concrete subjected to RIVE, expansion, cracking, and localized damage. The mean capacities at varying damage depths δ (i.e., 0, 10, 15, and 20 cm) under horizontal loading only, as well as horizontal and vertical loading, are generated from LDPM simulations (see Table 9). These computations are based on experimental validation and theoretical scaling of material properties under extreme conditions [12, 80, 81].

The COV for capacity is assumed to be 20%, consistent with general observations in probabilistic nuclear design studies [11, 95, 106, 111, 112]. Research by Biwer et al. [22] indicates that mechanical properties such as compressive and tensile strength in degraded concrete tend to exhibit COVs between 10% and 20%. A high-end value of 20% is selected herein to incorporate not only intrinsic material variability but also uncertainties in irradiation modeling and LDPM approximations.

6.3.1.2 Load Modeling

LOCA Loading

LOCA loading forces are derived from RELAP5 thermal-hydraulic simulations previously documented in the report. RELAP5 models are employed to capture peak differential pressures across CBS walls and associated jet impingement forces on RPV supports during a design-basis LOCA event. Based on these simulations, the mean jet impingement forces are determined considering a full break area (e.g., 1A) or a partial break area (e.g., 0.5A, at 50% of the total) (see Table 7), and a COV of 15% is assumed. This choice aligns with Biwer et al. [22], where thermal hydraulic pressure variability in LOCA analyses is reported to fall within a 10–20% range due to uncertainties in break location, fluid dynamics, and thermal boundary assumptions. In general, a reasonable assumption for the COV of the LOCA load is typically in the range of 10–25%, depending on factors such as the precision of the fluid dynamic models, material properties, and boundary conditions [103, 106, 113–115].

Seismic Loading

Seismic forces are evaluated using a simplified but conservative approach that considers the SSE ground motion and the weight of the RPV. Seismic load F_{SSE} at each support (e.g., four supports are considered herein for this example) is calculated as

$$F_{SSE} = (5 \cdot 9.81 \cdot a_s + 2.85)\left(\frac{m_{RPV}}{4}\right), \tag{27}$$

where a_s is the spectral acceleration at the SSE level and m_{RPV} is the RPV effective mass. This simplified approach to calculating the equivalent horizontal forces on the RPV supports was developed by considering a structurally equivalent system shown in Figure 93. Note that to simplify the calculations, the rigid links can safely be considered as truss elements. The dimensions shown in Figure 93 can easily be adapted to the geometrical constraints of any RPV. These assumptions ensure that the probabilistic evaluation of seismic reliability reflects realistic seismic conditions while maintaining compliance with established regulatory frameworks.

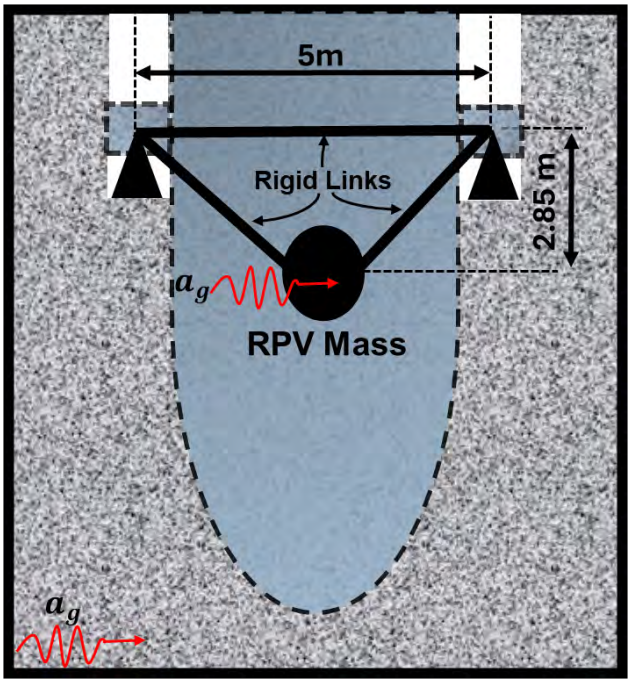

Figure 93. Structurally equivalent system of the RPV.

The RPV weight distribution is derived from international RPV specifications listed in Table 11. Based on these data, a mean RPV weight of 491.2 metric tons and a standard deviation of 96.8 metric tons (i.e., $COV = 21.5\%$) is assumed. The lognormal distribution is chosen to model weight variability due to inherent manufacturing and design differences, consistent with studies on PWR designs [9, 22, 53].

Table 11. RPV total weights across major PWR designs (including internals).

Reactor Design	Total RPV Weight (metric tons)	Source
Westinghouse AP1000 (Gen III, 2-loop PWR)	~417	[116]
Framatome EPR (Gen III, 4-loop PWR)	~580	[117, 118]
KEPCO APR-1400 (Gen III, 4-loop PWR)	~700	[119]
VVER-440 (Soviet 6-loop PWR, small)	~439	[120]
VVER-1000 (V-320) (Soviet 4-loop PWR)	~320	[121, 122]

According to the NRC Regulatory Guide 1.60 [52], the design basis for nuclear facilities generally assumes an SSE ground acceleration in the range of 0.2g to 0.3g at the foundation level. Additional site-specific analyses of certain reactors, particularly in higher seismic hazard regions, suggest slightly higher accelerations. Kennedy et al. [106] report SSE accelerations ranging from 0.2g to 0.4g in

regions with moderate to high seismic activity. In extreme cases, and particularly for reactors located in seismically active regions, values up to 0.5g may be considered. For the purposes of this study, a mean SSE acceleration value of 0.3g is selected. This value reflects expected conditions in moderate seismic regions and includes a safety margin to account for higher-than-expected ground motion. This approach aligns with previous studies in seismic nuclear design [53, 106] and remains well within the bounds defined by regulatory guidelines.

The variability in SSE acceleration arises from multiple sources, including:

- Uncertainty in regional seismic hazard analysis: Ground motion predictions used to derive SSE spectra vary due to uncertainties in probabilistic seismic hazard assessments.
- Variability in spectral response amplification: Differences in soil conditions, structural heights, and damping mechanisms result in site-specific amplification effects [52].
- Modeling and simulation approximations: Assumptions embedded in seismic analysis models contribute additional variability in SSE acceleration values [103, 104].

For seismic design applications, a typical COV for SSE accelerations lies between 20% and 40%, depending on the specific reactor's design and location. Kennedy and Ravindra [106] suggest using a COV of 25%-30% in reliability assessments, highlighting that this range adequately accounts for the combined uncertainty in ground motion variation and structural response modeling. Similarly, Zentner et al. [115] emphasize that variability in SSE loading should reflect the inherent unpredictability of seismic events, particularly in probabilistic seismic hazard analyses. In this work, a COV of 30% is adopted, which provides a representative measure of uncertainty without being overly conservative. This value reflects both the physical variability of ground motions and the variability in the structural modeling used for nuclear reactors.

6.3.2 Sample Random Variables

All random variables in the model, including resistance R and loading effects L (including the weight of the RPV and SSE acceleration), are assumed to follow lognormal distributions. The justification for selecting lognormal distributions lies in their ability to model strictly non-negative variables (e.g., capacities and loads) that exhibit right-skewed behavior, a common characteristic of both material properties and extreme environmental loads. This assumption aligns with recommendations from JCSS [95], Biwer et al. [22], and Melchers [100]. Furthermore, lognormal distributions are widely employed in seismic fragility analyses for nuclear structures, including in studies such as Kennedy et al. [103] and Zentner et al. [104].

LHS is incorporated for efficiently sampling the statistical space of each random variable while reducing variance in Monte Carlo estimates. This method is preferred over simple random sampling due to its improved convergence properties for small failure probabilities [95, 101]. LHS mitigates excessive computational costs associated with Monte Carlo sampling while maintaining accurate representation of low probabilities of failure. In this study, 1 million LHS samples are used for each random variable considered. A comprehensive table of all random variables used in this study and their associated means and COVs is shown in Table 12. Note that all random variables herein are assumed to follow lognormal distributions.

6.3.3 Limit State Evaluation

Each limit state function is defined as $g = R - L$, where R is the capacity, and L is the applied load. Failure occurs when $g \leq 0$, implying that demand exceeds resistance. Five limit states were evaluated:

Table 12. Statistical properties of random variables.

Random Variable	Mean	COV (%)
Resistance R	Table 9	20 [11, 22, 95, 106, 111, 112]
Maximum Jet Impingement Force, 1A Case L_{LOCA}	6.03 MN (Table 7)	20 [22, 103, 106, 113–115]
Maximum Jet Impingement Force, 0.5A Case L_{LOCA}	3.01 MN (Table 7)	20 [22, 103, 106, 113–115]
SSE Acceleration a_s	0.3 g [52, 53, 106]	30 [52, 103, 104, 106, 115]
RPV Mass m_{RPV}	451.2 metric tons (Table 11)	20.1 (Table 11)

1. LOCA force from 1A pipes.
2. LOCA force from 0.5A pipes.
3. Seismic horizontal force.
4. Combined LOCA (1A) and seismic force.
5. Combined LOCA (0.5A) and seismic force.

6.3.4 Outputs and Results

The failure probabilities P_f were computed as the proportion of realizations for which $g \leq 0$, and reliability indices β were derived using

$$\beta = \Phi^{-1}(1 - P_f), \tag{28}$$

where Φ^{-1} represents the inverse normal CDF. This formulation adheres to methodologies introduced by Hasofer and Lind [97, 98] and is adopted across contemporary nuclear reliability guidelines [95, 103]. This metric provides a standardized measure of reliability. The analysis also produces PDFs for both resistance and demand under various scenarios that reveal the probabilistic distributions' overlap, highlighting conditions where demand may exceed capacity. These results highlight the robustness of probabilistic methods in quantifying risks for nuclear facilities and provide clear benchmarks for assessing structural adequacy under multi-hazard conditions.

6.4 RELIABILITY ANALYSIS AND RESULTS

The computational reliability framework, as described in Section 6.3, was applied to evaluate the structural performance of safety-related concrete systems under varying levels of irradiation-induced degradation. The mean capacity values used in this analysis were determined through LDPM simulations, as detailed in Table 9.

Three distinct structural scenarios were considered.

1. **Plain concrete (without reinforcement):** This case provides a baseline to evaluate the contribution of unreinforced concrete when exposed to irradiation effects.
2. **Reinforced concrete with $\rho_s = 0.8\%$:** A minimally reinforced case.
3. **Reinforced concrete with $\rho_s = 1.6\%$:** The most heavily reinforced case considered; it closely matches the actual reinforcement content in the CBS and RPV supports. This scenario enables a realistic understanding of the effects of irradiation on structures of critical importance in nuclear facilities.

The steel reinforcement ratio, ρ_s, is defined as the ratio of the cross-sectional area of the steel reinforcement to the total cross-sectional area of a concrete member. Analyzing all three scenarios allows for a robust understanding of variations in reliability under different structural resistances.

Each structural case is analyzed under two load configurations:

- *Horizontal Loads Only:* This configuration simulates lateral pressures due to transient accident loads, including effects such as seismic excitations or pressure pulses.
- *Combined Horizontal and Vertical Loads:* This configuration accounts for both lateral (horizontal) loads and vertical axial compression, better replicating realistic conditions acting on CBS walls and RPV supports.

These configurations are evaluated under five representative accident load cases, consistent with US nuclear design standards. The cases considered are as follows:

- L_1 (1A LOCA): A full-scale LOCA representing one of the most demanding pressure scenarios.
- L_2 (0.5 LOCA): A less severe half-LOCA loading scenario.
- L_3 (SSE): SSE conditions.
- L_4 (1A LOCA + SSE): A simultaneous occurrence of a full LOCA with a SSE, representative of the most extreme operating condition for safety-related concrete in nuclear facilities.
- L_5 (0.5 LOCA + SSE): A less severe combined event involving a half-LOCA and seismic excitation.

6.4.1 Plain Concrete Case

For the plain concrete case, the analysis focuses exclusively on unreinforced concrete within the CBS. This approach isolates the contribution of concrete as the sole load-resisting material, without support from embedded steel reinforcement. Consequently, the structural resistance of plain concrete is entirely governed by its inherent mechanical properties, which deteriorate progressively under irradiation. The mean capacity values used in the analysis were obtained from Table 9 for four irradiation damage depths $\delta = 0$, 10, 15, and 20 cm. These depths represent increasing levels of radiation penetration into the CBS cross-section, simulating long-term irradiation effects associated with the operation of nuclear facilities over extended service periods. By incorporating varying irradiation levels, the study aims to quantify how such deterioration impacts structural reliability and safety margins.

The analysis evaluates reliability from two complementary perspectives: deterministic and probabilistic. Deterministic capacity–demand relationships assess whether the mean resistance of the concrete exceeds the imposed accident load demands. This aspect provides an intuitive and direct comparison of average margins. Probabilistic reliability, on the other hand, incorporates uncertainty in both resistance and load. This approach quantifies failure probabilities using statistical overlap between resistance and load distributions, generating the reliability index β and the probability of failure P_f. Together, these perspectives offer a comprehensive framework for understanding the vulnerability of plain concrete under accident scenarios.

The numerical results for β and P_f are provided in Table 13 through Table 16, while Figure 94 through Figure 96 illustrate the relationship between resistance, demand, and irradiation effects. These figures demonstrate how radiation impacts both mean resistance and the probability distributions, leading to increased likelihoods of structural failure as the irradiation depth increases.

The monotonic decline in the mean resistance R of plain concrete as a function of irradiation depth δ is depicted in Figure 94. The figure compares the resistance curves for two loading configurations, horizontal loads only and combined horizontal and vertical loads, against constant mean magnitudes of five representative accident loads (i.e., L_1–L_5). For unirradiated conditions (i.e, $\delta = 0$ cm), plain concrete shows positive safety margins for low-severity load cases like L_2 (0.5 LOCA) and L_3 (SSE). However, the mean resistance is insufficient to resist high-severity demands such as L_1 (full LOCA) and L_4 (LOCA + SSE), where load demands already exceed resistance, leading to a complete lack of safety margin even before irradiation. At $\delta = 10$ cm, mean resistance deteriorates below nearly all load demands, leaving only negligible or nonexistent safety margins for L_2 and L_3. By $\delta = 20$ cm, resistance becomes inadequate for all but the mildest load scenario (i.e., L_3), and even this marginal adequacy is significantly compromised when probabilistic uncertainties are considered.

A more detailed understanding of plain concrete's structural behavior under accident loads is provided by the PDFs in Figure 95 and Figure 96. These figures depict the distributions of resistance and load for specific irradiation depths (i.e, $\delta = 0$, 10, 15, and 20 cm). Overlap between the resistance and load PDFs corresponds directly to probabilities of failure P_f.

For mild load cases like L_3, resistance at $\delta = 0$ cm lies predominantly to the right of the load distribution, with limited overlap yielding relatively low P_f values (e.g., $P_f = 8.14 \times 10^{-2}$ for horizontal-only loading, as shown in Table 14). However, as δ increases, the resistance PDF shifts leftward due to radiation-induced degradation, increasing the overlap area. By $\delta = 20$ cm, L_3 exhibits substantial overlaps, and failure probabilities rise to $P_f = 0.422$ (horizontal loading) or $P_f = 0.207$ (combined loading).

For high-demand load cases like L_1 and L_4, even at $\delta = 0$ cm, resistance and load PDFs already overlap significantly, resulting in near-unity P_f values. Irradiation further exacerbates this failure probability,

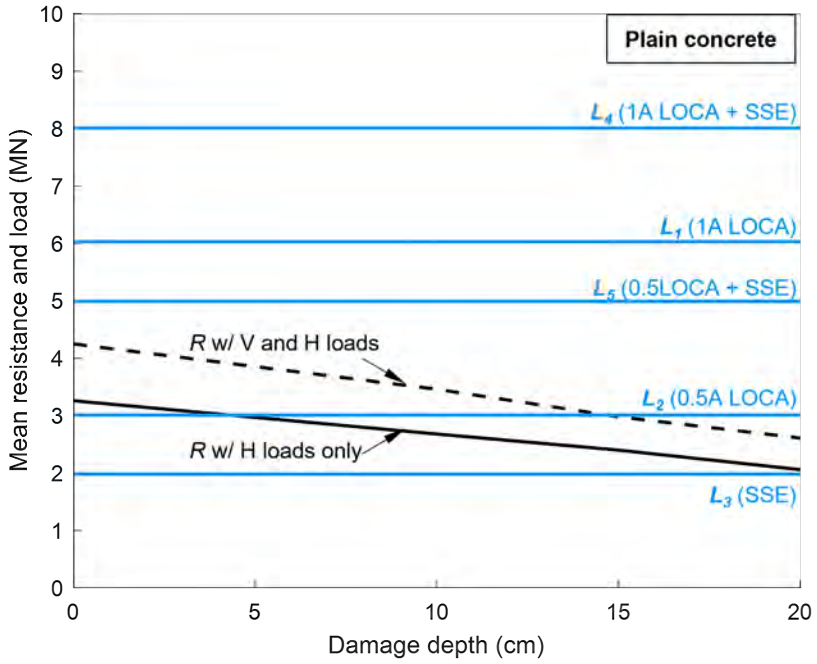

Figure 94. Mean resistance R of plain concrete as a function of irradiation damage depth δ, compared against mean accident load demands L_1–L_5.

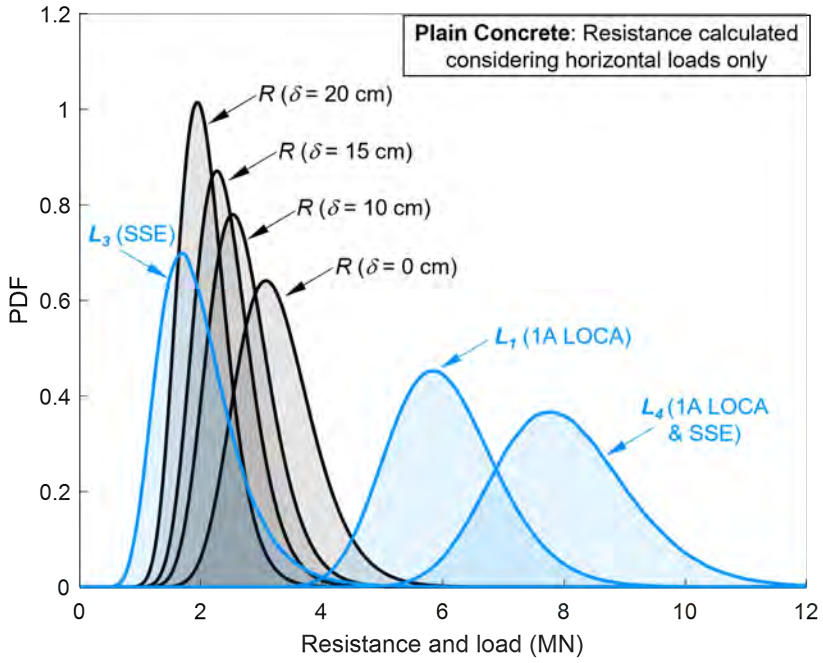

Figure 95. PDFs of resistance and load for plain concrete at irradiation damage depths δ = 0, 10, 15, and 20 cm (considering horizontal loads only).

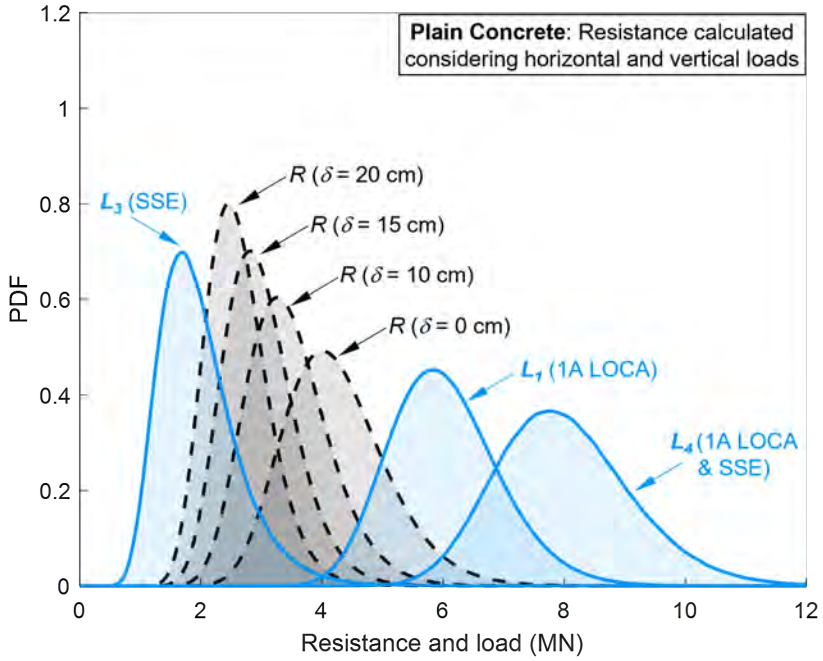

Figure 96. PDFs of resistance and load for plain concrete at irradiation damage depths δ = 0, 10, 15, and 20 cm (considering combined horizontal and vertical loads).

effectively guaranteeing structural failure (i.e., $P_f \approx 1.0$) for these load scenarios as soon as δ exceeds 5–10 cm.

The addition of vertical loading introduces slight improvements to resistance, shifting the resistance PDF rightward relative to horizontal-only configurations. This reduces P_f by approximately 10–20%, as reflected across Table 14 and Table 16. However, this marginal improvement does not mitigate the dominant influence of degradation caused by irradiation.

US nuclear safety codes such as ASCE 43-05 [5], ACI 349-13 [47], and NRC NUREG-0800 [9] require stringent reliability thresholds for safety-related structures. Specifically, ASCE 43-05 [5] mandates a reliability index $\beta \geq 3.719$, equivalent to a probability of failure $P_f \leq 10^{-4}$, under design basis earthquake (DBE) or design basis accident (DBA) conditions.

Plain concrete consistently fails to meet these benchmarks. Reliability indices β (i.e., Table 13 and Table 15) are negative for severe accidents (i.e., L_1, L_4, and L_5) even before irradiation begins and degrade rapidly with increasing δ. Values for milder accidents like L_3 drop below acceptable thresholds as δ increases, with β falling to 0.196 by $\delta = 20$ cm under horizontal-only loading. Corresponding P_f values for L_3 rise sharply to 0.422 under the same conditions, grossly exceeding the nuclear safety limit of 10^{-4}. For severe accidents like L_4, reliability indices remain catastrophically low (e.g., $\beta = -3.754$ at $\delta = 0$ cm and $\beta = -6.000$ at $\delta = 20$ cm), with $P_f \approx 1.0$ at all damage depths.

These results clearly demonstrate that plain concrete is unsuitable for use in nuclear safety–related structures under irradiated conditions. Probabilities of failure for all but the mildest load scenarios exceed nuclear safety thresholds by several orders of magnitude, and reliability indices consistently fall short of the ASCE 43-05 [5] requirement of $\beta \geq 3.719$. Furthermore, ACI 349-13 [47] and NRC NUREG-0800 [9] emphasize the need for robust structural margins and resilience under extreme accident scenarios, both

of which plain concrete fails to provide. The inability of plain concrete to maintain structural integrity underscores the necessity of considering alternate materials or construction strategies in radiation-prone environments, including reinforced concrete designs.

Table 13. Reliability index β for plain concrete with only horizontal loads applied as a function of irradiation damage depth δ.

Loading Case	$\delta = 0$ cm	$\delta = 10$ cm	$\delta = 15$ cm	$\delta = 20$ cm
L_1 (1A LOCA)	−2.510	−3.324	−3.766	−4.344
L_2 (0.5 LOCA)	0.288	−0.502	−0.947	−1.568
L_3 (SSE)	1.396	0.885	0.598	0.196
L_4 (1A LOCA + SSE)	−3.754	−4.417	−6.000	−6.000
L_5 (0.5A LOCA + SSE)	−1.726	−2.522	−2.964	−3.612

Table 14. Probability of failure P_f for plain concrete with only horizontal loads applied as a function of irradiation damage depth δ.

Loading Case	$\delta = 0$ cm	$\delta = 10$ cm	$\delta = 15$ cm	$\delta = 20$ cm
L_1 (1A LOCA)	9.94×10^{-1}	1.00	1.00	1.00
L_2 (0.5 LOCA)	3.87×10^{-1}	6.92×10^{-1}	8.28×10^{-1}	9.42×10^{-1}
L_3 (SSE)	8.14×10^{-2}	1.88×10^{-1}	2.75×10^{-1}	4.22×10^{-1}
L_4 (1A LOCA + SSE)	1.00	1.00	1.00	1.00
L_5 (1A LOCA + SSE)	9.58×10^{-1}	9.94×10^{-1}	9.98×10^{-1}	1.00

Table 15. Reliability index β for plain concrete with combined horizontal and vertical loads applied as a function of irradiation damage depth δ.

Loading Case	$\delta = 0$ cm	$\delta = 10$ cm	$\delta = 15$ cm	$\delta = 20$ cm
L_1 (1A LOCA)	−1.443	−2.270	−2.867	−3.400
L_2 (0.5 LOCA)	1.358	0.528	−0.0746	−0.611
L_3 (SSE)	2.077	1.547	1.160	0.817
L_4 (1A LOCA + SSE)	−2.671	−3.523	−4.056	−4.611
L_5 (1A LOCA + SSE)	−0.661	−1.487	−2.091	−2.624

Table 16. Probability of failure P_f for plain concrete with combined horizontal and vertical loads applied as a function of irradiation damage depth δ.

Loading Case	δ = 0 cm	δ = 10 cm	δ = 15 cm	δ = 20 cm
L_1 (1A LOCA)	9.26×10^{-1}	9.88×10^{-1}	9.98×10^{-1}	1.00
L_2 (0.5 LOCA)	8.72×10^{-2}	2.99×10^{-1}	5.30×10^{-1}	7.29×10^{-1}
L_3 (SSE)	1.89×10^{-2}	6.09×10^{-2}	1.23×10^{-1}	2.07×10^{-1}
L_4 (1A LOCA + SSE)	9.96×10^{-1}	1.00	1.00	1.00
L_5 (1A LOCA + SSE)	7.46×10^{-1}	9.31×10^{-1}	9.82×10^{-1}	9.96×10^{-1}

6.4.2 Minimally Reinforced Concrete Case

For this scenario, the performance of minimally reinforced concrete with a steel reinforcement ratio $\rho_s = 0.8\%$ is analyzed. In contrast to the plain concrete case, the inclusion of steel reinforcement provides an additional source of resistance, primarily through enhanced tensile strength and ductility. However, at $\rho_s = 0.8\%$, the contribution of reinforcement is modest, leaving this configuration vulnerable to irradiation-induced degradation of the concrete matrix, especially under severe load cases.

This analysis used the computational reliability framework described in Section 6.3 to examine how irradiation damage depth δ impacts safety margins. The reliability is evaluated in terms of both deterministic and probabilistic measures. Deterministic capacity–demand comparisons assess whether the mean resistance exceeds the imposed accident demands, while probabilistic measures (e.g., reliability indices β and failure probabilities P_f) quantify the statistical likelihood of structural failure. The results, reported at irradiation depths $\delta = 0$, 5, 10, 15, and 20 cm, allow for a comprehensive understanding of how irradiation worsens the performance of minimally reinforced systems.

The results of the reliability analysis are presented in Table 17 through Table 20. Figures for minimally reinforced concrete (i.e., Figure 97 through Figure 99) show the evolution of mean resistance and PDFs as a function of irradiation depth and accident load scenarios (i.e., L_1–L_5).

Figure 97 illustrates the deterioration of mean resistance R for reinforced concrete ($\rho_s = 0.8\%$) with increasing irradiation depth δ. Two loading configurations—horizontal-only and combined horizontal and vertical loads—are compared against constant mean accident load demands for the five representative load cases. At $\delta = 0$ cm, mean resistance exceeds load demands for moderate accident scenarios like L_2 and L_3, reflecting initial safety margins. The incorporation of minimal reinforcement improves reliability compared to plain concrete, allowing higher resistance levels at shallow damage depths. For example, L_2 achieves positive reliability indices (e.g., $\beta = 2.110$ at $\delta = 0$ cm for horizontal loads, see Table 17). However, under severe accident scenarios like L_1 and L_4, mean resistance falls below load demands, yielding negative safety margins even before irradiation begins (i.e., $\beta = -0.693$ for L_1 and $\beta = -1.890$ for L_4 at $\delta = 0$ cm considering horizontal loads only). As irradiation progresses to $\delta = 20$ cm, mean resistance diminishes across all load cases, reflecting the compounding effects of radiation-induced concrete degradation. While safety margins remain for L_2 and L_3 at intermediate depths (e.g., $\delta = 10$ cm), these margins erode substantially by $\delta = 20$ cm. By this stage, no load case achieves sufficient reliability, consistent with the reliability index trends shown in Table 17 and Table 19.

Figure 98 and Figure 99 depict the PDFs of resistance and load for reinforced concrete ($\rho_s = 0.8\%$) across irradiation depths ($\delta = 0$, 5, 10, 15, and 20 cm) under horizontal-only and combined loading configurations. The overlap between resistance and load PDFs corresponds directly to the probability of failure P_f, as presented in Table 18 and Table 20.

For low-severity load cases like L_3, resistance PDFs lie predominantly to the right of the load distribution, resulting in small overlap areas and low P_f values. For example, horizontal loads yield $P_f = 5.31 \times 10^{-3}$ for L_3 at $\delta = 0$ cm (see Table 18). Severe load cases (i.e., L_1 and L_4) exhibit substantial overlap with load distributions, yielding excessively high P_f values (e.g., $P_f = 7.56 \times 10^{-1}$ for L_1 at $\delta = 0$ cm. Irradiation damage induces a steady leftward shift in resistance PDFs, reflecting reduced mean resistance and decreasing uncertainty (i.e., as δ increases, the peak value of the PDF of R increases while its spread decreases) due to degraded material properties. This shift significantly increases overlap areas and corresponding P_f values. By $\delta = 10$ cm, L_3 experiences growing overlap, raising P_f to 1.32×10^{-2}, while for L_2, P_f reaches 5.85×10^{-2}, approaching unacceptable limits (for horizontal loads only). At $\delta = 20$ cm, for L_3, P_f reaches 3.45×10^{-2} (horizontal loads only) and 1.12×10^{-1} (combined horizontal and vertical loads). Severe accident load cases like L_4 experience effectively total overlap, with $P_f \approx 1.0$ for

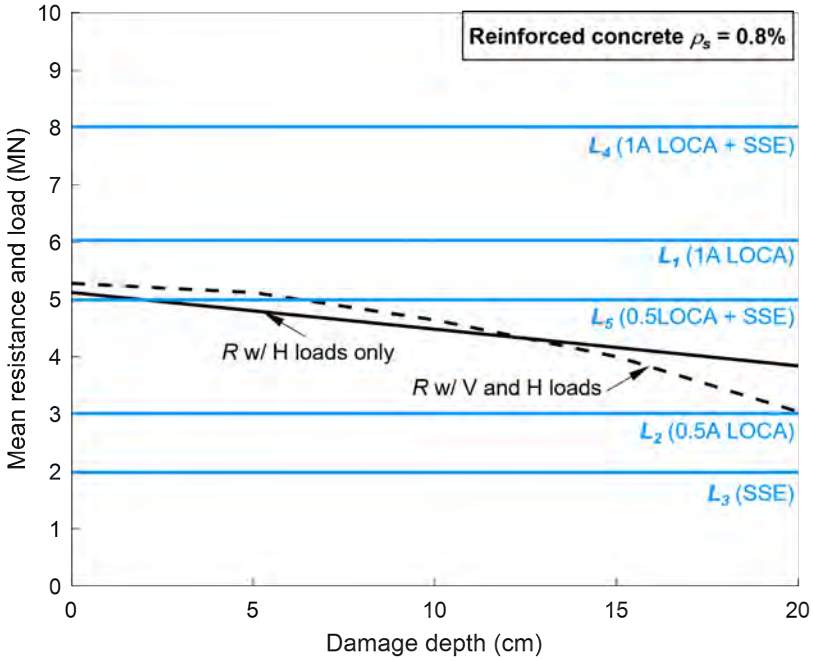

Figure 97. Mean resistance R of reinforced concrete $\rho_s = 0.8\%$ as a function of irradiation damage depth δ, compared against mean accident load demands L_1–L_5.

all configurations. While combined horizontal and vertical loading configurations delay the increase in P_f, this benefit diminishes beyond $\delta = 10$ cm.

US nuclear safety codes such as ASCE 43-05 [5] require stringent reliability thresholds for safety-related structures: $\beta \geq 3.719$ or $P_f \leq 10^{-4}$. Results for minimally reinforced concrete ($\rho_s = 0.8\%$) consistently fail to meet these limits. For L_3, while initial (i.e., at $\delta = 0$ cm) P_f values are modest (i.e., $< 10^{-3}$), deterioration to 3.45×10^{-2} by $\delta = 20$ cm (horizontal loads only) grossly exceeds allowable thresholds by over one order of magnitude. Severe accident scenarios like L_4 reach $P_f \approx 1.0$ at shallow irradiation depths (i.e., $\delta = 5$ cm), which violates safety margins by six orders of magnitude. Similarly, reliability indices β decline sharply with increasing δ, often starting below the required threshold and degrading further. For instance, for L_2, $\beta = 2.110$ at $\delta = 0$ cm (horizontal load only) drops below zero by $\delta = 20$ cm, reaching $\beta = 0.947$. For severe cases such as L_4, β degrades to -3.080 by $\delta = 20$ cm (horizontal loads only).

Although minimally reinforced concrete ($\rho_s = 0.8\%$) has a larger load-carrying capacity when compared to plain concrete, it fails to maintain reliability under extended irradiation exposure. Severe accident loads violate US nuclear safety codes even at shallow irradiation depths, and P_f values for moderate loads exceed thresholds at deep irradiation depths [5]. Structural designs for irradiated environments must incorporate higher reinforcement ratios or advanced materials to ensure compliance with nuclear reliability codes.

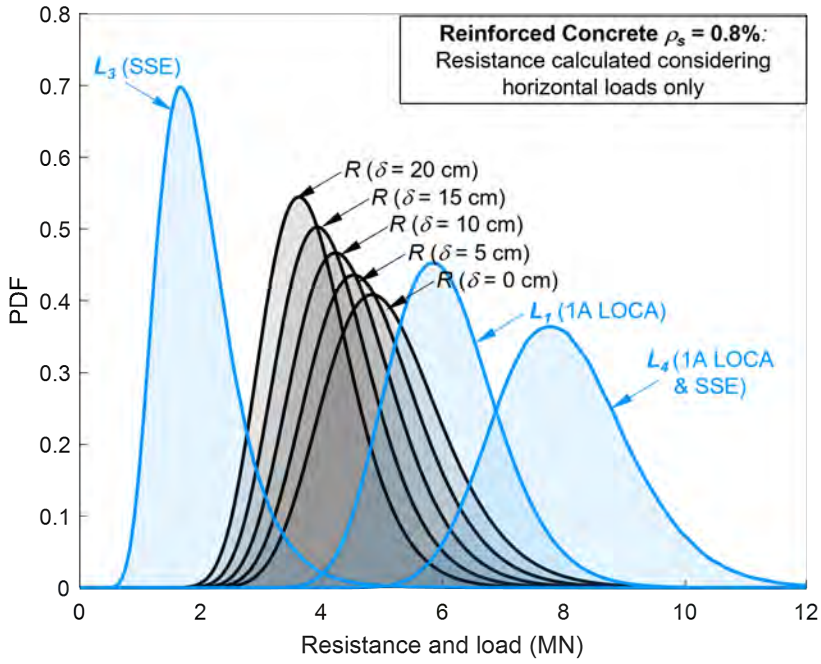

Figure 98. PDFs of resistance and load for reinforced concrete $\rho_s = 0.8\%$ at different irradiation depths δ (horizontal loads only).

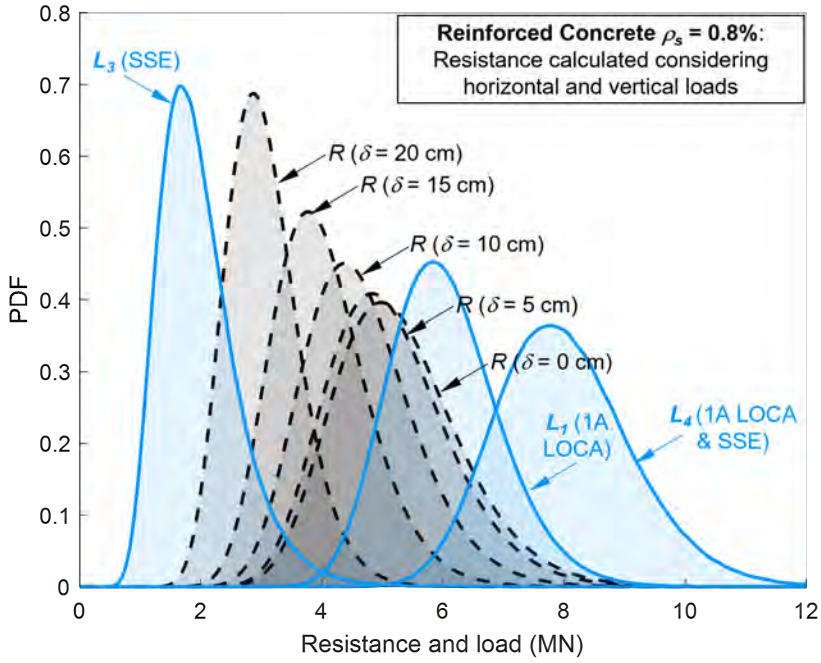

Figure 99. PDFs of resistance and load for reinforced concrete $\rho_s = 0.8\%$ at different irradiation depths δ (combined horizontal and vertical loads).

Table 17. Reliability index β for reinforced concrete ($\rho_s = 0.8\%$) with only horizontal loads applied as a function of irradiation damage depth δ.

Loading Case	$\delta = 0$ cm	$\delta = 5$ cm	$\delta = 10$ cm	$\delta = 15$ cm	$\delta = 20$ cm
L_1 (1A LOCA)	−0.693	−0.954	−1.230	−1.530	−1.850
L_2 (0.5 LOCA)	2.110	1.850	1.570	1.270	0.947
L_3 (SSE)	2.550	2.390	2.220	2.020	1.820
L_4 (1A LOCA + SSE)	−1.890	−2.160	−2.440	−2.760	−3.080
L_5 (1A LOCA + SSE)	0.079	−0.177	−0.451	−0.746	−1.070

Table 18. Probability of failure P_f for reinforced concrete ($\rho_s = 0.8\%$) with only horizontal loads applied as a function of irradiation damage depth δ.

Loading Case	$\delta = 0$ cm	$\delta = 5$ cm	$\delta = 10$ cm	$\delta = 15$ cm	$\delta = 20$ cm
L_1 (1A LOCA)	7.56×10^{-1}	8.30×10^{-1}	8.91×10^{-1}	9.37×10^{-1}	9.68×10^{-1}
L_2 (0.5 LOCA)	1.73×10^{-2}	3.22×10^{-2}	5.85×10^{-2}	1.02×10^{-1}	1.72×10^{-1}
L_3 (SSE)	5.31×10^{-3}	8.35×10^{-3}	1.32×10^{-2}	2.15×10^{-2}	3.45×10^{-2}
L_4 (1A LOCA + SSE)	9.71×10^{-1}	9.85×10^{-1}	9.93×10^{-1}	9.97×10^{-1}	9.99×10^{-1}
L_5 (1A LOCA + SSE)	4.69×10^{-1}	5.70×10^{-1}	6.74×10^{-1}	7.72×10^{-1}	8.57×10^{-1}

Table 19. Reliability index β for reinforced concrete ($\rho_s = 0.8\%$) with combined horizontal and vertical loads applied as a function of irradiation damage depth δ.

Loading Case	$\delta = 0$ cm	$\delta = 5$ cm	$\delta = 10$ cm	$\delta = 15$ cm	$\delta = 20$ cm
L_1 (1A LOCA)	−0.569	−0.694	−1.090	−1.690	−2.790
L_2 (0.5 LOCA)	2.230	2.110	1.710	1.110	0.005
L_3 (SSE)	2.640	2.560	2.300	1.920	1.210
L_4 (1A LOCA + SSE)	−1.770	−1.900	−2.310	−2.920	−4.030
L_5 (1A LOCA + SSE)	0.202	0.079	−0.310	−0.902	−2.010

Table 20. Probability of failure P_f for reinforced concrete ($\rho_s = 0.8\%$) with combined horizontal and vertical loads applied as a function of irradiation damage depth δ.

Loading Case	$\delta = 0$ cm	$\delta = 5$ cm	$\delta = 10$ cm	$\delta = 15$ cm	$\delta = 20$ cm
L_1 (1A LOCA)	7.15×10^{-1}	7.56×10^{-1}	8.62×10^{-1}	9.55×10^{-1}	9.97×10^{-1}
L_2 (0.5 LOCA)	1.30×10^{-2}	1.75×10^{-2}	4.32×10^{-2}	1.33×10^{-1}	4.98×10^{-1}
L_3 (SSE)	4.09×10^{-3}	5.31×10^{-3}	1.08×10^{-2}	2.73×10^{-2}	1.12×10^{-1}
L_4 (1A LOCA + SSE)	9.61×10^{-1}	9.71×10^{-1}	9.89×10^{-1}	9.98×10^{-1}	1.00
L_5 (1A LOCA + SSE)	4.20×10^{-1}	4.69×10^{-1}	6.22×10^{-1}	8.17×10^{-1}	9.78×10^{-1}

6.4.3 Fully Reinforced Concrete Case

Reinforced concrete with a steel reinforcement ratio of $\rho_s = 1.6\%$ reflects the closest approximation to actual reinforcement configurations in critical nuclear structures such as the CBS and RPV supports. This level of reinforcement enhances tensile resistance and mechanical stability, significantly mitigating the adverse effects of radiation compared to plain or minimally reinforced concrete.

The system reliability was evaluated under various irradiation damage depths (i.e., $\delta = 0$, 5, 10, 15, and 20 cm) that are representative of long-term radiation effects on the CBS. The reliability assessment covers both horizontal-only and combined horizontal and vertical loading configurations for accident load scenarios (i.e., L_1–L_5). The results focus on mean structural capacity R, reliability indices β, and failure probabilities P_f. Compliance with US nuclear safety regulations, primarily ASCE 43-05 [5] (i.e., $\beta \geq 3.719$ or $P_f \leq 10^{-4}$), was also assessed.

The results of the reliability analysis are presented in Table 21 through Table 24. Figures for reinforced concrete with $\rho_s = 1.6\%$ (i.e., Figure 100 through Figure 102) show the evolution of resistance and PDFs as a function of irradiation depth and accident load scenarios (i.e., L_1–L_5).

Figure 100 illustrates the mean resistance R of reinforced concrete ($\rho_s = 1.6\%$) as a function of irradiation damage depth, compared to constant accident load demands (i.e., L_1–L_5).

At $\delta = 0$, the mean resistance indicates significant safety margins for moderate loads. For L_2, mean resistance corresponds to a reliability index of $\beta = 4.080$ under horizontal loads and 4.420 under combined horizontal and vertical loads (see Table 21 and Table 23). Even for severe accidents like L_1 and L_5, positive safety margins exist, with $\beta = 1.260$ and 1.970, respectively, for horizontal loading. For $5 < \delta < 20$ cm, deterioration in structural properties due to irradiation reduces mean resistance across all load cases. For moderate loads (i.e., L_2 and L_3), resistance remains sufficient, with positive margins observed even at $\delta = 20$ cm (e.g., $\beta = 3.110$ and 3.190, respectively, for horizontal loading only). Severe loads like L_4 are more vulnerable to irradiation. By $\delta = 10$ cm, mean resistance drops below mean L_4 load demands, resulting in negative reliability indices (i.e., $\beta = -0.215$) and substantial failure probabilities (i.e, $P_f = 5.85 \times 10^{-1}$) under horizontal loading.

Figure 101 and Figure 102 portray the PDFs of resistance and load for horizontal-only and combined loading configurations across all irradiation depths. The overlap regions directly correspond to failure probabilities P_f, detailed in Table 22 and Table 24. For low-severity scenarios like L_3, resistance distributions lie predominantly to the right of the load PDFs, resulting in low P_f. Even at $\delta = 20$ cm, P_f remains at 7.15×10^{-4} (horizontal loads) and 1.36×10^{-3} (combined loads), which are compliant with ASCE 43-05 thresholds [5]. For L_2, initial (i.e., at $\delta = 0$ cm) P_f values are relatively small (i.e., $< 10^{-4}$); however, at $\delta = 20$ cm, horizontal loading results in $P_f = 9.48 \times 10^{-4}$, which is just within acceptable limits. For severe accident scenarios like L_4, overlap between resistance and load PDFs increases rapidly with δ. By $\delta = 20$ cm, horizontal loading produces $P_f = 8.07 \times 10^{-1}$, far exceeding allowable values. For L_1 at $\delta = 20$ cm, significant overlap results in $P_f = 5.01 \times 10^{-1}$ for the combined horizontal and vertical loading case.

For moderate-load cases such as L_2 and L_3, compliance with ASCE 43-05 standards is observed [5]. Specifically, for L_2, reliability indices for both horizontal and combined loading configurations remain above 3.719 at irradiation damage depths $\delta < 15$ cm. Additionally, failure probabilities for this load case remain consistently below the ASCE 43-05 [5] limit of $P_f \leq 10^{-4}$ for $\delta < 15$ cm. For L_3, safety margins are sufficient across irradiation depths $\delta < 10$ cm, demonstrating compliance with regulatory requirements for $\delta < 10$ cm. In contrast, compliance is not maintained for severe accident scenarios like L_4 and L_1. For L_4, the reliability index drops below zero by $\delta = 10$ cm, with corresponding failure probabilities exceeding $P_f > 5.85 \times 10^{-1}$, signaling non-compliance. By $\delta = 20$ cm, failure under combined loading for L_4 becomes

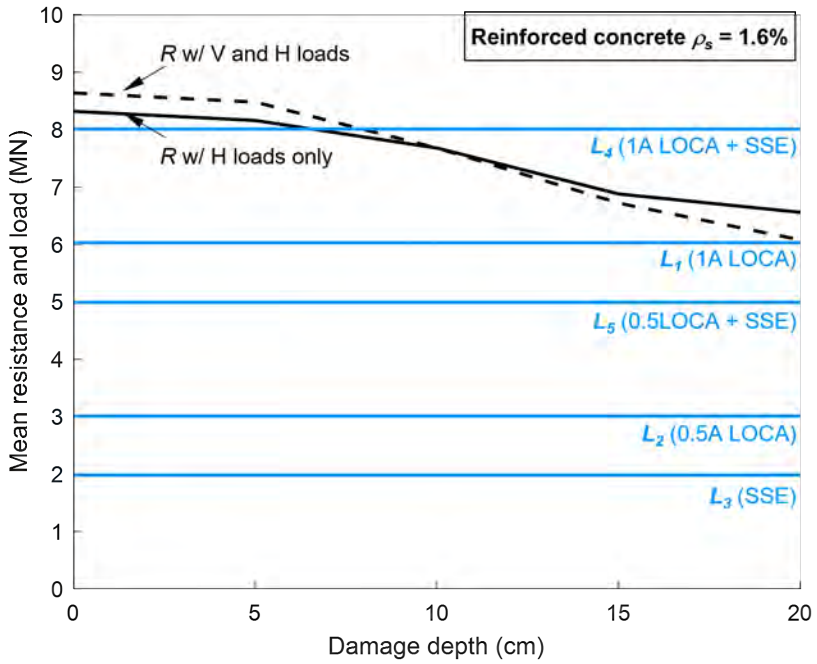

Figure 100. Mean resistance R of reinforced concrete $\rho_s = 1.6\%$ as a function of irradiation damage depth δ, compared against mean accident load demands L_1–L_5.

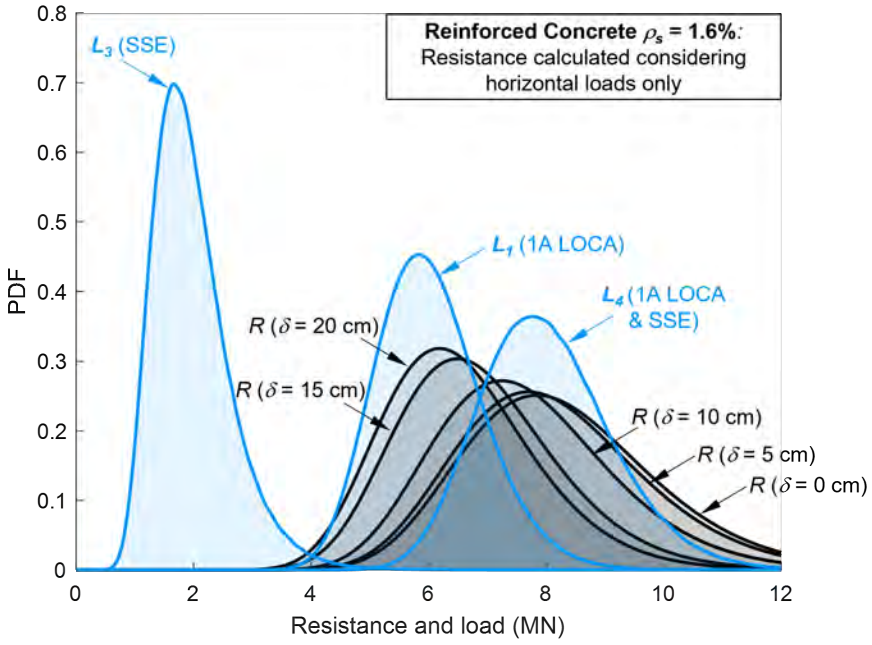

Figure 101. PDFs of resistance and load for reinforced concrete $\rho_s = 1.6\%$ at different irradiation depths δ (horizontal loads only).

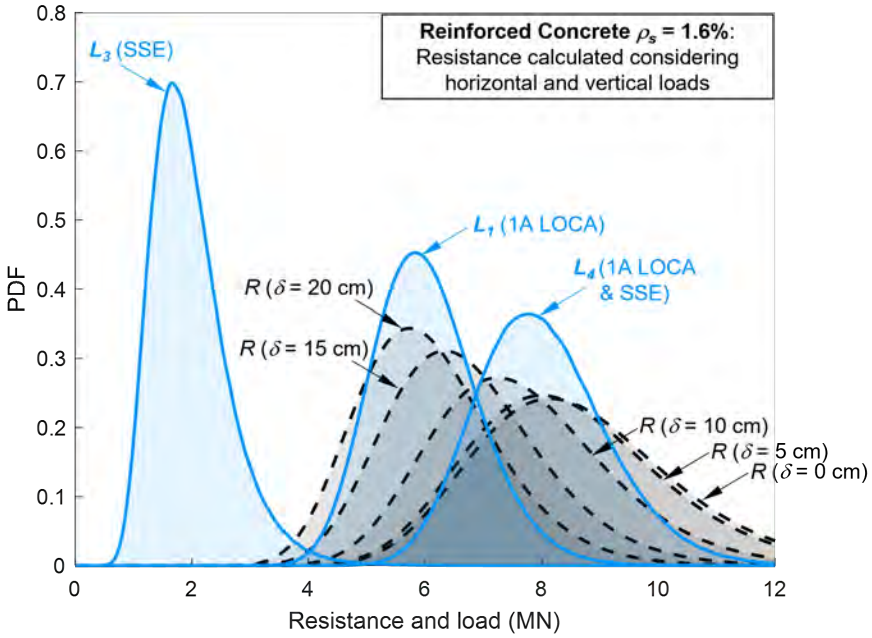

Figure 102. PDFs of resistance and load for reinforced concrete $\rho_s = 1.6\%$ at different irradiation depths δ (combined horizontal and vertical loads).

virtually certain, with $P_f = 8.81 \times 10^{-1}$. Similarly, for L_1, reliability indices and failure probabilities suggest marginal compliance at shallow irradiation depths (i.e., $\delta \leq 5$ cm); however, this degrades to non-compliance as the depth increases, with $\beta = 0.305$ at $\delta = 20$ cm considering horizontal loads only.

Reinforced concrete ($\rho_s = 1.6\%$) offers substantial improvements over lesser reinforcement scenarios, ensuring compliance with ASCE 43-05 for moderate load cases (e.g., L_2 and L_3) even under moderate irradiation damage depths [5]. However, for high-demand scenarios like L_1 and L_4, failure probabilities exceed allowable limits, particularly as irradiation progresses. These findings suggest that while $\rho_s = 1.6\%$ is reliable for intermediate demands, enhanced design strategies are necessary, considering the configuration of RPV supports outlined herein.

Table 21. Reliability index β for reinforced concrete ($\rho_s = 1.6\%$) with only horizontal loads applied as a function of irradiation damage depth δ.

Loading Case	δ = 0 cm	δ = 5 cm	δ = 10 cm	δ = 15 cm	δ = 20 cm
L_1 (1A LOCA)	1.260	1.180	0.940	0.497	0.305
L_2 (0.5 LOCA)	4.080	4.000	3.750	3.290	3.110
L_3 (SSE)	3.820	3.770	3.600	3.310	3.190
L_4 (1A LOCA + SSE)	0.116	0.037	−0.215	−0.671	−0.867
L_5 (1A LOCA + SSE)	1.970	1.900	1.670	1.240	1.050

Table 22. Probability of failure P_f for reinforced concrete ($\rho_s = 1.6\%$) with only horizontal loads applied as a function of irradiation damage depth δ.

Loading Case	$\delta = 0$ cm	$\delta = 5$ cm	$\delta = 10$ cm	$\delta = 15$ cm	$\delta = 20$ cm
L_1 (1A LOCA)	1.03×10^{-1}	1.18×10^{-1}	1.74×10^{-1}	3.10×10^{-1}	3.80×10^{-1}
L_2 (0.5 LOCA)	2.30×10^{-5}	3.20×10^{-5}	8.90×10^{-5}	4.96×10^{-4}	9.48×10^{-4}
L_3 (SSE)	6.70×10^{-5}	8.30×10^{-5}	1.59×10^{-4}	4.73×10^{-4}	7.15×10^{-4}
L_4 (1A LOCA + SSE)	4.54×10^{-1}	4.85×10^{-1}	5.85×10^{-1}	7.49×10^{-1}	8.07×10^{-1}
L_5 (1A LOCA + SSE)	2.43×10^{-2}	2.90×10^{-2}	4.79×10^{-2}	1.08×10^{-1}	1.47×10^{-1}

Table 23. Reliability index β for reinforced concrete ($\rho_s = 1.6\%$) with combined horizontal and vertical loads applied as a function of irradiation damage depth δ.

Loading Case	$\delta = 0$ cm	$\delta = 5$ cm	$\delta = 10$ cm	$\delta = 15$ cm	$\delta = 20$ cm
L_1 (1A LOCA)	1.420	1.340	0.941	0.402	−0.00136
L_2 (0.5 LOCA)	4.420	4.160	3.720	3.170	2.800
L_3 (SSE)	3.920	3.880	3.590	3.260	3.000
L_4 (1A LOCA + SSE)	0.272	0.195	−0.214	−0.768	−1.180
L_5 (1A LOCA + SSE)	2.120	2.040	1.660	1.150	0.756

Table 24. Probability of failure P_f for reinforced concrete ($\rho_s = 1.6\%$) with combined horizontal and vertical loads applied as a function of irradiation damage depth δ.

Loading Case	$\delta = 0$ cm	$\delta = 5$ cm	$\delta = 10$ cm	$\delta = 15$ cm	$\delta = 20$ cm
L_1 (1A LOCA)	7.82×10^{-2}	9.01×10^{-2}	1.73×10^{-1}	3.44×10^{-1}	5.01×10^{-1}
L_2 (0.5 LOCA)	5.00×10^{-6}	1.60×10^{-5}	9.90×10^{-5}	7.57×10^{-4}	2.56×10^{-3}
L_3 (SSE)	4.50×10^{-5}	5.20×10^{-5}	1.65×10^{-4}	5.61×10^{-4}	1.36×10^{-3}
L_4 (1A LOCA + SSE)	3.93×10^{-1}	4.23×10^{-1}	5.85×10^{-1}	7.79×10^{-1}	8.81×10^{-1}
L_5 (1A LOCA + SSE)	1.70×10^{-2}	2.06×10^{-2}	4.80×10^{-2}	1.26×10^{-1}	2.25×10^{-1}

6.4.4 Discussion of the Results

The comparative analysis of plain concrete, minimally reinforced concrete $\rho_s = 0.8\%$, and fully reinforced concrete $\rho_s = 1.6\%$ highlights significant differences in performance under irradiation effects and accident load conditions L_1 through L_5. This analysis focuses on whether these materials meet stringent US nuclear safety standards such as ASCE 43-05 [5], which require a reliability index $\beta \geq 3.719$ or a probability of failure $P_f \leq 10^{-4}$ for critical structures like RPV supports under DBEs and DBAs.

Figure 103 shows the mean resistance R of all three concrete cases as a function of irradiation depth δ. These results are compared against the constant accident load demands L_1 through L_5 to evaluate safety margins. Plain concrete demonstrates rapid degradation in resistance, with R falling below load demands for severe scenarios like L_1 (full LOCA) and L_4 (LOCA + SSE) even at $\delta = 0$. This indicates structural inadequacy irrespective of irradiation effects or load configurations. Minimally reinforced concrete $\rho_s = 0.8\%$ exhibits moderate improvement over plain concrete, maintaining safety margins for mild to moderate loads L_2 and L_3 at shallow irradiation depths $\delta \leq 5$ cm. However, increasing irradiation $\delta > 10$ cm rapidly diminishes its resistance, leaving it insufficient to resist any load demands by $\delta = 20$ cm. Fully reinforced concrete $\rho_s = 1.6\%$ offers the best performance, with R remaining above load demands for mild to moderate accident cases L_2 and L_3 throughout the irradiation progression. Nevertheless, for severe scenarios L_1 and L_4, R falls below load levels as $\delta > 10$ cm, highlighting insufficient safety margins under high-demand conditions.

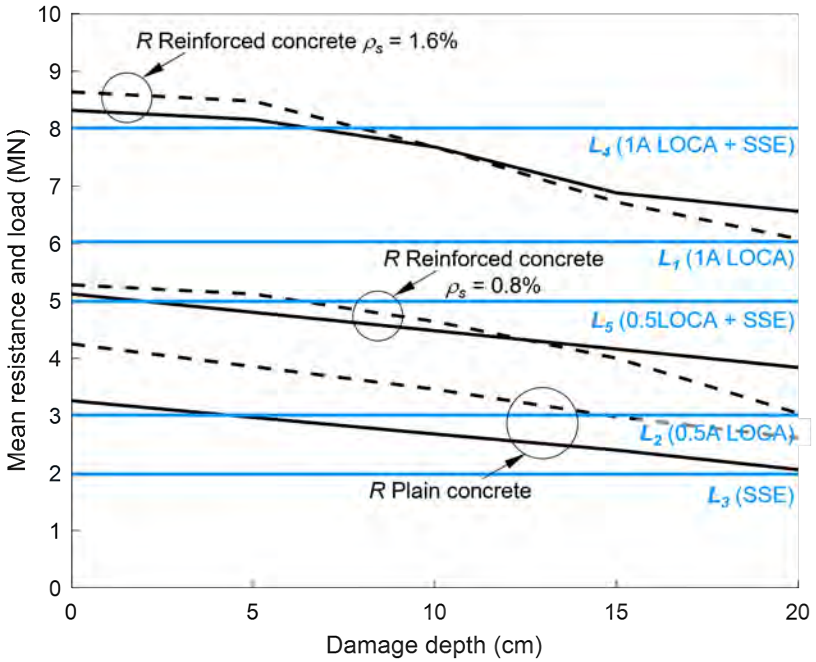

Figure 103. Mean resistance R as a function of irradiation damage depth δ, compared against mean accident load demands L_1–L_5.

Figure 104 and Figure 105 delve deeper into the reliability of these materials by examining the PDFs of resistance R and load L for unirradiated $\delta = 0$ cm and heavily irradiated $\delta = 20$ cm conditions, respectively. Plain concrete exhibits substantial PDF overlap with load distributions for all cases at $\delta = 0$, yielding high failure probabilities P_f, particularly for severe loads like L_3 and L_4. At $\delta = 20$ cm, resistance collapses entirely for plain concrete, with almost complete PDF overlap for all load scenarios and $P_f \approx 1.0$,

signaling inevitable failure. Minimally reinforced concrete $\rho_s = 0.8\%$ reduces PDF overlap initially for mild loads like L_3, producing modest failure probabilities (e.g., $P_f = 5.31 \times 10^{-3}$). For severe loads L_1 and L_4, however, significant overlap and high P_f are observed even at shallow irradiation ($\delta = 5$ cm). By $\delta = 20$ cm, resistance PDFs shift so far left that overlap occurs across all load cases, yielding $P_f \approx 1.0$ for severe scenarios. Fully reinforced concrete $\rho_s = 1.6\%$ achieves better separation of resistance and load PDFs. For mild to moderate cases L_2 and L_3, failure probabilities remain low under unirradiated and mildly irradiated conditions. However, severe scenarios (i.e., L_1 and L_4) show increasing overlap with deeper irradiation, resulting in $P_f > 0.5$ by $\delta = 20$ cm. This indicates that while $\rho_s = 1.6\%$ reinforcement offers reasonable reliability for moderate loads, it is insufficient for critical severe accident loads under irradiation.

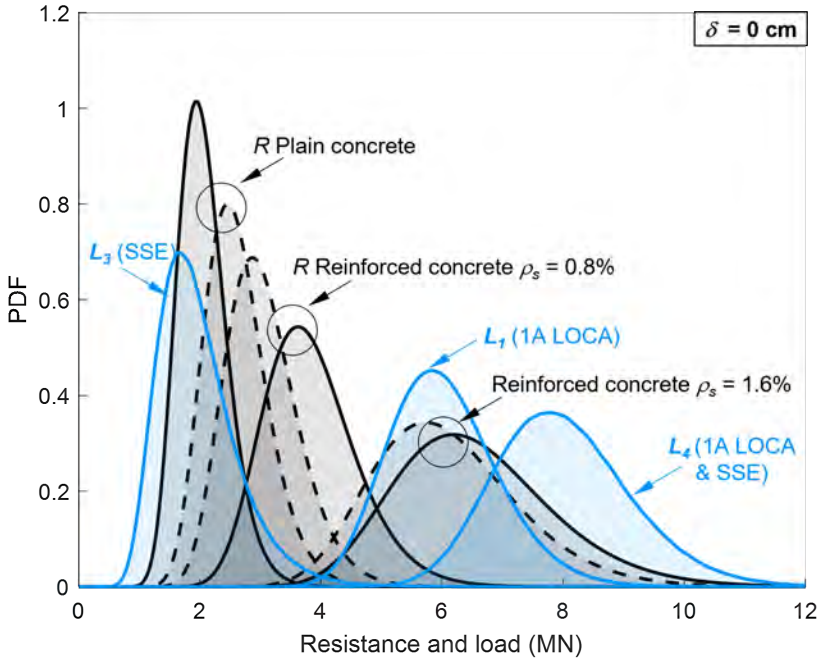

Figure 104. PDFs of resistance and load at irradiation damage depth $\delta = 0$ cm.

Figure 106 through Figure 108 provide a direct evaluation of reliability indices β for the three concrete configurations across irradiation depths δ for mild (e.g., L_3) and severe (i.e., L_1 and L_4) load scenarios. Plain concrete shows consistently negative β values for all severe load scenarios and across all depths, indicating catastrophic structural failure probabilities $P_f \approx 1.0$ even before accounting for irradiation. For mild scenarios like L_3, β starts above zero under unirradiated conditions but declines rapidly with irradiation, breaching the ASCE-required threshold ($\beta \geq 3.719$) as δ increases [5]. Minimally reinforced concrete $\rho_s = 0.8\%$ improves β values marginally compared to plain concrete, particularly for L_3 where initial reliability indices remain above threshold levels. With increasing irradiation, however, β for L_3 crosses below 3.719 by $\delta = 15$ cm, while β for severe loads like L_1 and L_4 remains negative across all depths. Fully reinforced concrete $\rho_s = 1.6\%$ achieves $\beta > 3.719$ for mild (i.e., L_3) and moderate (i.e, L_2) loads across most depths, maintaining compliance with ASCE standards [5]. However, for severe scenarios like L_1 and L_4, β declines rapidly as $\delta > 10$ cm, crossing below safe thresholds and effectively signaling noncompliance for high-demand conditions.

The comparative data clearly indicate that the current design of RPV support systems, even with a reinforcement ratio of $\rho_s = 1.6\%$, is insufficient to meet nuclear safety requirements under severe

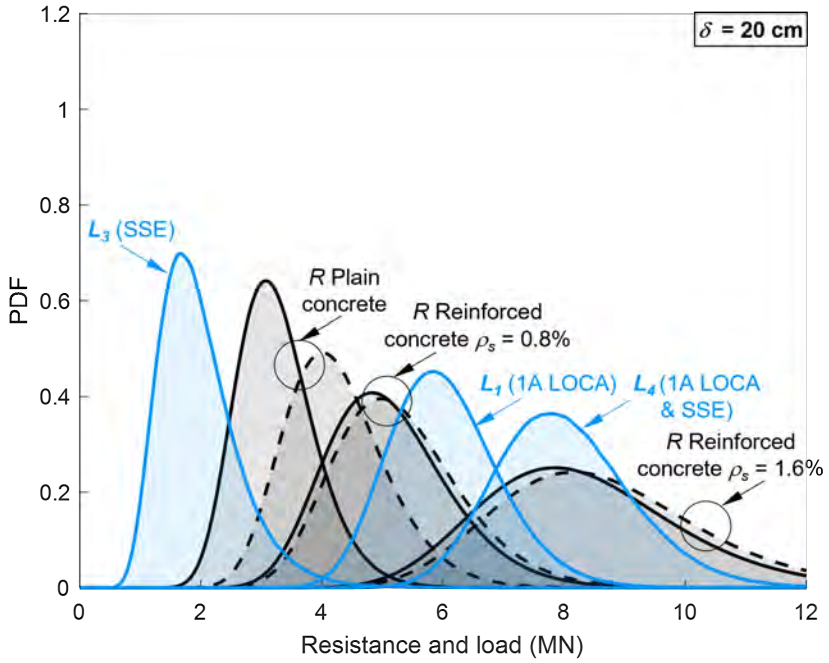

Figure 105. PDFs of resistance and load at irradiation damage depth $\delta = 20$ cm.

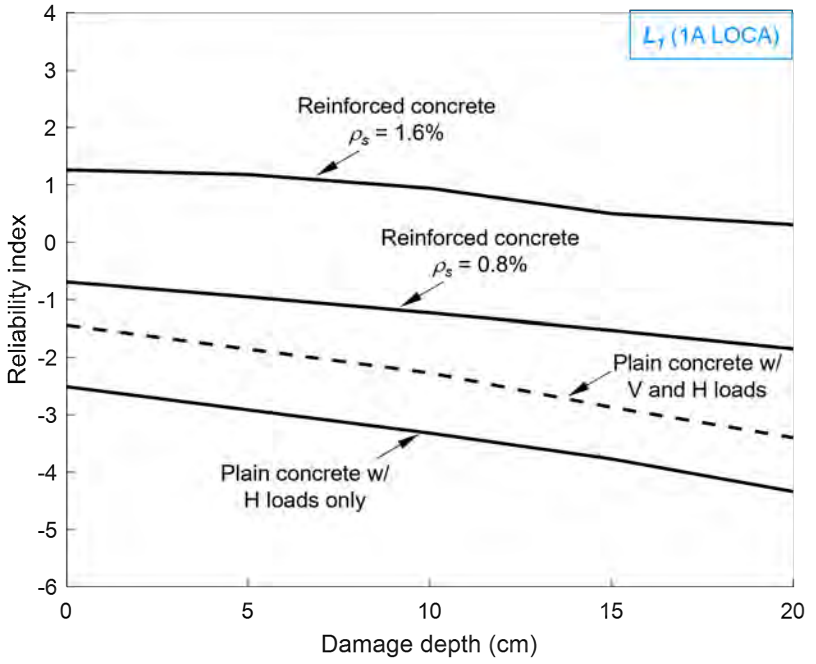

Figure 106. Reliability index for all reinforcement cases (i.e., none, $\rho_s = 0.8\%$, and $\rho_s = 1.6\%$) across different irradiation damage depths δ considering L_1 (full LOCA).

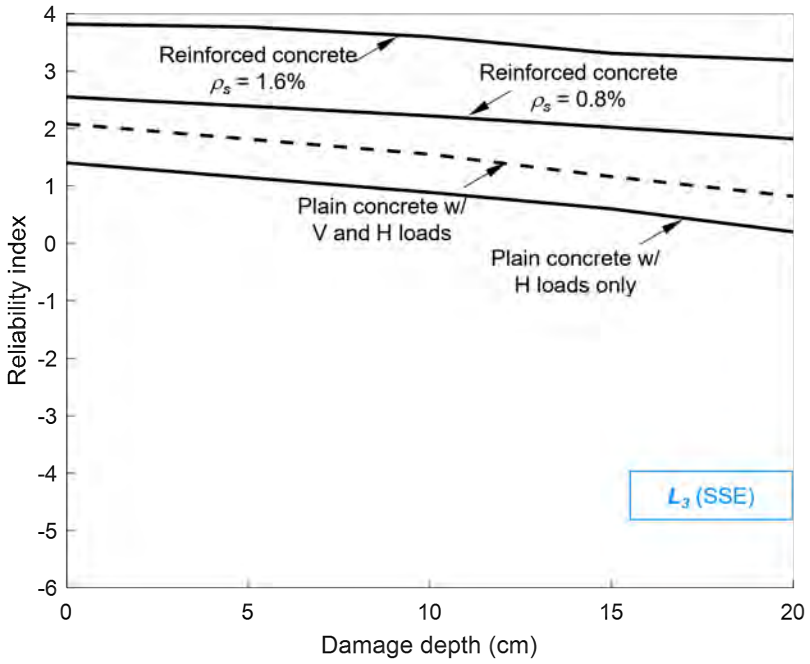

Figure 107. Reliability index for all reinforcement cases (i.e., none, $\rho_s = 0.8\%$, and $\rho_s = 0.8\%$) across different irradiation damage depths δ considering L_3 (SSE).

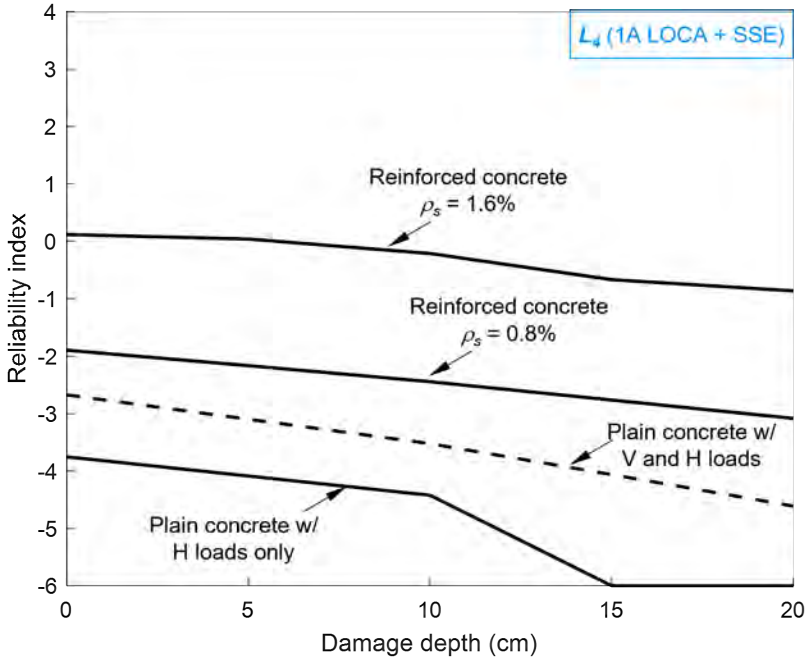

Figure 108. Reliability index for all reinforcement cases (i.e., none, $\rho_s = 0.8\%$, and $\rho_s = 1.6\%$) across different irradiation damage depths δ considering L_4 (LOCA + SSE).

accidental loading conditions. While fully reinforced concrete maintains acceptable reliability for mild to moderate loads, under severe accident scenarios (L_1 and L_4) and irradiation depths beyond $\delta = 10$ cm, failure probabilities exceed acceptable thresholds $P_f > 10^{-4}$, and reliability indices fall below safe limits ($\beta < 3.719$) [5]. This occurs because irradiation substantially degrades the mechanical properties of the concrete matrix, resulting in reduced resistance. Despite the increased reinforcement ratio, severe loads exacerbate these vulnerabilities, rendering the design non-compliant with ASCE 43-05 and other nuclear safety codes [5].

To address these shortcomings, enhancements beyond the current reinforcement ratio are necessary. Structural redundancy and conservative design measures should also be incorporated into RPV supports to ensure compliance with safety regulations under severe accident conditions. Overall, the existing reinforcement configuration is insufficient to ensure the reliability and safety of RPV support systems under accidental loading and irradiation effects, necessitating immediate re-evaluation and potential redesign.

7. CONCLUSIONS

This evaluation of the CBS and RPV supports under irradiation and accidental loading conditions highlights several key insights that are relevant for the design, reliability, and maintenance of nuclear infrastructure. The findings emphasize the importance of reinforcement in resisting extreme loads and the critical impact of irradiation-induced degradation on structural performance. While higher reinforcement ratios improve load-carrying capacity, long-term degradation due to neutron irradiation significantly reduces the material reliability of concrete, particularly under severe accident scenarios.

Reinforcement was found to have a pronounced impact on horizontal load resistance. For shallow irradiation damage depths (e.g., 0–5 mm), vertical loading enhances HL capacity by increasing friction below the support shoe without triggering shear failure or concrete crushing. At intermediate degradation depths (e.g., 10 mm), the beneficial contribution of vertical loading is nearly eliminated, as stress redistribution limits the frictional gains. For deeper degradation depths (e.g., 15 mm and beyond), vertical loading becomes detrimental, accelerating crack propagation, compression-induced shear, and localized concrete crushing beneath the shoe. This transition amplifies structural vulnerabilities as degradation intensifies and highlights the interplay between load distribution and material degradation.

Mesoscale simulations provide detailed insights into failure mechanisms. Degradation reduces the effective stiffness and load transfer efficiency by shortening the lever arm between compression under the shoe and tension in the reinforcement. As a result, horizontal reinforcement yields at lower forces under increased degradation, while concrete beneath the support shoe becomes increasingly susceptible to crushing. Even with a significant 67% increase in concrete strength (i.e., from 30 MPa to 50 MPa), ultimate load capacity improved by only 7.5%, indicating that steel reinforcement remains the governing factor in structural performance.

The reliability assessments conducted via probabilistic methods revealed important trends. For plain concrete and minimally reinforced concrete ($\rho_s = 0.8\%$), failure probabilities consistently exceeded acceptable thresholds for both moderate and severe accident scenarios. Fully reinforced concrete ($\rho_s = 1.6\%$) achieved reliable performance for moderate load scenarios, where reliability indices remained compliant with nuclear safety regulations for shallow irradiation depths. However, for severe load cases, reliability indices fell below acceptable limits as degradation depth increased. At deeper irradiation damage levels (e.g., beyond 10 cm), probabilities of failure rise sharply, indicating that current reinforcement designs fail to ensure compliance under severe conditions or extended operational lifetimes.

KEY FINDINGS

1. **Reinforcement Ratios**:
   Higher reinforcement ratios consistently increase load-bearing capacity, and steel yielding serves as the governing failure mode. While enhancing reinforcement improves structural reliability, it alone cannot fully offset the effects of severe material degradation.

2. **Impact of Vertical Loading**:
   At shallow irradiation damage depths (e.g, 0–5 mm), vertical loads are beneficial for horizontal load resistance in enhancing friction and stability beneath the support shoe. As irradiation damage depth increases (e.g., 15–20 mm), vertical loading promotes cracking, shear stresses, and concrete crushing, ultimately reducing horizontal load capacity.

3. **Effect of Irradiation-Induced Degradation**:

Irradiation significantly weakens mechanical properties through reduced compression zones, shorter lever arms, and higher reinforcement stresses. Concrete performance is constrained under irradiation even with increases in compressive strength; steel yielding continues to dominate the ultimate failure mode.

4. **Reliability Trends**:
   While fully reinforced concrete ($\rho_s = 1.6\%$) satisfies nuclear reliability standards under moderate loads and shallow irradiation degradation, it falls short for severe accidents or deeper degradation levels. Probabilities of failure for critical scenarios such as LOCA with seismic excitation exceed allowable thresholds at irradiation damage depths over 10 mm.
5. **Mechanical and Material Interactions**:
   As degradation progresses, the interplay between concrete crushing, crack propagation, and rebar yielding becomes more pronounced, reducing overall system reliability. Load redistribution mechanisms are increasingly compromised under combined vertical and horizontal forces.

LIMITATIONS OF THE PRESENTED WORK

This research represents a methodological approach to accurately and reliably assess the effects of irradiation on the structural capacity of the CBS and the RPV supports. In this work, a detailed analysis was presented for a shoe support that is based on available information about this support type. However, the analysis is not plant nor RPV specific and the results should not be taken as being specific to the plant used. Despite this limitation, this research emphasizes the importance of high fidelity modeling and rigorous reliability analysis in understanding complex failure mechanisms and its application to evaluating the performance of the CBS and RPV supports under extreme accident conditions.

Furthermore, a set of simplifying, but conservative assumptions were used in this study:

- Since the design details of the RPV supports were extracted from very old photo-scanned blueprints, many reinforcement details were missing. Thus, the research team had to depend on best engineering estimates rather than exact reinforcement details.
- The LOCA horizontal loading is overestimated since it does not account for the leak-before-break concept.
- The loads transferred from the RPV to the shoe support do not account for frictional losses between the support and the RPV pipes.
- The calculation of earthquake loading assumed rigid body motion for both the CBS and the RPV without including dynamic and damping effects.
- There was a conservative estimation of the damage depth due to irradiation. The concrete strength within that depth, as well as the change in the irradiation flux over the height of the RPV, were neglected.
- LOCA and earthquake loading effects were assumed to be algebraically additive. In reality, their conditional probability of occurrence and dynamic interactions need to be considered. However, this level of detailed dynamic analysis is not only out of the scope of this research but also requires plant and site specific details that were not available to the research team.
- Strength-based limit-state criteria were employed in the analysis. Even though significant load margins exist beyond the proposed failure criterion (e.g., steel yielding), the use of these limit states aligns with standard industry practice, which applies conventional limit-state criteria. It is generally acceptable in industry and regulatory practices to demonstrate that additional bearing capacity exists beyond the standard ultimate limit states.

With these limitations, the presented research furnishes a methodological approach for utility owners and stakeholders to use their site and plant specific data to obtain an accurate evaluation of their CBS and RPV support resilience against operational and accidental conditions as they age due to irradiation.

RECOMMENDATIONS FOR FUTURE WORK

To address the vulnerabilities identified in this work, several areas require further investigation and development.

- **Distributed Load-Path Designs**:
  Investigate advanced design geometries where load paths are distributed or redundant, which would reduce localized stresses beneath the support shoe and mitigate crack propagation.
- **Coupled Dynamic Analysis**:
  Extend simulations to account for time-dependent interactions between thermal gradients, dynamic earthquake loads, and pressure transients to better capture real-world failure conditions.
- **Revised Design Codes**:
  Develop enhanced nuclear design standards that integrate irradiation-aware degradation models, explicitly account for material and load uncertainties, and include probabilistic safety thresholds.
- **Service Life Planning**:
  Incorporate findings into operational guidelines for plants approaching 60–80 years of service life to ensure that preemptive measures are taken to safeguard infrastructure against extended irradiation and extreme load conditions.

By adopting these strategies, the nuclear industry can improve the safety margins of aging infrastructure, mitigate risks posed by long-term degradation, and enhance future designs to withstand extreme accident scenarios. The findings demonstrate that while current practices provide sufficient capacity for moderate scenarios, severe accidents coupled with irradiation highlight the need for more innovative and advanced structural solutions. These recommendations provide a foundation for future work aimed at ensuring the resilience and reliability of nuclear containment systems for decades to come.

8. REFERENCES

[1] D. Naus, "Primer on durability of nuclear power plant reinforced concrete structures - a review of pertinent factors," Oak Ridge National Laboratory and U.S. Nuclear Regulatory Commission, Washington, D.C., Technical Report NUREG/CR-6927, ORNL/TM-2006/529, Feb. 2007, H.L. Graves, III was the NRC Project Manager.

[2] International Atomic Energy Agency (IAEA), *Safety of Nuclear Power Plants: Design, Specific Safety Requirements*. Vienna, Austria: IAEA Safety Standards Series, SSR-2/1, 2012, Rev. 1.

[3] *ASME Boiler and Pressure Vessel Code Section III - Rules for Construction of Nuclear Facility Components Division 2 - Code for Concrete Containment*, American Society of Mechanical Engineers, 2007.

[4] International Atomic Energy Agency (IAEA), *Assessment and Management of Aging of Major Nuclear Power Plant Components Important to Safety* (TECDOC-1025 Volume II). Vienna, Austria: International Atomic Energy Agency, 1998.

[5] American Society of Civil Engineers (ASCE), *Seismic Design Criteria for Structures, Systems, and Components in Nuclear Facilities* (ASCE Standard 43-05). Reston, VA: ASCE, 2005.

[6] International Atomic Energy Agency (IAEA), *Severe Accident Management Programmes for Nuclear Power Plants*. Vienna, Austria: IAEA Safety Standards Series, NS-G-1.6, 2009, Safety Guide.

[7] European Committee for Standardization (CEN), *Eurocode 2: Design of Concrete Structures, General Rules and Rules for Buildings (EN 1992-1-1)*. Brussels, Belgium: European Standard, Comite Europeen de Normalisation (CEN), 2004, Available online at https://eurocodes.jrc.ec.europa.eu.

[8] United States Nuclear Regulatory Commission (NRC), *Regulatory guide 1.35: In-service inspection of prestressed concrete containment vessels and liners using tendon surveillance program*, Available online at https://www.nrc.gov, U.S. NRC, 2010.

[9] "Standard review plan for the review of safety analysis reports for nuclear power plants: Lwr edition," U.S. Nuclear Regulatory Commission, Tech. Rep. NUREG-0800, Formerly issued as NUREG-75/087.

[10] A. N. Society, "Design basis for protection of light water nuclear power plant against the effect of postulated pipe rupture," American Nuclear Society, Tech. Rep. ANSI/ANS 58.2, 1988.

[11] A. C. 318, "ACI CODE-318-19(22): Building code requirements for structural concrete and commentary (reapproved 2022)," American Concrete Institute, Tech. Rep., 2020.

[12] M. Kaplan, "Nuclear radiation and the properties of concrete," University of Cape Town, Tech. Rep. No. 35, 1983.

[13] S. Verrall and J. Fitzpatrick, "Design concepts to minimize the activation of the biological shield of light-water reactors," Commission of the European Communities, Tech. Rep. EUR 8804, 1985.

[14] I. Remec, "Radiation environment in concrete biological shields of nuclear power plants," Light Water Reactor Sustainability Program, 2013.

[15] P. Lobner, C. Donahoe, and C. Cavallin, "Overview and comparison of us commercial nuclear power plants - nuclear power plant system sourcebook," US Nuclear Regulatory Commission, Tech. Rep. NUREG/CR-5640, SAIC-89/1541, 1990.

[16] R. Cloud, "Structural mechanics applied to pressurized water reactor systems," *Nuclear Engineering and Design*, vol. 46, pp. 273–302, 1978.

[17] T. Mager et al., *Assessment and management of ageing of major nuclear power plant components important to safety: PWR pressure vessels*, International Atomic Energy Agency, IAEA-TECDOC-1120, Oct. 1999.

[18] A. Sharma, R. Eligehausen, and J. Asmus, "Experimental investigation of concrete edge failure of multiple-row anchorages with supplementary reinforcement," *Structural Concrete*, vol. 18, no. 1, pp. 153–163, 2017. DOI: https://doi.org/10.1002/suco.201600015

[19] A. Sharma, R. Eligehausen, and J. Asmus, "Analytical model for concrete edge failure of multiple row anchorages with supplementary reinforcement," in *9th International Comcference on Fracture Mechanics of Concrete and Concrete Structures*, V. Saouma, J. Bolander and E. Landis (Eds), 2016. DOI: https://doi.org/10.1002/suco.201600015

[20] B. Bokor, A. Sharma, and J. Hofmann, "Experimental investigations on the concrete edge failure of shear loaded anchor groups of rectangular and non-rectangular configurations," *Engineering Structures*, vol. 222, p. 111 153, 2020. DOI: https://doi.org/10.1016/j.engstruct.2020.111153

[21] I. Remec, T. Rosseel, K. Field, and Y. Le Pape, "Characterization of radiation fields for assessing concrete degradation in biological shields of NPPs," in *9th Topical Meeting of the Radiation Protection and Shielding Division of the American Nuclear Society – (RPSD-2016)*, Paris, France, Oct. 2016.

[22] B. Biwer, D. Ma, J. Xi, and Y. Jing2, "Review of radiation-induced concrete degradation and potential implications for structures exposed to high long-term radiation levels in nuclear power plants," US Nuclear Regulatory Commission, Tech. Rep. NUREG/CR-7280, ANL/EVS-20/8, 2021.

[23] S. Smith, "H.B. robinson unit 2 subsequent license renewal: Reactor vessel, vessel support and bioshield concrete exposure data," Westinghouse, Tech. Rep. CPL-REAC-TM-AA-000001, 2023.

[24] Y. Le Pape, M. Alsaid, and A. Giorla, "Rock-forming minerals radiation-induced volumetric expansion – revisiting the literature data," *Journal of Advanced Concrete Technology*, vol. 16, pp. 191–209, 2018. DOI: 10.3151/jact.16.191

[25] Y. Le Pape, K. Field, and I. Remec, "Radiation effects in concrete for nuclear power plants – Part II: Perspective from micromechanical modeling," *Nuclear Engineering and Design*, vol. 282, pp. 144–157, 2015.

[26] A. Cheniour et al., "A structural model of the long-term degradation of the concrete biological shield," *Nuclear Engineering and Design*, vol. 405, p. 112 217, 2023. DOI: https://doi.org/10.1016/j.nucengdes.2023.112217

[27] S. Sabatino et al., "Assessment of neutron-induced crack volume on aggregates of varied mineralogy and estimation of irradiation damage depth in the concrete biological shield," Oak Ridge National Laboratory, Tech. Rep. ORNL/SPR-2024/3581–M3LW-24OR0403035, 2024.

[28] D. Kambayashi, S. Sasano H. Sawada, K. Suzuki, and I. Maruyama, "Numerical analysis of a concrete biological shielding wall under neutron irradiation by 3D RBSM," *Journal of Advanced Concrete Technology*, vol. 18, pp. 617–632, 2020.

[29] J. Risner, A. Alpan, and J. Yang, "Radiation Evaluation Methodology for Concrete Structures," Oak Ridge National Laboratory, Oak Ridge, Tech. Rep. NUREG/CR-7281 ORNL/SPR-2020/1572, 2020.

[30] P. Bruck, "Guidance for aging management of concrete biological shields that utilize a neutron shield tank, basis for concrete biological shield wall for aging management," Electric Power Research Institute, Tech. Rep. 3002013051, 2018.

[31] U.S. Nuclear Regulatory Commission, "Nrc regulations title 10, code of federal regulations: Part 52 licenses, certifications, and approvals for nuclear power plants," US NRC, Tech. Rep. 10 CFR Part 52, 2024.

[32] I. Maruyama et al., "Development of the soundness assessment procedure for concrete members affected by neutron and gamma-irradiation," *Journal of Advanced Concrete Technology*, vol. 15, pp. 440–523, 2017.

[33] FENOC, “Beaver valley, unit 2, submittal of the updated final safety analysis report, revision 21,” First Energy Nuclear Operating Company, Tech. Rep. Docket No. 50-412, Shippingport, PA. ADAMS Accession No. ML14339A419. 2024.

[34] Exelon Generation, “Three mile island nuclear station, unit 1, updated final safety analysis report (ufsar), revision 24 fire hazards analysis report (fhar),” no. Revision 28 UFSAR and FHAR Reference Drawings Docket No. 50-289, ADAMS Accession No. ML19066A349, 2018.

[35] Entergy Operations Inc., “Arkansas nuclear one - unit 1 license renewal application,” no. Docket No. 50-313, ADAMS Accession No. ML003679667, 2000.

[36] Framatome, “Framatome reactor vessel and RCP TLAA and aging management review input to the ONS SLRA,” Tech. Rep. ANP-3898NP, Revision 0, 2021.

[37] Southern Nuclear, “Joseph m. farley nuclear plant updated final safety analysis report (revision 27),” BirminghamElleuch, AL, Tech. Rep. Docket Nos. 50-348 and 50-364, ADAMS Accession No. Chapter 3 Pt. 2 - ML17117A368; Chapters 4 and 5 - ML17117A369, 2017.

[38] M. Bolvin, Y. L’Huby, J. Quillico, J. Humbert, J. Thomas, and R. Hugenschmitt, “Mechanical behaviour of the reactor vessel support of a pressurized water reactor: Tests and analysis,” in *Proc. 8th Int. Conf. on Structural Mechanics in Reactor Technology (SMiRT-8)*, EDFx/Framatome collaborative test on PWR support ring, Brussels, Belgium, 1985, Paper H2/7.

[39] I. A. E. Agency, “Assessment and management of ageing of major nuclear power plant components important to safety: Reactor pressure vessels,” International Atomic Energy Agency, Tech. Rep. IAEA-TECDOC-1556, 2007, Contains description of WWER reactor pressure vessel design including support ring and thrust pads.

[40] Exelon Generation Company LLC, “Calvert cliffs nuclear power plant units 1 and 2, updated final safety analysis report, revision 49,” Kennett Square, PA, Tech. Rep. Docket Nos. 50-317 and 50-318, ADAMS Accession No. ML17354B239, 2017.

[41] Carolina Power & Light, “H.B. robinson steam electric plant, unit 2, revision 27 to updated final safety analysis report,” Tech. Rep. Docket No. 50-261, Hartsville, SC. ADAMS Accession No. ML17298A849 - Chapter 3, 2017.

[42] R. Cheverton, W. Pennell, G. Robinson, and R. Nanstad, “Impact of radiation embrittlement on integrity of pressure vessel supports for two pwr plants,” US Nuclear Regulatory Commission, Tech. Rep. NUREG/CR-5320, ONRL/TM010966, 1989, 249 p.

[43] Internal Analysis, *Rpv support seismic load calculation spreadsheet*, Unpublished internal design file, Horizontal 0.5g and Vertical 0.33g seismic load estimation method, 2025.

[44] S. Hosford, R. Mattu, R. Meyer, E. Throm, and C. Tinkler, “Asymmetric blowdown loads on pwr primary systems – resolution of generic task action plan a-2,” US Nuclear Regulatory Commission, Tech. Rep. NUREG-0609, Jan. 1, 1981.

[45] M. Alnaggar, Y.-J. Choi, and Y. Le Pape, “Assessment of the effect of the in-service irradiation-induced degradation on the structural performance of biological shields during a loss of coolant accidents,” Oak Ridge National Laboratory, Tech. Rep. ORNL/SPR-2023/3158, M3LW-23OR0403043, 2023.

[46] ASME, *ASME Boiler and Pressure Vessel Code, Section III: Rules for Construction of Nuclear Facility Components*, American Society of Mechanical Engineers, New York, NY, USA, 2023.

[47] American Concrete Institute, *ACI 349-13: Code Requirements for Nuclear Safety-Related Concrete Structures and Commentary*, American Concrete Institute, Farmington Hills, MI, USA, 2013.

[48] U.S. Nuclear Regulatory Commission, *Regulatory Guide 1.61: Damping Values for Seismic Design of Nuclear Power Plants*, Revision 1, U.S. NRC, Washington, DC, USA, 2007.

[49] U.S. Nuclear Regulatory Commission, *Regulatory Guide 1.92: Combining Modal Responses and Spatial Components for Seismic Response Analysis*, Revision 3, U.S. NRC, Washington, DC, USA, 2012.

[50] H. Özkan, "Effect of nuclear radiation on the elastic moduli of zircon," *Journal of Applied Physics*, vol. 47, pp. 4772–4779, 1976.
[51] H. Mohammed, H. Ahmed, R. Kurda, R. Alyousef, and A. F. Deifalla, "Heat-induced spalling of concrete: A review of the influencing factors and their importance to the phenomenon," *Materials*, vol. 15, no. 5, p. 1693, 2022. DOI: 10.3390/ma15051693
[52] U.S. Nuclear Regulatory Commission, "Regulatory Guide 1.60: Design response spectra for seismic design of nuclear power plants," US NRC Office of Nuclear Regulatory Research, Tech. Rep. Rev 2, 2014.
[53] J. Hong, "Studies of seismic analysis for reactor pressure vessel and internals of 600 mwe nuclear power plant," in *Proceedings of the 12th International Conference on Structural Mechanics in Reactor Technology (SMIRT12)*, 1993.
[54] T. R.-3. C. D. Team, "Relap5-3d code manual, volume 1: Code structure, system models and solution methods," Idaho National Laboratory, Tech. Rep. INL/MIS-15-36723, Jun. 1, 2018.
[55] C. Don Fletcher, C. B. Davis, and D. M. Ogden, "Thermal-hydraulic analyses of overcooling sequences for the H.B. robinson unit 2 pressurized thermal shock study," Idaho National Laboratory, Tech. Rep. NUREG/CR-3935, EGG-2335, 1985.
[56] D. Energy, "Updated final safety analysis report, revision no. 27, chapter 6, engineered safety features," US Nuclear Regulatory Commission, Tech. Rep. ADAMS ML17298A855, 2017.
[57] U. N. 2. Beaver Valley Power Station, "Updated final safety analysis report, revision 16, chapter 6," Vistra, Tech. Rep. NRC ADAMS ML14339A412, 2014.
[58] T. Esselman and P. Bruck, "Expected condition of concrete at age 80 of reactor operation," Lucius Pitkins, Inc., 36 Main Street, Amesbury, MA 01913, Tech. Rep. A13276-R-001, Sep. 2013.
[59] P. Bouniol and A. Aspart, "Disappearance of oxygen in concrete under irradiation: The role of peroxides in radiolysis," *Cement and Concrete Research*, vol. 28, no. 11, pp. 1669–1681, 1998.
[60] P. Bouniol, "State of knowledge on the water radiolysis in cemented waste forms and its approach by simulation," Commissariat à l'Energie Atomique, CEA / Saclay 91191 Gif-sur-Yvette Cedex France, Tech. Rep. CEA-R-6069, 2004, In French.
[61] V. Andreev and D. Kapliy, "Stress-state of a thick-walled cylindrical shell under the combined action of radiation and temperature field," *Advanced Materials Research*, vol. 1006-1007, pp. 177–180, 2014.
[62] Y. Le Pape, "Structural effects of radiation-induced volumetric expansion on unreinforced concrete biological shields," *Nuclear Engineering and Design*, vol. 295, pp. 534–548, 2015.
[63] Y. Le Pape, M. Alnaggar, and A. Cheniour, "Assessment of the effect of the irradiation-induced degradation on the in-service structural performance of the concrete biological shields," Oak Ridge National Laboratory, Tech. Rep. ORNL/SPR-2023/3031, M3LW-23OR0403013, 2023, 28 p.
[64] B. Pomaro, V. Salomoni, F. Gramegna, G. Prete, and C. Majorana, "Radiation damage evaluation on concrete within a facility for selective production of exotic species (SPES Project), Italy," *Journal of Hazardous Materials*, vol. 194, no. 0, pp. 169–177, 2011.
[65] P. Bruck, T. Esselman, B. Elaidi, J. Wall, and E. Wong, "Structural assessment of radiation damage in light water power reactor concrete biological shield walls," *Nuclear Engineering and Design*, vol. 350, pp. 9–20, 2019.
[66] Y. Khmurovska, P. Štemberk, T. Fekete, and T. Eurajoki, "Numerical analysis of VVER-440/213 concrete biological shield undernormal operation," *Nuclear Engineering and Design*, vol. 350, pp. 58–66, 2019.
[67] Y. Le Pape, "Irradiation effects on concrete used in nuclear power plants," *Nuclear Engineering and Design*, vol. 284, pp. 199–210, 2015. DOI: 10.1016/j.nucengdes.2014.12.036
[68] I. Remec, K. Field, and Y. Le Pape, "Progress in modeling radiation effects on concrete for nuclear applications," *Cement and Concrete Research*, vol. 140, p. 106 317, 2021.

[69] M. Elleuch and Y. Le Pape, "A model for estimating mechanical property degradation of concrete under neutron irradiation," *Journal of Nuclear Materials*, vol. 507, pp. 240–253, 2018.
[70] B. Pomaro, F. Gramegna, and G. Prete, "Numerical assessment of radiation-induced damage in the concrete biological shield of a pwr reactor," *Annals of Nuclear Energy*, vol. 38, no. 5, pp. 1199–1209, 2011. DOI: 10.1016/j.anucene.2010.12.005
[71] M. Cheniour, M. Alnaggar, and Y. Le Pape, "Modeling the structural degradation of irradiated concrete in nuclear reactor biological shields using nonlinear finite element analysis," *Engineering Structures*, vol. 285, p. 116 015, 2023. DOI: 10.1016/j.engstruct.2023.116015
[72] J. Mazars and G. Pijaudier-Cabot, "Continuum damage theory –application to concrete," *Journal of Engineering Mechanics – ASCE*, vol. 115, pp. 345–365, 1989.
[73] V. Bykov, A. Denisov, V. Dubrovskii, V. Korenevskii, G. Krivokoneva, and L. Muzalevskii, "Effect of irradiation temperature on the radiation expansion of quartz," *Atomnaya Energiya*, vol. 51, no. 3, pp. 593–595, Sep. 1981.
[74] Y. Le Pape, S. Sabatino, and E. Tajuelo Rodriguez, "Effects of aggregates mineralogy on the irradiation-induced damage in concrete biological shields," Oak Ridge National Laboratory, Tech. Rep. ORNL/SPR-2023/2912, 2023.
[75] N. Bowen, "The melting phenomenon of the plagioclase feldspars," *American Journal of Science*, vol. 35, no. 4th Series, pp. 577–599, 1913. DOI: http://dx.doi.org/10.2475/ajs.s4-35.210.577
[76] S. Goldich, "A study in rock-weathering," *The Journal of Geology*, vol. 46, no. 1, pp. 17–58, 1938.
[77] D. Whitney and B. Evans, "Abbreviations for names of rock-forming minerals," *American Mineralogist*, vol. 95, pp. 185–187, 2010.
[78] D. Beukelmann et al., "Safety assessment of reactor pressure vessel integrity for loss of coolant accident conditions," eng, *Journal of pressure vessel technology*, vol. 134, no. 1, 2012.
[79] WCAP-8082, "Pipe breaks for the LOCA analysis of the westinghouse primary coolant loo," Westinghouse Electric Corporation, P. O. Box 355, Pittsburgh, Pennsylvania 15230, Tech. Rep., 1973, proprietary.
[80] G. Cusatis, D. Pelessone, and A. Mencarelli, "Lattice discrete particle model (ldpm) for failure behavior of concrete. i: Theory," *Cement and Concrete Composites*, vol. 33, no. 9, pp. 881–890, 2011. DOI: 10.1016/j.cemconcomp.2011.02.021
[81] G. Cusatis, A. Mencarelli, D. Pelessone, and J. T. Baylot, "Lattice discrete particle model (ldpm) for failure behavior of concrete. ii: Calibration and validation," *Cement and Concrete Composites*, vol. 33, no. 9, pp. 891–905, 2011. DOI: 10.1016/j.cemconcomp.2011.02.022
[82] G. Cusatis, A. Mencarelli, D. Pelessone, and J. T. Baylot, "The lattice discrete particle model (ldpm) for the simulation of uniaxial and multiaxial behavior of concrete: Recent results," in *FraMCoS-7, Proceedings of the 7th International Conference on Fracture Mechanics of Concrete and Concrete Structures*, B. H. Oh and et al., Eds., Jeju, Korea: Korea Concrete Institute, 2010.
[83] M. Alnaggar, D. Pelessone, and G. Cusatis, "Lattice discrete particle modeling of reinforced concrete flexural behavior," *Journal of Structural Engineering*, vol. 145, no. 1, p. 04 018 231, 2019. DOI: 10.1061/(ASCE)ST.1943-541X.0002230
[84] J. Feng, W.-W. Sun, and B.-M. Li, "Numerical study of size effect in concrete penetration with ldpm," *Defence Technology*, vol. 14, no. 5, pp. 560–569, 2018. DOI: 10.1016/j.dt.2018.07.006
[85] E. A. Schauffert, G. Cusatis, D. Pelessone, J. L. O'Daniel, and J. T. Baylot, "Lattice discrete particle model for fiber-reinforced concrete. ii: Tensile fracture and multiaxial loading behavior," *Journal of Engineering Mechanics*, vol. 138, no. 8, pp. 834–841, 2012. DOI: 10.1061/(ASCE)EM.1943-7889.0000388

[86] M. Alnaggar, G. Cusatis, and G. D. Luzio, "Lattice discrete particle modeling (ldpm) of alkali silica reaction (asr) deterioration of concrete structures," *Cement and Concrete Composites*, vol. 41, pp. 45–59, 2013. DOI: 10.1016/j.cemconcomp.2013.04.007

[87] L. Shen, W. Li, X. Zhou, J. Feng, G. D. Luzio, and G. Cusatis, "Multiphysics lattice discrete particle model for the simulation of concrete thermal spalling," *Cement and Concrete Composites*, vol. 106, p. 103 462, 2020. DOI: 10.1016/j.cemconcomp.2019.103462

[88] M. Abdellatef and M. Alnaggar, "Energy-based coarse graining of the lattice-discrete particle model," *Journal of Engineering Mechanics*, vol. 146, no. 5, p. 04 020 026, 2020. DOI: 10.1061/(ASCE)EM.1943-7889.0001743

[89] L. Yang, M. Pathirage, H. Su, M. Alnaggar, G. D. Luzio, and G. Cusatis, "Computational modeling of expansion and deterioration due to alkali–silica reaction: Effects of size range, size distribution, and content of reactive aggregate," *International Journal of Solids and Structures*, vol. 234-235, p. 111 220, 2022. DOI: 10.1016/j.ijsolstr.2021.111220

[90] Y. L. Pape, M. Alnaggar, E. T. Rodriguez, and A. Brooks, "Irradiation effects on reinforced concrete structures – experimental and analytical study on irradiated concrete–steel bonding, modeling and simulation of structural response," NUREG/CR-7312, U.S. Nuclear Regulatory Commission, Tech. Rep., 2025.

[91] B. L. Smith, G. Cusatis, D. Pelessone, E. N. Landis, J. L. O'Daniel, and J. T. Baylot, "Discrete modeling of ultra-high-performance concrete with application to projectile penetration," *International Journal of Impact Engineering*, vol. 65, pp. 13–32, 2014. DOI: 10.1016/j.ijimpeng.2013.10.011

[92] M. Abdellatef, I. Boumakis, R. Wan-Wendner, and M. Alnaggar, "Lattice discrete particle modeling of concrete coupled creep and shrinkage behavior: A comprehensive calibration and validation study," *Construction and Building Materials*, vol. 211, pp. 629–645, 2019. DOI: 10.1016/j.conbuildmat.2019.03.274

[93] M. Alnaggar and N. Bhanot, "A machine learning approach for the identification of the lattice discrete particle model parameters," *Eng. Fract. Mech.*, vol. 197, pp. 160–175, Jun. 2018.

[94] Z. P. Bažant and E. Becq-Giraudon, "Statistical prediction of fracture parameters of concrete and implications for choice of testing standard," *Cem. Concr. Res.*, vol. 32, no. 4, pp. 529–556, Apr. 2002.

[95] J. C. on Structural Safety (JCSS), "Probabilistic model code," Joint Committee on Structural Safety, Zurich, Switzerland, 12th Draft JCSS-OSTL/DIA/VROU-10-11-2000, 2001, Online: http://www.jcss.byg.dtu.dk/Publications/Probabilistic_Model_Code.

[96] U. N. R. Commission and I. N. Laboratory, "An approach for using probabilistic risk assessment in risk-informed decisions on plant-specific changes to the licensing basis," U.S. Nuclear Regulatory Commission, Washington, DC, USA, NUREG/CR-7004 INL/EXT-10-19509, Sep. 2013, Available at https://www.nrc.gov/docs/ML1326/ML13260A310.pdf.

[97] C. A. Cornell, "A probability-based structural code," *Journal of the American Concrete Institute*, vol. 66, no. 12, pp. 974–985, 1969.

[98] A. M. Hasofer and N. C. Lind, "An exact and invariant first-order reliability format," *Journal of the Engineering Mechanics Division, ASCE*, vol. 100, no. EM1, pp. 111–121, 1974.

[99] A. H.-S. Ang and W. H. Tang, *Probability Concepts in Engineering Planning and Design, Volume II: Decision, Risk, and Reliability*. New York: John Wiley & Sons, 1984.

[100] R. E. Melchers, *Structural Reliability Analysis and Prediction*, 2nd. Chichester, UK: John Wiley & Sons, 2002.

[101] A. Olsson, G. Sandberg, and O. Dahlblom, "On latin hypercube sampling for structural reliability analysis," *Structural Safety*, vol. 25, no. 1, pp. 47–68, 2003.

[102] J. C. Helton and F. J. Davis, "Latin hypercube sampling and the propagation of uncertainty in analyses of complex systems," *Reliability Engineering & System Safety*, vol. 81, no. 1, pp. 23–69, 2003.
[103] R. P. Kennedy, C. A. Cornell, R. D. Campbell, S. Kaplan, and H. F. Perla, "Probabilistic seismic safety study of an existing nuclear power plant," *Nuclear Engineering and Design*, vol. 59, no. 2, pp. 315–338, 1980.
[104] I. Zentner, M. Gündel, and N. Bonfils, "Fragility analysis methods: Review of existing approaches and application," *Nuclear Engineering and Design*, vol. 323, pp. 245–258, 2017.
[105] U. N. R. Commission, "Assessment of combined accident sequences and seismic events," U.S. Nuclear Regulatory Commission, Washington, DC, USA, NUREG/CR-6919, Feb. 2007, Available at https://www.nrc.gov/docs/ML0703/ML070310029.pdf.
[106] R. P. Kennedy and M. K. Ravindra, "Seismic fragilities for nuclear power plant risk studies," *Nuclear Engineering and Design*, vol. 79, no. 1, pp. 47–68, 1984.
[107] A. S. Nowak and K. R. Collins, *Reliability of Structures*, 2nd. Boca Raton, FL: CRC Press, 2012.
[108] B. Ellingwood, T. V. Galambos, J. G. MacGregor, and C. A. Cornell, "Development of a probability based load criterion for american national standard a58," National Bureau of Standards, Washington, DC, USA, NBS Special Publication 577, 1980.
[109] U.S. Nuclear Regulatory Commission, "Design Guide – 1283: Safety-Related Concrete Structures for Nuclear Power Plants," U.S. Nuclear Regulatory Commission, Washington, DC, USA, Technical Report ID-NRC-2019-0100, 2019, Available at https://downloads.regulations.gov/NRC-2019-0100-0009/attachment_1.pdf.
[110] A. C. 349, "ACI CODE-349-23: Nuclear safety-related concrete structures—code requirements and commentary," American Concrete Institute, Tech. Rep., 2024.
[111] M. Kaplan, *Concrete radiation shielding, Nuclear physics, concrete properties, design and construction*. Longman Scientific and Technical, 1989.
[112] J. M. Biwer, S. D. Randeniya, and M. C. Vanderglas, "Variability analysis of compressive strength for irradiated concrete," *Nuclear Engineering and Design*, vol. 162, pp. 81–85, 1996. DOI: 10.1016/0029-5493(95)01151-6
[113] *Pra procedures guide: A guide to the performance of probabilistic risk assessments for nuclear power plants*, NUREG/CR-2300, available at: https://www.nrc.gov/reading-rm/doc-collections/nuregs/, U.S. Nuclear Regulatory Commission (NRC), 1983.
[114] S. M. Klug, G. A. Hache, S. J. Ball, and W. F. Harris, *Risk-informed assessment of degraded containment vessels*, NUREG/CR-6819, Available at: https://www.nrc.gov/reading-rm/doc-collections/nuregs/, U.S. Nuclear Regulatory Commission (NRC), Washington, D.C., 2001.
[115] I. Zentner, F. Poirion, and J. Sercombe, "Probabilistic seismic fragility analysis of reactor containment buildings," *Nuclear Engineering and Design*, vol. 237, no. 7, pp. 694–704, 2007. DOI: 10.1016/j.nucengdes.2006.10.003
[116] U. N. R. C. (NRC), *Ap1000 design control document, chapter 3, design of structures, components, equipment, and systems (tier 2)*, ML11171A453, Available online: https://www.nrc.gov/docs/ml1117/ml11171a453.pdf, Washington, D.C., 2011.
[117] P. Mag. "Areva installs finnish epr reactor vessel. "[Online]. Available: https://www.powermag.com/areva-installs-finnish-epr-reactor-vessel/
[118] Š. JS. "Škoda js will supply the french with key equipment for the british power plant. "[Online]. Available: https://www.skoda-js.cz/press/skoda-js-will-supply-the-french-with-key-equipment-for-the-british-power-plant/
[119] NucNet. "Steam generators and rpv installed at uae's barakah-4. "[Online]. Available: https://www.nucnet.org/news/steam-generators-and-rpv-installed-at-uae-s-barakah-4

[120] J. Tommila, “Thermal and structural analysis of reactor pressure vessel under design extension condition,” Master’s Thesis, LUT University, 2022.
[121] J. Misak, “History, specific design features, and evolution of vver reactors,” in *Nuclear Power Reactor Designs: From History to Advances*, J. Wang, S. Talabi, and S. B. y León, Eds., Academic Press (Elsevier), 2024, pp. 57–91.
[122] W. N. News. “Vessel installed at third tianwan unit. ”[Online]. Available: https://world-nuclear-news.org/Articles/Vessel-installed-at-third-Tianwan-unit
[123] S. Timoshenko and J. Goodier, *Theory of Elasticity*, T. Edition, Ed. McGraw-Hill, 1986.

APPENDIX A. SIMPLIFIED MODELING STRATEGY

APPENDIX A. SIMPLIFIED MODELING STRATEGY

The proposed structural model considers the effects of radiation and temperature within the thickness (i.e., r direction) of the biological wall. The constitutive model for irradiated concrete is assumed to be nonlinear elastic: the elastic parameters are a function of the radius r resulting from the irradiation damage. The free volumetric expansion and contraction of concrete are lumped into one single deformation $3\varepsilon_*$. The general constitutive equation is similar to that of thermo-elasticity, [123]:

$$\sigma_i = \left(k - \frac{2\mu}{3}\right) \mathrm{tr}\, \varepsilon + 2\mu\varepsilon_i - 3k\varepsilon_*, \tag{A.1}$$

where k and μ are, respectively, the local bulk and the shear moduli of the material, and ε_* is the unrestrained thermal expansion. The latter can be replaced by any other form of physically or chemically induced expansion, ε^*—the macroscopic expansion/contraction of concrete resulting from the effects of temperature elevation; shrinkage; and RIVE: $\varepsilon^* = f(\Delta T, \Delta m/m_0, \Phi)$, where ΔT, $\Delta m/m_0$ and Φ are the increase of temperature, the loss of mass (drying), and the neutron fluence, respectively. All these fields are spatially variable in the CBS. As a first approximation, a 1D cylindrical model is proposed, accounting primarily for the profiles of temperature, mass loss, and neutron fluence in the depth of the biological shield at the level of the RPV belt line, where the fluence is at its maximum. Hence, the materials properties subjected to degradation, volumetric expansion, and stress-strain fields are only functions of r. They represent the depth assuming the origin at the center of the reactor.

Because of the geometry of the biological shield, plane strain cylindrical conditions are assumed as $\varepsilon_z = 0$. The inner and outer radii of the biological shield wall are noted r_a and r_b, respectively. The displacement field u is only a function of the radius r. The radial and orthoradial strain fields derive from the displacement field:

$$\varepsilon_r = \frac{\partial u}{\partial r} \text{ and } \varepsilon_\theta = \frac{u}{r}. \tag{A.2}$$

The assumed confinement results in the development of vertical stresses:

$$\sigma_z = \lambda\left(\varepsilon_r + \varepsilon_\theta\right) - 3k\varepsilon^*. \tag{A.3}$$

The expressions of the radial and orthoradial stresses read as follows, respectively:

$$\sigma_r = M\varepsilon_r + \lambda\varepsilon_\theta - 3k\varepsilon^*, \tag{A.4}$$

$$\sigma_\theta = \lambda\varepsilon_r + M\varepsilon_\theta - 3k\varepsilon^*. \tag{A.5}$$

Local force equilibrium, $\partial\sigma_r/\partial r + (\sigma_r - \sigma_\theta)/r = 0$, yields after calculation to the ordinary differential equation (ODE):

$$M\frac{\partial^2 u}{\partial r^2} + \left(\frac{\partial M}{\partial r} + \frac{M}{r}\right)\frac{\partial u}{\partial r} + \left(\frac{\partial \lambda}{\partial r} - \frac{M}{r}\right)\frac{u}{r} - 3\frac{\partial}{\partial r}\left(k\varepsilon^*\right) = 0, \tag{A.6}$$

where M is the P-wave modulus, or $M = k + 4\mu/3 = E(1-\nu)/(1+\nu)/(1-2\nu)$, and λ is Lamé's first parameter, $\lambda = k - 2\mu/3$. Both M and λ are functions of the radius as a result of the irradiation damage.

The boundary conditions are obtained by writing the equality of the radial stress with the inner pressure p at the inner diameter (ID) and outer diameter (OD) of the biological shield—$\sigma_r(r_a) = p$ and $\sigma_r(r_b) = 0$. In-service, $p = 0$. During a LOCA, $p(t) \geq 0$.

The fluence profiles are inputs of the model.

It is not possible to obtain an analytical solution of the ordinary differential equation Eq. (A.6) in the general case of RIVE and elasticity varying with the radius. Its resolution is performed using a finite difference solver programmed with Scilab (open source software for numerical computation http://www.scilab.org/). For the sake of simplicity, an explicit scheme (second order forward) was chosen: $\partial u/\partial r \simeq (u_{n+1} - u_n)/\delta_r$ and $\partial^2 u/\partial r^2 \simeq (u_{n+2} - 2u_{n+1} + u_n)/\delta_r^2$, where δ_r is the discretized space-step. After development, the explicit displacement $u_{n+2} = u(r + 2\delta_r)$ is given by the equation

$$u_{n+2} = \left(2 - \frac{\delta_r}{r} - \frac{\delta_r}{M}\frac{\partial M}{\partial r}\right)u_{n+1} - \left(1 - \frac{\delta_r}{r} - \frac{\delta_r^2}{r^2} + \frac{\delta_r}{M}\frac{\partial M}{\partial r} + \frac{\delta_r^2}{rM}\frac{\partial \lambda}{\partial r}\right)u_n + 3\frac{\partial(k\varepsilon^*)}{\partial r}, \tag{A.7}$$

where u_{n+1} and u_n are the previously computed displacements at $r + \delta_r$ and r, respectively. The derivatives of M, λ, and $k\varepsilon^*$ are also computed with an explicit scheme. Recurrence relation (A.7) is valid for all n but requires the calculation of u_1 and u_2 to be applied. The pressure applied at the inner surface of the biological wall $\sigma_r(r_a) = p$ reads:

$$u_2 = u_1\left(1 - \frac{\lambda(r_a)}{M(r_a)}\frac{\delta_r}{r_a}\right) - 3\frac{k(r_a)}{M(r_a)}\varepsilon^*(r_a)\delta_r + \frac{p}{M}\delta_r. \tag{A.8}$$

Thus, once u_1 is given, $u_{n=2,\ldots}$ can be explicitly calculated using (A.8) once and can then be calculated using (A.7). The second boundary condition is given by the absence of radial stress at the outer surface of the biological shield, $\sigma_r(r_b) = 0$. Because of the second-order forward integration scheme chosen, this condition cannot be implemented explicitly. The solving algorithm iteratively finds u_1 so that the computed value of $|\sigma_r(r_b)| \leq \epsilon$, where ϵ is a given small error ($\approx 10^{-3}$ MPa).